

On the Development of Wideband Direct Detection Focal Plane Arrays for THz Passive Imaging Applications

van Berkel, S.L.

DOI

[10.4233/uuid:bf37535b-3f93-42ab-a337-22aec9cdf981](https://doi.org/10.4233/uuid:bf37535b-3f93-42ab-a337-22aec9cdf981)

Publication date

2020

Document Version

Final published version

Citation (APA)

van Berkel, S. L. (2020). *On the Development of Wideband Direct Detection Focal Plane Arrays for THz Passive Imaging Applications*. [Dissertation (TU Delft), Delft University of Technology]. <https://doi.org/10.4233/uuid:bf37535b-3f93-42ab-a337-22aec9cdf981>

Important note

To cite this publication, please use the final published version (if applicable). Please check the document version above.

Copyright

Other than for strictly personal use, it is not permitted to download, forward or distribute the text or part of it, without the consent of the author(s) and/or copyright holder(s), unless the work is under an open content license such as Creative Commons.

Takedown policy

Please contact us and provide details if you believe this document breaches copyrights. We will remove access to the work immediately and investigate your claim.

**On the Development of
Wideband Direct Detection Focal Plane Arrays
for THz Passive Imaging Applications**

**On the Development of
Wideband Direct Detection Focal Plane Arrays
for THz Passive Imaging Applications**

DISSERTATION

for the purpose of obtaining the degree of doctor
at Delft University of Technology
by the authority of the Rector Magnificus, Prof. dr. ir. T.H.J.J. van der Hagen,
Chair of the Board for Doctorates,
to be defended publicly on
Monday 13 July 2020 at 15:00 o'clock

by

Sven Leander VAN BERKEL

Master of Science in Electrical Engineering,
Delft University of Technology, The Netherlands,
born in Leiden, The Netherlands.

This dissertation has been approved by the promotor.

Composition of the doctoral committee:

Rector Magnificus,	Chairman
Prof. dr. N. Lombart Juan,	Delft University of Technology, promotor
Prof. dr. A. Neto,	Delft University of Technology, promotor
Dr. D. Cavallo,	Delft University of Technology, co-promotor

Independent members:

Prof. dr. J. Stake,	Chalmers University of Technology, Sweden
Prof. dr. J. Costa,	University Institute of Lisbon, Portugal
Prof. dr. K. Doris,	TU Eindhoven & NXP Semiconductors, Netherlands
Prof. dr. A. Yarovoy,	Delft University of Technology, Netherlands

Reserve member:

Prof. dr. L.C.N. de Vreede,	Delft University of Technology, Netherlands
-----------------------------	---



European Research Council
Established by the European Commission

The work presented in this thesis has been performed at TU Delft and financed by the Dutch Technology Foundation STW (Project Terahertz silicon-Integrated CAMera, TiCAM, 13325) and co-supported by the European Research Council starting grant (ERC-2014-StG LAA-THz-CC), No. 639749.

Keywords: millimeter-waves, submillimeter-waves, Terahertz, ultrawideband, passive imaging, radiometry, schottky barrier diodes, leaky-waves, double slot, connected array, CMOS, Focal Plane Arrays.

Cover design by: Daniele Cavallo & Sven van Berkel.

Printed by: Ipskamp Drukkers B.V., Enschede, Netherlands.

Copyright © 2020 by S.L. van Berkel. All rights reserved.

An electronic version of this dissertation is available at: <http://repository.tudelft.nl/>

ISBN 978-94-028-2093-5

To my family

Preface

The work presented in this dissertation is performed in the framework of a project that goes by the name TiCAM, which is an acronym standing for Terahertz silicon-Integrated CAM-era. The project TiCAM is funded by the Dutch Technology Foundation STW (13325), co-funded by a European Research Council starting grant (LAA-THz-CC 639749) and supported by NXP Semiconductors and Global Foundries. A tremendous growth in interest for Terahertz (THz) imaging and sensing applications has been observed in the last two decades. THz cameras can produce astonishing pictures of galaxies and deep-space, ancient mummies and fossils can be investigated and fatal diseases such as cancer can be investigated in a different way, hopefully coming to aid in this fight. Despite the great potential for more large-volume applications, such as pedestrian detection for the automotive industry, a widespread deployment is still restrained by the size, cost and performance of THz sources and detectors. The TiCAM project focuses on obtaining an in depth understanding of the design, modeling and characterization of THz imaging cameras with the purpose of realizing low-cost imaging applications. Low-cost and large-volume imaging applications might be enabled when many pixels can be fabricated simultaneously in silicon technologies such as CMOS, that are sufficiently sensitive so that they can operate without additional THz sources.

The work that is described in this dissertation is performed in a tight collaboration between the Terahertz Sensing Group and the Electronics Research Laboratory, at Delft University of Technology, Delft, The Netherlands. In total, three PhD-students were involved in this project. This thesis mainly focuses on the full system optimization, antenna (array) design and the quasi-optics. The dissertation of E.S. Malotaux will focus on the detection architecture and detail the different trade-offs occurring when targeting an advanced node CMOS integration. The dissertation of C. de Martino will detail on the high-frequency characterization and calibration of the passive and active devices used to realize such cameras.

The first prototypes, not reported in this dissertation, were fabricated using a TSMC bulk CMOS technology sponsored by NXP Semiconductors. These initial prototypes, together with the fruitful discussions with Maarten Vertregt who is with NXP Semiconductors, resulted in the vital design experience before fabricating the reported prototypes via the University Program of Global Foundries. The ERC starting grant supported a continuation of the project to investigate array architectures based on overlapped feeds, leading to the design and fabrication of a leaky-wave enhanced connected array.

Contents

Preface	i
Table of Contents	iii
1 Introduction	1
1.1 THz Imaging and Applications	1
1.1.1 Exploration of the Electromagnetic Spectrum	1
1.1.2 A Wide Variety of THz Imaging and Sensing Applications	3
1.1.3 State-of-the-Art of >1k-Pixel FPAs	4
1.2 Wideband Quasi-Optical Antennas	6
1.3 Low NEP THz Direct Detectors in CMOS	9
1.4 Goals and Methodology	10
1.5 Contributions in the Thesis	10
1.6 Outline of the Thesis	11
2 THz Imaging using Uncooled Wideband Direct Detection Focal Plane Arrays	15
2.1 Introduction	15
2.2 Quasi-Optical Radiometric System	17
2.2.1 Imaging Speed	18
2.2.2 Focal Plane Sampling and Jiggling	21
2.3 FPA Design	24
2.3.1 FPA Configurations	24
2.3.2 Bandwidth Utilization	25
2.3.3 Maximizing Imaging Speed with an Undersampled FPA	26
2.4 Image Quality in Undersampled Arrays	28
2.5 Realistic Feeds	32
2.6 Conclusion	35
3 Scenario Analysis: Pedestrian Detection for the Automotive Industry	37
3.1 Scenario Description	37
3.2 Field-of-View and Resolution	39
3.3 Temperature Sensitivity	40

3.3.1	Temperature Sensitivity for a Distributed Source	41
3.3.2	Coupling Efficiency to a Pedestrian	42
3.3.3	High Contrast: Temperature Sensitivity in Cold Weather	43
3.3.4	Low Contrast: Temperature Sensitivity in Warm Weather	45
3.4	Conclusion	46
4	Wideband Double Leaky Slot Lens Antennas in CMOS at THz Frequencies	47
4.1	Introduction	47
4.2	Leaky-wave Radiation in a CMOS Process	49
4.2.1	Leaky-Wave Radiation	50
4.2.2	Minimum Metal Density Requirements in CMOS	52
4.2.3	Effective Anisotropic Layers for Metal Fill	52
4.3	Center-fed Antenna for Direct Detection	54
4.3.1	Double Leaky Slot Design in Semi-Infinite Silicon	54
4.3.2	Simulated Antenna Performance with a dielectric lens	59
4.4	Design of a CPW-fed Antenna	61
4.5	Fabrication and Measurements Results of the CPW-fed Antenna	64
4.5.1	Impedance Measurement	66
4.5.2	Quasi-Optical Measurement Setup for Gain Patterns	67
4.5.3	Measured Near-Field Gain Patterns	69
4.5.4	Recovered Silicon Lens Antenna Gain Patterns	73
4.6	Conclusion	73
5	Radiometric Modeling and Performance of a THz Direct Detector in 22-nm CMOS	75
5.1	Introduction	75
5.2	Passive THz Imaging	77
5.3	Schottky Barrier Diodes in a Differential Voltage Read-Out	79
5.4	Radiometric Performance	84
5.4.1	Radiation Patterns	84
5.4.2	Noise Spectral Density	87
5.4.3	Detector Voltage Responsivity	90
5.4.4	Noise Equivalent Power and Temperature Sensitivity	94
5.5	Conclusion	97
6	Tightly Sampled Leaky-Wave Connected Array with Polarization Re-Usage	99
6.1	Introduction	99
6.2	Leaky-Wave Enhanced Feeds	102
6.3	System Parameters and Statement of the Problem	103
6.4	Mutual Coupling in Tightly Sampled Connected Arrays	105
6.5	Dual Polarized Array Design	109

6.6	12-Pixel Prototype in 22-nm CMOS	115
6.7	Conclusion	119
7	Conclusions and Future Prospects	121
7.1	Analysis of FPA Architectures in Imaging Speed and Resolution	122
7.2	Design of a Wideband THz Direct Detector in a CMOS Technology	123
7.2.1	Efficient Wideband Antennas in CMOS	123
7.2.2	Analysis of the Radiometric Performance of THz Direct Detectors	124
7.3	Design of Multi-Beam Wideband THz Direct Detector Arrays	124
7.4	Future Outlooks	125
7.4.1	Future Prospects for the Wideband Integrated FPA	125
7.4.2	Future Prospects for Future Passive Imaging Applications	125
7.5	Research Outputs	126
A	Resolution Limits for Isolated and Distributed Sources	127
A.1	Diffraction Limit in the Focal Plane	127
A.1.1	Isolated Sources	128
A.1.2	Distributed Sources	129
A.1.3	Rayleigh Limit and Diffraction Limit	130
A.2	Sampling and Interpolation	132
B	NEP for Cryogenically Cooled Focal Plane Arrays	135
B.1	Temperature Sensitivity, Imaging Speed and Noise Equivalent Power	135
B.2	FPA Design for Cooled Systems	138
B.2.1	FPA Configurations	138
B.2.2	Bandwidth Utilization	139
C	Greybodies and Sensitivity to Undesired Sources	141
C.1	Greybodies and Radiometric Temperature	141
C.2	Received Power by Undesired Sources	142
C.3	Sensitivity to Instrument Box and Sky-Background	145
D	Current Responsivity of Schottky Barrier Diodes	147
D.1	Lumped Element Model	148
D.2	Current Responsivity	150
D.2.1	Low Frequency Current Responsivity	150
D.2.2	Power Transfer Efficiency	154
D.2.3	High Frequency Current Responsivity	156
E	Experimental Extraction of SBD model	157
E.1	IV-curve	157
E.2	Junction Capacitance	159
	Bibliography	161

Summary	177
Samenvatting	179
List of Publications	183
Propositions Accompanying the Doctoral Thesis	187
About the Author	189
Acknowledgments	191

Chapter 1

Introduction

1.1 THz Imaging and Applications

1.1.1 Exploration of the Electromagnetic Spectrum

Imaging initially referred to the concept of recording the view that is seen by the human eye. Already in the 1800's the first photographs were recorded using the *camera obscura* phenomenon. In such camera, visible light was recorded on light-sensitive materials via a pinhole in the wall of a dark chamber, as shown in Fig. 1.1(a) and (b). However, in 1800, a form of radiation that cannot be seen by the human eye, the infrared (IR) rays, was already discovered by Sir William Herschel [1]. It was understood that an incredible amount of information can be observed in the universe, but without the proper tools and detectors this information is hidden from the human eye. The thermocouple, developed in 1830 by Leopoldo Nobili [2], and the bolometer invented in 1880 by Samuel Pierpont Langley [3], are the first mature detectors of IR radiation, both devices still being widely used in the present day. The first advanced civilian application was the detection of icebergs, for which the technology was patented by Bellingham in 1915 [4], a few years after the disastrous first trip of the Titanic in 1912.

The electromagnetic spectrum was explored much further at a fast pace since the demonstration of electromagnetic waves by Heinrich Hertz in 1889 [8]. Imaging was no longer only restricted to optical light that is defined by the electromagnetic radiation with a frequency roughly from 400 Terahertz (THz) to 800 THz. Higher frequencies such as X-rays were discovered by Röntgen in 1895 while microwave imaging was realized by the development of the radar that fast-tracked during World War II. Radiation in the THz regime, also referred to as submillimeter waves (submm-waves), is defined in the portion of the electromagnetic spectrum that lies between 300 GHz to 3 THz. Imaging in this regime remained more or less unexplored for a long time due to the absence of efficient electronics above 100 GHz and, secondly, the absence of thermal (black-body) sources or detectors below 10 THz. From the early 1960's, radio-astronomers began to work in the millimeter-wavelength region [9] while the interest in submm-wave astronomy rapidly increased in the 1970's [10]. It was in 1976 when transmission data of various dielectric

materials using a laser source below 1 THz was presented [6], while proving the applicability by producing the first THz images shown in Fig. 1.1(c), demonstrating concealed object detection. Another application of THz imaging was demonstrated directly after in 1978 with a real-time quality-control of the insulation in power cables [11]. A ground-breaking first step towards passive THz imaging (radiometry) for concealed object detection was achieved by Hodges in 1980, where the feasibility of radiometric detection of metallic objects in the 100-220 GHz band was presented by using a heterodyne receiver with Schottky diode mixers [12]. Despite the extremely promising results in these works, the research for imaging applications was more or less put on hold since the technology was only suitable for demonstrations in a laboratory. The development of optically generated THz sources in the 1970s and 1980s [13, 14] was however the first step that led to the first THz time-domain spectroscopic instrument, developed in 1995 by Hu and Nuss [7, 15], that provided the first images from a THz time-domain system where the work presented a transmission image of a packaged integrated circuit and a fresh- and dried tree leaf, shown in Fig. 1.1(d).

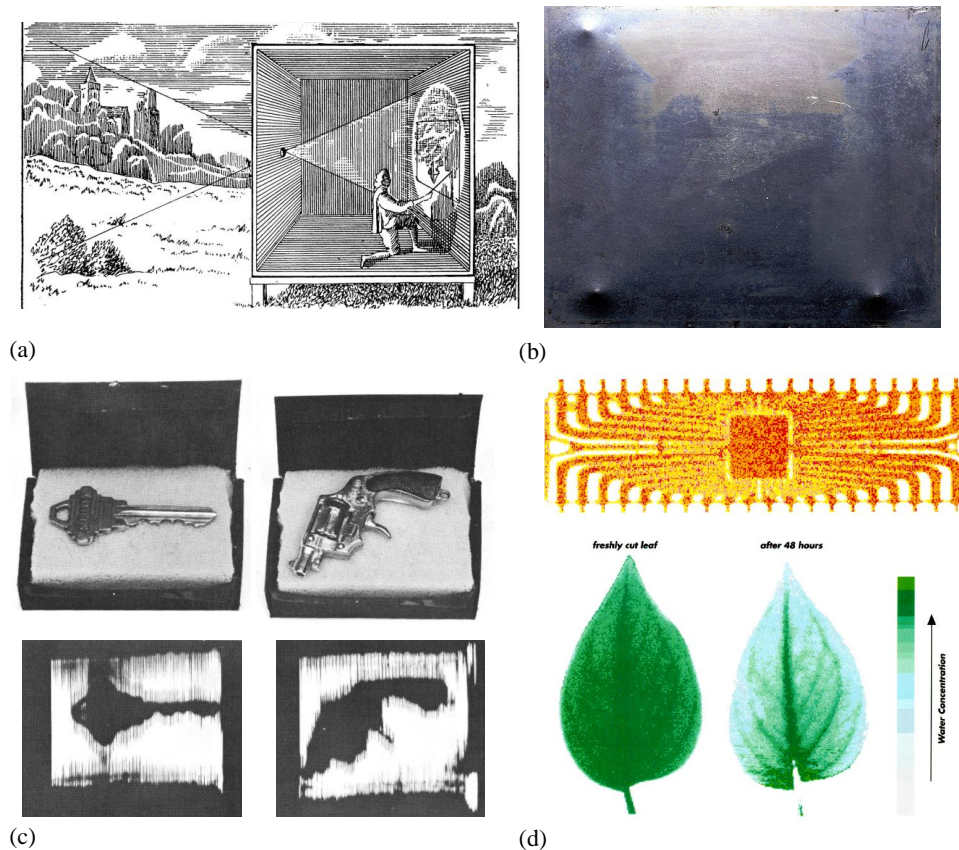


Figure 1.1: First images in the optical and THz regime. (a) Illustration of the camera obscura phenomenon [5]. (b) One of the oldest preserved photographs by Joseph Nicéphore Niépce in 1826. (c) First demonstration of concealed object detection using laser sources below 1 THz, 1976 [6]. (d) First images using a THz time-domain spectroscopic image of an integrated circuit packaged in plastic (top) and a fresh and dried tree leaf, 1995 [7].

Since then, there has been a vast increase in research efforts in THz sources, detectors and imaging methodologies and, with that, the amount of practical THz imaging applications that can be realized is still growing nowadays.

1.1.2 A Wide Variety of THz Imaging and Sensing Applications

The unique and intrinsic capability of THz radiation, as opposed to far-infrared and optical radiation, to propagate reasonably well through thin layers of plastics and clothing, and the spectroscopic capabilities due to many interesting molecular absorption lines while propagating through a non-vacuum, bring the fields of THz imaging and sensing to the attention of a wide range of applications, ranging from astronomy, medical and biological imaging, security screening, industrial process and quality control to pedestrian detection [16, 17].

As was already demonstrated in 1975 with the first THz images shown in Fig. 1.1(c) [6], a clear application has been concealed object detection [21, 22]. The unique spectral signatures of drugs [23] and explosives [24] allows for distinguishing those using spectroscopic imaging systems [25]. The transmission properties of THz radiation through clothing and plastics [22] allows for concealed weapon detection, while the low atmospheric attenuation in rain [26] and fog at relatively large distance (~ 25 meter) below 500 GHz [27] also enables stand-off detection. State-of-the-art THz imagers for stand-off detection have been realized as active radar [18, 28], fully passive with cooled superconducting bolometer arrays [29, 30] or a combination of passive sensors with active radar [31, 32]. In Fig. 1.2(a) an example is shown of the THz imaging radar at 675 GHz, presented in [18].

Apart from identifying explosives or drugs, spectroscopy is also extremely useful for astronomical applications [33] or different biological and medical applications [34, 35]. For example, breast and lung cancer, liver disease or diabetes can be analyzed via THz gas

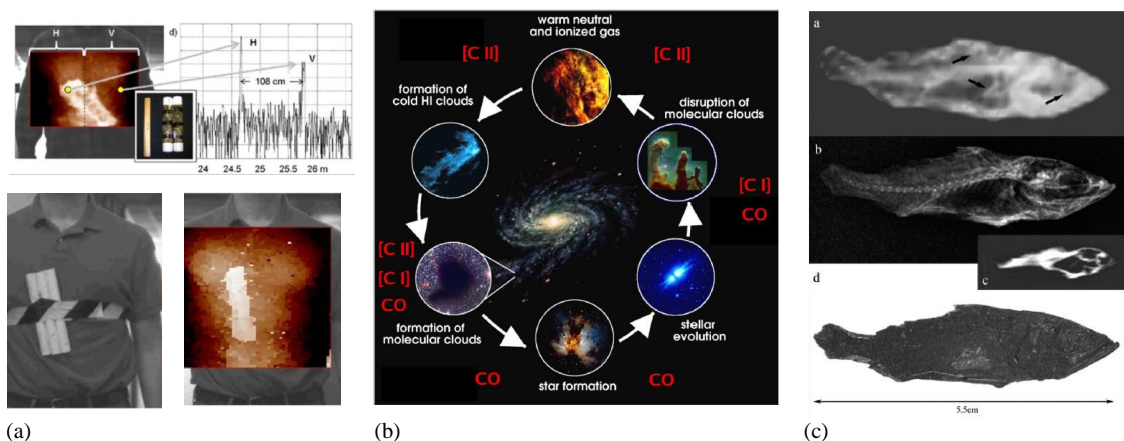


Figure 1.2: Examples of THz imaging applications. (a) THz imaging radar image at 675 GHz for concealed weapon detection [18] (b) Stages of interstellar clouds for molecular astronomy, after [19] (c) Terahertz (top), X-ray (middle), optical (bottom) image of an ancient Egyptian mummified fish, after [20].

spectroscopy since the absorption lines around 245 GHz and 500 GHz are biomarkers for those diseases [36]. The spectral lines in the THz regime also provide an immense amount of information regarding star and planet formation [19]. In Fig. 1.2(b) the life-cycles of interstellar clouds are shown that can be identified with molecular astronomy [19]. Large Focal Plane Arrays (FPAs) for astronomical THz imaging are often cryogenically cooled to achieve the extreme sensitivities or imaging speeds required [37, 38].

Another exciting application is THz tomography, that is demonstrated for archaeological findings such as ancient pottery [39], mummies and human bones [20, 40]. In Fig. 1.2 an ancient Egyptian mummified fish is shown in a Terahertz image (top), X-ray image (middle), optical image (bottom) [20]. Fast THz volume tomography has already been demonstrated [41, 42], whereas low-cost tomography using silicon sources has shown promising first results [43].

The aforementioned applications might not be considered to be consumer applications suitable for a widespread deployment and mass production. However, THz imaging and sensing might be very attractive for applications such as radar gesture control [44], pedestrian detection for the automotive industry, or automotive radar that now already operate up to 80 GHz [45, 46]. These radar systems could be extended to 140-300 GHz to reach better resolutions [47]. Ultimately, this is extended into the THz regime, which is however challenging due to absence of efficient coherent circuitry to retain the phase information of the signal. In general, the widespread deployment of THz imaging applications is still restrained by the size, cost and integration or packaging capabilities of THz equipment [43]. It is not only challenging to efficiently integrate THz sources but also the fabrication of large pixel arrays, necessary for a large instantaneous Field-of-View (FoV), is enormously more complex and costly in the submm-wave regime as opposed to large far-infrared bolometric arrays or optical CCD and CMOS cameras. Efforts have been made in the development of cameras that combine the unique radiation characteristics of these different EM-spectra [48].

Low-cost and large-volume THz imaging applications might be enabled when large >1k-Pixel FPAs can be fabricated in silicon technologies such as CMOS, that are sufficiently sensitive so that they can operate without additional THz sources. This dissertation focuses on the development of these arrays for passive imaging applications.

1.1.3 State-of-the-Art of >1k-Pixel FPAs

THz imaging can be performed active, i.e. with external illumination sources, or passive, i.e. radiometric. The detection of the coherent or incoherent signal can also be performed coherently with active circuitry that down converts the signal to IF with mixers and local oscillators, or incoherently with (thermal) absorbing or rectifying devices that detect power [49]. In microwave and millimeter wave radiometry much effort has been made in the development of efficient amplification circuitry and tunable coherent circuitry for large arrays, such as the Local Oscillators (LOs) and mixers necessary for coherent (heterodyne) detection [50]. Using coherent circuitry, a higher Signal-to-Noise Ratio (SNR) can usually be achieved thanks to the efficient amplifiers available. However, in the sub-millimeter

regime of the electromagnetic spectrum, the design of compact (integrated) active circuitry is still considered to be a challenging task [43, 51]. Detection at sub-millimeter wave frequencies would then be preferably performed incoherently (i.e. direct detection), in the absence of (pre-)amplifiers or mixers. Such architectures require a quasi-optical system with lenses or reflectors in combination with a FPA in order to generate the image. Incoherent detectors also have the advantage of supporting an easier read-out and a lower power consumption. This enables the fabrication of a large number of detectors in the FPA when using integrated solutions such as CMOS [52] or superconducting technologies [38, 53]. Nowadays, the detection of THz radiation can be realized with numerous type of detection technologies and methods, all with different underlying physical principles [49]. The first passive (mm-wave) imaging systems, consisting of diodes operating around 90 GHz [22] and bolometers [54], only had few detectors, resulting in a large image acquisition time and/or a small Field-of-View (FoV). Since then, in order to achieve a sufficient SNR for fast frame rates and extreme sensitivities, FPAs have been cryogenically cooled to decrease the electronic/thermal noise contributions and fabricated in integrated technologies to increase the FoV [29, 48]. Ultimately, the SNR is limited by the (thermal) fluctuations of the signal itself, i.e. background-noise limited. For example, the cryogenically cooled FPA of antenna coupled kinetic inductance detectors (KIDs) in [38] is background-noise limited with a measured Noise Equivalent Power (NEP) of $\text{NEP} = 3 \cdot 10^{-19} \text{ W}/\sqrt{\text{Hz}}$. In a low-cost consumer application, the detectors cannot be cooled until the background-noise limit and the systems will be detector-noise limited.

The performance of a radiometric imaging system can be quantified using its temperature sensitivity, i.e. the minimum temperature difference of the blackbody source that can be distinguished from the noise contributions. This temperature sensitivity is referred to as

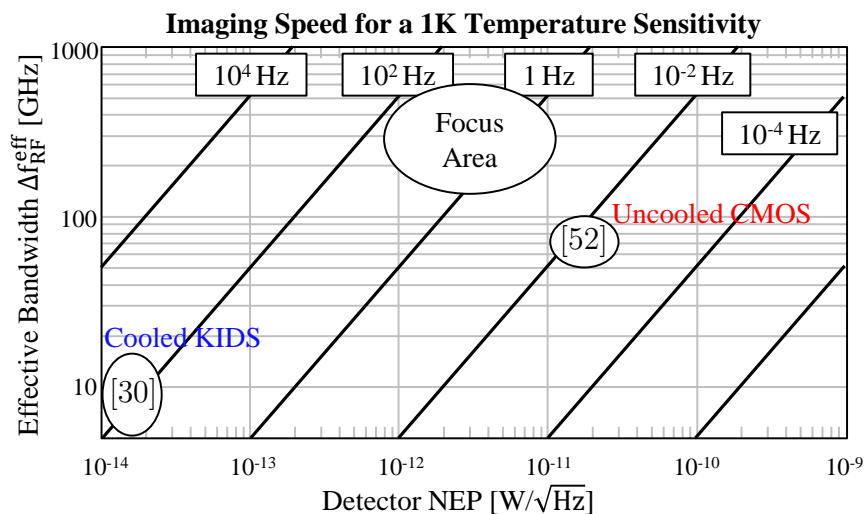


Figure 1.3: Imaging speed for 1 K temperature sensitivity as is defined by (2.1) in Chapter 2 for state-of-the-art passive imagers with more than 1k-pixels and a measured temperature sensitivity: Cryogenically cooled kinetic inductance bolometers in [30] and uncooled CMOS detectors in [52]. Furthermore, the focus area of this work is indicated.

the Noise Equivalent Temperature Difference (NETD). In [55] it is shown that a sub-Kelvin NETD is required for a proper detection in a security imaging scenario. Such requirement will be similar for applications such as pedestrian detection for the automotive industry. In Fig. 1.3 the achievable imaging speed is shown with the diagonal lines when a 1K NETD is required. As will be derived in Chapter 2, for a detector noise limited system, the imaging speed and NETD depend on the detector NEP and bandwidth of the system. For real-time applications, a detector NEP in the order of a few $\text{pW}/\sqrt{\text{Hz}}$ is required together with a few hundred of GHz of bandwidth, as indicated by the *Focus Area* in this figure.

Measurements of the temperature sensitivity, using a calibrated black body source, have been done for [30] and [52]. A cooled FPA of KIDs operating at 7 K has been proposed in [30]. This FPA is detector-noise limited, with a measured NETD between 110 and 190 mK for 0.5 s of detector integration time with a parallel read-out of the detectors. The optical efficiencies presented in [30] suggest an effective bandwidth around 10 GHz.¹² The *uncooled* FPA in [52], based on 32×32 CMOS ring antennas, has sensitivity measurements presented in [56], yielding a 20.86 K sensitivity for an integration time of 5.7 minutes with a consecutive read-out of the detectors.³ The measured noise, integrated over a 500 kHz post-detection bandwidth, is reported to be 12 nW.⁴ The maximum imaging speeds of [52] and [30] to achieve a 1 K temperature sensitivity (2.1) are compared in Fig. 1.3, yielding a 55 to 165 Hz refresh-rate for [30] and a $7 \cdot 10^{-3}$ Hz refresh-rate⁵ for [52]. Other large uncooled FPAs, without sensitivity measurements, have been presented to operate with microbolometers [57, 58, 59], heterostructure backward diodes [60], or MOSFETs in CMOS [61].

From Fig. 1.3 it is clear that there is a need of wideband quasi-optical antennas together with detector characterized with a detector NEP in the order of $1 \text{ pW}/\sqrt{\text{Hz}}$.

1.2 Wideband Quasi-Optical Antennas

A few hundreds of GHz of antenna bandwidth requirement can easily be realized with narrowband antennas that operate with a central frequency higher than 2 THz. Such high frequency is beneficial for the resolution of the system. However, the very high atmospheric attenuation makes this frequency range unsuitable for most terrestrial imaging applications [22] and frequencies lower than 1 THz are often considered instead. In that case, the requirement of a few hundreds of GHz of absolute bandwidth implies a very large relative bandwidth in the order of 3:1, e.g. from 200 GHz to 600 GHz. Furthermore,

¹Effective bandwidth will be defined in Chapter 2 as the system efficiency integrated over bandwidth.

²Using (2.1), the theoretically estimated $\text{NEP} = 1.6 \cdot 10^{-14} \text{ W}/\sqrt{\text{Hz}}$ in [30] is verified.

³This integration time is obtained by averaging frames at 30 Hz during 5.7 minutes. Every frame contains 1024 pixels which are consecutively read out.

⁴Assuming a flat noise spectral density, the NEP can be obtained using $\text{NEP} = \frac{12 \text{ nW}}{\sqrt{500 \text{ kHz}}} = 17 \text{ pW}/\sqrt{\text{Hz}}$ [52].

⁵Since the pixels are consecutively read out, in 5.7 minutes (342 seconds) of frame averaging, every pixel is effectively integrated during $\tau_{int} = \frac{342}{1024} = 0.334$ seconds.

the antenna should be planar in order to facilitate an easy integration together with the read-out and digital back-end.

A widely used planar antenna is a double slot-antenna [62, 63] with a fractional bandwidth of 10% to 20%. By optimizing the shape of the slots, the relative bandwidth can be extended efficiently to 2:1 [60] or 3:1 [64]. Even extreme bandwidths of 5:1 [65, 66] have been demonstrated with single slots in planar technologies. The latter solutions are leaky-wave type antennas that efficiently illuminate a dielectric lens. Leaky-wave type antennas are also very suitable for multi-beam applications as is shown in [65, 67] for a connected array in combination with a dielectric lens. Other ultra-wideband antennas have been demonstrated to operate with dielectric lenses [68, 69]. In [68], a planar sinuous antenna is connected to a zero bias Schottky diode and covers a 3:1 frequency range. Also, recently an ultra-wideband dual-polarized on-chip ring antenna in $0.13\ \mu\text{m}$ SiGe is demonstrated with a close antenna-detector co-design to operate with heterojunction bipolar transistors over a near-THz fractional bandwidth [69].

In order for an antenna to be suitable for low-cost consumer applications it is desirable to fabricate the planar antenna in a CMOS technology. An inevitable hindrance and obstacle in designing CMOS antennas is the low-resistivity silicon of the technology. Without shielding the antenna layer from the bulk silicon, only approximately $1/\epsilon_r^{3/2}$ ($\approx 3\%$ for silicon with relative permittivity of $\epsilon_r \approx 11.9$) [78] of the total power will be radiated away from the lossy silicon. The remaining power will be launched into surface-waves that are supported in the thick substrate. In [70], unwanted surface-wave modes in the unthinned $250\ \mu\text{m}$ substrate of the technology are suppressed using ring antennas with a grounded aperture, operating at 280 GHz. The bandwidth and average efficiency of this antenna is indicated in Fig. 1.4 for comparison. The surface-wave mode suppression, however, is

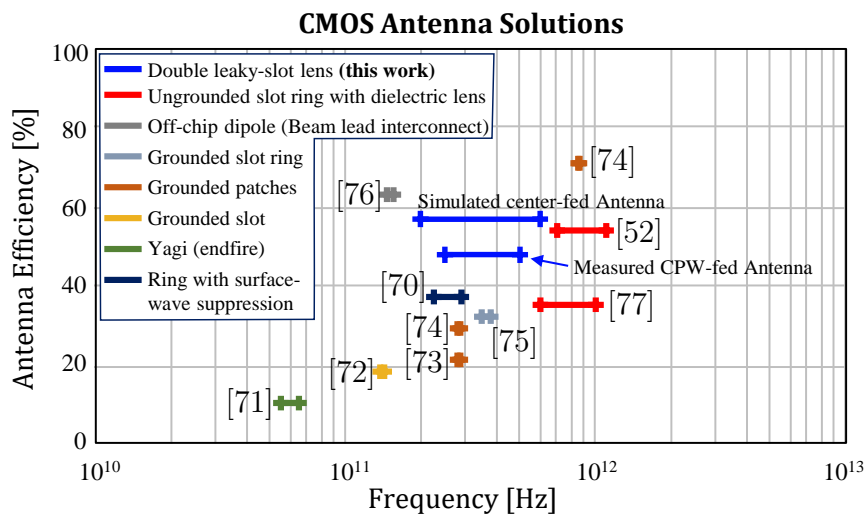


Figure 1.4: Different antenna solutions from literature, fabricated in CMOS technologies, are indicated in terms of their bandwidth and average efficiency. The efficiency includes ohmic dissipation in both metal and low-resistivity silicon of the CMOS technologies as well as, if applicable, the illumination efficiency of a dielectric lens that is glued to the silicon.

based on resonance frequencies of the grounded aperture and is therefore a narrowband solution. Furthermore, the ungrinded substrate of a standard CMOS technology can be 600 μm or even more, making this solution unusable as more surface-wave modes need to be suppressed. Instead, most CMOS antenna solutions [79] avoid radiating into the bulk silicon by shielding the antenna layer with a ground plane, usually separated by only a few μm of silicon dioxide (SiO_2). Even at relatively high frequencies (up to 300 GHz), this distance is electrically very small such that the radiation resistance can be as low as 0.1 Ω [80]. In that scenario, the total resistance is dominated by the ohmic loss of the metallization layers and the radiation efficiency of the antenna drops to 20% or even lower. State-of-the-art shielded antenna solutions at relatively low frequencies are Yagi antennas at 60 GHz in [71], slot antennas at 140 GHz in [72] or patch antennas at 280 GHz [73]. As the frequency increases, the distance between the antenna plane and shielding ground increases, improving the radiation resistance and therefore the efficiency. In [74, 81] it is demonstrated that the radiation efficiency of a grounded patch antenna can be increased from 25% at 280 GHz to 59% at 650 GHz or even 70% at 860 GHz. However, in the discussed shielded antenna solutions, the strict metal fill density rules that apply for all metallization layers are not accounted for. In [75], different metal fill cases, between patch antennas and the shielding ground plane, are investigated. It is shown that the metal fill can result in an additional loss of -3 dB. For this reason, [76] proposes off-chip antenna solutions (using beam-lead interconnects) achieving a radiation efficiency of 63% at 150 GHz using a dipole antenna, which is a significantly higher efficiency than the slot antenna with 18% efficiency at 140 GHz in [72]. The increase in efficiency is, however, a trade-off with increased system cost and complexity and is unfeasible to implement at submm-wave frequencies.

Other possible CMOS antenna solutions, to avoid high surface-wave excitation losses in the silicon of the technology, consist of either gluing an Artificial Dielectric Layer (ADL) with a high relative permittivity to the chip [82] or gluing a dielectric lens to the low-resistivity silicon. In the latter case, the low-resistivity silicon can be thinned down to 200 μm or even less to minimize ohmic dissipation. Simultaneously, the lens can be used to create an FPA of antennas in order to create scanning capabilities for the purpose of imaging applications. In [52, 83] a state-of-the-art 1 k-pixel THz imaging camera is presented, based on ring-antennas radiating with an (approximated) 54% radiation efficiency from 0.7 – 1.1 THz (45% fractional bandwidth)⁶ through the bulk silicon that is thinned down to 150 μm and is glued to a dielectric lens. This efficiency could be easily improved with an anti-reflection coating applied to the lens.⁷ The same research group recently redesigned the antenna [77] in the same technology as the one in which the demonstrators in this dissertation are fabricated (i.e. 22-nm FD-SOI CMOS [84]), *fully compliant with the metal density rules* and reported a radiation efficiency of 19–52% for 0.7 – 1 THz.⁸ One reason

⁶Reported NEP bandwidth below 50 pW/ $\sqrt{\text{Hz}}$.

⁷In [83], a 70-77% radiation efficiency in semi-infinite silicon is reported. The dielectric lens, without anti-reflection coating, will have at least an additional reflection loss of $\eta = 1 - |(1 - \epsilon_r^{0.5}) / (1 + \epsilon_r^{0.5})|^2 \approx 0.7$ between the air-silicon interface.

⁸Reported 3-dB NEP Bandwidth, with NEP below 40 pW/ $\sqrt{\text{Hz}}$.

of the reduction in radiation efficiency is the increased ohmic losses due to the tight fill density requirement, together with a thicker silicon substrate of 255 μm . Nevertheless, the lens-antenna solutions [52, 77] still shows unprecedented performance in terms of efficiency and bandwidth for standard CMOS technologies.

Wideband antennas, operating below 1 THz with a large 3:1 relative bandwidth, have not yet been demonstrated in literature to operate efficiently when integrated in CMOS technology and while complying with strict minimum metal density requirements .

1.3 Low NEP THz Direct Detectors in CMOS

When a large portion of the available spectrum in the submm-wave regime is utilized, fully passive THz imaging can be realized when detectors are available with a NEP of only a few $\text{pW}/\sqrt{\text{Hz}}$. These NEPs have been demonstrated in high performance III-V technologies [85]. In lower-performance CMOS technologies, however, achieving similar NEPs is difficult [49] and the availability of good device and system models is vital to be able to push the technologies ability to enable passive THz imaging. Previous silicon related publications have reported detectors based on pn-junction diodes [86], Schottky Barrier Diodes (SBDs) and transistors.

The first CMOS THz FPA array, a 3×5 array operating at 600 GHz with a NEP of $400 \text{ pW}/\sqrt{\text{Hz}}$ [87], is based on distributed resistive self-mixing of MOSFETs, which are optimized using a theoretically study [88] based on the Dyakonov–Shur plasma-wave theory [89] where the radiation is coupled to the gate of the MOSFETs. Alternatively, in [90], a patch antenna couples the incident radiation at 595 GHz to the drain of the MOSFETS. The modeling efforts are extended to include the efficiency of the antenna and the impedance matching of antenna-detector combination.

The high cut-off frequency of SBDs makes them very attractive in submm-wave applications [91] and are in fact the preferred detector in GaAs technologies [92]. In CMOS technologies, SBD detectors, in combination with grounded patch antennas, were demonstrated with NEPs of $29 \text{ pW}/\sqrt{\text{Hz}}$ at 280 GHz [73, 74] and $42 \text{ pW}/\sqrt{\text{Hz}}$ at 860 GHz [74]. The lumped element model of the SBD [93] allowed for parametric responsivity and NEP optimization studies at high frequency and proved to be a useful tool in the design process presented in [73] and [74]. The same authors of [73, 74] extended these high-frequency models for diode-connected NMOS transistors, placed in a differential configuration, and a minimum NEP of $12.6 \text{ pW}/\sqrt{\text{Hz}}$ was measured in [94]. In [95], two MOSFET devices connected differentially to a ring antenna were characterized with a minimum NEP of $14 \text{ pW}/\sqrt{\text{Hz}}$ at 724 GHz. The state-of-the-art NEP of $12 \text{ pW}/\sqrt{\text{Hz}}$ is recently achieved in the same technology as the one in which the demonstrators in this dissertation are fabricated (i.e. 22-nm FD-SOI CMOS) by using a pair of nFETs, driven differentially from a ring antenna [77]. The NEP and bandwidth in [77] is approaching the level where first THz passive imagers might be realized. Alternatively to the Dyakonov–Shur plasma-wave theory, FET devices can also be accurately modeled similarly to diode devices as shown in [96] for graphene FETS (GFETS) and in [97] for FETS in standard CMOS. In [96], the model,

extracted from S-parameters and IV-curve, is derived from a Volterra series and has shown excellent agreement to probed measurements at millimeter-wavelengths and predicted qualitatively accurate device operation at submm-wavelength operation [98]. In [97], the model, based on second order Taylor expansions, was derived for CMOS FETs operating at 500 GHz with a measured NEP of $29 \text{ pW}/\sqrt{\text{Hz}}$.

Research efforts also has been done in combining the unbeaten performance of high frequency devices in the higher performance III-V semiconductor technologies [85] with silicon technologies that are leveraging in the high yield and density of complicated RF-circuits [99]. This is done in a wafer-level integration approach that would replace chip-to-chip connections with monolithic integration.

1.4 Goals and Methodology

This dissertation is focusing on the realization of low-cost THz imaging applications. The current absence of efficient and compact coherent circuitry and sources, such as those used for microwave imaging, requires the development of large direct detection Focal Plane Arrays (FPAs) in combination with a quasi-optical system, e.g. dielectric lenses. To date, such fully passive and uncooled THz imager is still unprecedented.

Therefore, in this dissertation, the figures of merit for passive imaging are first derived from where the requirements for both the antenna and detector, and potential useful spectral bandwidth, are defined for a specific application, i.e. automotive imaging cameras. The study in passive imaging systems will also provide the optimal trade-off between focal plane sampling, bandwidth and sensitivity considering, first, aperture based focal plane arrays with single element per beam.

Subsequently, theory and modeling approaches to design wideband direct detection schemes in CMOS are developed. These approaches are tested by means of the design and detailed characterization of a single-pixel direct detector with a highly efficient and wide-band on-chip antenna. The use of in-packaged antennas is not considered due to their limitation when scaling the system towards large array.

Lastly, a focal plane array architecture will be designed that fulfills the derived sampling and bandwidth requirements previously derived in the passive imaging system analysis. The main optimization goal will be the maximization of the gain at the edge of coverage (i.e. gain at the cross-over between two adjacent beams), over a wide-bandwidth, in order to realize a near diffraction limited resolution array with state-of-the-art efficiency. Such FPA configuration could enable future THz passive imaging, if integrated with $\text{sub-pW}/\text{Hz}^{0.5}$ NEP detectors.

1.5 Contributions in the Thesis

The novel aspects of this thesis are summarized in the following:

- The design guidelines for FPA architectures are provided that maximizes imaging

speed for a diffraction limited resolution. It is shown that by exploiting a very large bandwidth, sub-Kelvin imaging capabilities can be achieved with real-time refresh rates, provided that the detectors have a NEP in the order of $1 \text{ pW}/\sqrt{\text{Hz}}$. Ultimately the imaging speed is maximized by overdimensioning the optics.

- Two double leaky slot lens antennas are designed for wideband imaging applications at submm-wavelengths. One antenna is suitable for center-fed direct detection scenarios and features a state-of-the-art relative bandwidth of 3:1 with a high simulated average efficiency of 57% over the full bandwidth from 200 GHz to 600 GHz. CMOS antennas with higher efficiency are either narrowband or do not fully comply to the severe minimum metal density rules in CMOS technologies. A second, CPW-fed, double leaky slot antenna (operating from 250 GHz to 500 GHz with a 47% average efficiency) is designed that serves as a mean of verification for the center-fed antenna but could also be used with on-chip active circuitry other than small direct detectors. The performance of the two lens antennas are also indicated in Fig. 1.4 and compared with the state-of-the-art solutions.
- The designed center-fed double leaky-slot antenna is packaged into a THz direct detector using a differential Schottky Barrier Diode voltage read-out. A complete radiometric system model has been derived that accurately predicts the NEP and temperature sensitivity over a large bandwidth, taking into account the antenna, detection circuit and impedance matching between those. An excellent agreement between measured and simulated system NEP is observed. The model is derived from the lumped element model of a Schottky Barrier Diode and will allow for a close antenna-detector co-design for future wideband THz direct detectors.
- A highly efficient, tightly sampled FPA configuration is introduced, offering high edge of coverage gain while simultaneously retaining a high aperture efficiency. The array is based on a connected array of tapered dipoles that support leaky-wave radiation in combination with a dielectric lens. The tapering angle of 45° results in a checkerboard configuration that efficiently exploits two polarizations simultaneously such that a near diffraction limited resolution is achieved.

1.6 Outline of the Thesis

A detailed description of the chapters of this dissertation is given in the following:

- **Chapter 2** presents the design considerations for the preferred detection architecture for uncooled multi-pixel THz imaging scenarios. For this preferred type of detection, i.e. direct detection architectures, the figures of merit for passive imaging are derived, starting from the expression of the Signal-to-Noise Ratio. The figures of merit, imaging speed, temperature sensitivity and resolution are compared for different focal plane array architectures and design guidelines are provided. In **Appendix A**, a

more in-depth study of the resolution limits for both isolated and distributed sources is presented. **Appendix B** extends the design considerations in the case that the arrays are cryogenically cooled. Lastly, **Appendix C**, reports the study on the effect of non-ideal sources and the sensitivity of a radiometer to undesired sources such as the sky-background or instrument box.

- **Chapter 3** presents a case-study of using passive THz imagers in the scenario of pedestrian detection for the automotive industry. In this scenario, the achievable temperature sensitivity is analyzed for a pedestrian that is standing up to 10 m distance from the imager, in foggy weather conditions. Three different FPA sampling configurations are studied with feeds that operate from 200 GHz to 600 GHz in combination with a detector that is characterized with a NEP of $1 \text{ pW}/\sqrt{\text{Hz}}$. It is also shown how the temperature of the atmosphere is affecting the temperature sensitivity requirements of the imager.
- **Chapter 4** presents the design and performance of two double leaky slot lens antennas, suitable for integration in commercial CMOS technologies. It is shown that leaky-wave type antennas suffer minimally from ohmic dissipation losses when complying to the strict metal density rules that are imposed by CMOS technologies. The design and simulated performance are presented for a center-fed double leaky slot antenna, suitable for direct detection scenarios, that operates from 200 GHz to 600 GHz with an average efficiency of 57% over the bandwidth. A second, CPW-fed, verification antenna is manufactured in a 22-nm CMOS technology and characterized, in terms of impedance and gain patterns, using an ad-hoc quasi-optical measurement setup. This antenna, operating from 250 GHz to 500 GHz with an average efficiency of 47%, could also potentially be connected to other on-chip circuitry.
- **Chapter 5** presents the design and performance of a single pixel THz direct detector that is based on the center-fed antenna designed and presented in Chapter 4. The antenna is connected to a differential pair of Schottky Barrier Diodes (SBDs) and a load resistor that enables a voltage read-out. A radiometric system model is used that accurately can predict the NEP of the system over a large bandwidth. It is shown that performing low-frequency measurements on a standalone SBD is sufficient to predict the system performance at submm-wave frequencies in terms of responsivity and system NEP. In **Appendix D**, the lumped element model of a SBD is introduced and the diode current responsivity and NEP is derived. The components of the lumped element model are derived in **Appendix E** from low-frequency measurements that were performed on the standalone SBD.
- **Chapter 6** discusses the trade-off between efficiency and resolution in multi-beam scenarios. The study is focused on a single-beam-per-feed in combination with a single aperture solution. In such architecture, a smaller feed sampling periodicity leads to high angular resolutions but also to increased spill-over or mutual coupling losses. The design and performance of a connected array of dipoles is presented that

supports a leaky-wave in the presence of a dielectric lens. The dipoles are tapered such that two polarization can be exploited simultaneously. In this way, after a feed sampling periodicity optimization study, a diffraction limited resolution is achieved with a 2.5 dB increase in edge of coverage gain w.r.t. uniform aperture feeds. As demonstrator, the design of a 12 pixel FPA, fabricated in the same 22-nm FD-SOI CMOS technology, is presented.

- **Chapter 7** concludes this dissertation by reviewing the most significant results and provides recommendations for future work.

Chapter 2

THz Imaging using Uncooled Wideband Direct Detection Focal Plane Arrays

In millimeter and sub-millimeter wave radiometric imaging systems a persistent goal is the increase in the speed of acquisition of the image while maintaining a high sensitivity. Typically the highest sensitivity is achieved by cryogenically cooling the detectors, specifically in astronomical applications. However, for the purpose of low-cost imaging applications, it is desirable to operate at room temperature. Without cryogenically cooling, the electronic noise introduced by the detectors becomes dominant, making the detectors less sensitive. Resorting to detection architectures containing amplification circuitry might be impractical for implementation in large focal plane arrays (FPAs) fabricated in integrated technologies. This chapter derives the focal plane architecture that maximizes the imaging speed of radiometers operating at room temperature without using any amplification circuitry. It is shown that in such scenario a practical image acquisition speed can still be achieved when a very broad portion of the THz-band is exploited. Ultimately, the imaging speed is maximized when the FPA is undersampled, implying a trade-off in the size of the optics. The analysis is substantiated by a case study using wideband leaky lens antenna feeds operating from 200 GHz to 600 GHz.

2.1 Introduction

A cornerstone in the dimensioning and characterization of direct detection systems that are based on absorbers or background-noise limited detectors is presented by Griffin et al. [100], where different FPA configurations are compared in terms of imaging speed and SNR. However, [100] focuses only on cooled detectors and the effect of bandwidth is not included. Cryogenically cooling the detectors is expensive and results in a bulky system; for the purpose of low-cost imaging applications it is desired to have a large integrated FPA operating at room temperature. In this scenario, the electronic noise introduced by the

detectors is much higher such that none of the existing uncooled direct detectors operate near the background-noise limit [101]. The current state-of-the-art uncooled passive sub-millimeter wave imagers are insufficiently sensitive to operate without actively illuminating the source of interest.

This chapter derives a focal plane architecture, for antenna coupled direct detectors, that is able to provide a practical sensitivity and imaging speed (e.g. 1 K [55] at near real-time refresh rates for security screening) without cooling, amplification or active illumination. As will be derived in Sec. 2.2.1, the temperature sensitivity, also referred to as the Noise Equivalent Temperature Difference (NETD), of a direct detector after τ_{int} seconds of integration and without any pre-amplification can be expressed as:

$$\text{NETD} = \frac{\text{NEP}}{k_B \Delta f_{\text{RF}}^{\text{eff}} \sqrt{2\tau_{\text{int}}}} \quad (2.1)$$

with $k_B = 1.38 \times 10^{-23} \text{ m}^2 \text{ kg s}^{-2} \text{ K}^{-1}$ being Boltzmann's constant, $\Delta f_{\text{RF}}^{\text{eff}}$ is the effective bandwidth¹ and NEP is the Noise Equivalent Power for a 1 Hz post-detection bandwidth, Δf_{PD} .² As is clear from (2.1), the crucial aspect in achieving a practical NETD is the utilization of detectors characterized by a low NEP that are matched over a broad portion of the THz-spectrum to an antenna. To illustrate this, Fig. 1.3 shows the imaging speed as $1/\tau_{\text{int}}$ versus $\Delta f_{\text{RF}}^{\text{eff}}$ and NEP such that the minimum practical temperature sensitivity of 1 K in (2.1) is achieved. An important aspect, that is not touched in this dissertation, is the stability of the system due to noise-contributions. The stability of the system limits the maximum integration time, τ_{int} , of the signal before the system becomes unstable. This stability can be analyzed by calculating the Allan variance and is limited by the Flicker-noise contributions [103]. The stability can be improved by modulating the signal beyond the Flicker-noise corner, where white-noise contributions are dominant.

Nowadays, detectors suitable for array implementation have been shown with room temperature NEPs as low as $12.6 \text{ pW}/\sqrt{\text{Hz}}$ in CMOS technologies [73, 94], $2.4 \text{ pW}/\sqrt{\text{Hz}}$ for commercially available zero-bias Schottky-barrier diodes [104] and even $0.48 \text{ pW}/\sqrt{\text{Hz}}$ in III-V technologies [85]. Therefore, with this order of magnitude in NEP, one can utilize a large operational bandwidth to achieve a practical sensitivity and imaging speed. Novel integrated wideband antenna concepts that can be exploited in this kind of scenario are connected arrays [65] or leaky lens antennas [66] which have been recently developed. The focus area of this work is indicated in the Introduction in Fig. 1.3; the work describes the FPA design steps to maximize the effective bandwidth for uncooled FPAs. Of course, an important condition to facilitate the efficient use of a large operational bandwidth is a wideband impedance match of the antenna feeds with the detector. When the antenna and detector are co-designed, an impedance match over a relative bandwidth of $\nu = f_{\text{max}}/f_{\text{min}} = 3 : 1$ can be achieved.

¹Effective bandwidth is defined as the average optical efficiency, $\bar{\eta}_{\text{opt}}$, times the absolute bandwidth, Δf_{RF} : $\Delta f_{\text{RF}}^{\text{eff}} = \bar{\eta}_{\text{opt}} \Delta f_{\text{RF}}$ (See Sec. 2.2.1)

²A 1 Hz post-detection bandwidth is equivalent to 0.5 s of detector integration time; $\Delta f_{\text{PD}} = 1/(2\tau_{\text{int}})$ [102].

This chapter is structured as follows. In Sec. 2.2, the theory used throughout this chapter is derived by following an EM-approach assuming ideal and uniformly illuminated circular feeds placed in a square array in the focal plane of a symmetric quasi-optical system, as shown in Fig. 2.1. Figures of merit such as sensitivity, imaging speed and noise equivalent power are introduced, which are used to analyze the optimal FPA configuration in terms of imaging speed in Sec. 2.3 and resolution in Sec. 2.4. In Sec. 2.5, the analysis is substantiated by evaluating the imaging speed of leaky lens antennas operating from 200 GHz to 600 GHz. Accompanying to the chapter is Appendix A, where a more rigorous study in resolution limits is studied. There, the resolution is not only studied with isolated sources, but also by introducing distributed source. In more commercial applications, such as automotive or security imaging, sources can often be considered distributed. Subsequently, in Appendix B the sampling considerations are revised in the case that the FPA is cryogenically cooled. Lastly, in Appendix C the influence of incident radiation of undersired sources is studied in a detector noise limited scenario and a background noise limited scenario, where temperature limits for a 10% sensitivity accuracy are presented.

2.2 Quasi-Optical Radiometric System

Radiometry is the primary tool used to characterize the electromagnetic power spectrum of emission due to sources distributed in space. The key observable parameter is the spectral brightness distribution, $B(f, \Omega)$, of the source that is defined over a source solid angle, Ω_S , with a temperature distribution, $T_S(\Omega)$, as is shown in Fig. 2.1. In fact, the spectral brightness distribution characterizes an incoherent source at temperature T and can be described by Planck's law in units of $[\text{W m}^{-2} \text{Sr}^{-1} \text{Hz}^{-1}]$ [105]:

$$B(f, \Omega) = \frac{f^2}{c^2} \frac{2hf}{e^{\frac{hf}{k_B T(\Omega)}} - 1} \quad (2.2)$$

with f the frequency, $c = 2.99 \times 10^8$ m/s the speed of light and $h = 6.626 \times 10^{-34}$ Js being Planck's constant. In the specific case that the radiometer is operating in the Rayleigh-Jeans region w.r.t. the source, i.e. when $hf \ll k_B T$ such as for room temperature sources, a convenient approximation of the spectral brightness can be used:

$$B(f, \Omega)|_{hf \ll k_B T} \approx B^{\text{RJ}}(f, \Omega) = \frac{f^2}{c^2} 2k_B T(\Omega) \quad (2.3)$$

For sources with $T > 270$ K and $f < 1$ THz, the error in this approximation is less than 10%. It is worthwhile to mention that in the Wien's limit, i.e. when $hf \gg k_B T$, the spectral brightness can be approximated using $(e^{\frac{hf}{k_B T}} - 1)^{-1} \approx e^{-\frac{hf}{k_B T}}$; this term decreases exponentially with frequency and therefore only the lowest frequencies in the band contribute to the imaging speed. This implies that utilizing a large operational bandwidth is not very beneficial to increase the SNR when the radiometer is operating in the Wien's limit w.r.t. the source such as is the case for deep-space sensing. Accordingly, optimal FPA configurations in the Wien's limit can be studied as in [100]. In the rest of this chapter,

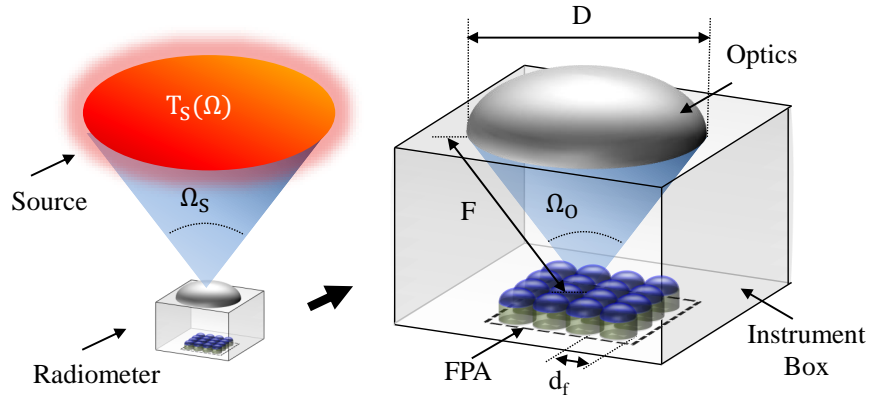


Figure 2.1: Investigated quasi-optical system in the presence of an incoherent source with temperature distribution $T_S(\Omega)$ distributed over a source solid angle Ω_S . The radiometer consists of a FPA placed in an instrument box at a focal distance F from optics with diameter D that subtend the FPA with a solid angle of Ω_O . The investigated FPA is a square array containing antennas with diameter d_f .

it is assumed that the radiometer is operating in the Rayleigh-Jeans limit (2.3) w.r.t. to the source. A simplified configuration of the complex optics of a radiometer is shown in Fig. 2.1. In this configuration, antenna feeds are placed in a square FPA with an inter-element spacing of d_f (in both directions) at a focal distance of F from the optics with a diameter of D ($F_{\#} = F/D$). The optics are assumed to be characterized by large $F_{\#}$ and subtend the FPA with a solid angle of Ω_O . In order to generalize the analysis, ideal antenna feeds are initially assumed to be characterized by uniformly illuminated circular apertures. Moreover, the efficiency of each of the antenna feeds and associated intensity patterns after the optics are assumed to be the same for all FPA elements, apart from the pointing angle. The feed apertures have the same diameter as the inter-feed spacing d_f . The array is placed in an uncooled instrument box.

2.2.1 Imaging Speed

For direct detection schemes, the Signal-to-Noise Ratio (SNR), after τ_{int} seconds of detector integration, can be expressed as [54, 102, 106]:

$$\text{SNR} = \frac{P_a}{\text{NEP} \sqrt{\Delta f_{\text{PD}}}} = \frac{P_a}{\text{NEP}} \sqrt{2\tau_{\text{int}}} \quad (2.4)$$

where P_a is the average power accepted by the detector during the integration time interval τ_{int} . The expression of the SNR (2.4) follows from the NEP, which is defined as the average input power that is necessary to equate the root-mean-square (RMS) noise power fluctuations when the post-detection bandwidth $\Delta f_{\text{PD}} = 1$ Hz and therefore making the SNR unity. The image acquisition time, τ_i , is typically larger than the detector integration time, τ_{int} , if one has fewer detectors, N_{det} , operating simultaneously than the number of pixels in the desired FoV, N_{pix} . In that case $\tau_i = N_t \tau_{\text{int}}$ with $N_t = N_{\text{pix}}/N_{\text{det}}$ defined as

an integration time penalty to form a single image in τ_i seconds. This illustrates the great efforts that are done to fabricate large FPAs.

The average received power, during the detector integration time interval, from an incoherent source by the n -th single polarized antenna feed, P_a^n , can be expressed as an integration of the spectral brightness (2.2) over the operational bandwidth $\Delta f_{\text{RF}} = f_{\text{max}} - f_{\text{min}}$ and over the source solid angle viewed and weighted by the effective area $A_{\text{eff}}^O(f, \Omega)$ of the quasi-optical system:

$$P_a^n = \frac{1}{2} \int_{f_{\text{min}}}^{f_{\text{max}}} \int_{\Omega_S} A_{\text{eff}}^O(f, \Omega - \Omega_n) B(f, \Omega) d\Omega df \quad (2.5)$$

Focusing on the on-axis element ($n = 0$), the effective area of the quasi-optical system can be related to the directivity $D^O(f, \Omega)$;

$$A_{\text{eff}}^O(f, \Omega) = \frac{c^2}{f^2} \frac{1}{4\pi} \eta_{\text{opt}}(f) D^O(f, \Omega) \quad (2.6)$$

where $\eta_{\text{opt}}(f) = \eta_{\text{feed}}(f) \eta_{\text{so}}^{\Omega_O}(f)$ is the system's optical efficiency that is separated in a radiation efficiency of the feed, $\eta_{\text{feed}}(f)$, and spill-over efficiency w.r.t. the optics, $\eta_{\text{so}}^{\Omega_O}(f)$. The feed efficiencies are for example impedance matching and conductor-/ dielectric losses, while $\eta_{\text{so}}^{\Omega_O}(f)$ is a more significant term defining how well the antenna feed pattern is coupled to the angular region subtended by the optics, Ω_O . The spill-over efficiency can be defined as:

$$\eta_{\text{so}}^{\Omega_O}(f) = \frac{\int^{\Omega_O} D^f(f, \Omega) d\Omega}{4\pi} \quad (2.7)$$

where $D^f(f, \Omega)$ is the directivity of the feed. In Fig. 2.2, the spill-over efficiency is shown as a function of the feed size, assuming large $F_{\#}$ and a uniformly illuminated circular aperture. It is evident that the spill-over efficiency, and therefore imaging speed, will be greatly affected by the choice of the feed size (which for simplicity corresponds to the inter-element period in the FPA, i.e. *sampling*). For this reason, the spill-over efficiency will be the key parameter used in the analysis to derive the optimal sampling configuration. One should also note that a low spill-over efficiency also implies that the system can become sensitive to the thermal radiation coming from the instrument box. We assume that the instrument-box, together with the quasi-optics, is kept at a stable temperature such that common calibration techniques can be applied. Substituting the effective area and the Rayleigh-Jeans approximation from (2.3) in (2.5) leads to:

$$P_a = \frac{k_B}{4\pi} \int_{\Omega_S} T(\Omega) G_{\text{eff}}(\Omega) d\Omega \quad (2.8a)$$

$$G_{\text{eff}}(\Omega) = \int_{f_{\text{min}}}^{f_{\text{max}}} \eta_{\text{opt}}(f) D^O(f, \Omega) df \quad (2.8b)$$

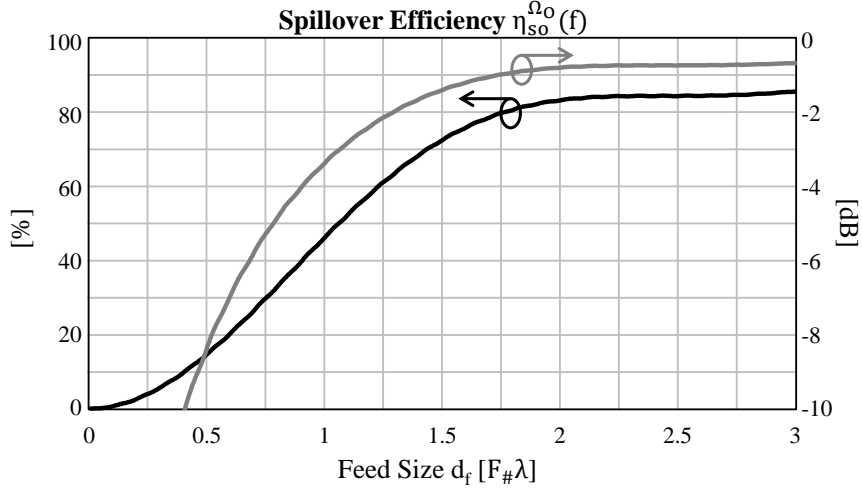


Figure 2.2: Spill-over efficiency as a function of the feed size d_f , normalized to $F_{\#} = \frac{F}{D}$ and wavelength λ . The curve is evaluated using a uniformly illuminated circular feed that is placed in the focal plane of optics characterized with large $F_{\#}$.

G_{eff} , the *effective gain pattern*, is obtained by weighting the spectral directivity by the optical efficiency of the quasi-optical system and by integrating the resulting term over the operational bandwidth.

A signal can be resolved by the system if the received power P_a (2.8a) integrated over time results in a SNR larger than 1 (2.4). In order to have a convenient way to compare the SNR for different FPA architectures, we make some assumptions in the evaluation of (2.8a). First, the source is considered to have an effective, constant, temperature \bar{T}_S over the entire solid angle such that it can be removed from the integral over source solid angle. Secondly, an important condition of the presented analysis is that the sources are distributed over a large solid angle w.r.t. intensity patterns after the optics, such that the angular integration in (2.8a) over the spectral directivity in (2.8b) is approximately 4π . The average received power, \bar{P}_a , by each antenna feed can now be written as (2.9a):

$$\bar{P}_a = k_B \bar{T}_S \bar{\eta}_{\text{opt}} \Delta f_{\text{RF}} \quad (2.9a)$$

$$\bar{\eta}_{\text{opt}} = \frac{1}{\Delta f_{\text{RF}}} \int_{f_{\text{min}}}^{f_{\text{max}}} \eta_{\text{opt}}(f) df \quad (2.9b)$$

Here we defined an average optical efficiency, $\bar{\eta}_{\text{opt}}$. A convenient definition to characterize the performance of the quasi-optical system is its *effective bandwidth* $\Delta f_{\text{RF}}^{\text{eff}} = \bar{\eta}_{\text{opt}} \Delta f_{\text{RF}}$. This definition of effective bandwidth is used in Fig. 1.3.

Let us consider an incoherent source with an effective temperature of \bar{T}_S . A temperature difference ΔT in the incoherent source then results in a difference in average received power, ΔP_a , according to $\bar{P}_a + \Delta P_a = k_B (\bar{T}_S + \Delta T) \bar{\eta}_{\text{opt}} \Delta f_{\text{RF}}$. The purpose of detector integration is to average the fluctuating received power over time in order to detect ΔP_a . Substituting

$\Delta P_a = k_B \Delta T \bar{\eta}_{\text{opt}} \Delta f_{\text{RF}}$ in (2.4) and by forcing $\text{SNR} = 1$, we can solve for ΔT . This defines the sensitivity of the quasi-optical system as has been introduced in (2.1) [106]:

$$\text{NETD} \triangleq \Delta T|_{\text{SNR}=1} = \frac{\text{NEP}}{k_B \bar{\eta}_{\text{opt}} \Delta f_{\text{RF}} \sqrt{2\tau_{\text{int}}}} \quad (2.10)$$

One should be careful in interpreting the NEP and its impact on sensitivity. Usually, the NEP can be divided into two contributions; $\text{NEP}^2 = \text{NEP}_{\text{det}}^2 + \text{NEP}_b^2$. The detector noise, NEP_{det} , is intrinsic to the detector characteristics and strongly influenced by the read-out mechanism, while the background noise, NEP_b , is associated with the thermal fluctuations of the signals arriving at the input of the detector. For uncooled and fully passive systems, NEP_b is often a few orders of magnitude lower than NEP_{det} and can be neglected.³ Rearranging (2.10) and substituting $\tau_{\text{int}} = \frac{\tau_i}{N_t}$ gives us an expression of the imaging speed s (2.11).

$$s = \frac{1}{\tau_i} = \left(\frac{\text{NETD} \cdot k_B \bar{\eta}_{\text{opt}} \Delta f_{\text{RF}}}{\text{NEP}} \right)^2 \frac{2}{N_t} \quad (2.11)$$

Fig. 1.3, from the introduction, is generated using (2.11) as a function of $\Delta f_{\text{RF}}^{\text{eff}} = \bar{\eta}_{\text{opt}} \Delta f_{\text{RF}}$ and NEP, after fixing $N_t = 1$, and $\text{NETD} = 1$ K. When comparing two different configurations, α and β , [100] suggests focusing on the ratio in imaging speed (SR):

$$\text{SR} = \frac{s^\alpha}{s^\beta} = \left(\frac{\bar{\eta}_{\text{opt}}^\alpha \Delta f_{\text{RF}}^\alpha}{\bar{\eta}_{\text{opt}}^\beta \Delta f_{\text{RF}}^\beta} \right)^2 \frac{N_t^\beta}{N_t^\alpha} \quad (2.12)$$

The imaging speed ratio SR indicates how much faster configuration α (with imaging speed s^α) is relative to configuration β (s^β). With the introduction of such SR, the optimal configuration as a function of the bandwidth or the focal plane sampling can easily be investigated qualitatively. One should note the cancellation of the NEP in (2.12).⁴

2.2.2 Focal Plane Sampling and Jiggling

The resolution of an imaging system, $\Delta\theta$, is defined by its ability to distinguish between multiple sources. Suppose that two point-sources are angularly displaced by $\Delta\theta$ in the far-field of the quasi-optical system. The diffracted field arriving in the focal plane is a summation of two Airy discs⁵ which are transversely displaced in the focal plane by $\Delta\rho$ as is shown in Fig. 2.3(a). The geometrical relation between the angular displacement ($\Delta\theta$)

³In the case that the system is cooled or any amplification circuitry is present, the background noise NEP_b [54, 107, 108] can become dominant. In such scenario, the NEP will also depend on source temperature, operational bandwidth and optical efficiency. The NETD (2.10) will then reduce to an expression that is commonly found in microwave radiometer literature $\text{NETD} = \frac{T_S}{\sqrt{\Delta f_{\text{RF}} \tau_{\text{int}}}}$ [109, 110].

⁴Since we focus the study on uncooled power detectors, the NEP is considered to be independent on the signal received by the feeds.

⁵Airy disc = $C \frac{J_1(k \frac{\rho}{2F} D)}{k \frac{\rho}{2F} D}$ for broad-side illumination where C is an intensity constant, k is the wavenumber and ρ is the transversal focal plane position.

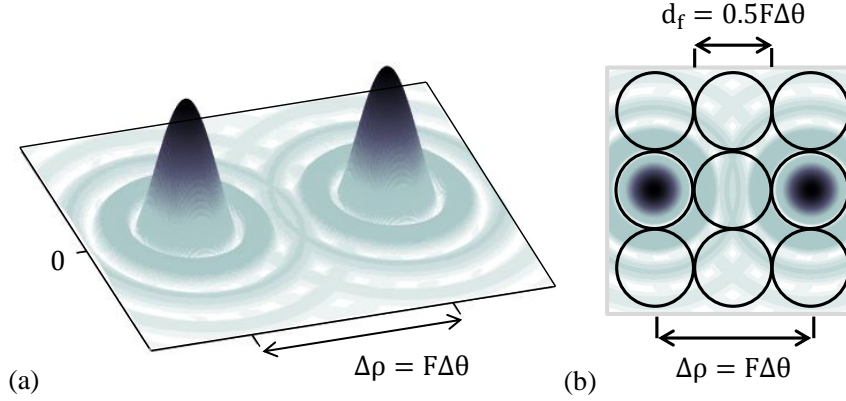


Figure 2.3: (a) Diffracted field in the focal plane due to two point-sources separated by $\Delta\theta$. The focal plane image is a summation of two Airy discs which are separated by $\Delta\rho = F\Delta\theta$. (b) In order to resolve the sources in the focal plane, the feeds should be sampled with $d_f = 0.5F\Delta\theta$.

of the point-sources and transverse displacement ($\Delta\rho$) of the Airy discs in the focal plane of an optical system with large $F_{\#}$ can be shown to be $\Delta\rho = F\Delta\theta$. The diffracted field is then sampled with a finite amount of antenna feeds in the focal plane. As is illustrated in Fig. 2.3(b), in order to be able to distinguish between the two incoherent sources in the focal plane image, one not only needs to sample the peaks of the Airy discs but also needs to sample in between in order to actually see a decrease in intensity and discriminate between the two peaks. The relation between an angular source separation, $\Delta\theta$, and the required sampling, d_f , is then $d_f = \frac{\Delta\rho}{2} = 0.5F\Delta\theta$. By inverting this relationship we can say that for a feed-size of d_f , the resolution of the imaging system is (2.13),

$$\Delta\theta = 2\frac{d_f}{F} \quad (2.13)$$

It is not possible to continue decreasing the feed-size d_f to achieve any resolution $\Delta\theta$ that is desired. The smallest resolution is indeed limited by the diffraction with the optics when the superposition of the two Airy discs only show one peak in the focal plane image. This minimal resolution, $\Delta\theta^{\text{lim}}$, is approximately the -3dB beamwidth of the diffracted intensity patterns [111]:

$$\Delta\theta^{\text{lim}} \approx \frac{\lambda_c}{D} \quad (2.14)$$

where λ_c is the wavelength at the center frequency $f_c = \frac{f_{\text{min}} + f_{\text{max}}}{2}$ of the operational frequency band in which the antenna feeds are operating. Equating (2.14) with (2.13) gives rise to the sampling rule (2.15) stating that the diffraction limited resolution $\Delta\theta^{\text{lim}}$ can be reached when the sampling points in the focal plane are separated by [111]⁶:

$$d_f^{\text{lim}} = 0.5F_{\#}\lambda_c \quad (2.15)$$

⁶This sampling rule only applies when the signal is detected in intensity.

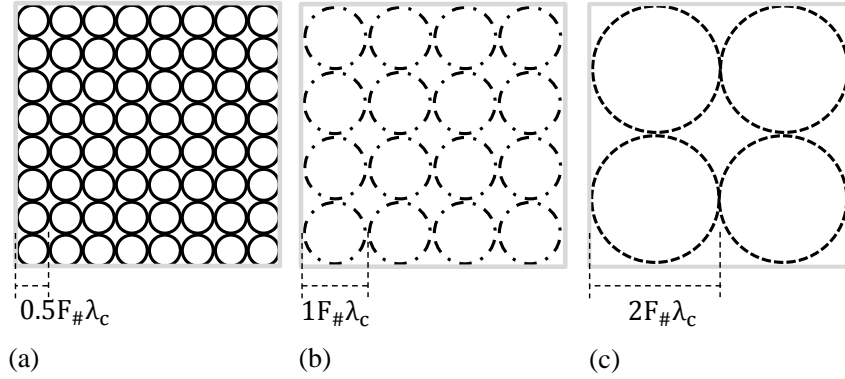


Figure 2.4: Possible sampling configurations. Full sampling ($d_f = 0.5F_{\#}\lambda_c$), coherent sampling ($d_f = 1F_{\#}\lambda_c$) and maximum gain sampling ($d_f = 2F_{\#}\lambda_c$).

When the antenna feeds are sampled according to (2.15) the FPA is referred to as *fully sampled*. Sparser sampling (i.e. *undersampling*) will result in a loss in resolution while denser sampling (i.e. *oversampling*) is never useful since the quasi-optical system's diameter limits the resolution. A more extensive investigation of resolution limited resolution and focal plane image reconstruction is given in Appendix A. In this dissertation we will make use of undersampled arrays in order to maximize the imaging speed. The resolution will increase linearly with the undersampling factor N . The relationship between feed-size d_f and resolution $\Delta\theta$ can be written as

$$d_f = N \cdot 0.5F_{\#}\lambda_c \iff \Delta\theta = N \cdot \Delta\theta^{\text{lim}} \quad (2.16)$$

The resolution of an undersampled array ($N > 1$) is not diffraction limited, but as we will explain in the next section it is shown that the image quality does not only depend on the nominal resolution but also on the beam efficiency. A fully sampled FPA ($N = 1$) features the advantage that the image of the full FoV (with $\Delta\theta^{\text{lim}}$ resolution) is acquired without an integration time penalty ($N_t = 1$ in (2.11)) and with diffraction limited optics. Unfortunately, the sampling requirement (2.15) leads to a low spill-over efficiency w.r.t. the quasi-optics ($\eta_{\text{so}}^{\Omega_o} \approx 0.15$) as shown in Fig. 2.2. This low efficiency will enter quadratically in the equation of the imaging speed (2.11). Luckily, the sampling rule (2.15) does not require the sampling points to be acquired simultaneously. Instead, one can decide to increase the size (and spacing) of individual feeds to $d_f = 1F_{\#}\lambda_c$ or $d_f = 2F_{\#}\lambda_c$ in order to increase the spill-over efficiency at the cost of the integration time. The sampling configurations $d_f = [0.5 \ 1 \ 2]F_{\#}\lambda_c$, as shown in Fig. 2.4, are respectively referred to as *fully-, coherent- and maximum gain sampling*. For coherent- and maximum gain sampling, the spill-over efficiency will be increased to $\eta_{\text{so}}^{\Omega_o} \approx 0.46$ and $\eta_{\text{so}}^{\Omega_o} \approx 0.84$ respectively. The normalized patterns after the optics associated with two adjacent feeds are shown in Fig. 2.5 for the three different sampling configurations. The focal plane is undersampled for coherent- and maximum gain sampling. In order to obtain all the required sample-points in a rectangular FPA, the optics have to be pointed in $N_t = 2 \times 2 = 4$ and $N_t = 4 \times 4 = 16$ directions respectively for coherently- and maximum gain sampled FPAs. This process of

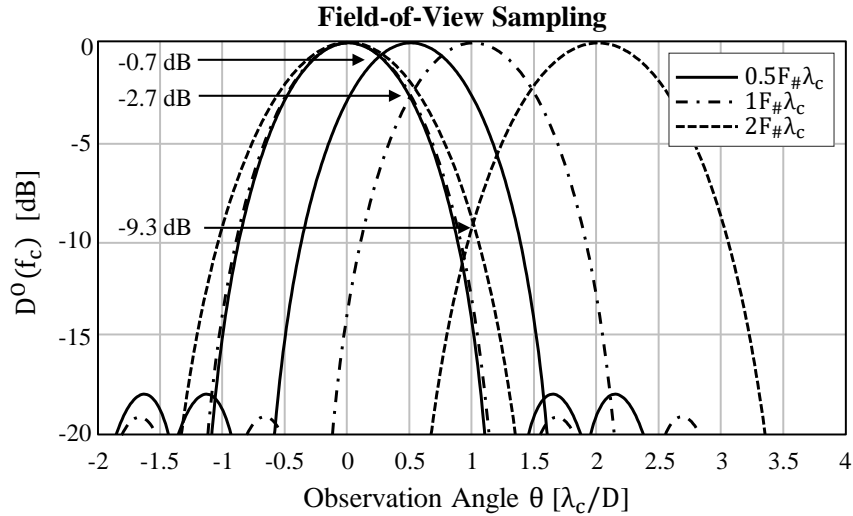


Figure 2.5: Normalized patterns $D^O(f_c)$ after the optics of the on-axis and first adjacent feed for all sampling configurations. Coherent sampling ($1F_{\#}\lambda_c$) and maximum gain sampling ($2F_{\#}\lambda_c$) requires jiggling in order to have a fully sampled FoV. Indicated is the cross-over level of the two adjacent pixels and a non-uniform illumination for larger feeds is taken into account.

mechanical scanning is referred to as *jiggling*. For small focal plane arrays, i.e. when $N_t = N_{\text{pix}}/N_{\text{det}} \gg 1$, the main limitation in achieving high imaging speeds is the implementation of the scanner [112]. However, as it is shown in Table I of [112], even for relatively small arrays (<100 elements), near real-time imaging speeds have been achieved. Therefore, with a maximum of only $N_t = 16$ scanning positions in this analysis, an additional time penalty associated with the mechanical scanner has been neglected.

2.3 FPA Design

In this section, we will compare the imaging speed for different sampling configurations. Subsequently, the increase in imaging speed that one can obtain by exploiting a large operational frequency band is quantified. In the last subsection it is illustrated that the imaging speed can further be improved by trading off in resolution.

2.3.1 FPA Configurations

The three different sampling configuration from Fig. 2.4 are compared relatively to each other using the imaging speed ratio defined in (2.12). The different FPAs are assumed to be operating with the same operational bandwidth Δf_{RF} and are sampled $d_f = [0.5 \ 1 \ 2]F_{\#}\lambda_c$ at the center frequency f_c . When including only the spill-over efficiency $\eta_{\text{so}}^{\Omega_O}$ in the analysis ($\eta_{\text{feed}} = 1$), the average optical efficiency can be approximated to be the spill-over efficiency at f_c , i.e. $\bar{\eta}_{\text{opt}} \approx [0.15 \ 0.46 \ 0.84]$ for the sampling configurations $d_f = [0.5 \ 1 \ 2]F_{\#}\lambda_c$ respectively, as can be seen in Fig. 2.2. In the comparison of the different sampling

configurations, we define the imaging speed ratio, $SR = \frac{s^\alpha}{s^\beta}$, as the speed ratio of the coherent- and maximum gain sampled FPAs, $s^\alpha = s^{[1\ 2]F\#\lambda_c}$, w.r.t. to the reference case of a fully sampled FPA, $s^\beta = s^{0.5F\#\lambda_c}$. The imaging speed ratio approaches the limits as summarized in the fourth column of Table 2.1.

Table 2.1: Imaging Speed Ratio w.r.t. a fully sampled array

d_f	$\bar{\eta}_{opt}$	N_t	SR
$0.5F\#\lambda_c$	0.15	1	1
$1F\#\lambda_c$	0.46	4	2.35
$2F\#\lambda_c$	0.84	16	1.96

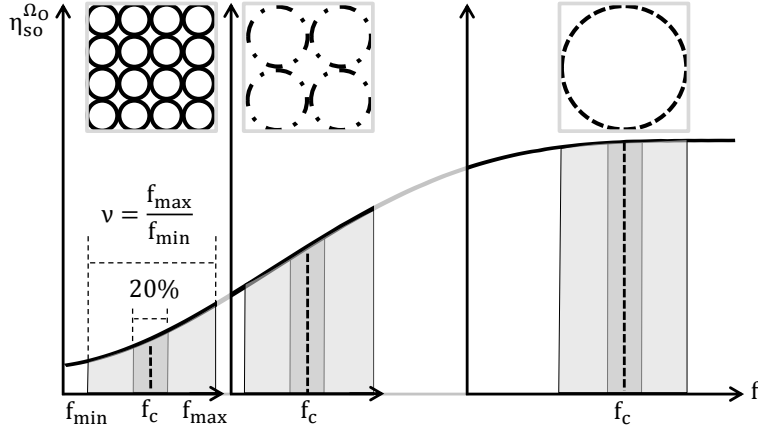
It is beneficial to sample the feeds in the FPA coherently with $d_f = 1F\#\lambda_c$ and to accept a small integration time penalty of $N_t = 4$ to sample the full FoV. A coherently sampled array is approximately 2.35 times faster w.r.t. the fully-sampled FPA ($d_f = 0.5F\#\lambda_c$). The fully-sampled array is, in fact, the slowest focal plane architecture. The increase in spill-over efficiency for larger feed size is more significant than the introduced integration time penalty of $N_t = 4$.

2.3.2 Bandwidth Utilization

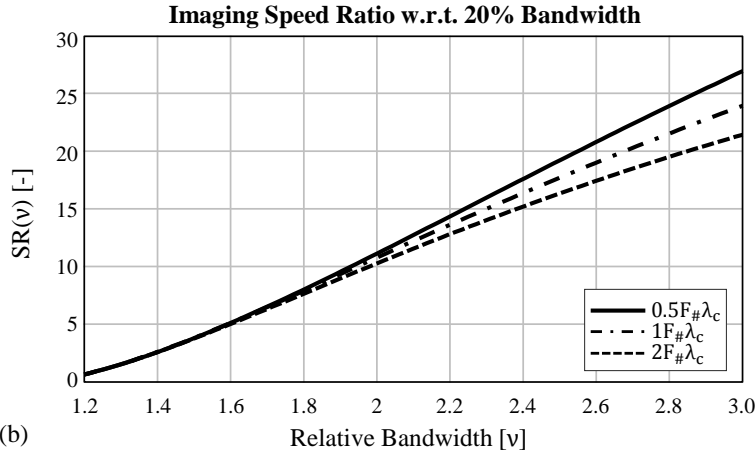
Most sub millimeter-wave radiometric detectors are connected to integrated antennas that operate within a 20% fractional bandwidth [63]. A solution to make the detectors more sensitive is to increase the absolute bandwidth Δf_{RF} by using wideband antenna solutions [64, 65, 66]. The imaging speed increases quadratically with the effective bandwidth $\bar{\eta}_{opt}\Delta f_{RF}$ (2.11). Let us investigate the improvement in imaging speed that one can obtain when a relative bandwidth, ν , up to $\nu = f_{max}/f_{min} = 3$ centered around f_c , is used for each of the sampling configurations. The imaging speed ratio is defined as a function of this relative bandwidth ν ,

$$SR(\nu) = \frac{s^\alpha(\nu)}{s^\beta(\nu = 1.22)} \quad (2.17)$$

The reference case $s^\beta(\nu = 1.22)$ is defined with a 20% fractional bandwidth (20% fractional bandwidth is equivalent to a $\nu \approx 1.22$ relative bandwidth). This is illustrated in Fig. 2.6(a), where the three sampling configurations $d_f = [0.5\ 1\ 2]F\#\lambda_c$ are sampled at f_c and have as reference case a 20% fractional bandwidth (dark gray area below the spill-over efficiency curve). For each configuration, the relative bandwidth ν is increased (light gray area below $\eta_{so}^{\Omega_o}$) and is compared in speed to the reference case. This leads to the imaging speed ratios as are summarized in Fig. 2.6(b). For example, with a relative bandwidth of $\nu = 3$, the absolute bandwidth is increased by a factor of 5 w.r.t. the reference case, resulting in an increase in imaging speed of approximately 25. Since the average spill-over efficiency does not change significantly as a function of the bandwidth (when sampled around f_c) there is



(a)



(b)

Figure 2.6: The effect of using a large operational frequency band is studied w.r.t. the reference case of 20% fractional bandwidth as shown in (a). All three sampling configurations are shown in (a), $d_f = 0.5F_{\#}\lambda_c$ (left), $d_f = 1F_{\#}\lambda_c$ (middle) and $d_f = 2F_{\#}\lambda_c$ (right) with ν relative bandwidth centered around f_c and with their associated reference cases of 20% fractional bandwidth. In (b) is the imaging Speed Ratio $SR(\nu) = \frac{s^\alpha(\nu)}{s^\beta(\nu=1.22)}$ as a function of the relative bandwidth $\nu = \frac{f_{\max}}{f_{\min}}$.

not much difference between the imaging speed ratios of the three sampling configurations. Mainly due to this reason, it is important to note that also for wideband systems the coherent sampling configuration $d_f = 1F_{\#}\lambda_c$ is still the optimal FPA configuration: For the same absolute bandwidth, coherently sampling is faster with a factor of 2.35 w.r.t. the fully sampled FPA, as we concluded in the previous subsection (Table 2.1).

2.3.3 Maximizing Imaging Speed with an Undersampled FPA

In the case that the detectors are not sufficiently sensitive at the desired imaging speed, two practical solutions exist to improve the sensitivity or imaging speed at the cost of (potential) resolution: by increasing the feed size d_f (until $2F_{\#}\lambda_c$) or by translating the

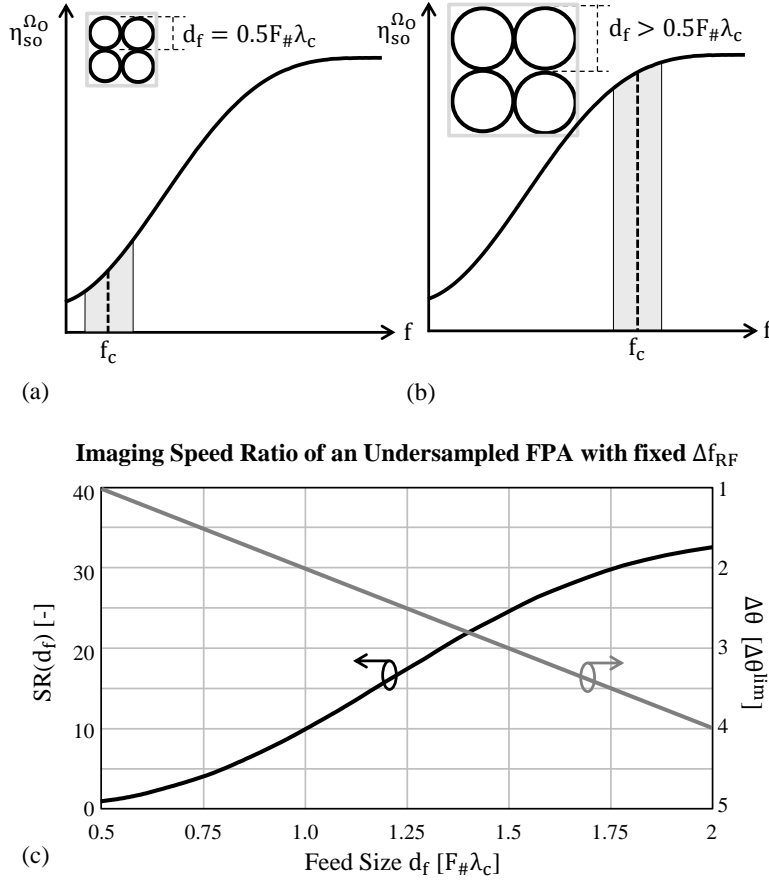


Figure 2.7: In (c) the imaging speed ratio $SR(d_f) = \frac{s^\alpha(d_f)}{s^\beta(d_f=0.5F_{\#}\lambda_c)}$ and resolution are shown as a function of the feed size d_f . The reference case, with imaging speed $s^\beta(d_f = 0.5F_{\#}\lambda_c)$, is shown in (a) and is a fully sampled FPA with $\Delta\theta^{lim} = \lambda_c/D$ resolution. The reference case is compared to $s^\alpha(d_f)$ as shown in (b), where the feed size is increased leading to an undersampled array.

frequency band of operation to a higher portion in the spectrum (assuming the NEP is not affected). As explained in Sec. 2.2.2, without performing any jiggling the FPA becomes undersampled for $d_f > 0.5F_{\#}\lambda_c$ such that the optics do not offer a diffraction limited resolution (2.16).

In the first solution, the feed size d_f is increased. Let us define the imaging speed ratio as a function of the feed size,

$$SR(d_f) = \frac{s^\alpha(d_f)}{s^\beta(d_f = 0.5F_{\#}\lambda_c)} \quad (2.18)$$

The reference case, with imaging speed $s^\beta(d_f = 0.5F_{\#}\lambda_c)$, is a fully sampled FPA as is illustrated in Fig. 2.7(a). The feed size is increased while the bandwidth is kept fixed with a 20% fractional bandwidth centered around f_c . A larger feed size results in an increase in spill-over efficiency and therefore imaging speed $s^\alpha(d_f)$, as illustrated in Fig. 2.7(b) and quantified in Fig. 2.2. The imaging speed ratio $SR(d_f)$ is shown in Fig. 2.7(c) with the

black curve and left y-axis. For the same absolute bandwidth and without jiggling, the imaging speed ratio is increasing quadratically with the spill-over efficiency. When the feed size is $d_f = 2F_{\#}\lambda_c$, the FPA is faster with a factor of 32. This increase in imaging speed comes at the cost of resolution. Referring back to (2.16), for a feed-size of $d_f = 2F_{\#}\lambda_c$ the resolution is not diffraction limited: $\Delta\theta = 4\Delta\theta^{\text{lim}}$ since the pointing direction of the patterns associated with two adjacent feeds ($n = 0$ and $n = 1$ $d_f = 2F_{\#}\lambda_c$ in Fig. 2.5) is increased. The resolution, as a function of the feed size, is shown by the gray curve and right axis in Fig. 2.7(c). Of course, one could compensate for this decrease in resolution by increasing the size of the optics.

The second option, if the technology and application allows for it, is to translate the frequency band of operation to a higher portion in the spectrum. This higher frequency band is defined with a new center frequency f'_c . Although the physical feed size remains unchanged, the electrical size (in terms of λ'_c) grows linearly with f'_c/f_c , which contributes to the same increase in imaging speed as shown in Fig. 2.7(c). Furthermore, an additional increase of $(f'_c/f_c)^2$ in imaging speed can be expected since the absolute bandwidth increases with a factor f'_c/f_c when the fractional bandwidth is kept fixed.

For example, if one initially operates with a fully sampled FPA $d_f = 0.5F_{\#}\lambda_c$ around f_c but decides to increase in imaging speed by translating the frequency band to $f'_c = 4f_c$ (i.e. maximum gain sampling $d_f = 2F_{\#}\lambda'_c$ with the same physical feed size) one expects a factor of $32 \times 16 = 512$ increase in imaging speed where the factor 32 is the result of the increase in spill-over efficiency and the factor $(f'_c/f_c)^2 = 16$ is the result of the increase in absolute bandwidth.

In the following section, we will see that in an imaging scenario an undersampled array is actually beneficial in terms of image quality.

2.4 Image Quality in Undersampled Arrays

In the previous section, it was explained that a significant increase in imaging speed can be achieved when operating in a higher frequency band with center frequency $f'_c > f_c$. When the physical feed-size is not altered, the resolution is not changed, although it is not anymore diffraction limited (2.16). In this section, we will see that in an imaging scenario the image quality of an undersampled array does improve w.r.t. a fully sampled array with the same resolution. For this study we introduce a beam efficiency of the effective gain patterns ($G_{\text{eff}}(\Omega)$ defined in (2.8b)). The beam efficiency is, in essence, the spill-over efficiency of a pixel w.r.t. the angular region associated with that specific pixel. This angular region we refer to as the *pixel region* (referring to the centered feed $n = 0$ in Fig. 2.5, its associated pixel region subtends $\phi \in (0, 2\pi), \theta \in (0, \frac{\lambda_c}{4D})$).

Let us consider a fully sampled array as is illustrated in the left hand side of Fig. 2.8(a). We consider both a narrowband ($\nu = 1.22$) and wideband ($\nu = 3$) FPA. The normalized effective gain patterns of three adjacent feeds in the FPA are shown on the left-hand side of Fig. 2.8(b). The beam patterns of adjacent feeds have a significant overlap. This means that a pixel shares a significant portion of incident power with adjacent pixels; the pixels

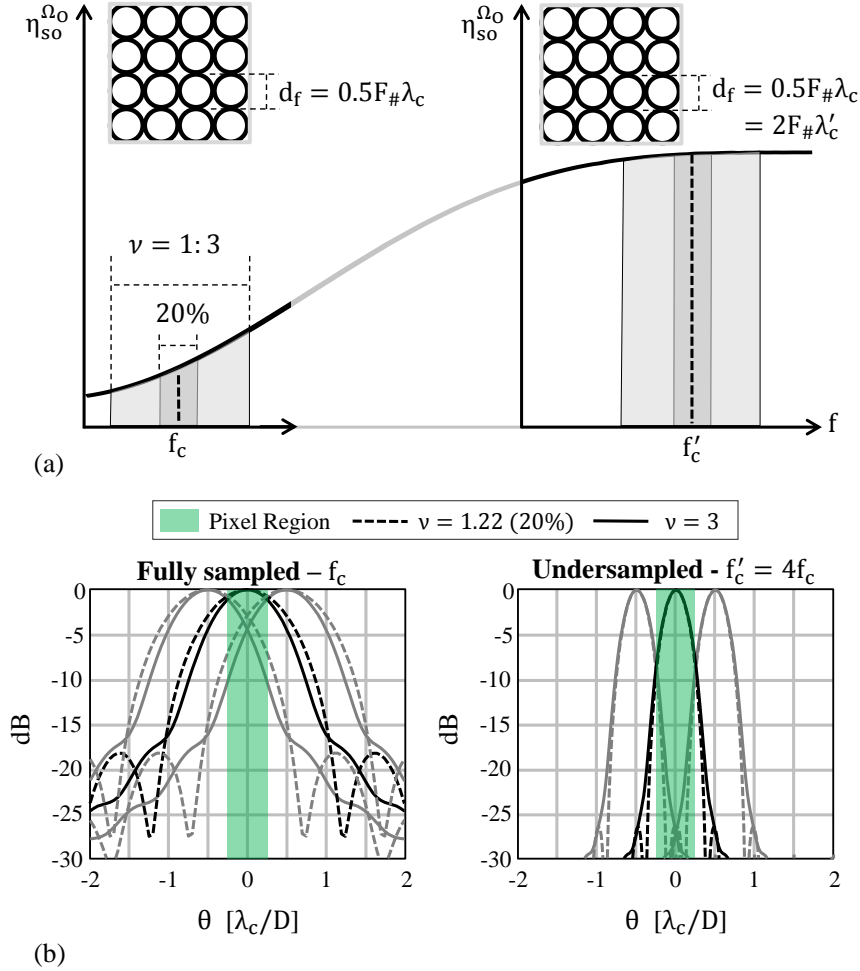


Figure 2.8: In (b) the normalized effective gain patterns (2.8b) of three adjacent feeds for the two FPAs depicted in (a) are shown. For both FPAs a $\nu = 1.22$ and a $\nu = 3$ relative bandwidth are investigated. The angular pixel region associated with the on-axis pixel is highlighted.

are not well restricted to their own pixel region. This pixel region is also indicated in Fig. 2.8(b) by the green bar.

Consider now the same FPA but operating in a frequency band around $f'_c = 4f_c$, as illustrated in the right-hand side of Fig. 2.8(a). The normalized effective gain patterns of adjacent feeds are shown on the right-hand side of Fig. 2.8(b). Since the feed size remains the same, the pointing direction of the beam patterns is also unchanged. Both FPA configurations have therefore the same resolution. However, the FPA operating around $f'_c = 4f_c$ operates in a higher frequency band such that the beam patterns become more directive. The pixels are significantly better isolated in their pixel region.

Let us quantify this pixel isolation by introducing a beam efficiency, BE, that describes how well the effective gain pattern is isolated from the patterns associated with adjacent pixel regions. The beam efficiency can be defined by angularly integrating the beam pattern

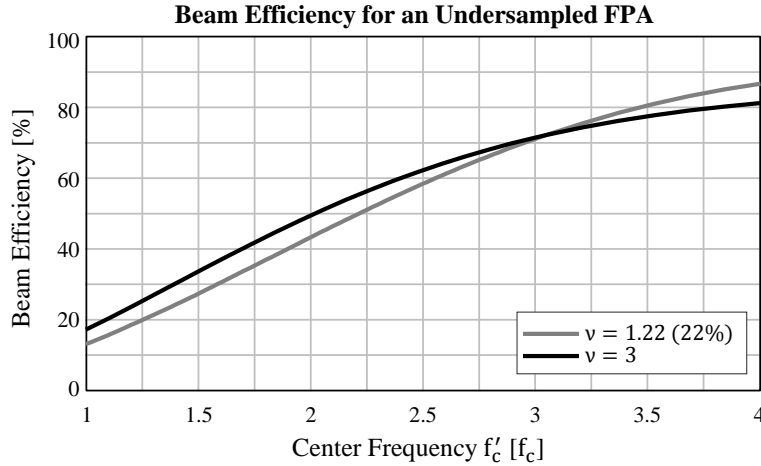


Figure 2.9: Beam efficiency as calculated with (2.19). The beam efficiency describes how well the effective gain pattern is coupled to the angular region subtended by the pixel ($\phi \in (0, 2\pi), \theta \in (0, \frac{\lambda_c}{4D})$) for the centered feed).

over the pixel region that is associated with that particular feed, which for the on-axis feed results in (2.19):

$$\text{BE} = \frac{\int_0^{2\pi} \int_0^{\frac{\lambda_c}{4D}} G_{\text{eff}}(\theta) \sin(\theta) d\theta d\phi}{\int_0^{2\pi} \int_0^{\pi/2} G_{\text{eff}}(\theta) \sin(\theta) d\theta d\phi} \quad (2.19)$$

The beam efficiency is shown in Fig. 2.9 as a function of the translated center frequency f'_c . If the array is fully sampled for the frequency band of operation ($f'_c = f_c$), the beam patterns are not well restricted to their own pixel region; with a BE $\approx 15\%$ the feed will mainly integrate power from adjacent pixel regions. Instead, by undersampling the FPA to $f'_c = 4f_c$, the beam patterns will be more directive and the beam efficiency is higher than 80%, i.e. the beam patterns are well isolated from adjacent feeds. No significant difference in BE between narrowband and wideband systems can be observed.

The beam efficiency does impact the temperature sensitivity of the system. Despite the fact that the analysis is derived for distributed sources, it should be noted that a high BE implies that the system is less sensitive to isolated sources at the edges of a pixel region. Instead, for distributed sources, a high BE improves the sensitivity since the BE can, in fact, be included as an additional spill-over term in the evaluation of P_a^n (2.5), while simultaneously considering the power arriving from adjacent pixels to be contributing to the noise power.

Consider the following imaging example to investigate the effect of the beam efficiency on the quality of image reconstruction. The THz-Sensing-Group logo is defined with a source temperature $T_S(\Omega)$ and is angularly distributed in space. The logo is projected in the u, v -domain ($u = \sin(\theta)\cos(\phi)$ and $v = \sin(\theta)\sin(\phi)$) in Fig. 2.10. The solid angle subtended by the source distribution is assumed so small such that $\sin(\theta) \approx \theta$ and the projection in the u, v domain can be normalized to the angular pixel dimension, $\lambda_c/2D$.

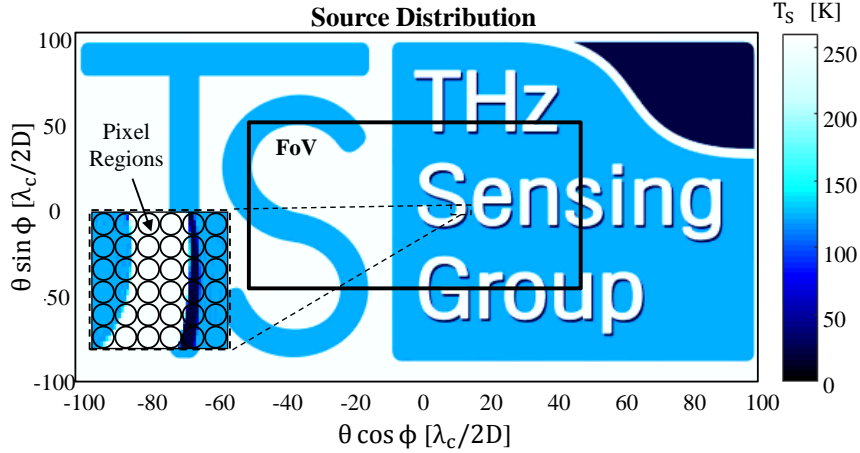


Figure 2.10: THz-Sensing Group logo as source distribution projected in the u, v -domain using $u = \theta \cos(\phi)$ and $v = \theta \sin(\phi)$. Indicated is the FoV of a 100×100 element FPA and a zoom-in on the letter S showing the pixel regions of 6×6 elements. The color bar on the right shows the temperature distribution T_s of the logo.

The temperature distribution, $T_S(\Omega)$, is defined from 0 to 255 K, as is shown by the color bar. Indicated by the box is the FoV under investigation, which corresponds to the FoV of 100×100 elements in a fully sampled FPA. A zoom-in on the letter S is shown, illustrating the pixel regions of 6×6 elements in the FPA. The received power by the n -th feed, P_a^n , can be calculated by using (2.8a). Subsequently, by using the approximation on average received power, \bar{P}_a (2.9a), the temperature distribution of the source can be reconstructed to be (2.20):

$$T_S^{\text{rec}}(\Omega_n) = \frac{P_a^n}{k_B \bar{\eta}_{\text{opt}} \Delta f_{\text{RF}}} = \frac{\int_{\Omega_S} T_S(\Omega) G_{\text{eff}}(\Omega - \Omega_n) d\Omega}{4\pi \bar{\eta}_{\text{opt}} \Delta f_{\text{RF}}} \quad (2.20)$$

The reconstructed thermal image of the source distribution, T_S^{rec} , is shown in the top two figures of Fig. 2.11 for the fully sampled FPA ($f'_c = f_c$) with its associated effective gain pattern in the left sub-figure in Fig. 2.8(b). By repeating the procedure with the effective gain pattern (right sub-figure in Fig. 2.8(b)) of the undersampled array ($f'_c = 4f_c$), one obtains the bottom two reconstructed images in Fig. 2.11. When both reconstructed images are compared, we can see that the letters *Sens* and the transition from white to blue are significantly sharper for the undersampled array due to a higher beam efficiency. Whereas the feeds in a fully sampled array, with a BE $\approx 15\%$, receives power from several pixel regions away, the undersampled array is better isolated with BE $\approx 80\%$, which results in an improved image reconstruction.

For this reason, the image quality can be qualified both in terms of the nominal resolution $\Delta\theta$ due to the angular discretization of the beams and in terms of the beam efficiency.

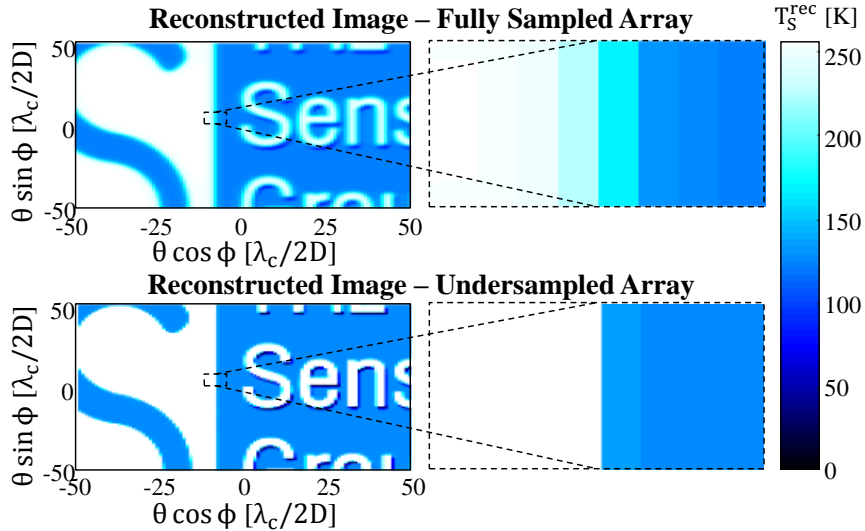


Figure 2.11: Reconstructed image of the source distribution shown in Fig. 2.10 in the case that the image is acquired using a fully sampled FPA and an undersampled FPA with $f'_c = 4f_c$. The reconstructed image is calculated by using (2.20). A zoom-in of the transitions between the white and blue regions are shown.

2.5 Realistic Feeds

In the previous analysis, we made use of uniformly illuminated and ideal feeds. In this section, we will instead show the performance of a realistic antenna design. The modeling techniques that are used in this section are the same that have been used in the last years by some of the authors for the development and characterization of lens antenna FPAs for passive astronomical instruments. The predicted performance of the lens antennas show excellent agreement with measurements [113, 38].

In order to appreciate the applicability of this study we will consider a FPA containing wideband leaky lens antenna feeds as is shown in Fig. 2.12(a) [66]. The radiation performance of a single leaky lens has been measured at low frequency in [114] and at high frequency in [115, 116]. After introducing the quasi-optical system containing leaky lens feeds, a comparison in terms of imaging speed will be made with narrowband conical horn antenna feeds.

The leaky lens feeds operate from 200 GHz to 600 GHz ($\nu = 3$) and illuminate a parabolic reflector with $F_{\#} = 2.5$. In order to optimize the imaging speed, we place the feeds in a maximum gain sampled array ($d_f = 2F_{\#}\lambda_c$) at $f_c = 400$ GHz *without* mechanically jiggling the FPA. Note that this FPA is equivalent to the scenario discussed in Fig. 2.7 with $d_f = 2F_{\#}\lambda_c$; the array is undersampled to maximize the imaging speed. The resolution is not diffraction limited with $\Delta\theta = 4\Delta\theta^{\text{lim}} = 4\frac{\lambda_c}{D}$. The feeds are optimized and analyzed by numerical CST simulations [117], leading to the dimensions of the slot and elliptical lens as are shown in Fig. 2.12(b) and Fig. 2.12(c) respectively. The dimensioning of the elliptical lens is corrected for a phase center of $126 \mu\text{m}$ behind the slot and the 50° truncation is at approximately the -10 dB beamwidth of the fields inside the lens at

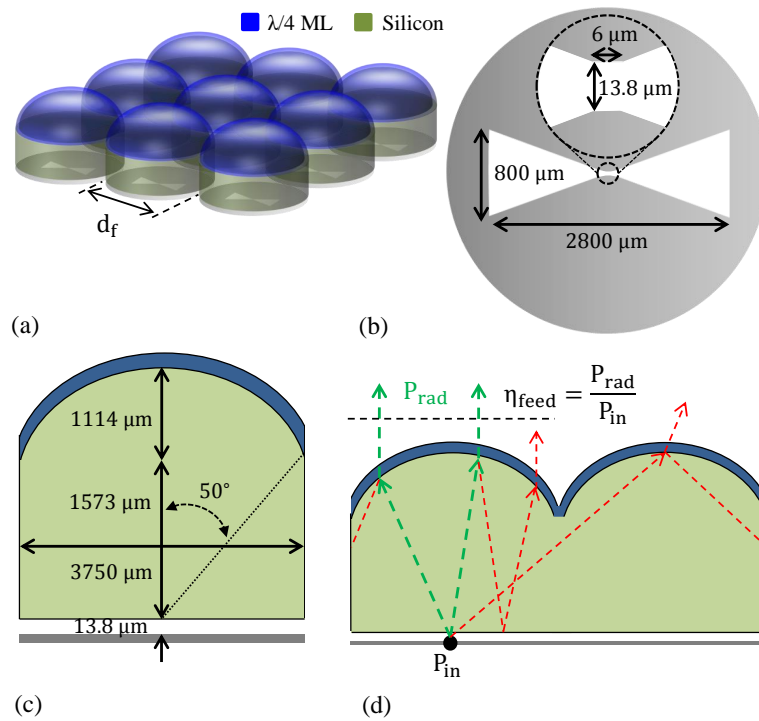


Figure 2.12: Leaky lens antennas [66] serving as reflector feeds in FPA as depicted in (a). The dimensions of the slot and elliptical lenses are shown in (b) and (c) respectively. The definition of feed efficiency is illustrated in (d).

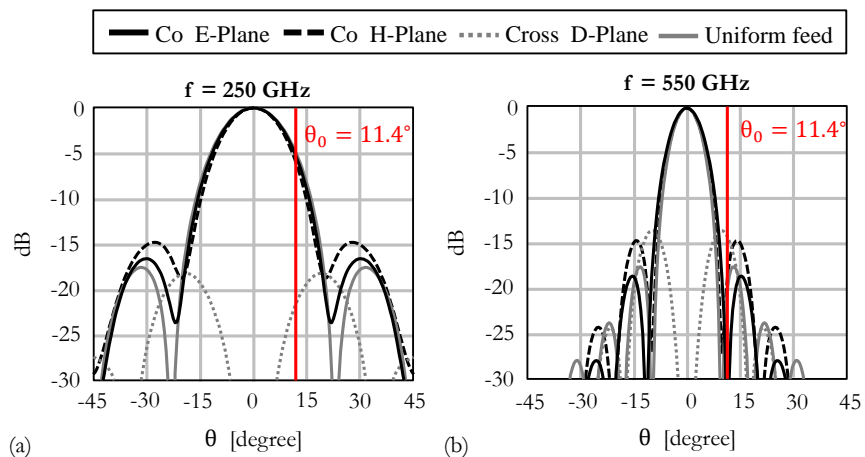


Figure 2.13: Feed patterns of the leaky lens antennas compared to the pattern of a uniformly illuminated feed with the same diameter. Indicated with θ_0 is the angle subtended by a reflector for a $F_{\#} = 2.5$ configuration.

200 GHz. In Fig. 2.13(a) and Fig. 2.13(b), the patterns of the leaky lens antennas are respectively plotted for $f = 250$ GHz and 550 GHz. As a reference, the patterns indicated with *Uniform* are associated with uniformly illuminated feeds with the same feed size, d_f ,

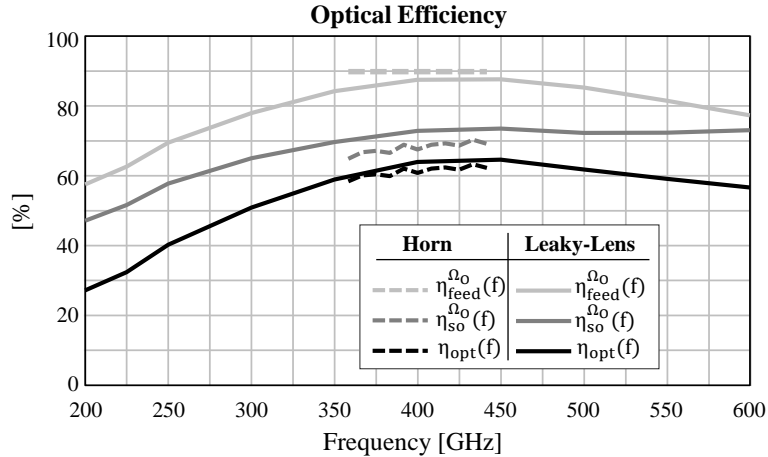


Figure 2.14: Optical efficiency for both the leaky lens (solid) FPA and horn (dashed) FPA.

as those used throughout the previous sections. The pattern region that is subtended by the reflector is indicated by θ_0 . The reflector patterns are obtained by physical-optics (PO) in GRASP [118].

The feed efficiency, η_{feed} , the spill-over efficiency w.r.t. the reflector, $\eta_{\text{so}}^{\Omega_O}$, and the optical efficiency $\eta_{\text{opt}} = \eta_{\text{feed}}\eta_{\text{so}}^{\Omega_O}$ are shown in Fig. 2.14 by the solid lines. It is important to note that the feed efficiency is defined as the ratio of the power radiated by the leaky lens, P_{rad} , and the power presented to the port, P_{in} , where any radiated power that is first reflected inside the lens or substrate is omitted. This is visualized in Fig. 2.12(d), where only the green, reflection free, rays contribute to the radiated power, P_{rad} . Power leaving the leaky lens after the first reflection is not expected to be captured by the reflector. The average optical efficiency of the reflector system illuminated by the leaky lenses is $\bar{\eta}_{\text{opt}} = 55.3\%$, leading to an effective bandwidth of $\Delta f_{\text{RF}}^{\text{eff}} = 0.553 \cdot 400 \text{ GHz} = 221 \text{ GHz}$.

A significant advantage of the described leaky lens structure is that it is fully integrated. This means that it can be used in large FPAs. Furthermore, impedance matching over the full operational bandwidth is simple to achieve. Instead, feeding- and matching-architectures for a large integrated FPA based on horn antennas is proven to be a difficult task [119] when fractional bandwidths larger than 20% are desired. Let us compare the leaky lens FPA with a FPA containing conical horn antennas, sampled identically to the leaky lens antennas with $d_f = 2F_{\#}\lambda_c$. The horn antennas are operating in a 20% fractional bandwidth from 360 GHz to 440 GHz, as indicated in Fig. 2.14. Their efficiencies are shown by the dashed lines. The horn antennas are simulated without any losses or feeding network. Instead, we define the feed efficiency optimistically at 90% over the full band. The average optical efficiency is 61.5% leading to an effective bandwidth of $\Delta f_{\text{RF}}^{\text{eff}} = 49.2 \text{ GHz}$. The imaging speed ratio (2.12) of the leaky lens based FPA w.r.t. the horn-antenna based FPA is $\text{SR} = \frac{s^{\text{Leaky-Lens}}}{s^{\text{Horn}}} = \left(\frac{221}{49.2}\right)^2 = 20$. This SR is indeed close to the predicted value in Fig. 2.6 of $\text{SR}(\nu = 3) = 21.5$.

Referring back to Fig. 1.3, an effective bandwidth of 221 GHz is sufficient to achieve a

1 K sensitivity and a 10 Hz refresh rate imaging requirement, provided that the detectors have a NEP of $1.4 \text{ pW}/\sqrt{\text{Hz}}$. Recently conducted measurements [120] of a *dual polarized* leaky lens antenna show that the received power (2.5) from an incoherent source is increased by a factor of 2 compared to a single polarized version of the antenna. In that scenario, the requirement on the detector NEP is relaxed by the same factor. This demonstrates that a practical sensitivity and imaging speed can be achieved with an uncooled and fully passive integrated FPA. The horn antenna based FPA on the other hand, with an effective bandwidth of 49.2 GHz, will require cooling or amplification circuitry to achieve the practical imaging requirements.

2.6 Conclusion

Uncooled sub-millimeter wave direct detectors are characterized by moderate sensitivities due to high electronic noise and thus are not often proposed for real-time imaging. In this chapter, the design guidelines for focal plane architectures based on antenna coupled direct detectors are proposed with greatly enhanced potential speeds thanks to the efficient use of the available spectral bandwidth at sub-millimeter wavelengths. Relying on the guidelines and focal plane architectures introduced in this chapter, it is shown that real-time imaging with high sensitivities can be achieved with already available practical detectors.

Chapter 3

Scenario Analysis: Pedestrian Detection for the Automotive Industry

In order to demonstrate the applicability of using direct detection THz FPAs for future large-volume imaging applications, the study presented in Chapter 2 is applied to a scenario analysis. In this case-study, the radiometric performance of passive THz imagers is analyzed in the scenario of pedestrian detection for the automotive industry. Autonomous driving is an ambitious goal for automotive manufacturers, which can only be achieved when the car can properly sense its surroundings, and thus close-by pedestrians, in all atmospheric conditions and without a single exception. This is not an easy task for a single sensor to achieve. Optical camera's can not detect in the night, whereas infrared (IR) cameras show significant performance degradation in rainy and foggy conditions. The ability of THz radiation to penetrate reasonably well through clothing and foggy weather conditions, make such imagers ideal candidates to complement existing optical or IR imagers to increase the detection probability of pedestrians.

3.1 Scenario Description

In Chapter 2 it was shown that when a few hundreds of GHz of absolute bandwidth is exploited to efficiently couple incoherent radiation coming from blackbody sources to detectors that feature a NEP in the order of $1 \text{ pW}/\sqrt{\text{Hz}}$, a sub-Kelvin imaging capability might be realized at real-time refresh-rates. In this chapter, a case-study is performed where such passive imager, operating from 200 GHz to 600 GHz with a $\text{NEP} = 1 \text{ pW}/\sqrt{\text{Hz}}$, is used for pedestrian detection. A study on the temperature sensitivity as function of sampling periodicity and range is performed, taking into account atmospheric attenuation in foggy weather conditions.

It is assumed that the imaging cameras can be installed in the front-side of the car. The maximum aperture diameter of the camera is assumed to be $D = 5 \text{ cm}$. As illustrated

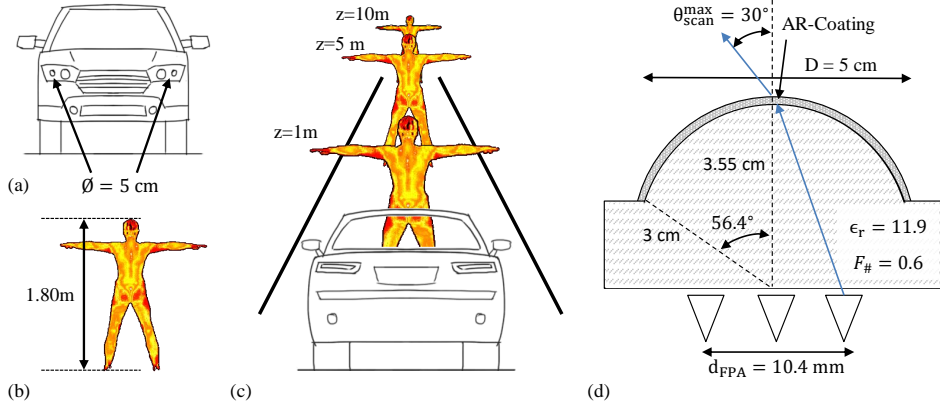


Figure 3.1: Scenario description for the considered pedestrian detection application. (a) It is assumed that a sensor with a diameter of 5 cm can be integrated in the front of the car, possibly two sensors to allow for stereo-imaging. (b) The considered pedestrian is an adult of 1.80 m in height. (c) The pedestrian is positioned at three different range: $R = 1$ m, 5 m and 10 m. (d) A standard silicon elliptical lens is used with a $F_{\#} = 0.6$ and a diameter of $D = 5$ cm. It is assumed that the maximum scanning angle is 30° , which defines the maximum dimension of the FPA.

in Fig. 3.1(a), one could decide to integrate two cameras on the front-side, that will enable stereo-imaging capabilities. In a stereo-imaging configuration, the distance of the pedestrian to the car can be resolved. The pedestrian under consideration in this case-study is shown in Fig. 3.1(b) and is assumed to be 1.80 m tall. The pedestrian, who is spreading the arms for a resolution study presented in Sec. 3.3.2, is placed at a distance of $R = 1$ m, 5 m and 10 m in front of the car, as shown in Fig. 3.1(c). The study will be performed for the three sampling configurations, $d_f = 0.5F_{\#}\lambda_c$, $1F_{\#}\lambda_c$ and $2F_{\#}\lambda_c$ as was shown in Fig. 2.4 and the imaging performance is analyzed using their associated multi-beam patterns that are shown in Fig. 2.5. The diameter of the optics is determined by the maximum aperture diameter of the sensor, that was fixed to $D = 5$ cm. The physical sampling periodicity is determined by assuming that a standard silicon elliptical lens is used with a typical focal number of $F_{\#} = 0.6$, as is depicted in Fig. 3.1(d). The feeds are sampled at the center frequency of 400 GHz. The physical sampling periodicity for the different sampling configurations is summarized in Table 3.1. The maximum scanning angle is fixed to $\theta_{\text{scan}}^{\text{max}} = \pm 30^\circ$ and no scan loss or pattern aberration is taken into account for this scenario analysis. In reality, such elliptical lens will result in a moderate scanning performance, as is also presented in Sec. 6.5. The maximum scanning angle, together with the $F_{\#}$ of the

Table 3.1: Different sampling configurations under configuration and their associated efficiencies

Sampling [$F_{\#}\lambda_c$]	Sampling [μm]	N_{feeds} [-]	Resolution $\Delta\theta$ [$^\circ$]	Radiation Efficiency	Spillover Efficiency	Optical Efficiency
0.5	66	157×157	0.43	70%	15%	11%
1	132	78×78	0.86	70%	46%	32%
2	264	39×39	1.72	70%	84%	59%

lens, determines the maximum size of the FPA, which is derived to be $d_{\text{FPA}} = 10.4 \text{ mm}$. The number of feeds that will fit in this FPA, N_{feeds} , is summarized in Table 3.1 for the different sampling configurations and leads to $N_{\text{feeds}} = 157 \times 157 \approx 25 \text{ kPixels}$ for the fully sampled array ($d_f = 0.5F_{\#}\lambda_c$) and $N_{\text{feeds}} = 39 \times 39 \approx 1.5 \text{ kPixels}$ for the maximum gain sampled array ($d_f = 2F_{\#}\lambda_c$). All feeds of the array are assumed to have the same average radiation efficiency of $\bar{\eta}_{\text{rad}} = 70\%$ over the full frequency band, and a spill-over efficiency that was derived in Chapter 2 and summarized in Table 2.1. In this scenario, with low $F_{\#}$ optics, the spill-over efficiency also includes mutual coupling losses between the different FPA elements. The three sampling configurations $d_f = 0.5F_{\#}\lambda_c$, $1F_{\#}\lambda_c$ and $2F_{\#}\lambda_c$ have an average optical efficiency of 11 %, 32 % and 59 % respectively.

3.2 Field-of-View and Resolution

The angular FoV was fixed to be $\theta_{\text{scan}}^{\text{max}} = \pm 30^\circ$, as illustrated in Fig. 3.2(a). The illustration also shows the definition of spatial FoV, as function of imaging distance R . The spatial FoV is shown in Fig. 3.2(b) and is around 11 m wide at an imaging distance of $R = 10 \text{ m}$. The angular resolution, $\Delta\theta$, is defined by the sampling periodicity as $\Delta\theta = \lambda_c/2D = 0.43^\circ$, $\lambda_c/D = 0.86^\circ$ and $2\lambda_c/D = 1.72^\circ$ and are summarized in Table 3.1. The spatial resolution, $\Delta X = R\Delta\theta$ in Fig. 3.2(c), is shown in Fig. 3.2(d) as function of imaging distance R . A

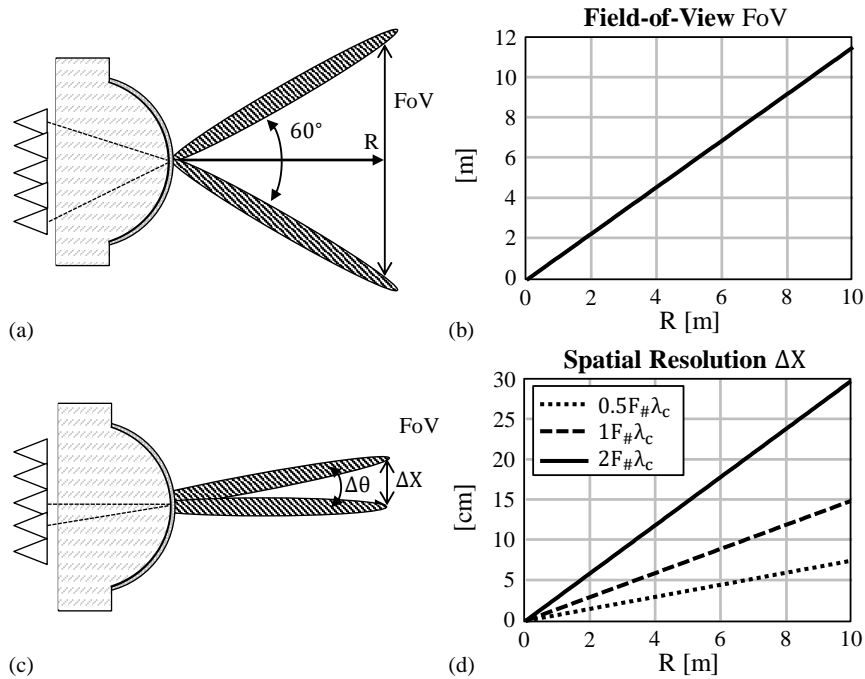


Figure 3.2: Field-of-View and Spatial resolution. (a) The Field-of-View is defined by size of the FPA and was assumed to be 60° angularly and leads to the spatial resolution reported in (b) as function of distance. (c) The angular resolution, $\Delta\theta$ is defined by the sampling periodicity and is summarized in Table 3.1. The spatial resolution, as function of imaging distance is shown in (d).

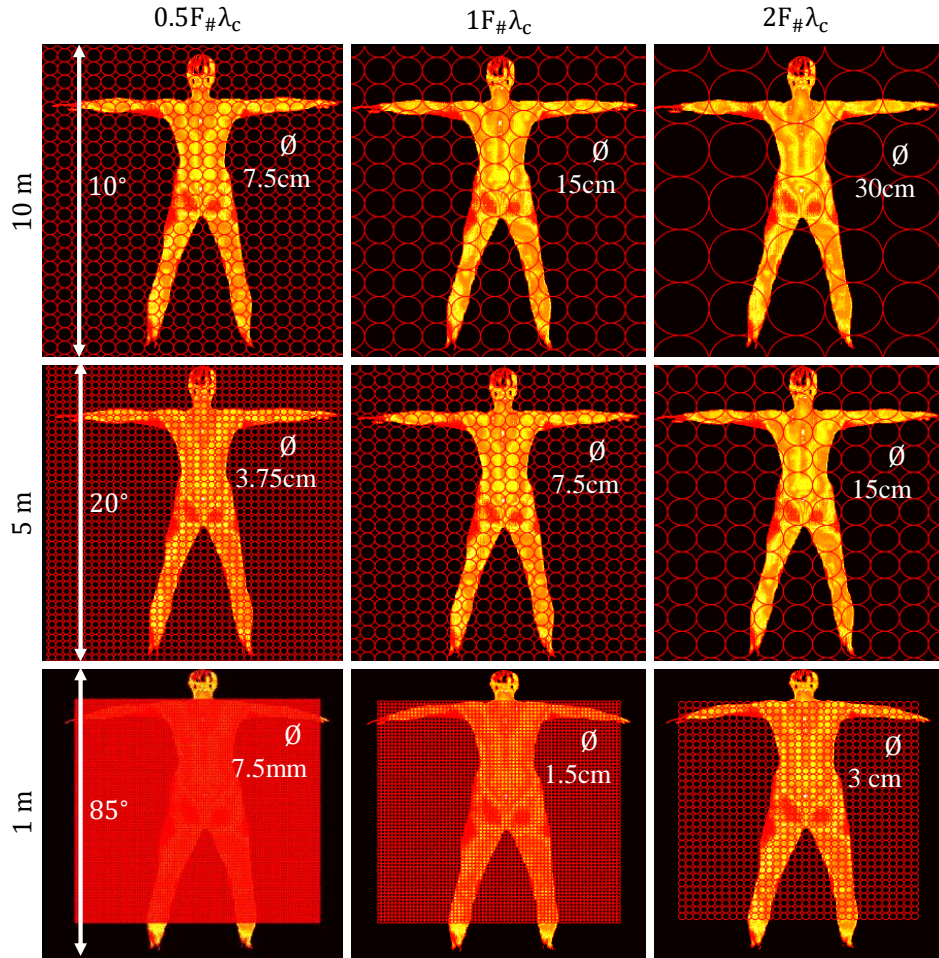


Figure 3.3: Spatial resolution of the THz imager at the distances $R = 1, 5, 10$ m and for a sampling periodicity of $d_f = 0.5F\#\lambda_c$, $0.5F\#\lambda_c$ and $2F\#\lambda_c$. Indicated is the total angle that the pedestrian is subtending w.r.t. the imager. Also indicated is the spatial resolution, visualized with the red circles.

visualization of the spatial resolution, as function of sampling configuration and imaging distance, is shown in Fig. 3.3. The red circles indicate the spatial resolution and can be as large as $\Delta X = 30$ cm at 10 m distance with the $2F\#\lambda_c$ sampling configuration. The angle that the pedestrian is subtending w.r.t. the imager is also indicated.

3.3 Temperature Sensitivity

In Chapter 2, the temperature sensitivity, NETD, was derived assuming that the sources are distributed, i.e. sources that completely subtend the main-lobe and first side-lobes of the beam pattern such that the feeds only integrate power coming from the source and not the (sky-)background. In reality, this is not always the case and the coupling of each pixel's beam pattern to a source of with a given angular dimension, should be taken into

account. In Sec. 3.3.1, the distributed source NETD is evaluated as function of imaging distance, taking into account the atmospheric attenuation for a foggy weather condition. Then, in Sec. 3.3.2, the coupling of each of the pixels to the pedestrian is introduced, after which the temperature sensitivity of each pixel to the pedestrian is calculated in Sec. 3.3.3 and Sec. 3.3.4 for cold and warm weather conditions.

3.3.1 Temperature Sensitivity for a Distributed Source

The atmospheric transmission through fog is analyzed using the models that are accepted by the International Telecommunication Union (ITU). For the foggy weather condition, the model of attenuation due to atmospheric gases (oxygen and saturated water) [121] is combined with the model of attenuation due to fog and clouds [122]. The atmosphere is assumed to have a temperature of 23° , a relative humidity of 55% and a pressure of

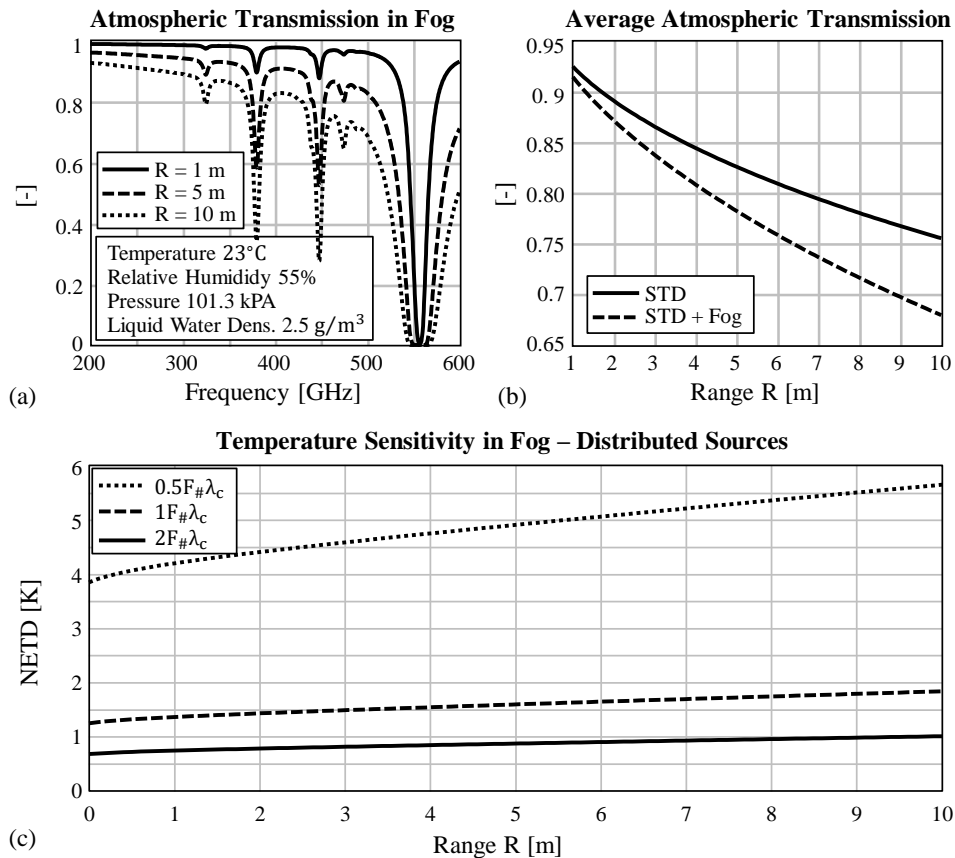


Figure 3.4: Temperature sensitivity for distributed sources in a foggy weather condition. (a) Atmospheric transmission, $\eta_{atm}(f)$, as function of frequency for the three imaging distances. The atmospheric conditions are indicated. (b) The atmospheric transmission, averaged over frequency, as function of imaging range, $\bar{\eta}_{atm}(R)$ for the standard weather condition (STD) and the foggy weather condition (STD+Fog). (c) Distributed source temperature sensitivity for the foggy weather condition and a 10 Hz refresh rate, as defined by (3.2).

101.3 kPa. The fog is characterized with a liquid water density of 2.5 g/m^3 . The atmospheric transmission, $\eta_{\text{atm}}(f, R)$, as function of frequency and for the different imaging distances, is shown in Fig. 3.4(a). In the evaluation of the temperature sensitivity, an average atmospheric transmission is calculated using (3.1).

$$\bar{\eta}_{\text{atm}}(R) = \frac{1}{\Delta f_{\text{RF}}} \int_{\Delta f_{\text{RF}}} \eta_{\text{atm}}(f, R) df \quad (3.1)$$

The average atmospheric transmission of the standard weather condition (STD) and the foggy condition that includes the liquid water density (STD+Fog) are shown in Fig. 3.4(b). After calculating the average atmospheric transmission as function of range, the distributed source NETD can now be defined as (3.2):

$$\text{NETD}(R) = \frac{\text{NEP}_{\text{det}}}{k_B \bar{\eta}_{\text{so}} \bar{\eta}_{\text{rad}} \bar{\eta}_{\text{atm}}(R) \Delta f_{\text{RF}} \sqrt{2\tau_{\text{int}}}} \quad (3.2)$$

where $\text{NEP}_{\text{det}} = 1 \text{ pW}/\sqrt{\text{Hz}}$, $k_B = 1.38 \times 10^{-23} \text{ m}^2 \text{ kg s}^{-2} \text{ K}^{-1}$ being Boltzmann's constant, $\bar{\eta}_{\text{so}}$ and $\bar{\eta}_{\text{rad}}$ as summarized in Table 3.1, $\Delta f_{\text{RF}} = 400 \text{ GHz}$ and $\tau_{\text{int}} = 0.1 \text{ s}$ (i.e. a 10 Hz refresh-rate). The NETD as function of imaging distance is shown in Fig. 3.4(c) for the three sampling configurations. It can be seen that for a maximum gain sampled array ($d_f = 2F_{\#}\lambda_c$), a sub-Kelvin imaging capability can be achieved. The fully-sampled array ($d_f = 0.5F_{\#}\lambda_c$) features an NETD larger than 4K.

3.3.2 Coupling Efficiency to a Pedestrian

The distributed source NETD presented in Fig. 3.4(c) assumes that the pixel is integrating power coming only from the pedestrian and not from the (sky)-background. However, not all pixels are pointing towards the pedestrian and, what can be seen in the top-right of Fig. 3.3, the pixels that are pointing towards the pedestrian can still have a significant spill-over with respect to the background due to their poor spatial resolution. If the pixel is not fully subtended by the pedestrian, a loss in temperature sensitivity to the pedestrian is experienced. This loss in temperature sensitivity can be quantified using a coupling efficiency, $\bar{\eta}_{\text{co}}(\Omega_n)$, of the pixel to the pedestrian (3.3):

$$\bar{\eta}_{\text{co}}(\Omega_n) = \frac{1}{4\pi} \int_{\Omega_s} D(f = 400 \text{ GHz}, \Omega - \Omega_n) d\Omega \quad (3.3)$$

The coupling efficiency is evaluated using the directivity pattern at 400 GHz where Ω_n shifts the broad-side directivity pattern in the scanning direction of the n -th pixel and the integration is performed only over the source solid angle Ω_s that describes the position of the pedestrian. In Fig. 3.5(a), the Field-of-View is shown for the fully sampled array at 1 m distance. The red-square is in fact a collection of the 157×157 red circles associated to each of the pixels. The coupling efficiency of each pixel to the pedestrian is shown in Fig. 3.5(b). The small spatial resolution of $\Delta X = 7.5 \text{ mm}$ in this scenario, results in a sharp transition from a 0% coupling efficiency to a 100% coupling efficiency. The worst case scenario is shown in Fig. 3.5(c), with a $d_f = 2F_{\#}\lambda_c$ sampling configuration at a 10 m imaging distance.

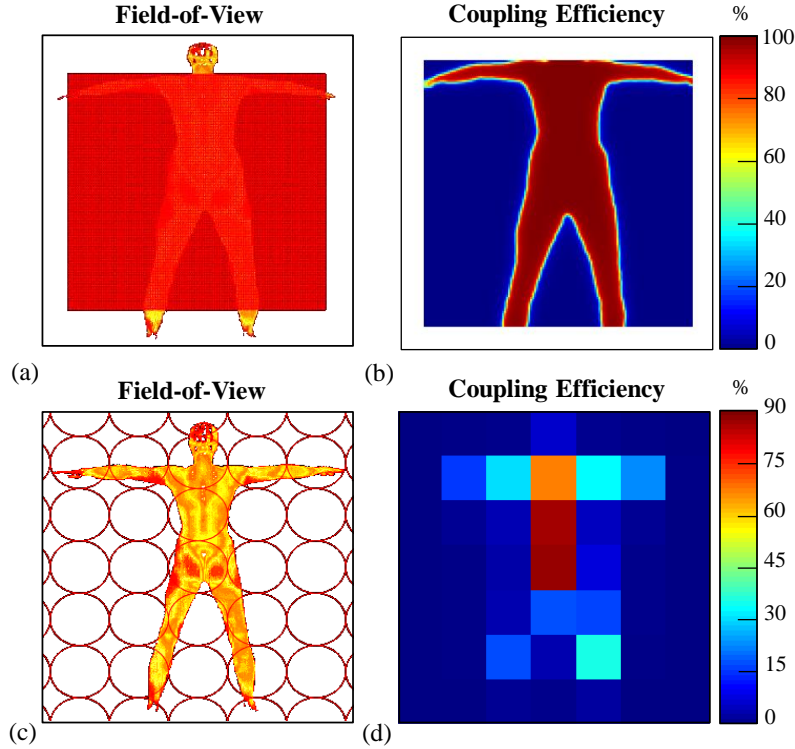


Figure 3.5: Coupling efficiency of each pixel to the pedestrian, as defined by (3.3). In (a) the Field-of-View and spatial sampling is shown for the $d_f = 0.5F\#\lambda_c$ sampling configuration at $R = 1$ m distance. (b) Shows the coupling efficiency for the $d_f = 0.5F\#\lambda_c$ sampling configuration at $R = 1$ m distance. In (c), the spatial sampling for a $d_f = 2F\#\lambda_c$ sampling configuration at $R = 2$ m distance is shown with its associated coupling efficiency to a pedestrian shown in (d).

The large spatial resolution of $\Delta X = 30$ cm results in the fact that the pedestrian cannot be approximated as a distributed source for any of the pixels. The coupling efficiency for each pixel is shown in Fig. 3.5(d). The pixels that are pointing towards the arms of the pedestrian are mostly integrating power from the atmospheric background. This effect reduces the temperature sensitivity of the imager to the pedestrian and can be included as an efficiency term in the expression of the NETD (3.4).

$$\text{NETD}_n(R, \Omega_n) = \frac{\text{NEP}_{\text{det}}}{k_B \bar{\eta}_{\text{so}} \bar{\eta}_{\text{rad}} \bar{\eta}_{\text{atm}}(R) \bar{\eta}_{\text{co}}(\Omega_n) \Delta f_{\text{RF}} \sqrt{2\tau_{\text{int}}}} \quad (3.4)$$

With this definition of NETD, the required contrast between the radiometric temperature of the (sky-)background with respect to the temperature of the pedestrian can be analyzed.

3.3.3 High Contrast: Temperature Sensitivity in Cold Weather

In order for the imager to be able to distinguish the pedestrian from the atmospheric background, the temperature contrast between the pedestrian and its background should be larger than the NETD, otherwise the pedestrian will disappear as noise in the image.

This effect is studied in [55], where a concealed knife is strapped on a persons chest with a contrast of 5 K in temperature. In images that are taken with a 5 K NETD, the knife more or less disappears in the noise of the image. Only in images with a better temperature sensitivity, the knife can be distinguished. In fact, an NETD that is $10\times$ better (NETD=0.5 K) is shown to be desirable for a proper detection.

In the scenario of pedestrian detection, there should also be a sufficiently high contrast with the background. In [22], the apparent radiometric sky temperature is studied for different atmospheric conditions. It is shown that, above a frequency of 300 GHz, the apparent radiometric temperature is equal to the physical temperature of the atmosphere. For this reason, the atmospheric condition is not only important for the atmospheric attenuation of the power coming from the pedestrian, but also on the NETD requirement of the imaging system.

Suppose that the contrast between the temperature of the pedestrian and the atmosphere is 20 K. Calculating the NETD of every pixel (3.4) and by limiting the scale of NETD to 20 K leads to Fig. 3.6 for the three different sampling configurations and dis-

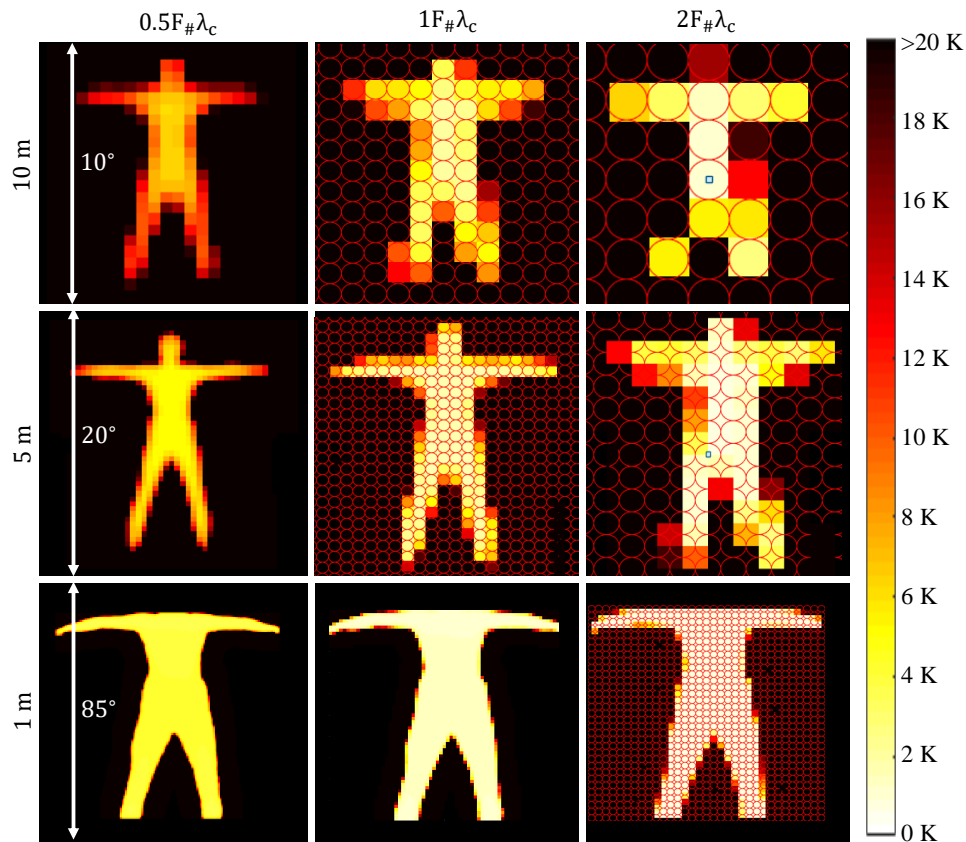


Figure 3.6: Temperature sensitivity of the imager to the pedestrian for a 10 Hz refresh rate, as defined by (3.4) in cold weather conditions. A limit of 20 K is set on the scale of the NETD, to indicate the imaging capabilities in cold weather conditions where the contrast between the radiometric temperature of the pedestrian and the apparent radiometric temperature of the atmospheric is 20 K.

tances that are considered. It can be seen that the pedestrian can theoretically be detected in all scenarios. One should be aware that, for an improved dynamic range, the NETD should be preferably be $10\times$ better, i.e. in the order of 2 K [55]. The presented plot merely shows the theoretical limit where the pixel receives more power than the noise fluctuations on top of the background image.

3.3.4 Low Contrast: Temperature Sensitivity in Warm Weather

Equivalently, the colorbar from Fig. 3.6 can be adjusted to analyze any other contrast scenarios. For example, on warm days, the contrast between the pedestrian and the background can be 3 K or even lower. Such scenario increases the performance requirements on the imager. The temperature sensitivity of each pixel to the pedestrian in the different considered sampling and distance configurations, is shown in Fig. 3.7 for a contrast of 3 K. It is clear that the fully sampled array is not able to distinguish the pedestrian from the noise fluctuations and the background. Instead, the resolution should be compromised to

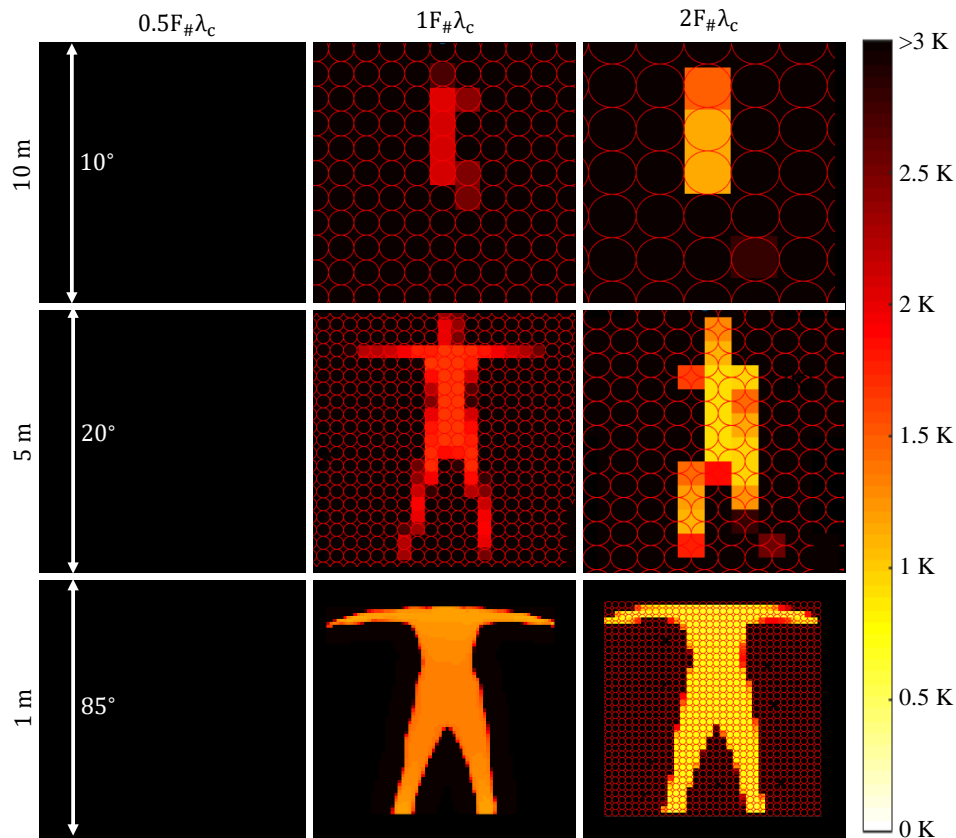


Figure 3.7: Temperature sensitivity of the imager to the pedestrian for a 10 Hz refresh rate, as defined by (3.4) in warm weather conditions. A limit of 3 K is set on the scale of the NETD, to indicate the imaging capabilities in warm weather conditions where the contrast between the radiometric temperature of the pedestrian and the apparent radiometric temperature of the atmospheric is only 3 K.

improve in temperature sensitivity so that the pedestrian can be detected during warm weather days. A larger spatial resolution will, however, also result in a poor coupling efficiency of the pixels to the arms and legs of the pedestrian, as was discussed in Sec. 3.3.2, such that these features disappear quickly from the image, as can be seen from Fig. 3.7. A good compromise between resolution and sensitivity is to sample the FPA coherently, i.e. $d_f = 1F_{\#}\lambda_c$.

3.4 Conclusion

In this chapter, a scenario analysis has been presented that evaluates the imaging performance of passive THz imaging FPAs for the purpose of pedestrian detection for the automotive industry. The FPA consists of feeds that operate over a 3:1 relative frequency band from 200 GHz to 600 GHz. The feeds are characterized with a radiation efficiency of 70% and a spill-over efficiency w.r.t. a dielectric lens. It is assumed that the detectors are characterized with an NEP of $1 \text{ pW}/\sqrt{\text{Hz}}$. A case study of system temperature sensitivity is performed in the scenario of pedestrian detection. In this analysis, the atmospheric attenuation due to a foggy weather condition is taken into account, as well as the coupling of a pixel's beam pattern to the pedestrian. The temperature sensitivity requirements of the imager are derived from the temperature contrast between the background and the pedestrian.

It is shown that a slightly undersampled array, with $d_f = 1F_{\#}\lambda_c$, is a good compromise between resolution and sensitivity. Such FPA configuration results in a temperature sensitivity of 2 K to 4 K for the detection of pedestrians up to 10 m with an acceptable resolution. Foggy weather conditions are most likely to appear at lower atmospheric temperatures, implying a high temperature contrast between the atmosphere and the pedestrian that can be 20 °C or higher. With such contrast, a pedestrian can be detected with a dynamic range of 5 to 10 times with respect to the noise fluctuations in the image. If the contrast is as low as 3 °C, however, the NEP of the detectors should be decreased in order to compensate for the increased sensitivity requirements. An increase of bandwidth is not useful due to the high atmospheric attenuation above 500 GHz. If imaging ranges larger than 10 m are desired, resolution should be improved due to a poor beam coupling efficiency to a pedestrian at larger distances. This can be achieved by using bigger lenses.

Chapter 4

Wideband Double Leaky Slot Lens Antennas in CMOS at THz Frequencies

In this chapter, the design and performance of two wideband double leaky slot lens antennas, suitable for integration in commercial CMOS technologies, are presented. It is shown that antennas that are of leaky-wave nature are extremely suitable for CMOS integration as the impact of the metal density rules is minimized while simultaneously a dielectric lens can be efficiently illuminated. One antenna, operating over an ultra-wide bandwidth from 200 GHz to 600 GHz with a state-of-the-art simulated average efficiency of 57 %, is suitable for center-fed direct detection scenarios. As a mean of antenna performance verification, a CPW-fed antenna, that operates from 250 GHz to 500 GHz with an average efficiency of 47 %, is designed, fabricated and characterized. This antenna, that potentially could be interfaced to other on-chip active elements, is fabricated and characterized in terms of s-parameters and gain patterns with excellent agreement with simulation, thanks to the use of an ad-hoc quasi-optical measurement setup.

4.1 Introduction

The practicality of many appealing THz imaging and sensing applications is still limited in terms of system cost and level of integration of required active components [43, 123]. The capability of a digital co-integration that is provided by CMOS technologies allows to integrate, on the same chip, the antenna together with several calibration and digital functions and, moreover, allows for an accurate control, modeling and co-design of the interface between them to reach the desired system performance. Off-chip implementations of the antenna would require the usage of technologies with limited parasitic control, especially at high frequencies [76, 124]. The challenges in designing efficient CMOS antennas lie in complying with the severe metal density rules that prohibit large areas without metallization in the dielectric back end of line, as well as high ohmic dissipation in the semiconductor

front end of line of the technology. The bandwidth and efficiency of state-of-the-art CMOS antennas are indicated in Fig. 1.4 of Sec. 1.2 for comparison. Most CMOS antenna solutions avoid radiating into the bulk silicon by shielding the antenna layer [79]. Shielding the antenna results in small bandwidths, but also in low radiation resistances [80] so that the antenna is susceptible to high losses in the metal fill that can be as high as 3 dB, as studied in [75]. This is unfortunate, as the efficient utilization of wideband antenna solutions that operate over hundreds of GHz of bandwidth would demonstrate an important step towards low-cost and compact passive THz imaging applications.

Wideband CMOS antennas can be realized when the antenna layer is not shielded from the bulk silicon, but in that case nearly all of the power will be launched into surface-waves [78] which can be suppressed using Artificial Dielectric Layers (ADLs) [82] or dielectric lenses. A lens can then also be used to realize multi-pixel imaging arrays as in [52]. The state-of-the-art performance of lens-integrated antennas in CMOS literature raises the interest to investigate the performance of leaky-wave type of antennas that are proven to be ultra-wideband [67, 114]. Single slots in planar technologies have achieved bandwidths of 5:1 [65, 66] while the bandwidth of the widely used double slot antenna [62, 63] has been extended to 2:1 [60] or 3:1 [64]. Therefore, in this work, leaky-wave radiation phenomena in a commercial CMOS technology are studied and exploited to realize, in simulation, a 3:1 relative bandwidth double leaky slot lens antenna with average efficiency of 57% from 200 GHz to 600 GHz. The double slot illuminates a silicon elliptical lens, visualized in Fig. 4.1(a), with directive patterns thanks to a novel approach to truncate the ground plane, indicated in Fig. 4.1(b). The center-fed double leaky slot lens antenna is designed for the purpose of THz imaging applications using direct detectors that can be connected to the vias in the center of the antenna. A second, CPW-fed, double leaky slot antenna is designed as a mean of verification for the center-fed antenna, as a first step towards evaluating complete system NEP performance over a wide bandwidth, that is presented in Chapter 5. Potentially, the CPW-fed antenna could be used with on-chip circuitry other than small direct detectors [43, 51]. The CPW-fed antenna, of which a micrograph is shown in Fig. 4.1(c), is fabricated and measured and operates from 250 GHz to 500 GHz with an average efficiency of 47%. An ad-hoc quasi-optical measurement setup is presented that facilitates high frequency gain pattern measurements of integrated lens antennas via landing probes.

The chapter is structured as follows. First in Sec. 4.2, leaky-wave radiation in the considered CMOS stratification is studied. In Sec. 4.3, the design of the center-fed antenna is presented. The design of the CPW-fed is presented in Sec. 4.4 whereas the fabrication and measurements, using a quasi-optical measurement setup, of the CPW-fed antenna are presented in Sec. 4.5.

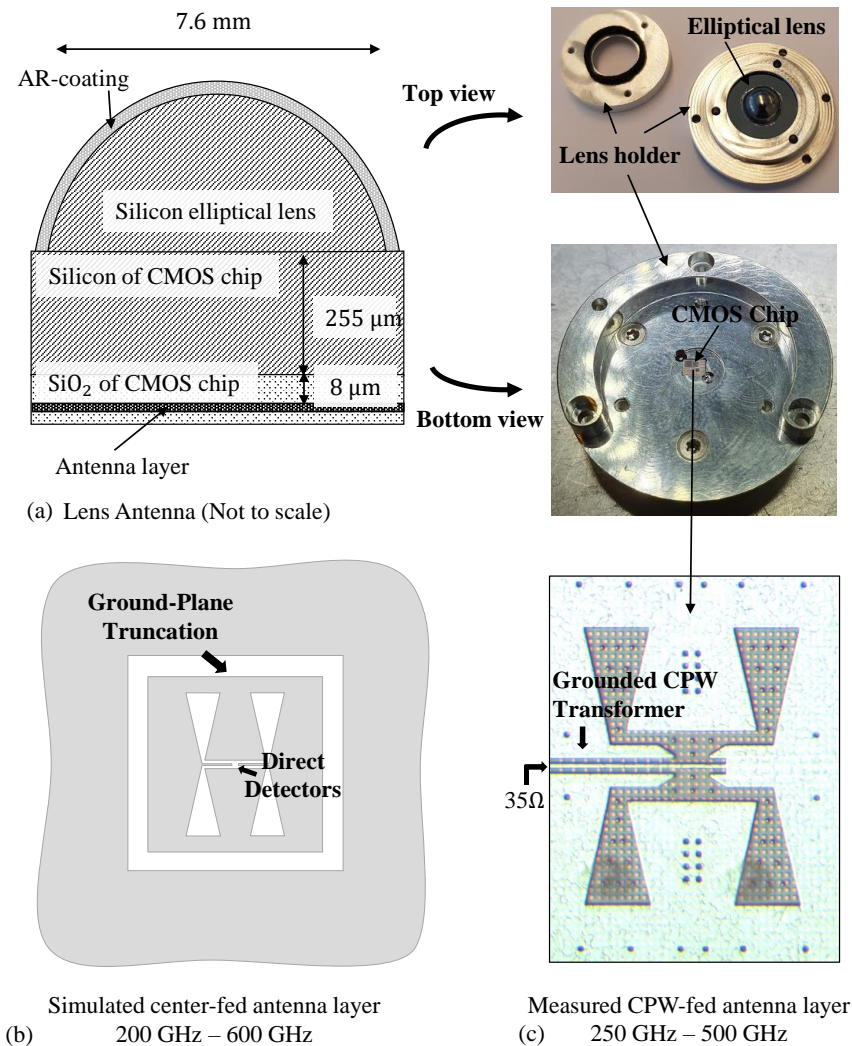


Figure 4.1: The proposed double leaky slot lens antennas. (a, left) Schematic of a lens antenna consisting of a silicon elliptical lens (top right of (a)) that is glued to the bulk silicon of a CMOS chip (bottom right of (a)). Two antenna layers proposed in this chapter are (b) a simulated center-fed antenna that is suitable for direct detection and (c) a fabricated and measured CPW-fed that provides an interface to on-chip active elements.

4.2 Leaky-wave Radiation in a CMOS Process

In this work, the goal is to exploit antennas of leaky-wave nature to achieve wideband operation while they operate under the strict metal density rules, as defined by the technology platform. In this section, we will first investigate the effect of the SiO_2 layers of the CMOS stratification on the leaky-wave radiation of an infinite slot. Furthermore, the SiO_2 layers will be loaded with metal patches, fully complying with the strict metal density rules of the process, and the impact on leaky-wave radiation and ohmic dissipation losses will be studied, showing that leaky-wave type of antennas are, in fact, suitable to realize wideband

and highly efficient antennas that are integrated in CMOS technologies. The considered technology in this dissertation is a commercial 22-nm FD-SOI CMOS process [84].

4.2.1 Leaky-Wave Radiation

Leaky-wave radiation can be realized by printing a long slot between two different infinite homogeneous dielectrics [125]. The dominant transverse electric mode, traveling along the slot, will propagate with a phase velocity, v_p , that will be an average of the speed of light, c_i , in the two different infinite media: $c_1 < v_p < c_2$. Since the current will travel faster than the speed of light in the denser medium, $v_p > c_1$, it will radiate in that medium while propagating with an exponential decay along the slot. The angle of radiation, θ , into the dense medium, with respect to the direction of propagation, increases as the contrast between the two velocities increases, $\cos(\theta) = c_1/v_p$ [126]. Consider an infinite slot printed directly on semi-infinite silicon (representing a silicon dielectric lens) as shown in Fig. 4.2(a). The slot width is $w_s = 25 \mu\text{m}$ ($\equiv \lambda_0/20$ at $f = 600 \text{ GHz}$) and is fed by an electric dipole transverse to the slot. The E- and H-plane radiation patterns inside the silicon, are shown by the red curves in Fig. 4.2(e). A radiation angle of 45° from broadside can be observed in the H-plane and a non-directive pattern in the E-plane of the slot. In such a scenario, the illumination of a typical silicon lens results in significant reflection losses as the critical angle of the air-silicon interface is close to the direction of radiation. Instead, the phase velocity of the leaky-wave current traveling along the slot can be increased by realizing an airgap between the slot and the dense dielectric medium [114], as illustrated in Fig. 4.2(b). As shown by the green curves in Fig. 4.2(e), the increase in phase velocity along the slot results in a more directive beam ($\theta \approx 20^\circ$) in the H-plane. Moreover, the excitation of the transverse magnetic (TM_0) leaky-wave mode, that is supported in the airgap [114], now also realizes a directive radiation pattern in the E-plane of the slot. A dielectric lens can be illuminated very efficiently while simultaneously the non-dispersive nature of this leaky-wave radiation allows for an ultra-wideband operation.

In CMOS processes, however, we do not have the freedom to implement such airgap, as the stratification is determined by the technology. The considered CMOS stratification consists of several dielectric layers with a total thickness of approximately $12 \mu\text{m}$, containing 10 metallization layers and dielectric layers with a relative permittivity varying from $\epsilon_r \approx 2.5 \leftrightarrow 5.5$. In the case that the slot is fabricated in the top metal layer, there is $8 \mu\text{m}$ of dielectric layer separation to the silicon interface, with an effective permittivity of approximately $\epsilon_r^{\text{eff}} \approx 4.7$, as illustrated in Fig. 4.2(c). The radiation pattern of the same slot is simulated in the considered CMOS stratification and is indicated by the blue lines in Fig. 4.2(e). The decreased phase velocity of the leaky-wave current along the slot embedded in SiO_2 , results in a decrease in directivity ($\theta \approx 33^\circ$) with respect to configuration Fig. 4.2(b) but still exhibits enhanced radiation characteristics w.r.t configuration Fig. 4.2(a). The TM_0 leaky-wave mode is still excited but highly attenuative such that the E-plane does not experience a significant increase in directivity. Directive patterns in the E-plane should then be achieved by introducing an array factor (double leaky slot) [60,64]. Truncating and tapering the leaky slots will also allow for shaping the pattern in the

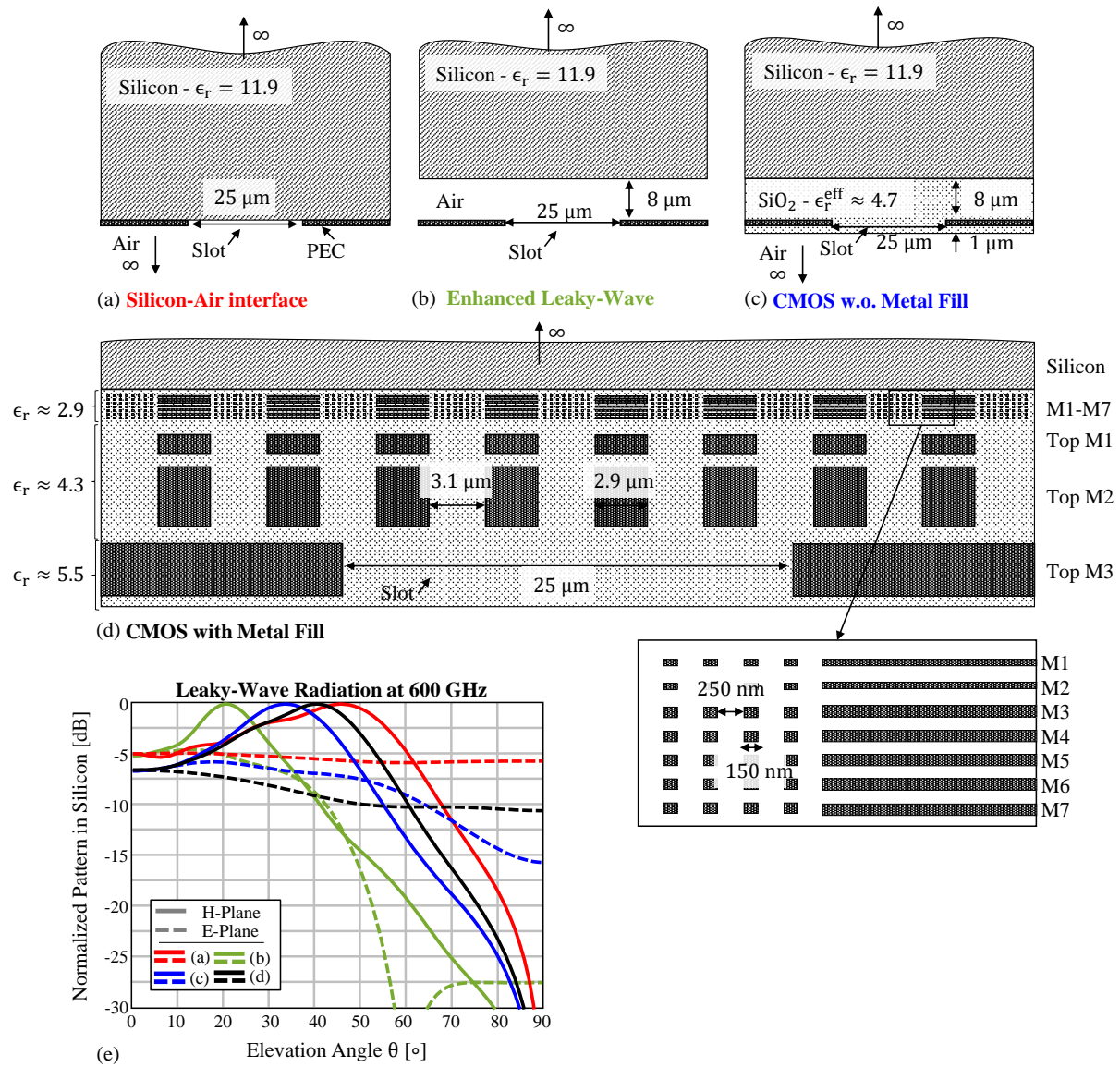


Figure 4.2: Study of leaky-wave radiation in different stratifications. The radiation is generated from a voltage current traveling along an infinite slot of $25 \mu\text{m}$ width. The four stratifications under investigation are: (a) Slot printed directly on silicon, (b) Airgap of $8 \mu\text{m}$ between the slot and silicon, (c) Slot printed in the top metal layer of the considered CMOS stratification, (d) Same as (c) but the required metal fill is included. The slot is printed in Top M3 and a zoom-in is shown of M1-M7. In (e) the radiation patterns, inside semi-infinite silicon, are shown for the considered stratifications.

H-plane, leading to an efficient illumination of the lens.

4.2.2 Minimum Metal Density Requirements in CMOS

As per technology requirements, all metallization layers are subject to minimum metal metallization density rules. The effect on leaky-wave radiation is studied using the same infinite slot. A side view of the stratification containing the metal fill that fulfills the density rule is shown in Fig. 4.2(d). The stratification has ten metal layers and the antenna is fabricated in the Top M3. The metal blocks in all other metallization layers are approximately $2.9\ \mu\text{m} \times 2.9\ \mu\text{m}$ with $3.1\ \mu\text{m}$ separation and their thickness is determined by the technology. The metal fill is distributed equivalently in the plane that is orthogonal to the side-view in Fig. 4.2(d). In the lower metal layers, M1-M7, more minimum size squares are homogeneously distributed around the larger metal fill. In the top metal layers, the metal density is approximately 23% whereas for M1-M7 the density is approximately 28%. The conductivity is approximately $5.5 \cdot 10^7\ \text{S/m}$ for the top metal layers Top M1M2 and $2.8 \cdot 10^7\ \text{S/m}$ for M1-M7. An extremely computationally heavy finite element method (FEM) numerical simulation in CST Microwave Studio [127] is performed, including the larger tiling but excluding the minimum size tiling in M1-M7, to evaluate the radiation patterns and ohmic dissipation losses in the metal tiling. The simulated radiation pattern is shown by the black curves in Fig. 4.2(e). It can be seen that the leaky-wave radiation angle has increased to approximately 40° . More importantly, the simulated ohmic dissipation losses in the metal fill are only 0.2 dB. The low ohmic dissipation loss shows great potential for leaky-wave type of antennas, to realize highly efficient wideband antenna solutions in CMOS technologies, fully compliant with the minimum metal density rules.

4.2.3 Effective Anisotropic Layers for Metal Fill

The small dimensions of the metal fill in terms of wavelength makes numerical simulations significantly more computationally heavy. An accurate solution to this problem is to substitute the dielectric layers containing the metal blocks with equivalent anisotropic dielectric layers. A simplified stratification of the considered CMOS stratification was shown in Fig. 4.2(d), where two (approximated) dielectric layers, with $\epsilon_r \approx 4.3$ and $\epsilon_r \approx 2.9$, have to comply with the minimum metal density rule. The two layers are also shown in Fig. 4.3(a) and (b). By following the steps in [128], one can substitute the dielectric layers with homogeneous, but anisotropic, dielectric layers as shown in Fig. 4.3(c) and (d). The layers are defined with relative electric permittivity and magnetic permeability tensors as well as anisotropic electric and magnetic tangent deltas.

For the dielectric layer shown in Fig. 4.3(a), numerical simulations in CST Microwave Studio are performed to obtain the TE/TM S-parameter values as required by [128]. The tensors are frequency dependent. In this study, the tensors are approximated with their

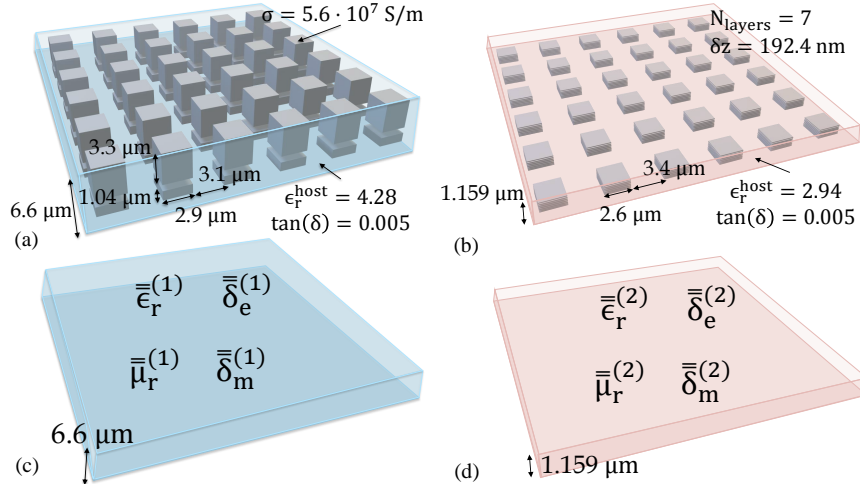


Figure 4.3: Two approximated SiO_2 layers of the considered CMOS stratification fulfilling to the metal density rules.

values at 400 GHz and these can be written in matrix form as (4.1).

$$\bar{\bar{\epsilon}}_r^{(1)} = \begin{bmatrix} 6.9 & 0 & 0 \\ 0 & 6.9 & 0 \\ 0 & 0 & 7.4 \end{bmatrix} \quad \bar{\bar{\delta}}_e^{(1)} = \begin{bmatrix} 0.0059 & 0 & 0 \\ 0 & 0.0059 & 0 \\ 0 & 0 & 0.0468 \end{bmatrix} \quad (4.1a)$$

$$\bar{\bar{\mu}}_r^{(1)} = \begin{bmatrix} 0.79 & 0 & 0 \\ 0 & 0.79 & 0 \\ 0 & 0 & 0.8 \end{bmatrix} \quad \bar{\bar{\delta}}_m^{(1)} = \begin{bmatrix} 0.0216 & 0 & 0 \\ 0 & 0.0216 & 0 \\ 0 & 0 & 0.0035 \end{bmatrix} \quad (4.1b)$$

The geometry of the 7 layers of thin metallic patches in Fig. 4.3(b), stacked with 192.4 nm periodicity, allowed for a quick numerical evaluation of the tensors using a software tool [129] that is based on the theory of [128] and results in the tensors (4.2):

$$\bar{\bar{\epsilon}}_r^{(2)} = \begin{bmatrix} 7.43 & 0 & 0 \\ 0 & 7.43 & 0 \\ 0 & 0 & 2.90 \end{bmatrix} \quad \bar{\bar{\delta}}_e^{(2)} = \begin{bmatrix} 0.005 & 0 & 0 \\ 0 & 0.005 & 0 \\ 0 & 0 & 0.005 \end{bmatrix} \quad (4.2a)$$

$$\bar{\bar{\mu}}_r^{(2)} = \begin{bmatrix} 1.00 & 0 & 0 \\ 0 & 1.00 & 0 \\ 0 & 0 & 0.59 \end{bmatrix} \quad \bar{\bar{\delta}}_m^{(2)} = \begin{bmatrix} 0 & 0 & 0 \\ 0 & 0 & 0 \\ 0 & 0 & 0.02 \end{bmatrix} \quad (4.2b)$$

A numerical validation has been performed, using the infinite slot from Fig. 4.2(d,e), in terms of pattern and ohmic dissipation losses in the metal patches (dielectric losses of the host medium are deembedded). The dielectric slabs containing the metal patches have been replaced with their equivalent anisotropic media. The results are shown in Fig. 4.4(a,b). A good match of the pattern at 600 GHz can be observed as well as a good agreement

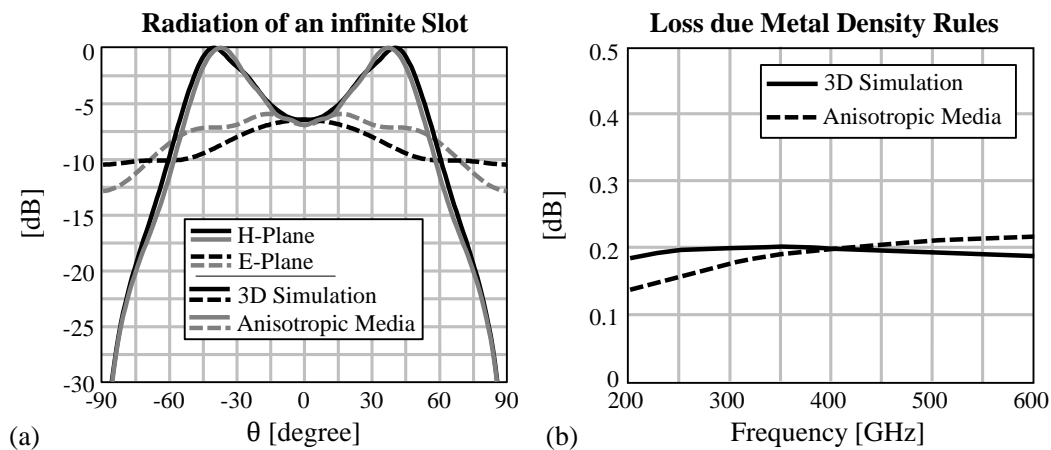


Figure 4.4: Validation of the equivalent anisotropic media using the infinite slot of Fig. 4.2(d) in terms of (a) Pattern at 600 GHz and (b) ohmic dissipation in the metal patches.

in ohmic dissipation losses. The slight difference in E-plane pattern is attributed to a numerical effect due to a smaller truncation of the ground plane in the transverse direction of the slot, in order to make the 3D-simulation computationally less heavy.

4.3 Center-fed Antenna for Direct Detection

This work is focused on designing an antenna operating over a 3:1 relative bandwidth from 200 GHz to 600 GHz. The frequency band is chosen such that the antenna can be used for the purpose of passive THz imaging applications. The proposed antenna can be integrated with transistors or diodes, connected to the vias in the center of the antenna as indicated in Fig. 4.1(b), to realize a THz direct detector.

4.3.1 Double Leaky Slot Design in Semi-Infinite Silicon

The (effective) relative permittivity of the SiO_2 layers does not provide a sufficiently high contrast with the silicon to be able to shape the pattern in the E-plane of a single slot, as was shown in Fig. 4.2. For this reason, two parallel slots are optimized, introducing an array factor in the E-plane. Moreover, truncation and tapering of the slots is used to shape the beam in the H-plane. The optimization of the antenna is performed in terms of efficiency and pattern quality using FEM-simulations in CST Microwave Studio [127]. At the lower frequency end, the beam patterns, radiating inside the silicon, should be sufficiently directive to ensure a low spill-over due to reflections inside the lens. At the higher frequency end, any sidelobes of the beam patterns should be approximately -15 dB or less. High sidelobe levels contribute to spill-over losses or significant destructive interference effects in the beam patterns after the lens. Firstly, the two slots are optimized on an infinite ground plane. The optimized antenna dimensions are shown in Fig. 4.5(a). The optimization in impedance and pattern is not straightforward. An increased separation

of the slots improves the E-plane directivity at the lower frequencies but also increases the side lobes at the higher frequencies. A truncation of the slots improves the H-plane directivity but can also make the slots resonant at the lower frequencies, complicating a wideband impedance match. The tapering angle and length of the slots affect the beam pattern and impedance match. The length ($222\ \mu\text{m}$) and separation ($100\ \mu\text{m}$) of the two slots are optimized at the highest frequency, i.e. $f = 600\ \text{GHz}$, to enforce clean and symmetric patterns with sidelobes of $-13\ \text{dB}$, as shown by the red curves in Fig. 4.5(b). The slots have a tapering angle of 25° to ensure a wideband impedance match [64]. The

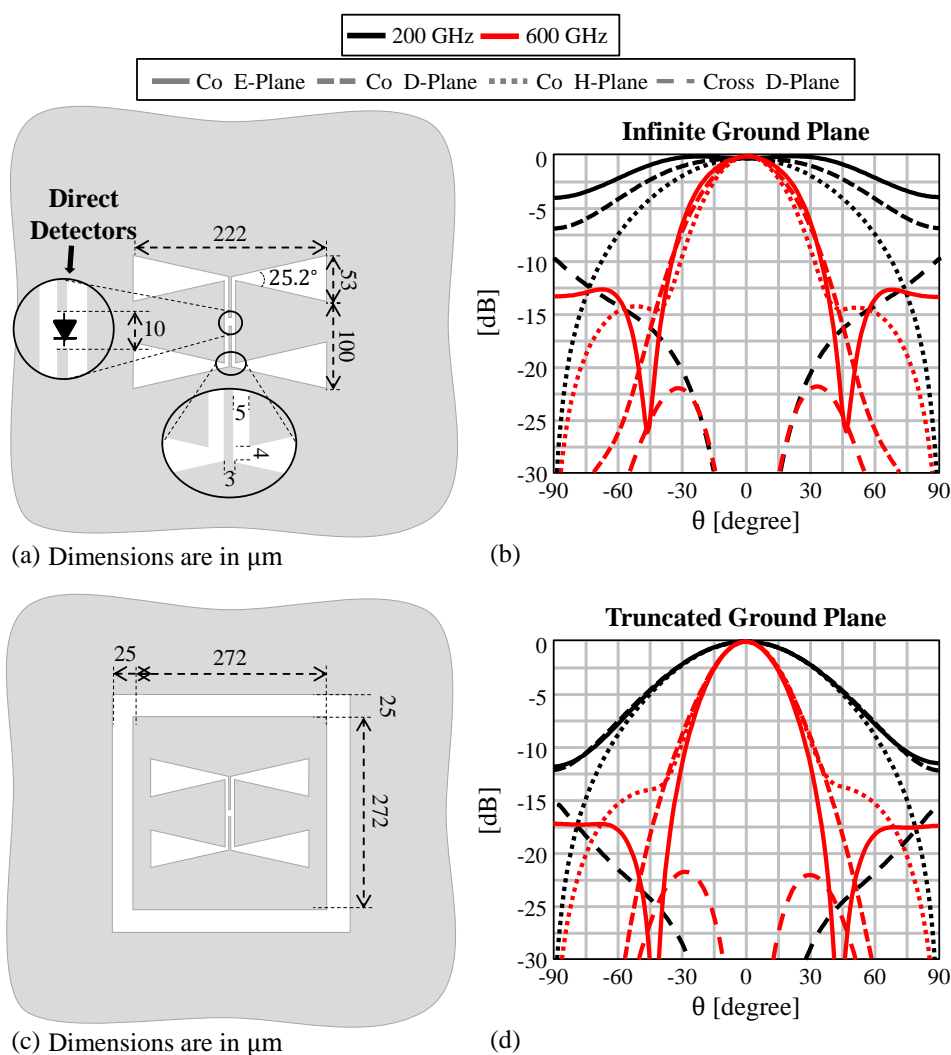


Figure 4.5: In (a) the dimensions, in μm , of the optimized double bow-tie slot antenna on an infinite ground plane is shown. The main planes (E-plane, H-plane, D-plane) of the simulated normalized radiation patterns, inside semi-infinite silicon, are shown (b). In order to increase directivity at the lower frequency end and to control the finiteness effects of the ground plane, the antenna ground plane is truncated as shown in (c), leading to the clean and symmetric radiation patterns as shown in (d).

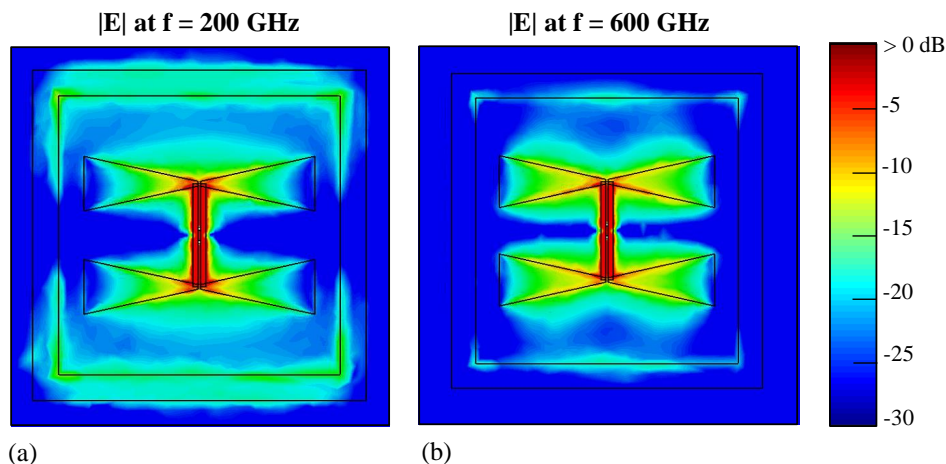


Figure 4.6: The normalized average amplitude of the electric field in the antenna layer at (a) 200 GHz and at (b) 600 GHz. The slot ring around the truncated antenna ground plane introduces an additional array factor in the E-plane at the lower frequencies. This effect improves the pattern symmetry as can be seen from Fig. 4.5.

distinct leaky-wave radiation peaks at 40° , Fig. 4.2(e), disappear due to both the tapering and the truncation of the slots. Unfortunately, the patterns at 200 GHz, shown by the black curves, do not experience a significant increase of directivity in the E-plane due to the array factor; the patterns are now asymmetric and will also result in high spill-over losses. Increasing the slot separation is not an option since the side-lobe level at higher frequencies will become unreasonably high.

An increase in directivity in the lower frequencies can be introduced by truncating the ground plane. In fact, truncating the ground plane is part of the antenna design and optimization procedure. Fabricating an antenna with an (apparent) infinite ground plane is considered infeasible, especially on expensive CMOS chip area. Since the radiation performance of the antenna can change significantly when the ground plane is finite, even when it is still multiple wavelengths in dimension, it should be part of the optimization process. The optimized antenna, with truncated ground plane, is shown in Fig. 4.5(c). The ground plane is $272\ \mu\text{m} \times 272\ \mu\text{m}$ in dimension and a slot of $25\ \mu\text{m}$ separates the antenna from an infinite ground plane that approximates other structures that will be embedded on the CMOS chip. The size of the antenna ground plane is optimized to enforce a symmetric radiation pattern at the lowest frequency 200 GHz. The normalized radiation patterns, at 200 GHz and 600 GHz, of the truncated antenna ground plane, but in presence of a surrounding ground plane, are shown in Fig. 4.5(d). An increase in directivity, mainly in the E-plane at the lower frequency bound, can be observed. To highlight this effect, the normalized average amplitude of the electric field in the antenna plane is shown in Fig. 4.6(a) for 200 GHz and Fig. 4.6(b) for 600 GHz. The higher average field intensity in the ring in the E-plane of the antenna at 200 GHz, illustrates the additional array factor that mainly contributes at the lower frequencies and in the E-plane.

A micrograph of the chip, manufactured with the antenna in the presence of other

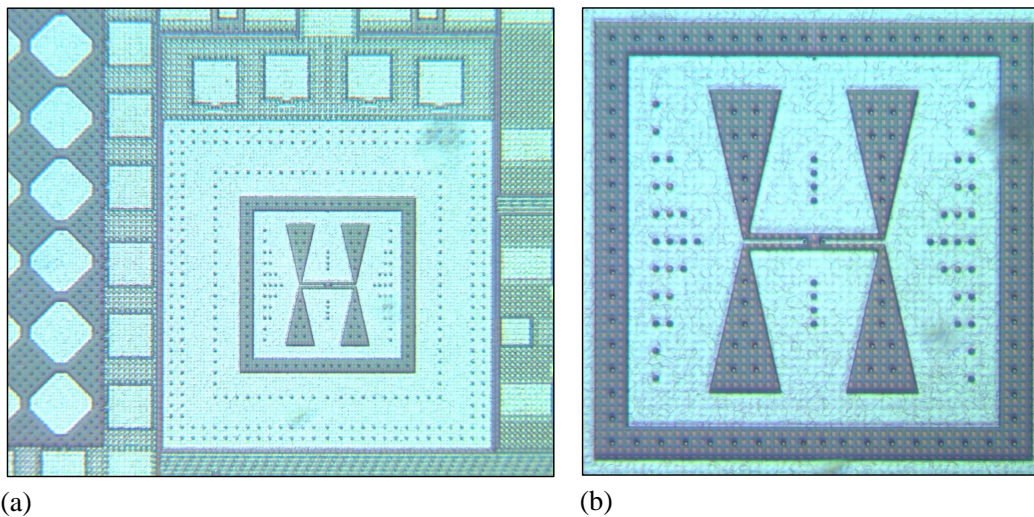


Figure 4.7: Micrograph of the antenna. In (a) the antenna is shown embedded on the chip with other surrounding test structures. In (b) a zoom-in is shown, clearly showing some additional metalization due to the minimum metal density rule.

structures embedded on the chip, is shown in Fig. 4.7(a). A zoom-in of the micrograph is shown in Fig. 4.7(b) where some additional metal patches as a result of the metal density rule are clearly visible. The top metal layer of the antenna, surrounded by the other embedded chip structures, is simulated. The simulated normalized radiation patterns, at 200 GHz and 600 GHz, radiating in semi-infinite silicon are shown in Fig. 4.8(a) and Fig. 4.8(b) respectively. After comparing the patterns to the ideal case with an infinite ground plane surrounding the truncated antenna, Fig. 4.5(c,d), some interference in the patterns due to the neighboring on-chip test structures can be identified. Overall, the patterns are clean and symmetric and will illuminate a dielectric lens efficiently. Indicated by the red boxes in Fig. 4.8(a,b) are the regions beyond the critical angle of an elliptical lens ($\theta_c \approx 70^\circ$). The simulated input impedance of the antenna is shown in Fig. 4.8(c) and is matched to a port impedance of $Z_{\text{port}} = 120\Omega$ over the full bandwidth with a reflection coefficient of $\Gamma < -10$ dB, as shown in Fig. 4.8(d). The length of the slot is designed such that the antenna operates just after its first resonance. It can be seen that the antenna is still resonant at the lower frequencies, whereas at the higher frequencies it becomes only weakly dispersive, thanks to its leaky-wave nature. It is important to note, however, that the antenna input impedance should be part of the co-design with the input impedance of the direct detection circuit. In fact, direct detectors in CMOS processes such as transistors or diodes are often characterized with a capacitive impedance profile of the imaginary part can be comparable or larger than the real part [52, 83, 69]. Any impedance match with the detector will have to be considered as an extra loss factor that is not considered here. The directivity and gain, at broadside ($\theta = 0^\circ$) and inside semi-infinite silicon, are shown in Fig. 4.8(e). The efficiency terms, contributing to the approximate 2 dB loss in gain, are shown in Fig. 4.8(f). The biggest degradation in radiation efficiency can be attributed to

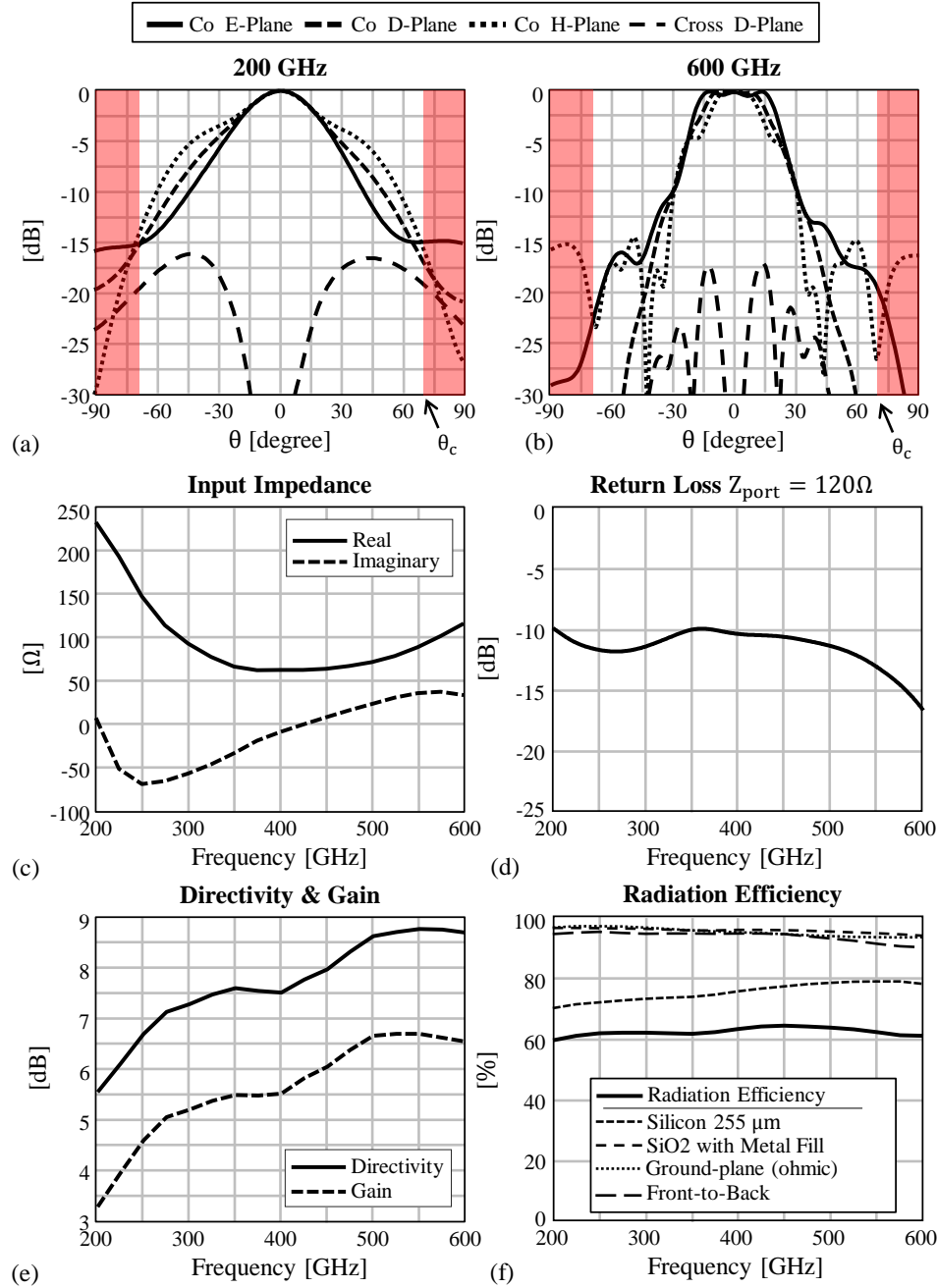


Figure 4.8: The performance of the double bow-tie slot antenna, as optimized in Sec. 4.3.1, is presented. The antenna, radiating inside infinite silicon, is simulated in CST Microwave Studio in the presence of the other test-structures on the chip as shown by the micrograph of the chip in Fig. 4.7(a). In (a) and (b) the patterns inside semi-infinite silicon is shown for 200 GHz and 600 GHz respectively; indicated by red boxes is the region $|\theta| > \theta_c$ beyond the critical angle of a typical silicon elliptical lens. (c) shows the input impedance which results in a return loss shown in (d) for $Z_{\text{port}} = 120 \Omega$. The directivity and gain inside the silicon, at broadside $\theta = 0^\circ$, are shown in (e) and radiation efficiency in (f).

the ohmic dissipation in the low-resistivity silicon of the technology (1 dB to 1.5 dB loss) that is 255 μm and has a resistivity of approximately $\rho = 10 \Omega \cdot \text{cm}$. Furthermore, it is important to highlight the low ohmic dissipation losses in the SiO_2 , with an approximated loss tangent of $\tan \delta \approx 0.005$ and metal fill from Fig. 4.2(d) (0.2 dB of simulated loss) and high front-to-back ratio (0.25 dB simulated losses), both thanks to the leaky-wave nature of the proposed antenna. The conductivity of the antenna ground plane is approximately $3.3 \cdot 10^7 \text{ S/m}$. The antenna has a simulated average radiation efficiency of 63% over the full bandwidth. This is not yet the antenna efficiency as reported in Fig. 1.4, since a silicon elliptical lens is required to suppress the surface-waves that are supported by the thick silicon of the technology. Gluing a dielectric lens to the CMOS chip will also result in directive radiation patterns and imaging capabilities when using FPAs.

4.3.2 Simulated Antenna Performance with a dielectric lens

In this work, the optimization of spill-over efficiency has priority in designing the dielectric lens, keeping in mind the purpose of maximizing imaging speeds in THz imaging applications. A loss in taper efficiency results in a loss in directivity (or resolution), which can be compensated by over-dimensioning the optics. For this reason, we decide to use an elliptical lens without truncation of the beams. The truncation is then determined by the critical angle ($\theta_c \approx 68^\circ$) of the silicon-air interface, resulting in a focal number of $F_\# = 0.56$. A drawing of the lens antenna consisting of the elliptical lens that is glued to the silicon chip (size of chip is not to scale for clarity) is shown in Fig. 4.9(a). The diameter of the elliptical silicon lens is $d_f = 7.6 \text{ mm}$, i.e. $5\lambda_0$ at 200 GHz and $15\lambda_0$ at 600 GHz. The diameter of the lens is arbitrary and should be dimensioned depending on the application requirements. The lens is provided with a matching layer (a 144 μm thick deposition of Parylene C), in order to reduce the high reflection losses (up to 1.5 dB) that occur at the silicon-air interface. The phase center of the radiation in the lens, approximately 25 μm behind the antenna layer, is placed in the focal point of the elliptical lens, after taking into account the 255 μm thick substrate of the chip.

The antenna performance, in presence of the dielectric lens, is analyzed in transmission using an in-house physical optics (PO) tool that is based on [130]. In this tool, the simulated radiation patterns in semi-infinite silicon, from Fig. 4.8(a,b), illuminate the dielectric lens and a surface radiation integral is performed to obtain the far-field. In Fig. 4.9(b) and (c) the simulated normalized radiation patterns outside the dielectric lens are shown for 200 GHz and 600 GHz respectively, showing clean and symmetric patterns over the full band. In Fig. 4.9(d), the antenna efficiency is shown, decomposed in the radiation efficiency from Fig. 4.8(f) and the reflection efficiency of the dielectric lens. The reflection efficiency includes the spill-over of radiation beyond the critical angle of the lens ($\theta_c \approx 68^\circ$) as well as the Fresnel loss due to the reflections that occur at the lens-air interface. The reflection efficiency is higher than 80% over the full bandwidth and confirms that the patterns inside the silicon lens are directive as a result of the truncation of the ground plane. The antenna efficiency, averaged over the full bandwidth, is simulated to be 57% and forms the claim of this chapter, as was summarized in Fig. 1.4. The directivity and gain of the lens antenna

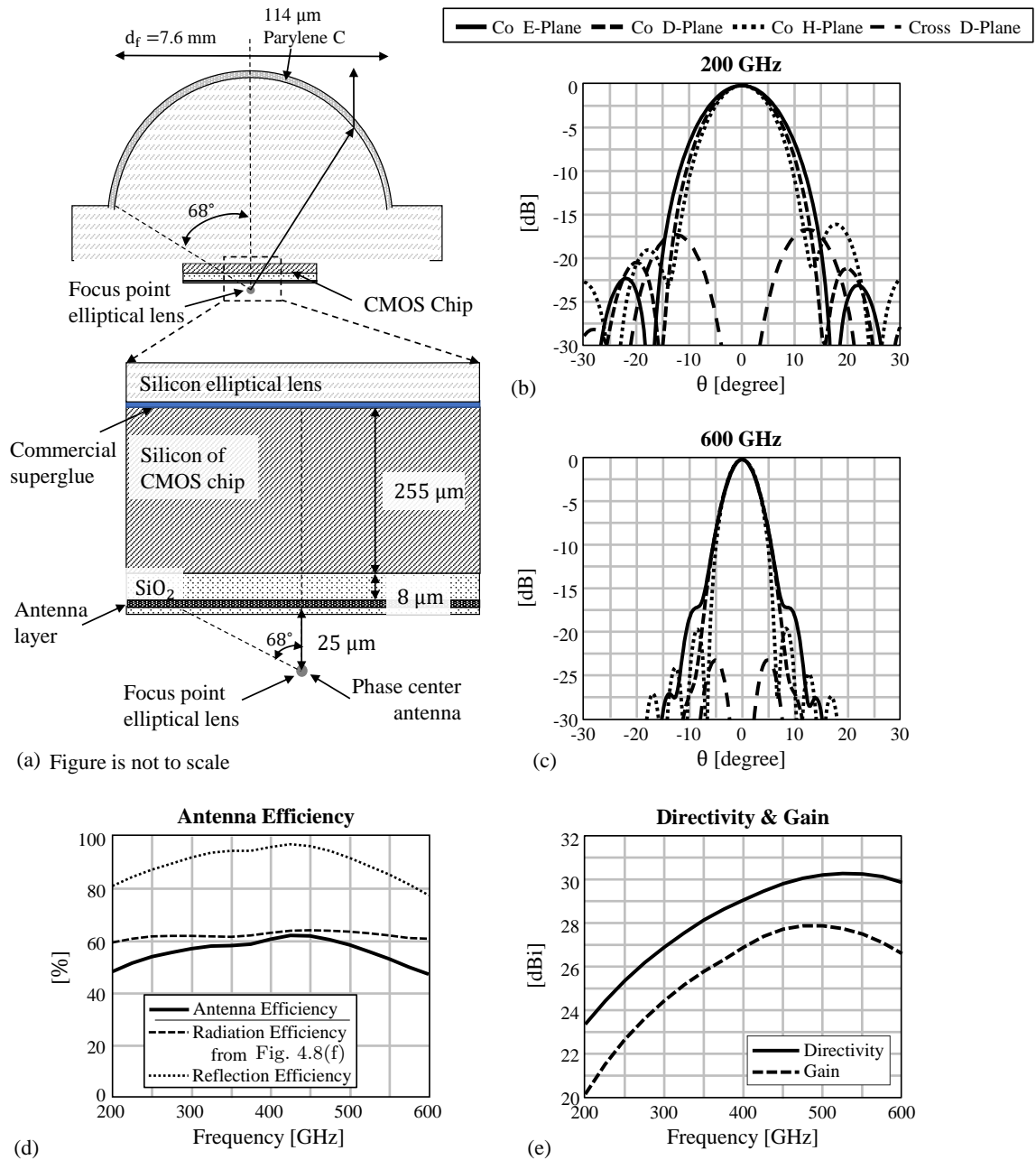


Figure 4.9: Simulated performance of the center-fed antenna in combination with an elliptical silicon lens. In (a) the lens geometry is shown. The beam patterns outside the dielectric lens are shown at 200 GHz (b) and 600 GHz (c). In (d), the simulated antenna efficiency consisting of the radiation efficiency in semi-infinite silicon from Fig. 4.8(f) and the reflection efficiency (spill-over and Fresnel loss in the dielectric lens) are shown. (e) Simulated directivity and gain of the lens antenna.

are shown in Fig. 4.9(e).

In [64], a similar double slot antenna is proposed that was directly printed on silicon and that also operates from 200 to 600 GHz. The bandwidth of the center-fed antenna is however higher in terms of pattern quality as the lens patterns in [64] show a side-lobe level larger than -8 dB at the boundary frequencies. The truncated ground plane and SiO_2 layers in this work results in more directive patterns in the silicon at the lower frequencies and lower sidelobes at the higher frequencies.

4.4 Design of a CPW-fed Antenna

A CPW-fed antenna, shown in Fig. 4.1(c), is designed to operate from 250 GHz to 500 GHz. The performance of the center-fed antenna, presented in the previous section, cannot be evaluated in terms of antenna gain and impedance once the antenna is connected to direct detectors, since the rectification characteristics of the detectors will be inherently part of the measurement. A CPW-fed antenna is designed to verify the center-fed antenna performance, as a first step towards evaluating complete system NEP over a wide bandwidth that is presented in Chapter 5. The antenna provides an interface, with a $35\ \Omega$ impedance matching condition, so that the antenna could potentially be used with on-chip circuitry other than small direct detectors.

In order to properly excite and access a double slot antenna in the center via a transmission line, the line needs to be connected via the E-plane, as shown in Fig. 4.10(a). This transmission line prohibits the implementation of the ground plane truncation and thus the level of the normalized radiation patterns in Fig. 4.5 increased from -10 dB to -3 dB at the truncation angle of the lens. Therefore, in order to make the patterns of the CPW-fed antenna more symmetric, the slot separation is increased from $100\ \mu\text{m}$ to $120\ \mu\text{m}$. As a result of this increase in separation, the side-lobe level at the higher frequencies is increased and thus the bandwidth is compromised. The length and width of the slots remain similar as well as the slot tapering angle. The dimensions of the antenna are annotated in Fig. 4.10(a). A micrograph of a zoom-in of the center of the antenna is shown in Fig. 4.10(b). The top-metal tiles, required to fulfill the metal density rule of the CMOS technology, can clearly be seen. The metal density rule also needs to be fulfilled in the grounded CPW transformer, of which a schematic top-view and cross-section are shown in Fig. 4.10(c).

The bandwidth of the CPW-fed antenna, defined by the pattern quality and impedance matching, is from 250 GHz to 500 GHz and the simulated patterns, inside semi-infinite silicon, are shown in Fig. 4.11(a) and (b) for these boundary frequencies. Apart from the reduced pattern bandwidth due to the absence of the ground plane truncation, the cross-polarization level increased due to the wide CPW ($33\ \mu\text{m}$ line width and $12\ \mu\text{m}$ slots, as indicated in Fig. 4.10(a)) that connect the two slots to the grounded CPW transformer ($3\ \mu\text{m}$ line width and $5\ \mu\text{m}$ slots). The grounded CPW transmission line, schematically shown in Fig. 4.10(c), also need to comply to metal fill density requirements. The simulated characteristic impedance is $Z_0 \approx 44\ \Omega$. The $96\ \mu\text{m}$ long grounded CPW is part of the

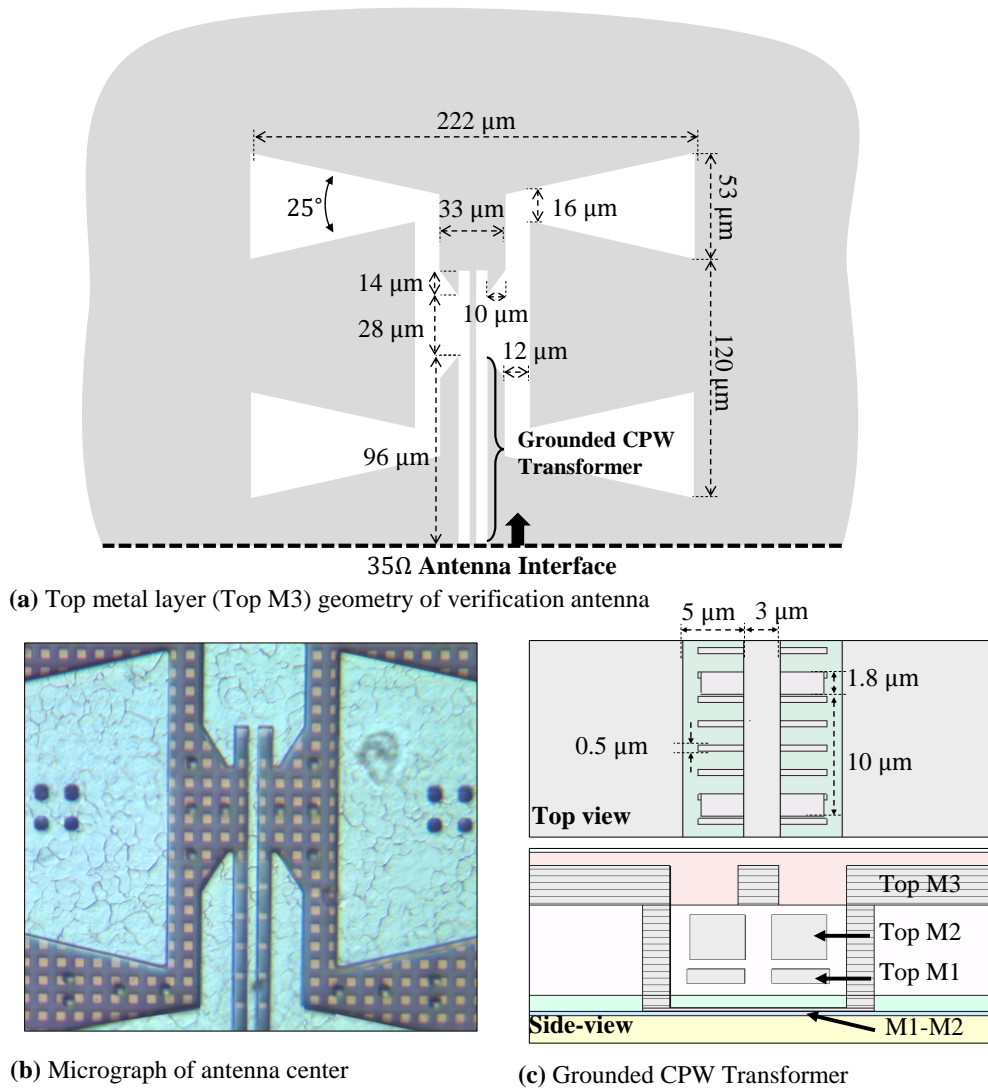


Figure 4.10: Fabricated and measured CPW-fed antenna. (a) Schematic of the top metal layer (Top M3) of the antenna with annotated dimensions. The grounded CPW transformer of $96\ \mu\text{m}$ is inherently part of the antenna and provides a $35\ \Omega$ impedance matching interface in the antenna interface to other circuitry. In (b) a micrograph of the center of the fabricated antenna is shown, the metallic patches due to the metal density rule are clearly visible. In (c) a schematic top view and cross-section of the grounded CPW transformer as is simulated in CST Microwave Studio is shown, including metal fill.

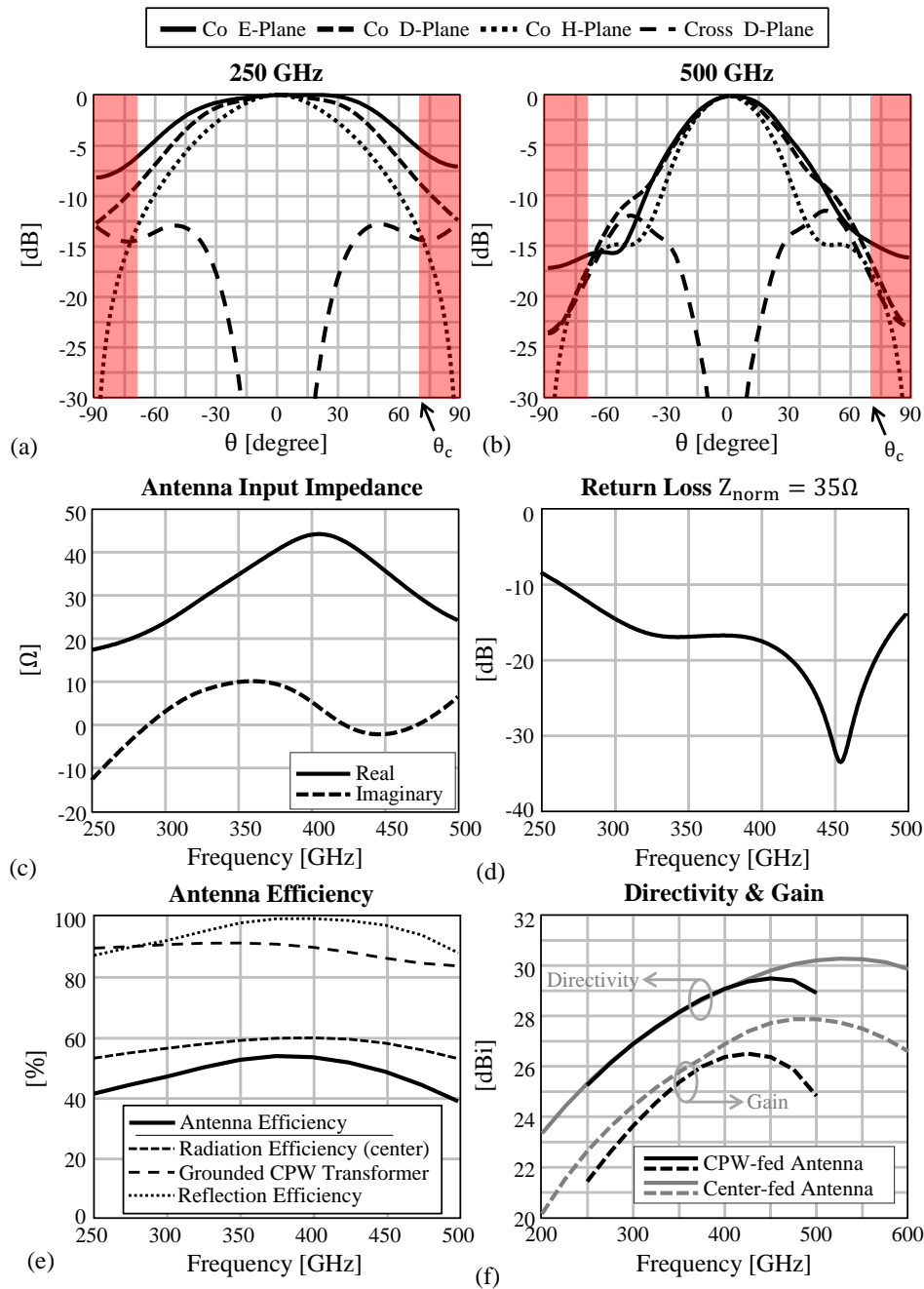


Figure 4.11: Simulated performance of the CPW-fed antenna shown in Fig. 4.10. (a,b) Radiation patterns inside semi-infinite silicon at 250 GHz and 500 GHz respectively. (c) Antenna input impedance. (d) Reflection coefficient when the antenna is connected to a load of 35Ω . (e) Antenna efficiency, decomposed in three contributions. The radiation efficiency is referred to the center of the antenna, in absence of the grounded CPW transformer and transmission line. The grounded CPW transformer is an integral part of the antenna until the antenna interface indicated in Fig. 4.10(a) and the reflection efficiency includes spill-over and Fresnel losses. (f) Directivity and gain of the CPW-fed lens antenna compared with the center-fed antenna from Fig. 4.9.

antenna and acts as an impedance transformer for an impedance match at the antenna interface indicated in Fig. 4.10(a). From this plane on, the antenna is defined. The antenna is operating in combination with the silicon elliptical lens that was introduced in Sec. 4.3.2. In Fig. 4.11(c), the antenna input impedance is shown which, when connected to a $35\ \Omega$ circuit, results in the wideband impedance match with return loss shown in Fig. 4.11(e). The simulated antenna efficiency, using the previously mentioned in-house PO-tool [130], is shown in Fig. 4.11(e). The antenna efficiency is decomposed in three components. The radiation efficiency in semi-infinite silicon is referred from the center of the antenna in absence of the grounded CPW transformer. The radiation efficiency is slightly lower compared to the radiation efficiency of the center-fed antenna presented in Fig. 4.8(f) due to higher losses in the SiO_2 . The grounded CPW transformer has a simulated loss of 0.5 dB to 1 dB. The reflection efficiency, including spill-over and Fresnel losses, is higher than 90% efficiency. The antenna has a simulated average antenna efficiency of 47% over the full 2:1 relative bandwidth from 250 GHz to 500 GHz and this performance is also summarized in Fig. 1.4. The lens antenna directivity and gain are shown in Fig. 4.11(f) and can be directly compared with the performance of the center-fed antenna that was designed in the previous section. A 1.2 dB decrease in directivity is observed at 500 GHz as a result of the increased slot separation that leads to more directive patterns and a reduced tapering efficiency on the lens surface. Additionally, the antenna efficiency is approximately 1.7 dB lower at 500 GHz resulting in an overall loss in gain of approximately 2.9 dB w.r.t. the center-fed antenna at 500 GHz. At lower frequencies, the performance of the two lens antennas is comparable.

4.5 Fabrication and Measurements Results of the CPW-fed Antenna

The antenna presented in the previous section is fabricated and packaged into a lens antenna that was introduced in Fig. 4.1. The diameter of the lens rim is fabricated with a $20\ \mu\text{m}$ accuracy and positioned tightly in the aluminum lens holder that is fabricated with a $50\ \mu\text{m}$ accuracy in the lens cavity. At the backside of the dielectric lens, Fig. 4.12(a), this metallic holder contains a chip cavity, Fig. 4.12(b), which is also fabricated with a $50\ \mu\text{m}$ accuracy in width and length, where the $2.0\ \text{mm} \times 2.5\ \text{mm}$ CMOS-chip ($20\ \mu\text{m}$ inaccuracy in each dimension) is positioned in this chip cavity, so that the phase center of the radiation in the lens aligns with the focal point of the elliptical lens, as was schematically shown in Fig. 4.9(a). Two holes, at two opposing corners of the chip cavity, allow the application of a commercial Loctite 406 superglue which, after application, flows between the chip and the dielectric lens. Some pressure is applied to minimize the thickness of the glue.

A micrograph of the fabricated antenna is shown in Fig. 4.12(c). In order to be able to measure the antenna using a Ground-Signal-Ground (GSG) probe that is connected to a Vector Network Analyzer (VNA), dedicated on-chip landing pads are required that are compatible with the GSG probe pitch. The GSG probes available, have a probe pitch of

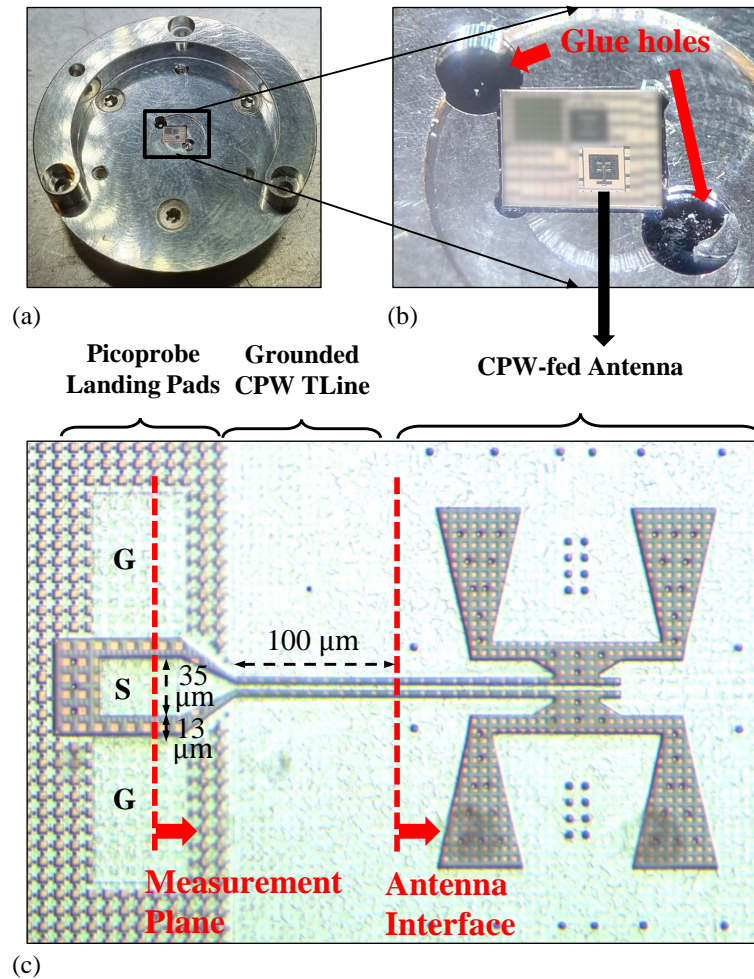


Figure 4.12: Fabrication of the CPW-fed antenna. (a) Back-side of the metallic holder that contains the elliptical lens (shown in Fig. 4.1). A zoom-in in (b) shows the cavity in the metallic holder that contains the CMOS chip. The holes where glue is applied are indicated. (c) Micrograph of the fabricated CPW-fed antenna that is connected to GSG landing pads via an extended grounded CPW transmission line. Indicated is the measurement plane up to where the measurement setup can be calibrated and the antenna interface from where the antenna is defined.

50 μm and are used with the landing pads indicated in Fig. 4.12(c) where the signal pad (S) is 35 μm wide and the gap to the ground pads (G) is 13 μm. A tapered transition is required to connect the large GSG landing pads with the grounded CPW. Moreover, the grounded CPW transformer is extended with 100 μm of transmission line with the same geometry to minimize the impact of the electrically large probe on the antenna performance. The antenna is measured in the WR3.4 frequency band from 225 GHz to 325 GHz and the WR2.2 frequency band from 325 GHz to 500 GHz, each with dedicated landing probes and frequency extenders connected to a VNA.

4.5.1 Impedance Measurement

The reference plane for the measured S-parameters is shifted just after the probe-tips, as indicated with *Measurement Plane* in Fig. 4.12(c) using a fused silica Short, Open, Load (SOL) calibration kit [131]. Photographs of the fused silica calibration kit are shown in Fig. 4.13(a), where on the left side a picture is shown of the landing probe and the fused silica wafer containing the calibration kit. Micrographs of the Short, Open and Load calibration structures are also shown. By using this calibration kit, the CPW transition within the landing probes to an on-chip CPW quasi-TEM transmission line mode, is de-embedded from the measurement. A photograph of the landed GSG probe is shown in Fig. 4.13(b). A small error in calibration will be introduced due to the different CPW geometries of the calibration kit [131] and the landing pads. The measured impedance at the measurement plane is shown in Fig. 4.13(c), and is derived from the calibrated S_{11} parameter that is shown in Fig. 4.13(d). Both figures are compared with simulation

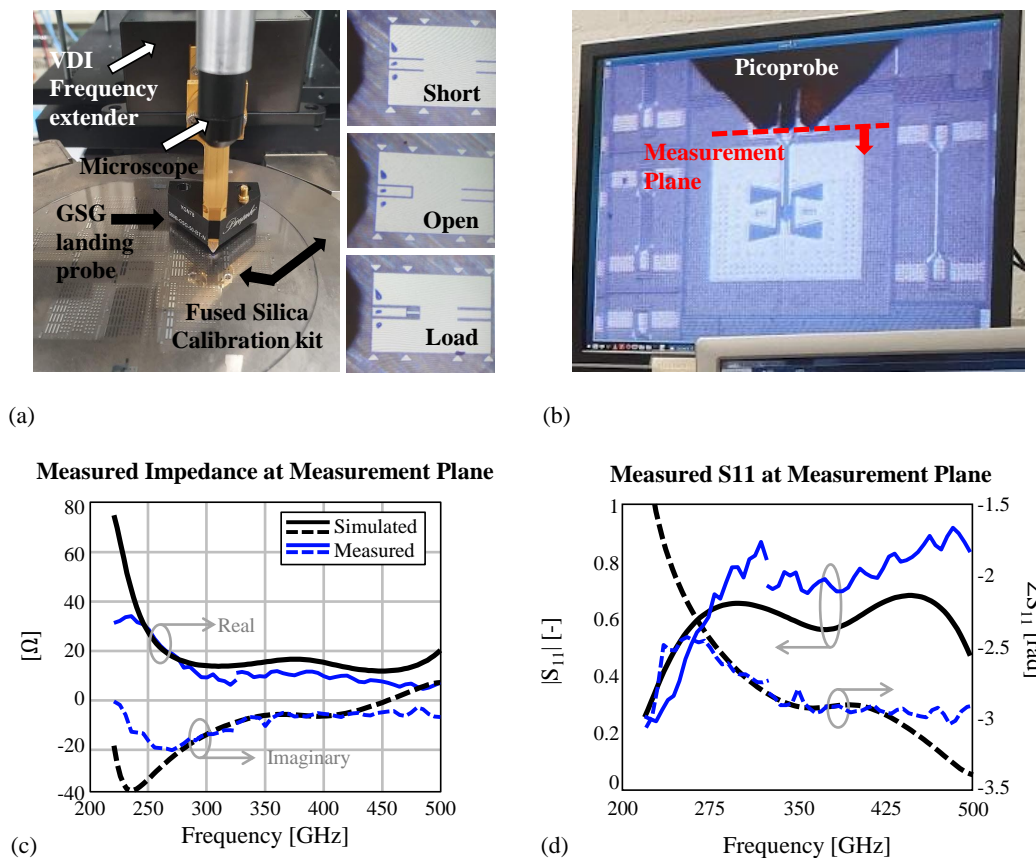


Figure 4.13: Impedance measurement at measurement plane. (a) Fused silica Calibration kit for the s-parameters at the measurement plane, indicated in Fig. 4.12(c), of the CPW-fed antenna. (b) Micrograph of the GSG probe landed on the landing pads of the CPW-fed antenna. (c) Simulated and measured impedance. (d) Simulated and measured reflection coefficient.

(black lines). The tapering transition that includes the landing pads prohibits a wideband impedance match at this measurement plane, but reasonable agreement with full-wave simulations is obtained.

4.5.2 Quasi-Optical Measurement Setup for Gain Patterns

The available measurement setup does not allow for landing a GSG landing probe on the back-side of the dielectric lens (where the chip is glued), while simultaneously performing a measurement scan at the top-side of the lens to evaluate the gain patterns. To allow for a planar scan in an upper plane while the probe is landed, a 180° reflection of the field radiated by the lens antenna needs to be introduced. To minimize interference between the GSG probe and the computer numerical controllable (CNC) arm, that performs the planar scan, the propagation path is larger than 30 cm, resulting in significant spreading losses. Moreover, a large measurement scanning angle of the lens pattern would require to calibrate out the pattern of the horn or, instead, to use an open waveguide probe. The use of a waveguide probe, together with the high reflection losses in the landing probe and at the measurement plane, could also limit the dynamic range of the gain pattern measurement to values lower than 30 dB. A proposed quasi-optical solution that facilitates measurements of such integrated lens antennas at sub-millimeter wavelengths, is to introduce a hyperbolic lens in the propagation path, as schematically shown in Fig. 4.14. Such measurement setup provides several advantages. Firstly, the free-space spreading losses are reduced (defined now only by the focal distance after the hyperbolic lens, F_2), since the hyperbolic lens refocuses the captured power. Secondly, the smaller scanning area required reduces the scanning time but allows for using a horn antenna for the measurement (if the focused spot-size is sufficiently larger than the aperture of the horn). And lastly, as will be explained in the remaining sections, Friis equation can still be applied to evaluate the system losses by introducing a near-field gain that is now defined by the hyperbolic lens [132]. The proposed measurement configuration increases the dynamic range with approximately 30 dB. In addition, the lens antenna performance, in terms of gain and patterns can be recovered via

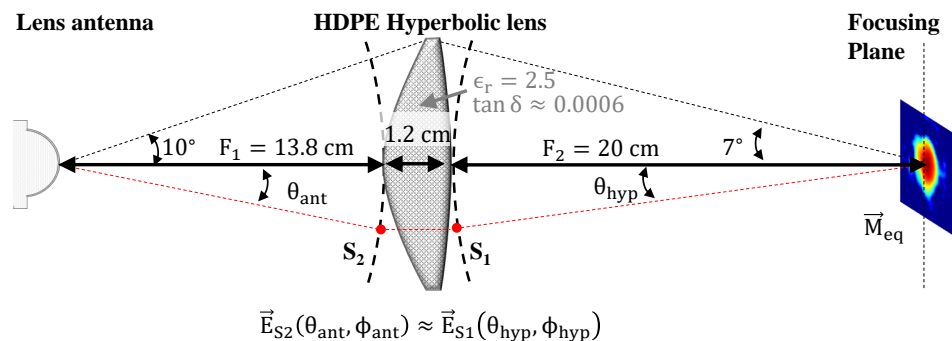


Figure 4.14: Simplified geometry for the quasi-optical measurement setup based on a hyperbolic lens. Also, the geometry is shown for the back propagation of the measured complex near-field in the focusing plane to the field radiated by the lens antenna on surface S_2 , as will be used in Sec. 4.5.4.

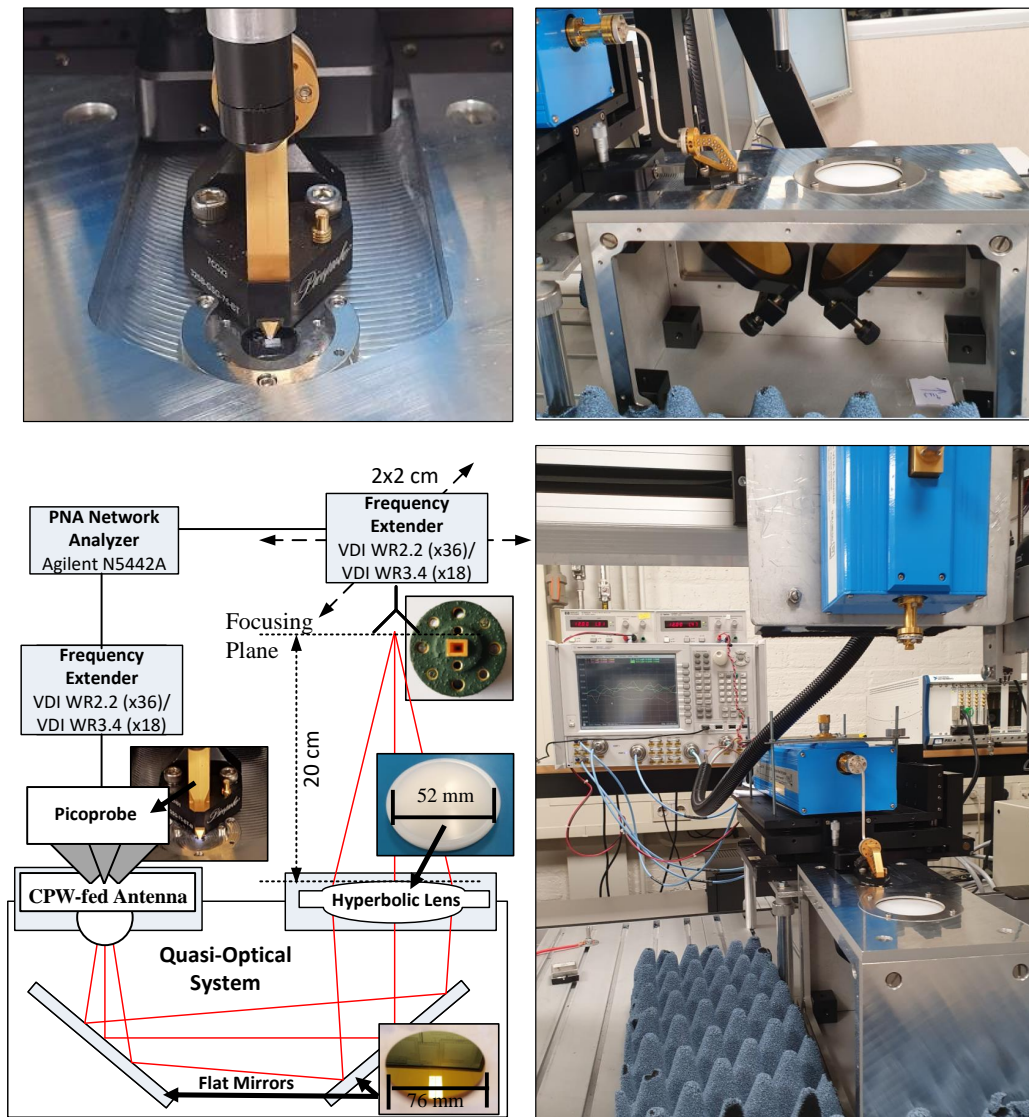


Figure 4.15: Packaging of the CPW-fed antenna in a quasi-optical focusing system and the measurement setup for the gain patterns. The bottom left hand side shows a schematic of the focusing system in combination with the measurement setup. The top left side shows a picture of the GSG probe landed on the chip. The top-right picture shows a side-view while the bottom right shows a perspective front-view of the measurement setup.

a back-propagation of the measured complex near-field, as explained in Sec. 4.5.4.

The quasi-optical measurement setup is schematically shown in Fig. 4.15. The GSG probe lands on the back-side of the chip, as shown in the top-left picture, so that the dielectric lens faces down. Two flat 3" gold mirrors position the antenna in the focus point of a HDPE hyperbolic lens. The hyperbolic lens has a diameter of 52 mm and creates a focused spot, with a -3 dB beam-waist of approximately 1 cm in diameter, in the focusing plane that is positioned 20 cm on top of the quasi-optical system. The hyperbolic lens is made of HDPE, characterized with a relative permittivity of $\epsilon_r = 2.5$ and the loss tangent is estimated to be $\tan \delta = 0.0006$. The simulated performance of the quasi-optical system is evaluated in GRASP [118], where the beam patterns after the elliptical lens are imported. The CNC arm, visible in the bottom right of Fig. 4.15, is used to perform a raster scan of $2 \text{ cm} \times 2 \text{ cm}$ in the focusing plane, using WR3.4 and WR2.2 frequency extenders which are connected to their corresponding rectangular horn antennas. A picture of the side-view of the focusing system is shown in the top right of Fig. 4.15, where the two gold mirrors can also be identified. In the pictures, a WR3.4 probe is connected to a WR3.4 frequency extender that is placed on a manipulator to be able to land the GSG-probe on the pads. The measurement setup is calibrated in terms of S-parameters and power up to the measurement plane. Two one-port calibrations are performed, including a vector corrected absolute power calibration at the waveguide ports [133]. The calibration procedure resorts to two single port calibrations to avoid the complexity and the derived errors due to cable movement of performing a full two port calibration when one of the extender is mounted on a plane that is orthogonal to the other. Therefore, the two ports are calibrated independently. The S-parameters are first calibrated at the waveguide heads of the frequency extenders by means of a (SSL) Short, Offset-Short, Load calibration kit. Subsequently, a VDI Erickson PM5 power meter is used to calibrate the power in output of the frequency extenders. The horn antenna is connected to the frequency extender which is mounted on the controllable arm and, after accounting for the losses of the horn, this horn is calibrated in terms of reflection coefficient and power. For the feeding port, the fused silica SOL calibration kit [131] that was shown in Fig. 4.13(a) is used to shift the reference plane of the S-parameters and power to the probe-tips.

4.5.3 Measured Near-Field Gain Patterns

The directivity (and gain) of an antenna is traditionally defined for antennas that focus in the far-field. However, the quality of near-field focused patterns, as is the situation for the considered measurement setup with a focusing hyperbolic lens, can be described equivalently as it was defined in [134] and later used in [132], where it is shown how Friis transmission equation can be used to calculate the *near-field directivity* or *near-field gain*, in focusing systems. The near-field directivity, $D_{\text{NF}}(x, y)$, can directly be evaluated from the uncalibrated S_{21} -parameter, S_{21}^{RAW} , of the measurement setup using (4.3):

$$D_{\text{NF}}(x, y) = \frac{4\pi |S_{21}^{\text{RAW}}(x, y)|^2}{\int_x \int_y |S_{21}^{\text{RAW}}(x, y)|^2 J_{\theta, \phi}(x, y) dy dx} \quad (4.3a)$$

$$J_{\theta,\phi}(x, y) = \left| \begin{array}{cc} \frac{\partial\theta(x,y)}{\partial x} & \frac{\partial\theta(x,y)}{\partial y} \\ \frac{\partial\phi(x,y)}{\partial x} & \frac{\partial\phi(x,y)}{\partial y} \end{array} \right| \sin((\theta(x, y))) \quad (4.3b)$$

where $\theta(x, y) = \tan^{-1}((x^2 + y^2)^{0.5}/(F_2)^2)$, with $F_2 = 20$ cm and $\phi(x, y) = \tan^{-1}(y/x)$. The measured normalized near-field directivity patterns are shown in Fig. 4.16(a-c) at the frequencies 250 GHz, 350 GHz and 500 GHz respectively. Cuts in the main planes and diagonal planes of the patterns are shown in Fig. 4.16(d-f) where the black curves indicate the simulated patterns evaluated in GRASP and the blue curves are the measurements. The maximum measured and simulated near-field directivity (at $x = y = 0$) is shown in Fig. 4.17(a). A ± 1 dB oscillation in the measurement can be attributed to reflections in the measurement setup (between the CNC-arm and the focusing system). At the center frequencies, the measured directivity is slightly higher than the simulation. The measured patterns are however clean and symmetric and overall, a good comparison between simulation and measurement exists. The near-field directivity curve shows a flat characteristic since the hyperbolic lens becomes under-illuminated as the frequency increases due to the more directive lens patterns, resulting in a near-constant beam-spot size in the focusing plane.

The near-field gain, G_{NF} , is calculated using Friis equation (4.4) as in [132] by using the ratio of calibrated received power by the horn, P_{Horn} , and calibrated accepted power by the antenna (after reflections), P_{Ant} :

$$\frac{P_{\text{Horn}}}{P_{\text{Ant}}} = G_{\text{NF}} G_{\text{Horn}} \left(\frac{\lambda_0}{4\pi F_2} \right)^2 \quad (4.4)$$

where G_{Horn} is the gain of the horn antenna and λ_0 is the free-space wavelength. Calculating the gain of a near-field focusing system using Friis equation is valid [134] since the focusing system is placed in the far-field of the horn antenna and since the horn dimension is significantly smaller than the focusing spot. The measured and simulated near-field gain is also shown in Fig. 4.17(a). A good agreement with the simulation can be observed. The total losses of the antenna fixture (i.e. the total loss between the measurement plane and focusing plane) are calculated by relating the measured near-field directivity, D_{NF} , to the measured near-field gain, G_{NF} : $L_{\text{dB}} = D_{\text{NF}} - G_{\text{NF}}$. The measured losses are shown in Fig. 4.17(b) by the blue curve and compared with simulation shown by the black curve. The simulated losses are decomposed in its simulated contributions. The gray curve represent the simulated losses of the antenna itself, referred to the antenna interface. The red curves represent simulated loss contributions of the measurement setup. The losses of the GSG landing pads and grounded CPW transmission line (up to the antenna interface) are simulated in CST Microwave Studio. The spillover losses w.r.t the hyperbolic lens are approximated using an angular integration of the simulated lens patterns until the angle that the hyperbolic lens is subtending the lens antenna (approximately 10° from broadside), w.r.t. to the total power in the lens pattern. The reflection efficiency at the interfaces of the hyperbolic lens are approximated using the wave impedance mismatch of the different media. The dielectric losses are evaluated using $\exp(-2\alpha t_{\text{lens}})$ where the maximum lens

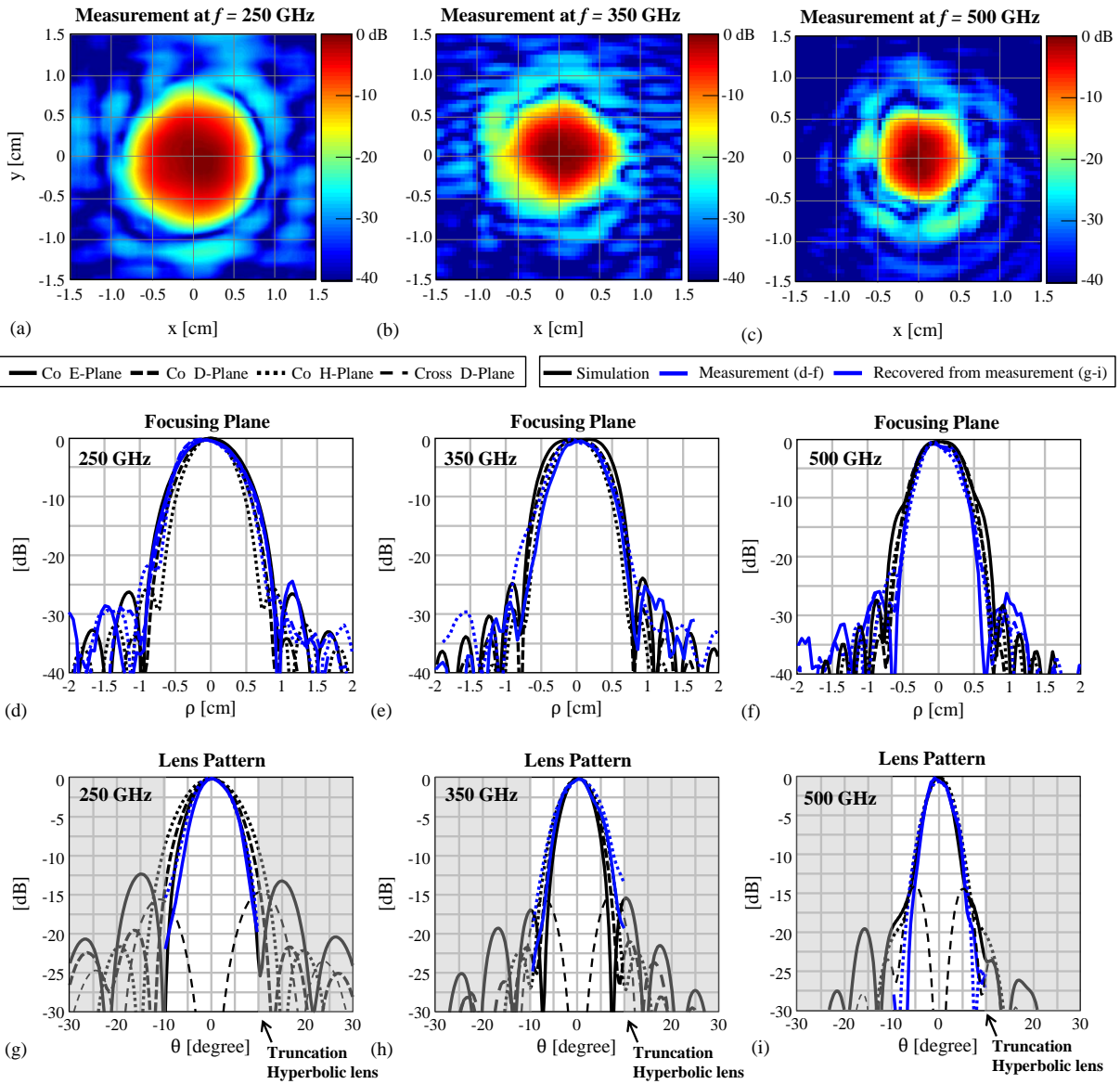


Figure 4.16: Patterns of the CPW-fed antenna at (a,d,g) 250 GHz, (b,e,h) 350 GHz and (c,f,i) 500 GHz. The measured 2D patterns in the focusing plane are shown in (a-c). Cuts of the simulated (black) and measured (blue) patterns in the focusing plane are shown in (d-f). The simulated patterns together with the back-propagated measured patterns, as explained in Sec. 4.5.4, are shown in (g-i). The gray areas in the lens pattern indicate the portion of the field that is truncated by the quasi-optical system.

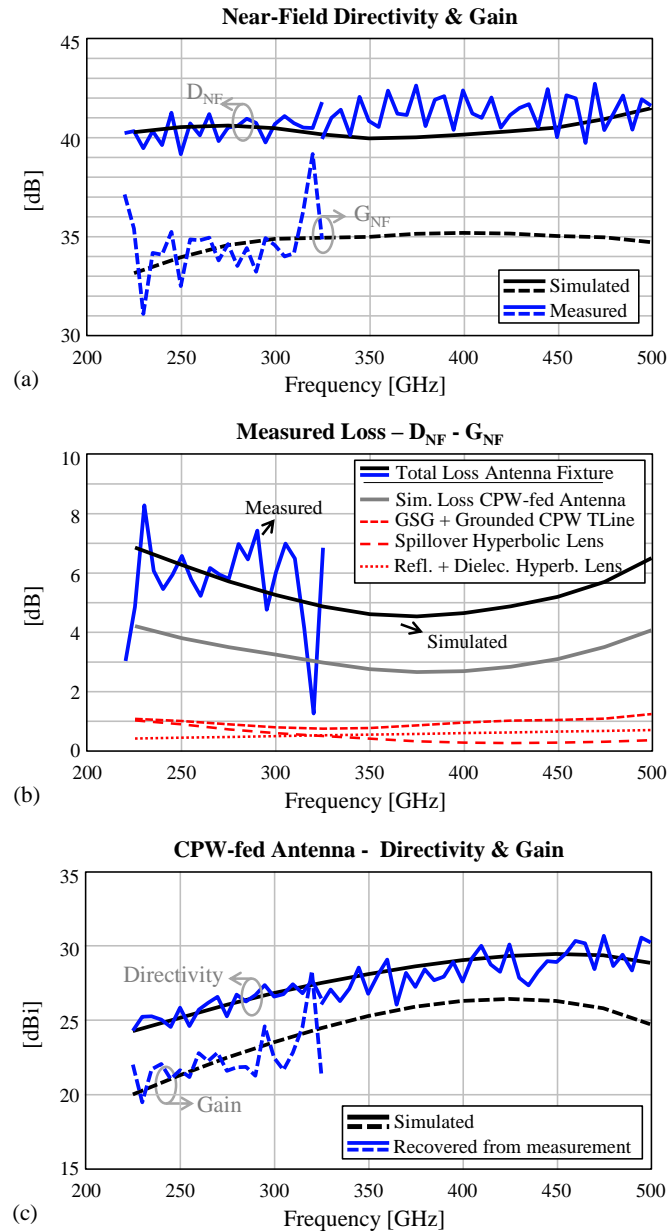


Figure 4.17: Performance and measurement results of the CPW-fed antenna placed in the quasi-optical system shown in Fig. 4.15. The simulated and measured near-field directivity (D_{NF}) and gain (G_{NF}) are shown in (a). The measured loss (defined as $D_{NF} - G_{NF}$) is shown in (b) by the blue curve and is compared with simulation (black). The simulated loss is decomposed in its simulated contributions: The loss of the CPW-fed antenna (gray), ohmic dissipation losses in the GSG pads and the additional transmission line to the antenna, the spillover efficiency of the lens patterns w.r.t. the hyperbolic lens and reflections and dielectric losses in the hyperbolic lens. The recovered silicon lens directivity and gain, derived in Sec. 4.5.4, are compared in (c) with simulation.

thickness of $t_{\text{lens}} = 1.2$ cm is used and $\alpha \approx k_d \tan \delta/2$ is the field attenuation with k_d being the wavenumber in the hyperbolic lens medium.

4.5.4 Recovered Silicon Lens Antenna Gain Patterns

Although the comparison between the measured and simulated losses of the quasi-optical measurement setup are in good agreement, it would be informative to relate the measurements to the performance of the silicon lens antenna in terms of patterns, directivity and gain. The silicon lens antenna performance can be recovered via a back-propagation of the measured complex near-field by using the free-space Green's functions to evaluate the field at the surface S_1 in Fig. 4.14, $E_{S1}(\theta_{\text{hyp}}, \phi_{\text{hyp}})$. In the case that only a broad-side beam is evaluated, with a large $F_{\#}$ hyperbolic lens that is made of a low relative permittivity material, any field aberration effects are neglected so that $E_{S2}(\theta_{\text{ant}}, \phi_{\text{ant}}) \approx E_{S1}(\theta_{\text{hyp}}, \phi_{\text{hyp}})$, where the antenna observation angle, θ_{ant} , can be approximated by $\theta_{\text{ant}} = \tan^{-1}(\tan(\theta_{\text{hyp}})F_2/F_1)$. In this manner, the lens patterns can be reconstructed up to the truncation angle of the hyperbolic lens. The simulated normalized lens patterns of the antenna are shown by the black curves in Fig. 4.16(g-i) at 250 GHz, 350 GHz and 500 GHz and compared with the reconstructed fields (blue curves). A conventional lens directivity calculation, applied to the recovered silicon lens patterns, overestimates the directivity since the integration of the lens pattern does not include the sidelobes beyond the truncation of the hyperbolic lens. The calculated directivity from the recovered lens patterns is therefore corrected with the simulated spillover losses that were reported in Fig. 4.17(b). The antenna directivity recovered from the measurement is shown in Fig. 4.17(c) with the blue curve and is compared with simulation. The lens antenna gain is recovered by subtracting the measured losses (blue curve in Fig. 4.17(b)) from the recovered directivity and by compensating for the simulated losses of the quasi-optical measurement setup (red curves in Fig. 4.17(b)). This leads to the recovered gain reported with the blue curve in Fig. 4.17(c) that shows an excellent agreement with simulation. It should be highly stressed that these results are recovered from the measurements and are mixed with simulated results. These results provide a valuable insight in antenna performance, but the true comparison between measurement and simulation is reported in Fig. 4.17(b) of the complete quasi-optical measurement setup.

4.6 Conclusion

Leaky-wave antennas, operating at sub-millimeter wavelengths, are shown to be extremely suitable for integration in commercial CMOS processes as the impact of the metal density rules is minimized while simultaneously a dielectric lens can be efficiently illuminated through the bulk silicon. The bandwidth of double leaky slot antennas can be significantly increased by using a novel approach to truncate the antenna ground plane as is demonstrated, in simulation, with an antenna design that is suitable for wideband THz direct detection from 200 GHz to 600 GHz featuring an average antenna efficiency of 57% over

the large 3:1 relative bandwidth. A second wideband, CPW-fed, antenna is designed, fabricated and characterized as means of verification and, potentially, could be connected to other on-chip elements via a grounded CPW interface. The latter antenna operates with an average efficiency of 47% from 250 GHz to 500 GHz and is characterized with an ad-hoc measurement setup based on a hyperbolic lens that facilitates high-frequency measurements of integrated lens antennas via a landing probe. The recovered silicon lens antenna directivity and gain show excellent agreement with the simulations.

Chapter 5

Radiometric Modeling and Performance of a THz Direct Detector in 22-nm CMOS

In order to achieve the required performance for passive imaging, a wideband antenna should efficiently couple incident THz radiation to detectors that are characterized with a Noise Equivalent Power (NEP) in the order of a $\text{pW}/\sqrt{\text{Hz}}$. An accurate modeling of the antenna-detector combination and read-out circuit over a large frequency band is crucial in order to predict radiometric performance in terms of NEP and temperature sensitivity. This chapter extends the lumped element model of a Schottky Barrier Diode (SBD) to predict the circuit performance of a differential diode direct detection circuit that is directly connected to a wideband double leaky slot lens antenna and load resistor for a voltage read-out. A wideband equivalent circuit is constructed that accurately predicts the final performance of the fabricated prototype, verified by high frequency measurements. The measured prototype is characterized with a minimum NEP of $20 \text{ pW}/\sqrt{\text{Hz}}$ and an average NEP of $90 \text{ pW}/\sqrt{\text{Hz}}$ from 200 GHz to 600 GHz. The deviation from the initially simulated average NEP of $2.7 \text{ pW}/\sqrt{\text{Hz}}$ is caused by a discrepancy in the SBDs series resistance and junction capacitance, which compromises the diode responsivity. By using the proposed modeling approaches, the reduction in diode efficiency and system performance is accurately predicted.

5.1 Introduction

In the design and fabrication of large Focal Plane Arrays (FPAs) operating in the sub millimeter wave (submm-wave) regime of the electromagnetic spectrum (i.e. 300 GHz and above), it is still challenging to use coherent detection circuitry such as amplifiers, mixers and oscillators integrated in silicon technologies [43,123]. Their power consumption and size prohibits them to be used in tightly sampled FPAs. Instead, direct detection architectures are preferred for large THz imaging arrays, since they offer an easy read-out

at relatively low frequencies and a low power consumption. In such detection architecture, a direct detector (such as a transistor or diode) rectifies a high frequency signal that is received by an antenna. If these arrays can be fabricated with sufficient performance in silicon technologies, such as CMOS, the practicality and cost of THz imaging systems will be significantly improved as they can be produced while benefiting from their mass reproducibility and the potential co-integration with read-out circuitry and digital back-end. Compact CMOS THz imaging cameras with more than 1000 pixels have already been presented [52]. Still, these cameras depend on active THz sources that illuminate the target of interest in order to achieve sufficient signal-to-noise ratio (SNR) [56]. In Chapter 2 it is shown that, when a large portion of the available spectrum in the submm-wave regime is utilized, fully passive THz imaging can be realized when detectors are available with a Noise Equivalent Power (NEP) of only a few $\text{pW}/\sqrt{\text{Hz}}$. These NEPs have been demonstrated in high performance III-V technologies [85]. In the more low-performance CMOS technologies, however, achieving similar NEPs is difficult and the availability of better device- and system models is vital to be able to push the technologies ability to enable passive THz imaging. An accurate representation of temperature sensitivity, taking into account bandwidth, antenna-detector impedance matching and read-out network, should be considered for an accurate prediction of radiometric operation.

In this chapter, the proposed antenna from Chapter 4 is packaged into a THz direct detection system. A model for the NEP, valid over a wide bandwidth and taking into account the effect of the antenna, is derived for such THz imagers. The detection circuit consists of a lens antenna that couples incident radiation to two SBDs in a differential configuration with a voltage read-out over a load resistor. The SBDs used in this design are the smallest one that were available in the library of the foundry. The model is based on the lumped element SBD model [93] that is already used in the design of THz imaging pixels [74, 135], and can be easily extended for transistor based differential read-out circuits [94]. These diode models are often only used for initial design considerations of the detector in terms of sizing and noise [74, 94, 135]. Final system responsivity results, however, are obtained by means of harmonic balance simulations [94] and discrepancies of more than 3 dB between simulation and measurement are not unusual.

This work extends the SBD model such that full radiometric operation in terms of the NEP and temperature sensitivity can be evaluated over over a wide frequency bandwidth, taking into account antenna efficiency, antenna-detector impedance matching, and the read-out network. A standard SBD that is available in the library of the foundry is used. With the predicted system NEP of only $2.7 \text{ pW}/\sqrt{\text{Hz}}$, according to the model that was used in the initial design phase, the direct detector would demonstrate an important step towards passive THz imaging applications with sub-Kelvin temperature sensitivities. However, measurements of the voltage responsivity of the direct detector indicated worse performance of the SBDs with a system NEP of approximately $90 \text{ pW}/\sqrt{\text{Hz}}$. Low-frequency measurements performed on the SBD, i.e. the IV-curve in DC and an S-parameter measurement at low-frequency (10 GHz), allowed for extracting the actual series resistance and junction capacitance of the diode. From there, an updated high frequency model of the detection circuit could be constructed that accurately matches the high frequency voltage

responsivity measurements of the direct detection system. Although no state-of-the-art performance in NEP is achieved, the wideband integrated analysis procedure can be used for a close antenna-detector co-design over a large frequency band, for future passive THz imaging applications.

This chapter is structured as follows. In Sec. 5.2, the figures of merit in the design of passive THz imaging cameras are introduced. In Sec. 5.3, the lumped element model of the SBD is extended to a complete system model of the THz direct detector, including the antenna. Some design considerations of the detection circuit are provided. In Sec. 5.4, the radiometric performance of the direct detector is presented in terms of radiometric pattern, RMS output noise voltage, voltage responsivity, NEP and temperature sensitivity. The diode model, and experimental extraction of the diode model, are discussed in the Appendices.

5.2 Passive THz Imaging

A schematic of a direct detection architecture is shown in Fig. 5.1. In such architecture, an antenna with antenna efficiency $\eta_{\text{ant}}(f)$, couples incident THz power, P_{sig} , to a detector circuit that contains devices with a non-linear behavior, such as transistors and diodes. A portion of the power that is captured by the antenna will be reflected due to the impedance mismatch between the antenna input impedance, Z_{ant} , and detector input impedance, Z_{det} , which should be conjugally matched to maximize the matching efficiency, η_{Ω} . The detector is biased to allow a certain DC current flowing through the detector, or voltage drop over the detector. Due to the non-linear current-voltage relationship of the detector, the power that arrives to the detection circuit, P_{det} , then induces an average incremental increase in DC-current (or low frequency, if the input signal is modulated), ΔI , flowing through the detector or voltage drop, ΔV , over the detector, in the case that the detector is biased via a load resistor. This RF-to-DC conversion is quantified by the detector current-, $\mathfrak{R}_i^{\text{det}}$, or voltage responsivity, $\mathfrak{R}_v^{\text{det}}$, which can be written as (5.1):

$$\mathfrak{R}_i^{\text{det}} \triangleq \frac{\Delta I}{P_{\text{det}}} \qquad \mathfrak{R}_v^{\text{det}} \triangleq \frac{\Delta V}{P_{\text{det}}} \qquad (5.1)$$

The rectified signal, ΔI or ΔV , can be integrated for τ_{int} seconds in order to achieve a sufficient Signal-to-Noise Ratio (SNR) after detection, provided that the system is stable and that the signal is not in the presence of Flicker-noise contributions. For uncooled detectors, the SNR is usually limited by the noise that is introduced by the detection circuit. The amount of power accepted by the detection circuit, P_{det} , that results in a $\text{SNR}_{\text{AD}} = 1$ after 0.5 second of integration (1 Hz of detection bandwidth), equals the detector NEP (NEP_{det}). Depending on the type of read-out, i.e. whether a change in current or voltage is measured, the noise is either the spectral RMS current noise, i_n , or spectral RMS voltage noise, v_n . For example, in [77] the detector is characterized in both voltage mode read-out and current mode read-out, resulting in two different values of

NEP. In this work, the read-out will be a voltage signal and the NEP is defined accordingly. The SNR after detection, SNR_{AD} , for such direct detection architectures can be expressed as (5.2a) [54, 102, 106]. This representation, however, is only applicable in narrowband scenarios. The amount of power that is accepted by the detection circuit, P_{det} , depends on the antenna efficiency $\eta_{\text{ant}}(f)$ as well as the antenna-detector impedance matching efficiency $\eta_{\Omega}(f)$, $P_{\text{det}}(f) = P_{\text{sig}}(f)\eta_{\text{ant}}(f)\eta_{\Omega}(f)$, and therefore depends on frequency. Moreover, in an ultra-wideband detection scenario, the NEP can also fluctuate significantly over frequency. Therefore, for wideband scenarios, a more appropriate representation of the SNR would be (5.2b),

$$\text{SNR}_{\text{AD}} = \frac{P_{\text{det}}}{\text{NEP}_{\text{det}}} \sqrt{2\tau_{\text{int}}} \quad (5.2a)$$

$$\text{SNR}_{\text{AD}} = \sqrt{2\tau_{\text{int}}} \int_{\Delta f_{\text{RF}}} \frac{P_{\text{sig}}(f)\eta_{\text{ant}}(f)\eta_{\Omega}(f)}{\text{NEP}_{\text{det}}(f)} df \quad (5.2b)$$

, where the spectral detector power and spectral NEP are divided firstly and then integrated over the absolute frequency bandwidth Δf_{RF} . In radiometry, differences in received signal power are attributed to differences in apparent temperature of the incoherent source(s) that are seen by the beam pattern of the imager. The temperature difference of an incoherent sources, that gives rise to a SNR of unity is a useful figure of merit and is defined as the temperature sensitivity, i.e. the Noise Equivalent Temperature Difference (NETD) of the radiometer. In Chapter 2, the NETD was derived from the SNR for incoherent sources that are in the Rayleigh-Jeans limit of Planck's law. In that case, the NETD can be expanded in spectral form as follows:

$$\text{NETD} = \frac{1}{k_B \sqrt{2\tau_{\text{int}}} \int_{\Delta f_{\text{RF}}} \frac{\eta_{\text{ant}}(f)\eta_{\Omega}(f)}{\text{NEP}_{\text{det}}(f)} df} \quad (5.3)$$

, where k_B is Boltzmann's constant, $\tau_{\text{int}} = 1/f_{\text{refresh}}$ with f_{refresh} being the refresh rate of

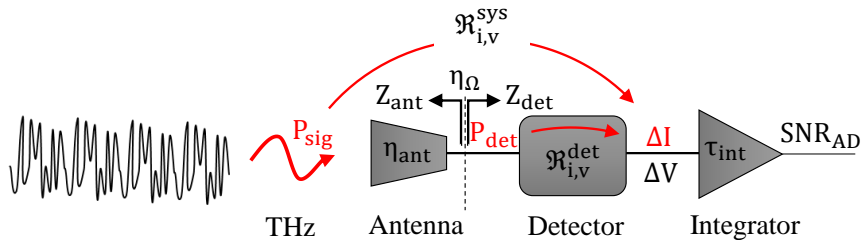


Figure 5.1: Schematic of an incoherent (direct) detection architecture, indicating its three main components; the antenna, detector and integrator.

the imager and $\text{NEP}_{\text{sys}}(f)$ is defined as the system NEP:

$$\text{NEP}_{\text{sys}} = \frac{v_n}{\Re_v^{\text{sys}}} = v_n \frac{P_{\text{sig}}}{\Delta V} = v_n \frac{P_{\text{det}}}{\Delta V} \frac{P_{\text{sig}}}{P_{\text{det}}} = \frac{\text{NEP}_{\text{det}}}{\eta_{\text{ant}} \eta_{\Omega}} \quad (5.4a)$$

$$\text{NEP}_{\text{det}} = \frac{v_n}{\Re_v^{\text{det}}} \quad (5.4b)$$

The **system** NEP or responsivity, NEP_{sys} and \Re_v^{sys} , include the impedance matching of the antenna detector combination as well as the optical efficiency of the lens antenna and is generally reported in literature. The **detector** NEP or responsivity, NEP_{det} and \Re_v^{det} , is informative in how well the detector circuit is operating, irrespective of the presence of antenna performance. In the case of radiometric THz imagers, also absolute bandwidth, Δf_{RF} , determines the radiometric performance of the imager in terms of NETD (5.3). The required NETD differs per application scenario. For example, a qualitative study of NETD in a security screening scenario is presented in [55], where it is shown that a sub-Kelvin temperature sensitivity is required for effective concealed weapon detection. Such requirement will be similar for applications such as pedestrian detection for the automotive industry.

5.3 Schottky Barrier Diodes in a Differential Voltage Read-Out

In Fig. 5.2(a), a schematic is shown of the detection scheme. The detectors used in the design are SBDs. SBDs are low power consuming devices that are also easy to integrate in large arrays. The detectors are positioned in a differential topology, enforcing a virtual RF-grounding point between the two SBDs. In this virtual RF-ground, the DC-/low frequency read-out network can safely be connected without any RF-power dissipation losses in the read-out network. Differential read-out schemes are commonly used in THz direct detection circuits [52, 77, 136]. The read-out network consists of a load resistor with resistance R_{load} , that converts the average incremental increase in rectified current flowing through the detector, ΔI , into a change in voltage-drop over the load resistor, ΔV . This defines the output signal. A reference branch, containing identical and equally biased SBDs, is not connected to the antenna terminals and therefore allows for a pseudo-differential read-out to directly read-out the output signal ΔV . Moreover, the reference branch will minimize noise contributions that are injected by the biasing source. In Fig. 5.2(b), a screenshot of the detector layout is shown, indicating the two active detectors that rectify the THz signal and the vias that connect the SBDs to the antenna terminals. The reference detectors of the reference branch are placed directly next to the active detectors and a ring of dummy detectors ensures a uniform distribution of the doped materials. In this work we make use of a SBD that was available in the library of the foundry. The minimum size of the considered SBD, available in the library, is $1.6 \mu\text{m} \times 1.6 \mu\text{m}$ in dimension. Smaller diodes

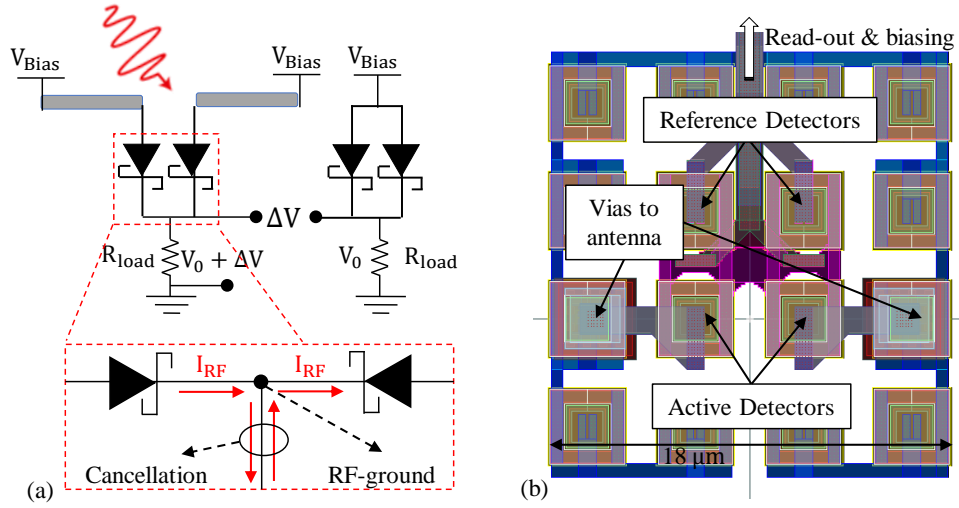


Figure 5.2: Detector architecture used for the THz direct detection system. In (a) a schematic is shown where the antenna ground plane is used for biasing SBDs in a differential configuration. A differential configuration introduces an RF-symmetry where the DC read-out network can be connected. A reference branch is added to enable a pseudo-differential read-out of ΔV . In (b) a screenshot of the detector layout is shown, indicating the vias that go up to the antenna terminals, four SBDs for the pseudo-differential read-out from (a) and a ring of dummy detectors.

are desirable in terms of NEP. A smaller magnitude in diode current reduces the shot-noise contributions.

The behavior of SBDs or p^+/n -well diodes, in terms of noise and responsivity, can be analyzed with a simple lumped element model as is well described in [93] and applied in [73, 74]. The model has been applied similarly to diode-connected NMOS transistors in [94]. In Appendix D, a concise derivation is presented of the current responsivity of a standalone SBD, $\mathfrak{R}_i^{\text{diode}}$, derived from the simulated IV-relationship, $I_D = f(V_D)$, and simulated value for the junction capacitance, $C_j(V_D)$. In this subsection, starting from the diode current responsivity, we will extend this model for the detector architecture presented in Fig. 5.2(a) to be able to evaluate NEP (and thus NETD) of the considered detection circuit over a large bandwidth, including antenna efficiency, antenna-detector impedance matching and the load resistor for read-out.

The equivalent DC-model, without reference branch, is shown in Fig. 5.3(a). The current flowing through the detector, I_D , is determined by the voltage drop over the diode, V_D . The $I_D = f(V_D)$ relationship of the diode is known from simulation or measurement and the required pixel biasing voltage, V_{bias} , in order to reach a desired diode biasing point can be calculated as function of the value of the load resistance as: $V_{\text{bias}} = 2I_D(V_D)R_{\text{load}} + V_D$. The value of the load resistor is $R_{\text{load}} = 2 \text{ k}\Omega$ and is chosen such that the optimal biasing conditions can be achieved with a pixel biasing voltages of $V_{\text{bias}} < 2 \text{ V}$ while maximizing voltage responsivity. At each diode biasing point, V_D , the small-signal model can be applied and the diode can be represented by its diode resistance $R_{\text{diode}}(V_D)$ as is shown in Fig. 5.3(b). Suppose now that P_{det} is absorbed in the detection circuit. The total current

flowing through the load resistance, I_{det} , is now perturbed: $I_{\text{det}} = 2I_D + \Delta I_{\text{det}}$. Each SBD effectively absorbs half of the power, $P_{\text{det}}/2$, and an average incremental DC-current, generated by each SBD, of $\Delta I_D/2$ is expected. The incremental increase in current is represented by the current generators as shown in Fig. 5.3(c). Using the superposition principle, all sources in the equivalent circuit in Fig. 5.3(c) can be investigated separately. Considering only the incremental current contributions due to the absorbed THz power, the circuit can be simplified to Fig. 5.3(d) the change in current flowing through the load resistor, ΔI_{det} can be calculated as:

$$\Delta I_{\text{det}} = \Delta I_D \frac{R_{\text{diode}}/2}{R_{\text{diode}}/2 + R_{\text{load}}} \quad (5.5)$$

Defining then the current responsivity of the differential detector circuit as $\mathfrak{R}_i^{\text{det}} = \Delta I_{\text{det}}/P_{\text{det}}$ gives:

$$\mathfrak{R}_i^{\text{det}} = \frac{\Delta I_{\text{det}}}{P_{\text{det}}} = \mathfrak{R}_i^{\text{diode}} \frac{R_{\text{diode}}/2}{R_{\text{diode}}/2 + R_{\text{load}}} \quad (5.6)$$

From (5.6), it can be seen that a high load resistor can significantly reduce the current responsivity (R_{diode} is only tens of Ohms at the optimal biasing conditions). However, the voltage responsivity, $\mathfrak{R}_v^{\text{det}}$, that relates the output signal ΔV , to the THz power absorbed in the entire detection circuit, P_{det} , increases linearly with the resistance and can be expressed as:

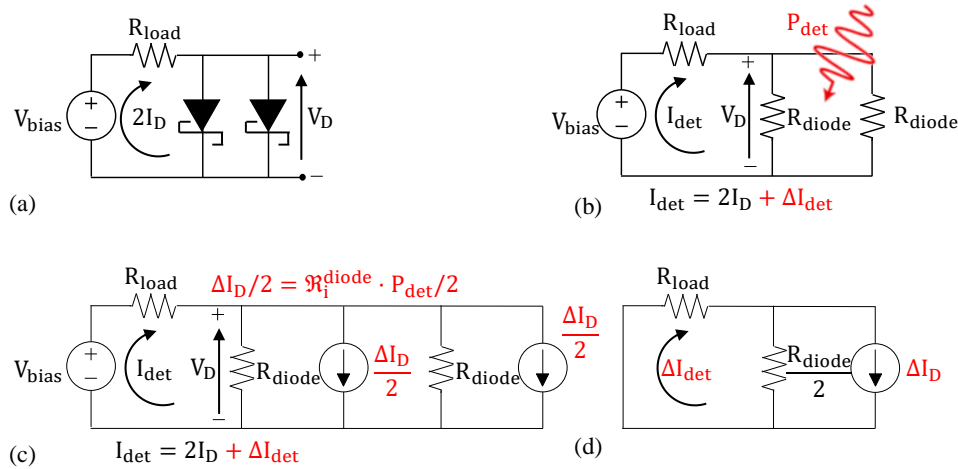


Figure 5.3: In (a) the DC-equivalent circuit model of a single branch of the detection architecture is shown. In (b), the SBDs are replaced with their small-signal resistances. An incremental change in DC-current flowing through the load resistance, ΔI_{det} , is the result of absorbed power P_{det} . Each of the diodes absorb half of the power and a current generator represents the current responsivity as shown in (c) and as has been derived in Appendix D. Considering only the incremental current sources in (c), the equivalent circuit can be simplified to (d) to derive the incremental pixel current.

$$\mathfrak{R}_v^{\text{det}} = \frac{\Delta V}{P_{\text{det}}} = \mathfrak{R}_i^{\text{det}} R_{\text{load}} = \mathfrak{R}_i^{\text{diode}} \frac{R_{\text{diode}} R_{\text{load}}}{R_{\text{diode}} + 2R_{\text{load}}} \quad (5.7)$$

The current- and voltage responsivity for $f_{RF} = 200$ GHz, 400 GHz and 600 GHz are shown in Fig. 5.4(a), where both the circuit model (derived from only the IV-curve and junction capacitance as derived in Appendix D) and a harmonic balance simulation of the full detection circuit are shown. The simulations are performed in the software tool Virtuoso Analog Design Environment by Cadence. The dominant noise contributions in the considered detection architecture are Flicker-noise, shot-noise generated by the junction and Johnson (thermal) noise generated by the load resistor and series resistance of the diode. Flicker noise is not included in the models provided by the foundry of the considered technology. We will investigate the remaining (white) noise contributions, beyond the 1/f corner. The Flicker noise contribution diminishes rapidly for frequency higher than this frequency point. For SBDs, a Flicker-noise corner around 4 MHz is expected [74]. The remaining white noise mechanisms are incoherent and the individual contributions should be summed in power. The total voltage noise, v_n in $V/\sqrt{\text{Hz}}$, can be expressed as:

$$v_n = \sqrt{|v_n^{\text{shot}}|^2 + |v_n^{R_{\text{load}}}|^2 + |v_n^{R_{\text{series}}}|^2} \quad (5.8)$$

where the individual contributions can be derived to be:

$$v_n^{\text{shot}} = \sqrt{4q|I_D|} \frac{r_j R_{\text{load}}}{R_{\text{diode}} + 2R_{\text{load}}} \quad (5.9a)$$

$$v_n^{R_{\text{load}}} = \sqrt{4k_B T_n R_{\text{load}}} \frac{R_{\text{diode}}}{R_{\text{diode}} + 2R_{\text{load}}} \quad (5.9b)$$

$$v_n^{R_{\text{series}}} = \sqrt{4k_B T_n R_{\text{series}}/2} \frac{2R_{\text{load}}}{R_{\text{diode}} + 2R_{\text{load}}} \quad (5.9c)$$

In (5.9), r_j is the dynamic junction resistance (see Appendix D), q is the elementary charge, k_B is the Boltzmann constant and T_n is the noise temperature in Kelvin. The total noise and their components are shown in Fig. 5.4(b) where they are compared with the simulations in Virtuoso. For low biasing voltages, the circuit is limited to the thermal noise introduced by the load resistor, whereas at higher biasing voltages, the noise will be limited to the shot-noise of the diodes. For the pseudo-differential read-out, using the reference branch as shown in Fig. 5.2(a), the spectral noise voltage is increased by a factor of $\sqrt{2}$. The benefit of this configuration is however the increased immunity of the pixel to both supply noise and electromagnetic interference from outside the circuit.

From the detector voltage responsivity (5.7), spectral voltage noise in output (5.8), the detector NEP (5.4b) can be defined as:

$$\text{NEP}_{\text{det}} = \frac{\sqrt{|v_n^{\text{shot}}|^2 + |v_n^{R_{\text{load}}}|^2 + |v_n^{R_{\text{series}}}|^2}}{\mathfrak{R}_i^{\text{diode}}} \frac{R_{\text{diode}} + 2R_{\text{load}}}{R_{\text{diode}} R_{\text{load}}} \quad (5.10)$$

Model Verification

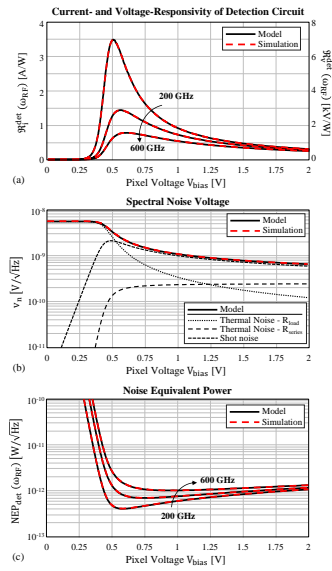


Figure 5.4: Validation of circuit model by means of simulation. A load resistor of $R_{load} = 2\text{ k}\Omega$ is taken and the frequencies $f_{RF} = 200\text{ GHz}$, 400 GHz and 600 GHz are evaluated. (a) Current (5.6) and voltage responsivity (5.7). (b) Spectral noise voltage (5.8) and the individual contributions (5.9). (c) Detector NEP (5.10).

We now have an expression of the detector NEP of the considered detection architecture that can be fully derived from the IV-curve and junction capacitance of the diode. The detector NEP is shown in Fig. 5.4(c) and compared with simulation. The parameter to optimize is NETD and thus system NEP. The system NEP is related to the detector NEP via the antenna efficiency and antenna-detector impedance matching efficiency. The input impedance of the differential detector circuit, seen from the antenna terminals, is $Z_{\text{det}} = 2Z_{\text{diode}}$. The reflection coefficient between the antenna-detector interface, indicated in Fig. 5.1, can be calculated as [137]:

$$\Gamma = \frac{Z_{\text{det}} - Z_{\text{ant}}^*}{Z_{\text{det}} + Z_{\text{ant}}} \quad (5.11)$$

from where the impedance matching efficiency, $\eta_{\Omega} = 1 - |\Gamma|^2$, is defined. The antenna efficiency of the double leaky slot lens antenna was presented in Fig. 4.9(e) and has an average efficiency of 57% over the full bandwidth. The system NEP can then be predicted as $\text{NEP}_{\text{sys}} = \text{NEP}_{\text{det}} / (\eta_{\text{ant}} \eta_{\Omega})$ (5.4b).

5.4 Radiometric Performance

The THz direct detection system and the packaging steps are shown in Fig. 5.5. The read-out terminals and power supply of the CMOS chip are bond-wired to a PCB as shown in the pictures Fig. 5.5(a,b). Before bond-wiring, the chip is glued, with a commercial Loctite 406, to the elliptical silicon lens with diameter 7.6 mm, Fig. 5.5(c). A proper position of the phase center of the antenna w.r.t. the focal point of the elliptical lens is ensured by means of an alignment hole that is part of a metallic holder for the lens Fig. 5.5(d). The metallic holder is attached on a fixture that can be attached to the measurement table Fig. 5.5(e).

5.4.1 Radiation Patterns

An overview of the measurement setup used to characterize the normalized antenna patterns and directivity is shown in Fig. 5.6(a) with Fig. 5.6(b) showing a zoom-in of the setup with the assembled THz direct detector, the surrounding absorbing material and the WR2.2 horn-antenna. The horn antenna is attached to a VDI WR2.2 frequency extender and placed 20 cm above the lens-antenna (in the Fraunhofer region). The horn and extender are attached on a Computer Numerical Controllable (CNC) machine and performs a 4×4 cm planar scan. Two PXI-5422 Waveform Generators from National Instruments (NI) are used to provide 100 kHz synchronized square-wave signals to an IQ-mixer that modulates the signal in input of the frequency extender. The signal is modulated in order to avoid high Flicker-noise contributions and therefore increase the dynamic range of the measurement. The signal is still in the presence of Flicker-noise since the $1/f$ corner frequency is estimated to be around 4 MHz. The pseudo-differential output of the detector is amplified using a low-noise instrumentation voltage gain amplifier (VGA) from Analog

Devices (AD8429), set to a gain of 60 dB and subsequently digitized using an NI PXI-5105 ADC. A Fourier transform of the pseudo-differential read-out, ΔV , is then computed and transformed to a voltage spectrum (or power spectral density). The power located at the first harmonic (100 kHz) of the modulation frequency is the signal. The directivity can be calculated directly using the measured ΔV since its magnitude is proportional to the incident power ($\Delta V \propto |E|^2$). The measured and normalized directivity at 400 GHz, is shown in Fig. 5.6(c). The planar scan coordinates (x, y) are translated into the uv-plane w.r.t. the lens. The cuts of the measured and simulated patterns in the main planes are shown in Fig. 5.6(d). A good agreement between measurement and simulation is observed. However, the dynamic range of the measurement is limited to 20 dB or less due to limited Tx output power combined with a lower detector responsivity than expected as is explained in Sec. 5.4.3. A comparison of the simulated directivity across the full band and the measured directivity in the WR-2.2 band is shown in Fig. 5.6(e). In the lower frequencies a ± 1 dB oscillation in directivity can be observed that might be attributed to standing waves in the measurement setup. A better validation of the spectral performance is presented in Chapter 4, by using a verification antenna. That antenna is fully evaluated in terms of gain patterns and input impedance in both the WR3.4 band and WR2.2 with a dynamic range of 40 dB.

Since a radiometer integrates and rectifies power simultaneously over the full frequency band of operation, an appropriate figure of merit in order to evaluate the resolution and

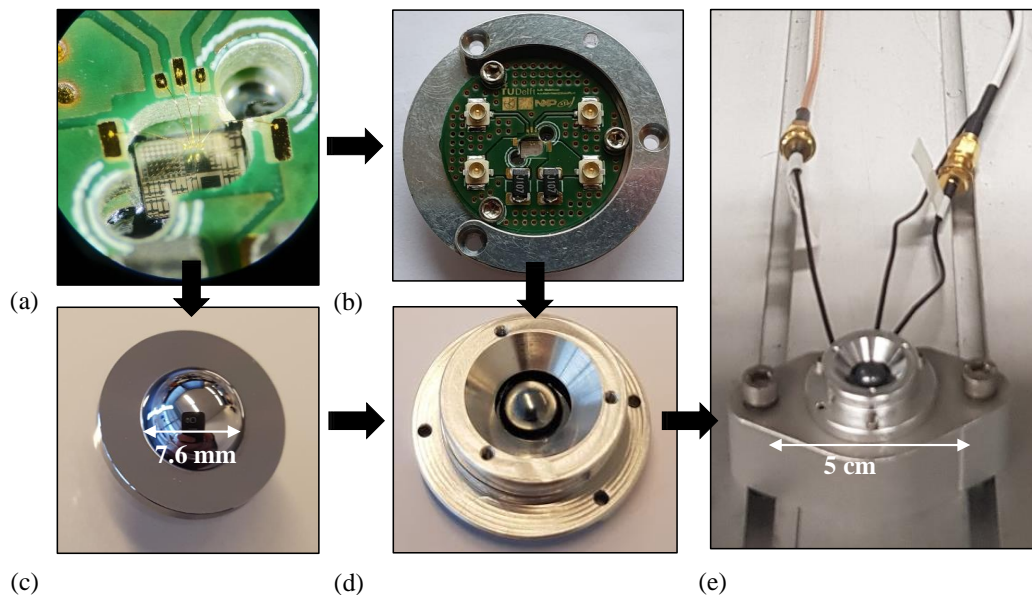


Figure 5.5: THz direct detection system. In (a) the CMOS chip is shown. The read-out and biasing terminals are bond-wired to a PCB (b) and glued to an elliptical silicon lens (c) that is provided with a matching layer. The alignment of the antenna w.r.t. the focal point of the elliptical lens is performed with an alignment hole (also visible in (a)) that is part of a metallic holder for the lens (d). The metallic holder is attached on a fixture that can be attached to the measurement table (e).

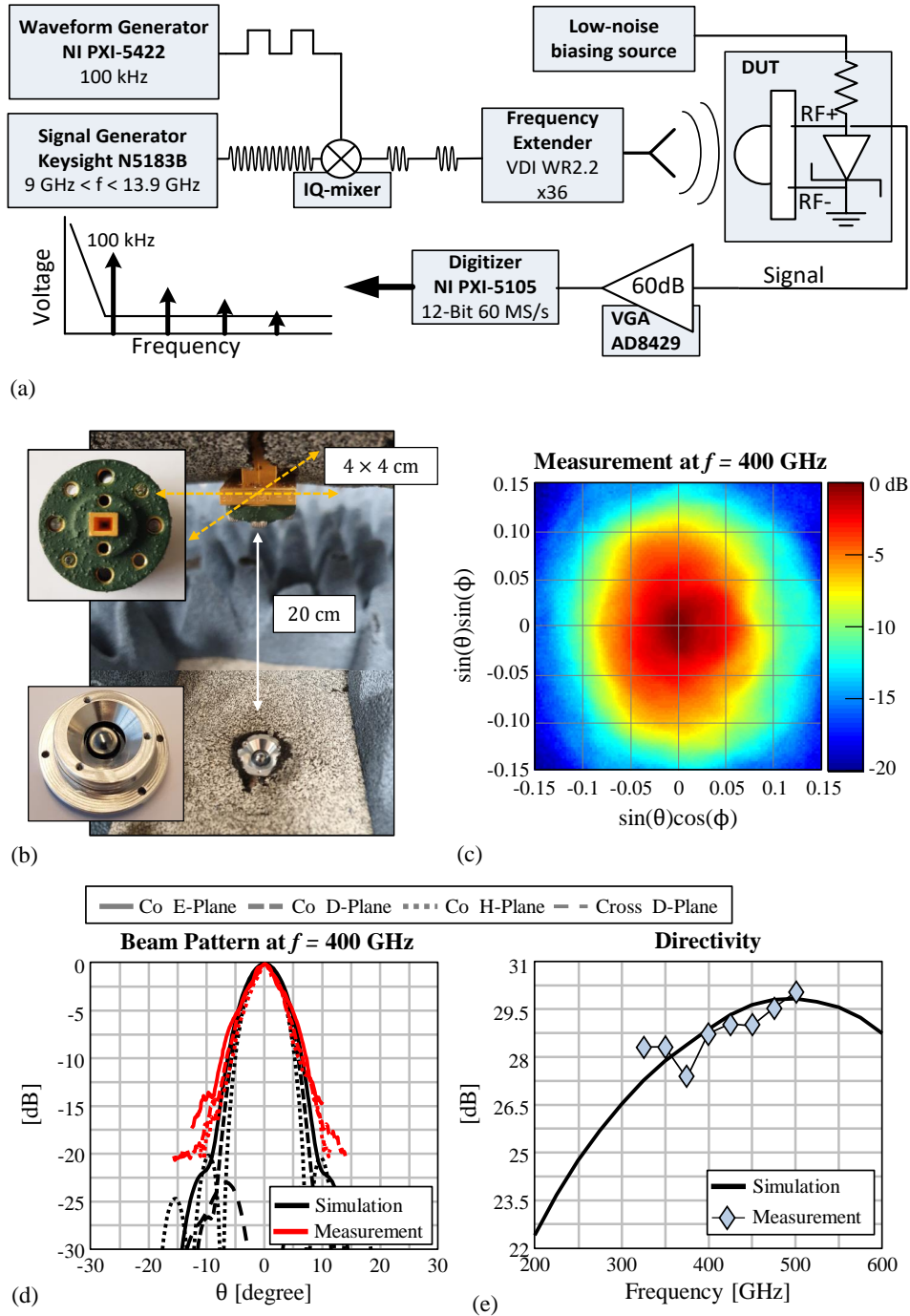


Figure 5.6: Measurement setup and results for the normalized radiation pattern of the THz direct detection system. In (a) a schematic the measurement setup is shown. (b) shows a zoom-in of the DUT and the horn-antenna that is placed in the Fraunhofer region of the lens. In (c) the normalized directivity at 400 GHz is shown while (d) shows the simulated and measured cuts in the main planes. The directivity is shown in (e) over the full frequency band of operation.

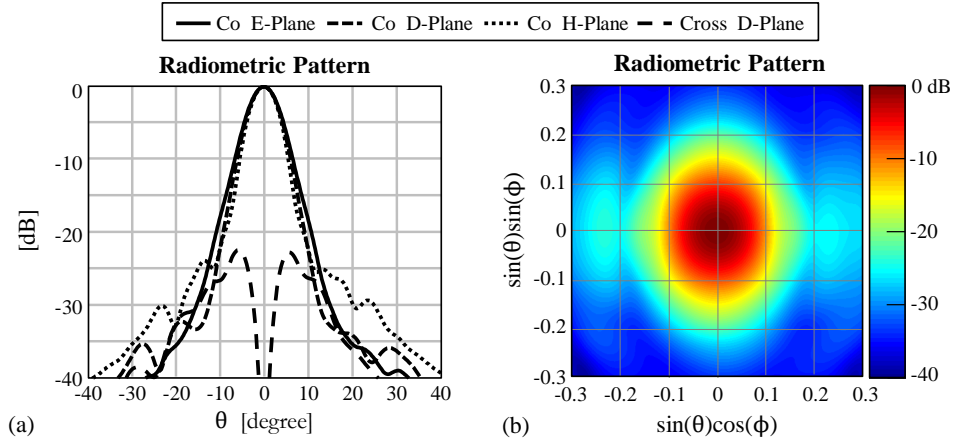


Figure 5.7: Simulated Radiometric Pattern as defined by (5.12).

imaging performance of a radiometer is the effective radiometric pattern, $G_{\text{lens}}^{\text{eff}}$, which can be defined as a spectral integration of the lens antenna gain, G_{lens} , as was equivalently introduced as (2.8b) in Chapter 2:

$$G_{\text{lens}}^{\text{eff}}(\theta, \phi) = \int_{\Delta f_{\text{RF}}} G_{\text{lens}}(\theta, \phi) df \quad (5.12)$$

The simulated radiometric pattern is shown in Fig. 5.7, by using the gain patterns as presented in Chapter 4. The pattern is symmetric and the -10 dB beamwidth is 12° . The radiometric pattern represents the incoherent integration of power by the detector and provides insight in how efficiently a radiometer is integrating power angularly.

5.4.2 Noise Spectral Density

The output noise of the THz direct detector is measured using the setup as illustrated in Fig. 5.8(a). The detector is inserted in a grounded metal can, Fig. 5.8(b), and biased by a battery supplied low-noise 18-bit DAC that is controlled through an SPI interface to avoid additional noise injections during the measurement that is attributed to the supply or the 50/60 Hz powergrid. The pseudo-differential output of the direct detector is again connected to the previously mentioned amplifier after which the output voltage is readout by a SR785 Dynamic Signal Analyzer (DSA) from Stanford Research Systems. The measured power spectral density of the noise at the output of the detector for different biasing voltages ranging from $V_{\text{bias}} = 0$ V to 1.5 V are shown in Fig. 5.8(c). Noise contributions of the measurement setup (measured with shorted LNA inputs) are incoherently subtracted from the raw measurement of the DUT. The frequency range of the measured power spectral densities is limited to 100 kHz since the cut-off frequency of both the DSA and the VGA (set to 60 dBV gain) is at this frequency. The Flicker noise corner can be extrapolated to be approximately at 4 MHz for biasing voltages larger than 1V and therefore, the measurement is still performed in the frequency range where Flicker-noise can be dominant. The

flicker noise of the SBD was not modeled in the provided process design kit (PDK), but a comparison of the analytically calculated (5.8), and by simulation verified white noise level is provided in Fig. 5.8(d) together with the measured noise at 80.36 kHz. In this figure the calculated noise contribution of both shot- and thermal noise, as described by (5.9), are also provided. For bias voltages from 0 to 400 mV there is good correspondence between the measured and calculated white noise level and the analytics clearly match the trend. However, at higher bias voltages frequency limitation of the setup and the increased flicker noise corner prohibited a clean measurement.

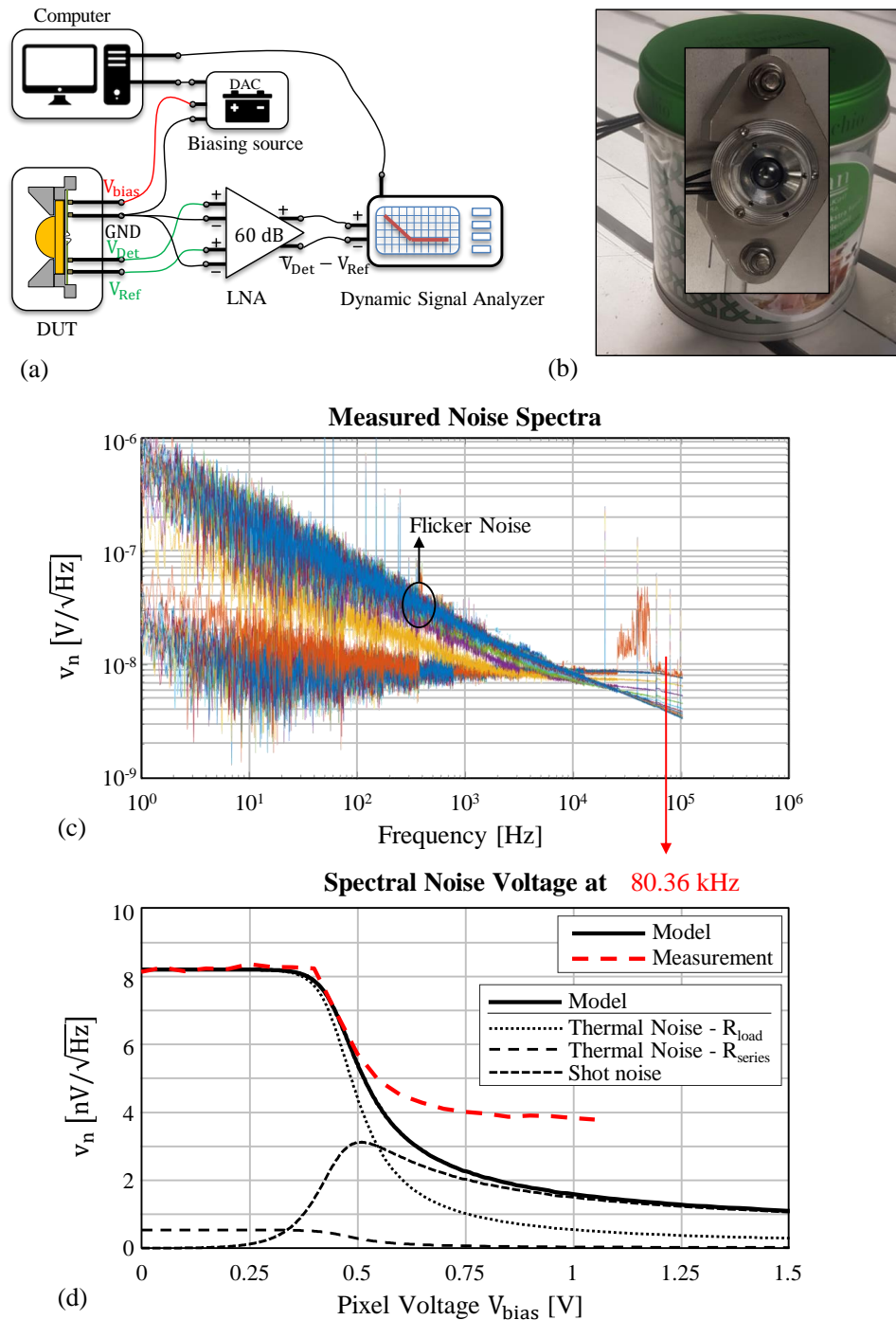


Figure 5.8: Noise measurement of the THz direct detection system. In (a) a schematic of the measurement setup is shown. (b) shows a can in which the DUT from (a) is shielded from noise sources coming from the environment. For different pixel biasing voltages the noise spectrum is measured as is shown in (c). The NEP is defined using the spectral noise in the white noise region of the pixel. The spectral noise voltage is shown in (d) and is compared with simulation. The simulated noise is also decomposed in its different contributions.

5.4.3 Detector Voltage Responsivity

In this section, the detector voltage responsivity (5.7) will be derived from a system voltage responsivity measurement done with the complete THz direct detector. The detector voltage responsivity, $\mathfrak{R}_v^{\text{det}}$ (5.7), describes how well the detection circuit (consisting of the two differential SBDs loaded with a resistor), rectifies the power absorbed in the circuit to a change in DC-voltage over the load resistor, as described by (5.13a). In Fig. 5.9(a), a diagram of the measurement setup is shown. In this setup, a WR2.2 horn antenna is positioned at broad side and 10 cm distance of the THz direct detection system (as shown by the photographic inset in Fig. 5.9(a)). The output response ΔV , after amplification, is measured as function of biasing voltage and frequency. The power in output of the WR2.2 frequency extender, P_{horn} , is measured and shown in Fig. 5.9(b). Friis transmission equation (5.13b) is used to calculate the power that is absorbed by the detector P_{det} . In this manner, the detector voltage responsivity can be calculated as (5.13a), as is done similarly in [74, 77, 94]:

$$\mathfrak{R}_v^{\text{det}} = \frac{\Delta V}{P_{\text{det}}} \frac{1}{G_{\text{VGA}}} \quad (5.13a)$$

$$P_{\text{det}} = \frac{P_{\text{horn}}}{4\pi r^2} G_{\text{horn}} G_{\text{lens}} \eta_{\Omega} \frac{\lambda^2}{4\pi} \quad (5.13b)$$

In (5.13), G_{VGA} is the 60 dBV voltage gain amplification, G_{horn} and G_{lens} are the gain of the horn-antenna and lens antenna, as shown in Fig. 5.9(c), together with the path loss $L = (\lambda/4\pi r)^2$. The impedance matching efficiency of the antenna-detector combination, η_{Ω} , is not yet included in the gain since it is also a function of biasing voltage, but instead it is explicitly included in Friis transmission equation. The raw measurement, after amplification, is shown in Fig. 5.9(d), leading to the detector responsivity as is shown in Fig. 5.10(a) as function of pixel biasing voltage and frequency. The average voltage responsivity, over the full WR2.2 band, as defined by (5.14), is shown in Fig. 5.10(c) with the blue curve and is compared with the model (black curve).

$$\overline{\mathfrak{R}_v^{\text{det}}} = \frac{1}{175 \text{ GHz}} \int_{325 \text{ GHz}}^{500 \text{ GHz}} \mathfrak{R}_v^{\text{det}}(f) df \quad (5.14)$$

In Fig. 5.10(c), a significant discrepancy between simulation and measurement is observed. The gain and impedance of the double leaky slot antenna, which are used to post-process the raw measurement (5.13b), are already validated in Chapter 4 by means of a verification antenna in absence of the detector. To verify the expected operation of the detector, several structures were fabricated alongside the THz direct detector and verification antenna. These consisted of several SBDs embedded in a SOLT/TRL compatible calibration/de-embedding fixture and the accompanying standards, which together allows for a device characterization at the terminals, conceptually similar to [138], from DC to the WR-2.2 waveguide frequency band. The extraction procedure used to characterize

the SBD from DC to 10 GHz is presented in Appendix E. This frequency range proved to provide sufficient accuracy to predict the measured performance of the combined pixel up to the WR2.2 frequency band and showed that the discrepancy between simulation and measurement can be attributed to a difference in the series resistance and junction capacitance of the SBD.

Updated Diode Model

Fig. 5.10(b) shows the calculated detector voltage responsivity (5.7), as function of frequency and biasing voltage after the refinement of the SBD model that followed from the stand-alone SBD characterization. Comparing to the measured responsivity in Fig. 5.10(a), one can observe that a good correlation between model (5.7) and measurement (5.13) is achieved. This becomes more apparent in Fig. 5.10(d) where cuts at 330 GHz and 475 GHz, and the average detector voltage responsivity (5.14) over the WR2.2 frequency band, are shown for both the model and the measurement. The discrepancy in responsivity between the initial model and the refined model is attributed to the efficiency of the diode. The stand-alone SBD characterization showed that the series resistance to be around 135 Ω in comparison to the 10 Ω obtained in simulation, while the junction capacitance of the diode increased from 8 fF to 20 fF. The series resistance and junction capacitance are the main parasitic elements of a SBD that decreases high-frequency performance. Only power that is absorbed in the junction of the SBD contributes to rectification. This is elaborated in Appendix D, where the power that is absorbed in the junction can be described by defining a diode efficiency, i.e. a power transfer efficiency (D.16) to the junction that depends on the effective series dynamic junction resistance and the series resistance. A higher series resistance implies more losses whereas the effective series dynamic junction resistance decreases quadratically proportional with the junction capacitance (D.15). The diode is now operating far beyond its cut-off frequency of $f_T = 1/(2\pi \cdot R_{\text{series}} \cdot C_j) = 60$ GHz versus 2 THz as predicted by the original model. This formula is only valid for $R_{\text{series}} \gg R_j$ [93, 139]. The diode efficiency, for the original and updated models, are shown in Fig. 5.11(a) and Fig. 5.11(b) respectively, for the full frequency band of operation. It can be seen that the junction of the diode is barely capable of rectifying the RF-signal and the diode has less than a few percent of efficiency for frequencies higher than 400 GHz.

Despite the degraded performance in measurements, the system model obtained after the standalone SBD characterization proved to be extremely accurate in predicting the detector voltage responsivity over a large frequency band, once the actual series resistance and junction capacitance were known. Such model then allows for accurately determining both NEP and temperature sensitivity of the system.

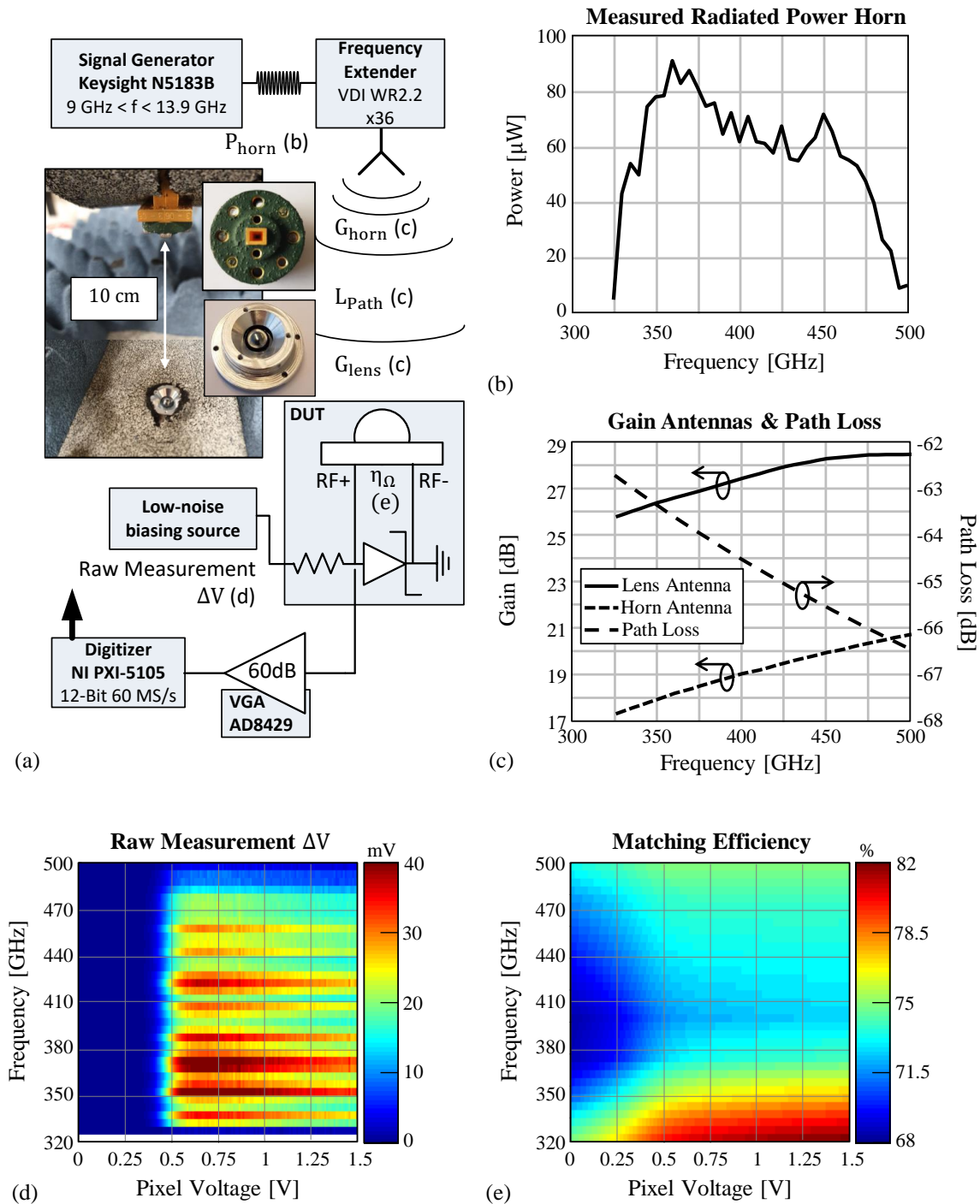


Figure 5.9: In (a) the measurement setup is shown. A WR2.2 horn antenna, placed 10 cm from the DUT, radiates P_{horn} Watt (b). The gain of the horn, the lens antenna and path loss are shown in (c). The antenna-detector matching efficiency (of the updated model) is shown in (e) as function of biasing voltage and frequency. The raw measurement, after a 60 dB VGA, is shown in (d). The measurement results are shown in Fig. 5.10.

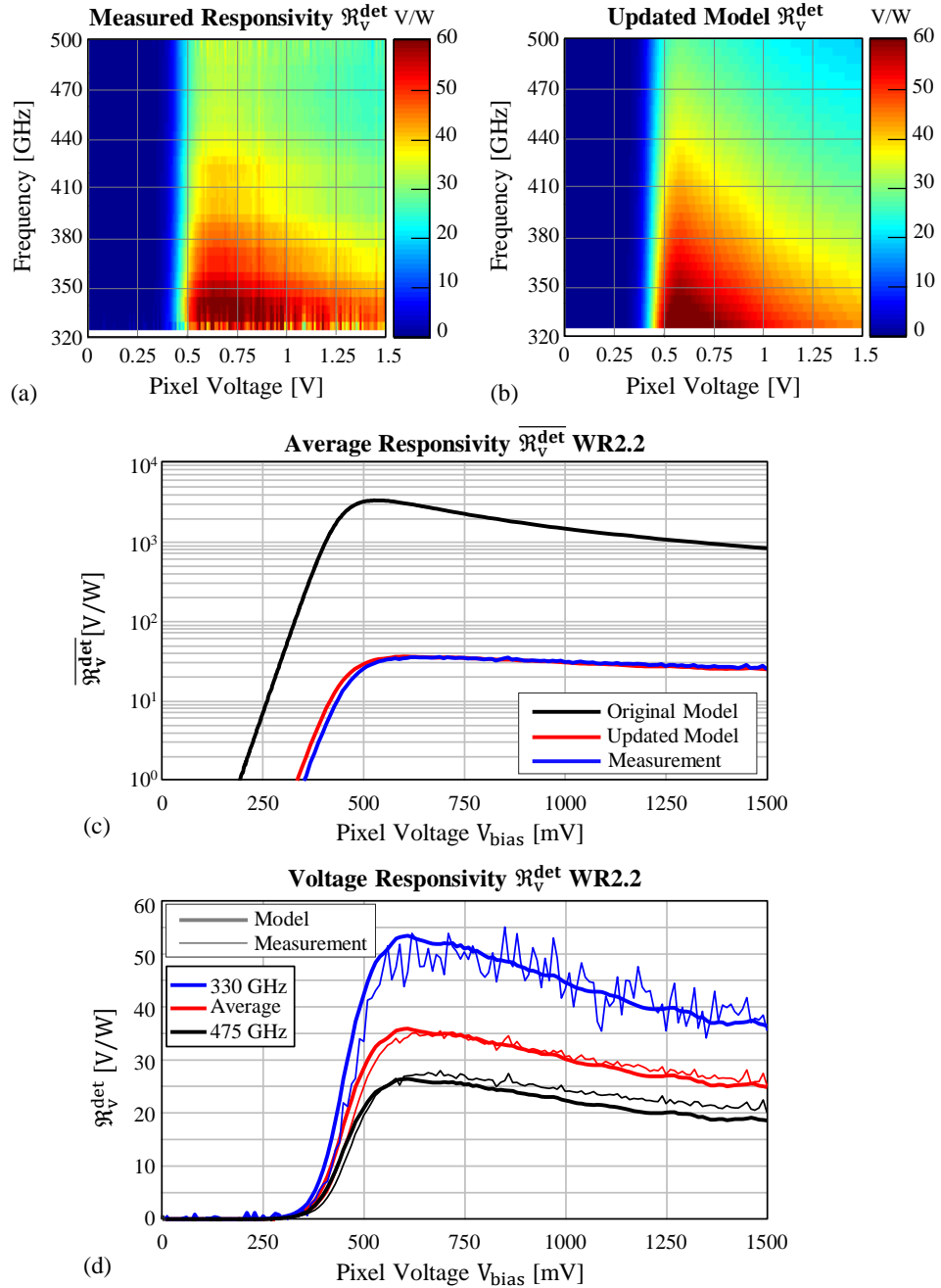


Figure 5.10: Measurement results of the voltage responsivity measurement from Fig. 5.9 are shown. By using Friis equation (5.13), the measured responsivity of the detector (5.7) is calculated as (a). An updated diode model, extracted from low-frequency measurements on the standalone SBD as presented in Appendix E, results in a good match with measurement. A 2D-plot of the updated model is shown in (b). The measured voltage responsivity, averaged over the WR2.2 band, is shown in (c) together with the original model and updated model. The cuts at 330 GHz and 475 GHz and the WR2.2 frequency averaged are shown in (d) for the measurement and updated model. The lower detector voltage responsive is attributed to a lower power transfer efficiency as shown in Fig. 5.11.

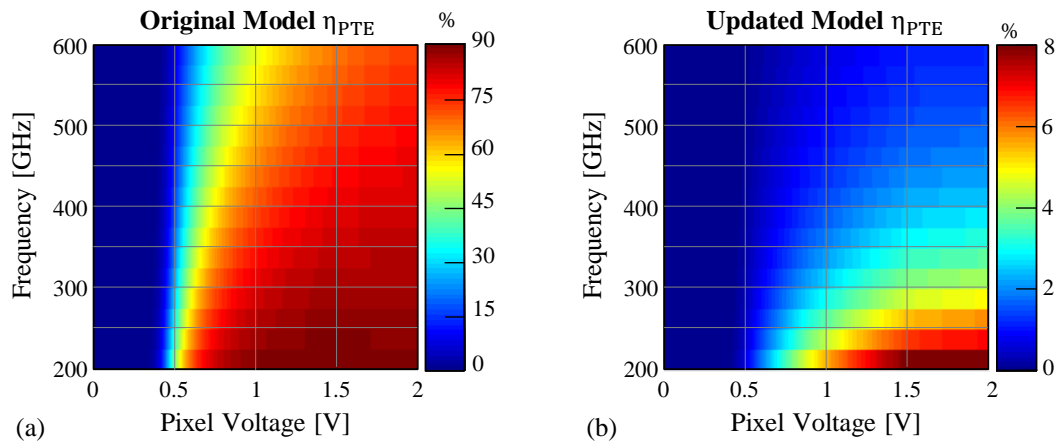


Figure 5.11: Diode power transfer efficiency. The lower detector voltage responsive reported in Fig. 5.10 is attributed to a lower power transfer efficiency to the junction of the diode, caused by a higher series resistance ($135\ \Omega$ instead of $10\ \Omega$) and junction capacitance ($20\ \text{fF}$ instead of $8\ \text{fF}$). (a) Original Model, (b) Updated model.

5.4.4 Noise Equivalent Power and Temperature Sensitivity

A proper figure of merit to evaluate the performance of a THz imager is the system NEP (5.4a) and, in the case of passive imaging applications, the temperature sensitivity (5.3). In the previous section, the system model is validated by means of measurements in the WR2.2 frequency band. In Fig. 5.12, the modeled performance in the complete frequency band of operation, from 200 GHz to 600 GHz, is shown. The system NEP, in single-ended voltage read-out, is shown in Fig. 5.12(a) at 200 GHz, 600 GHz and averaged over the full frequency band. The optimal NEP, at $V_{\text{Bias}} \approx 1.5\ \text{V}$, is shown in Fig. 5.12(b) as function of frequency for as well the original model and the updated model. Note that the minimum NEP is not at the peak of detector responsivity since the spectral voltage noise decreases further with increasing biasing voltage, as shown in Fig. 5.8(d). The NEP is at minimum at 200 GHz with $\text{NEP} = 20\ \text{pW}/\sqrt{\text{Hz}}$. An average NEP, averaged over the full frequency band, of $\overline{\text{NEP}}_{\text{sys}} = 90\ \text{pW}/\sqrt{\text{Hz}}$ is extracted, w.r.t. a $\overline{\text{NEP}}_{\text{sys}} = 2.7\ \text{pW}/\sqrt{\text{Hz}}$ predicted by the library model.

From the average system NEP, the temperature sensitivity (5.3) can be predicted as shown in Fig. 5.12(c). It can be seen that sub-Kelvin imaging capabilities could be achieved for NEPs of only a few $\text{pW}/\sqrt{\text{Hz}}$. The measured NEP is significantly higher, which is attributed to the higher series resistance of the diode as well as a higher junction capacitance. Unfortunately, the measured NEP does not facilitate real-time passive imaging scenarios in the THz regime, which requires a sub-Kelvin temperature sensitivity [55]. The predicted NETD of state-of-the-art THz imagers is shown in Table 5.1. The original diode model would have suggested a temperature sensitivity of 350 mK at 1 Hz refresh rate. Instead, the updated model predicts an $\text{NETD} = 12\ \text{K}$. Although passive THz imaging with sub-Kelvin temperature sensitivity is yet unprecedented, the high accuracy in predicting the system NEP over a large frequency band is vital for future passive imaging applications. The

recently presented state-of-the-art performance in NEP of NMOS transistors in differential mode [77], fabricated in the same technology as the prototype in this chapter, suggests to extend the model for this type of detector.

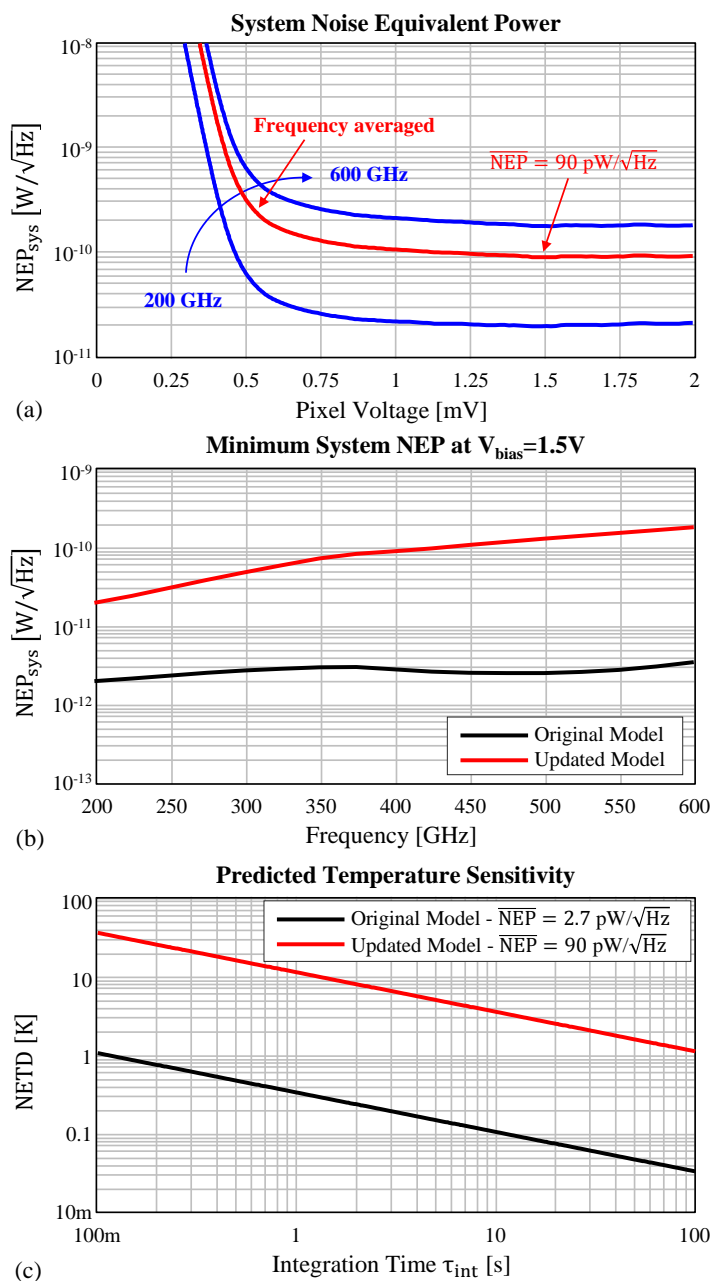


Figure 5.12: Radiometric performance. The system NEP is shown in (a). The NEP at optimal biasing condition, as function of frequency is shown in (b) for as well the original model as the updated model. The predicted temperature sensitivity, as function of detector integration time, is shown in (c). A system NEP of only a few pW/ \sqrt{Hz} , in combination with 400 GHz of absolute bandwidth, would facilitate real-time passive imaging scenarios in the THz regime.

Table 5.1: State-of-the-art THz Imagers in CMOS with predicted Temperature Sensitivity

Reference	CMOS Technology	Detector Architecture	Frequency (Bandwidth)	Min. System NEP (Frequency average)	Predicted NETD at 1 Hz refresh rate
[52]	65-nm	NMOS Differential in voltage mode	790 - 960 GHz (20% fractional) ⁱ	100 pW/ $\sqrt{\text{Hz}}$ (110 pW/ $\sqrt{\text{Hz}}$) ⁱⁱ	33 K
[95]	65-nm	MOSFET Differential in voltage mode	650 - 970 GHz (40% fractional)	14 pW/ $\sqrt{\text{Hz}}$ (30 pW/ $\sqrt{\text{Hz}}$) ⁱⁱ	5 K
[74]	130-nm	SBD in voltage mode	280 GHz (6% fractional) ⁱⁱⁱ 860 GHz (6% fractional) ⁱⁱⁱ	29 pW/ $\sqrt{\text{Hz}}$ (50 pW/ $\sqrt{\text{Hz}}$) 42 pW/ $\sqrt{\text{Hz}}$ (100 pW/ $\sqrt{\text{Hz}}$)	151 K 107 K
[94]	130-nm	Diode-connected NMOS in voltage mode	810 - 850 GHz (5% fractional) ⁱⁱⁱ	12.6 pW/ $\sqrt{\text{Hz}}$ (36 pW/ $\sqrt{\text{Hz}}$)	46 K
[77]	22-nm FD-SOI	nFET Differential in voltage mode nFET Differential in current mode	0.7 - 1 THz (35% fractional) —	22.65 pW/ $\sqrt{\text{Hz}}$ (30 pW/ $\sqrt{\text{Hz}}$) ⁱⁱ 12 pW/ $\sqrt{\text{Hz}}$ (-) ^{iv}	5 K (-) ^{iv}
This work	22-nm FD-SOI	SBD Differential in voltage mode	200 - 600 GHz (100% fractional)	20 pW/ $\sqrt{\text{Hz}}$ (90 pW/ $\sqrt{\text{Hz}}$)	12 K

ⁱ Reported 3-dB bandwidth.

ⁱⁱ Mean NEP is not reported, but estimated from the reported figures in the reference.

ⁱⁱⁱ Bandwidth is taken as the frequency span of the measurements and figures as they are reported in the reference.

^{iv} Mean NEP is not reported and no figures are available in the reference to estimate the mean NEP.

5.5 Conclusion

The radiometric modeling and performance of a THz direct detection system, developed for the purpose of passive THz imaging applications is presented. The system consists of a recently developed double leaky slot lens antenna that efficiently couples radiation from 200 GHz to 600 GHz to a differential detector circuit composed of Schottky Barrier Diodes (SBDs). A derivation of the temperature sensitivity, as function of spectral Noise Equivalent Power, is presented, based on the equivalent circuit model of a SBD. The model is constructed from measurements on a standalone SBD, i.e. the IV-curve and reflection coefficient at 10 GHz and an accurate antenna modeling. These SBD low frequency measurements indicated a discrepancy in the series resistance ($135\ \Omega$ vs $10\ \Omega$) and junction capacitance ($20\ \text{fF}$ vs $8\ \text{fF}$) with respect to the models provided by the process design kit. Using the proposed wideband system analysis procedure, the voltage responsivity of the direct detector, that includes antenna efficiency, antenna-detector impedance matching and detector circuit performance, was predicted in excellent agreement with the measurements. This work provides an accurate modeling approach for double leaky slot antenna-coupled SBDs placed in a differential configuration and proving a necessary step towards the realization of future passive THz imaging applications.

Chapter 6

Tightly Sampled Leaky-Wave Connected Array with Polarization Re-Usage

In multi-beam systems, the performance of a single-beam-per-feed configuration is limited in edge of coverage gain due to either a low roll-off at the cross-over with adjacent beams or a low aperture efficiency of the lens/reflector. A tight sampling of the feeds in the focal plane, required for a high angular resolution and a low roll-off, is directly imposing a limit on the feed directivity and thus the overall gain of the quasi-optical system. In this chapter, an enhanced feed directivity is realized by resorting to a connected array configuration, supporting a leaky-wave in the presence of a dielectric lens. The dipoles of the array are tapered with a 45° angle such that the amount of pixels is doubled by using the orthogonal polarization. In this manner, a minimum loss in edge of coverage gain of only -5.4 dB is realized w.r.t. the maximum directivity when the considered aperture would have a 100% aperture efficiency. This is an increase of 2.5 dB w.r.t. an equivalently sampled FPA of uniformly illuminated circular apertures. Moreover, the large 3:1 relative bandwidth from 200 GHz to 600 GHz, makes the array very suitable for future passive THz imaging applications. As demonstrator, twelve pixels of the array are connected to Schottky Barrier Diodes to realize a direct detection scenario. The array is integrated in the same 22-nm CMOS technology as the THz direct detector discussed in the previous chapter. Measurements of the prototype will be presented in the paper J1 listed on page 183. This chapter presents the design and simulated performance of the array.

6.1 Introduction

Multi-beam capabilities in quasi-optical systems are useful for different types of applications, varying from millimeter-wave (mmwave) automotive radar [140, 141], sub-mmwave imaging systems [142], satellite telecommunication systems [143, 144] and beyond 5G systems [145, 146]. In all these applications, there is the need for generating a large number

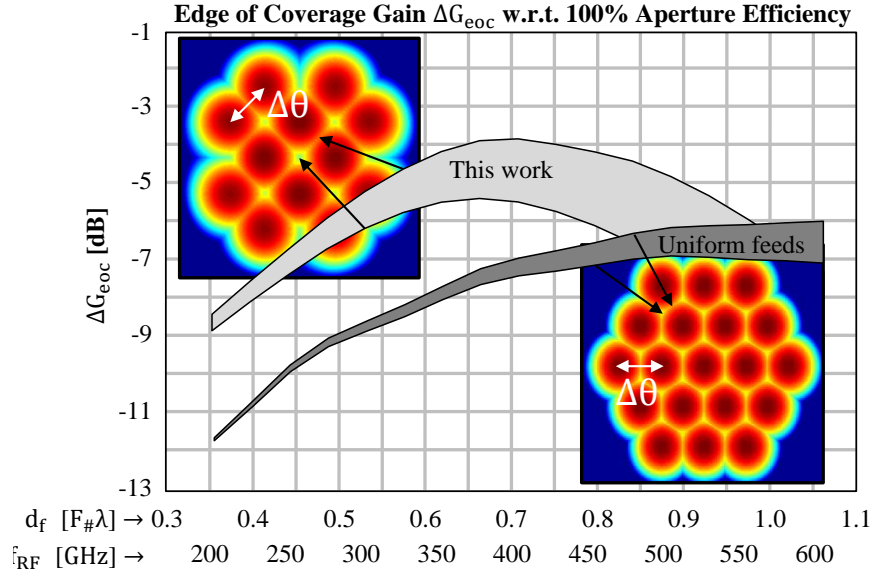


Figure 6.1: Edge of Coverage Gain, ΔG_{eoc} (6.2). The ΔG_{eoc} is shown for an hexagonal grid of uniformly illuminated aperture feeds that illuminate a reflector system by the darker gray bar as well as the ΔG_{eoc} performance of the proposed FPA in combination with a dielectric lens with $F\# = 0.65$ by the lighter gray bar. The bottom side of the bars represent the loss in edge of coverage for the least covered spot in the FPAs and the top-side represent the best case beam cross-over. The proposed array is operating from 200 GHz to 600 GHz.

of high gain beams to cover a certain Field-of-View (FoV). A higher beam-spot density of the system allows for a higher number of independent links in a communication scenario, as well as higher angular resolutions in imaging scenarios.

The most elegant and simplest solution for multi-beam generation is by using a single aperture (lens or reflector) in combination with a single-beam-per-feed focal plane array (FPA) configuration. In single-beam-per-feed configurations, the sampling periodicity of a FPA directly determines the angular separation of the beams, but also limits the efficiency of the system due to higher spill-over losses associated with smaller feed sizes. Moreover, the sampling also impacts the gain at the cross-over between adjacent beams, which is typically referred as edge of coverage gain (G_{eoc}) in a multi-beam communication scenario. For this scenario, the gain at this point should be maximized in order to avoid blind spots. However, the gain of coverage obtained in a single-beam-per-feed FPA of uniform feeds is too low for most of the applications. For instance, a FPA placed in the focal plane of a lens/reflector with diameter D and focal distance F , with a feed sampling periodicity of $d_f = \lambda F/D$ will lead to a ΔG_{eoc} of -7 dB with respect to the maximum achievable directivity of the considered aperture, i.e. a diffraction limited case. Any other sampling leads to comparable or worse ΔG_{eoc} due to the intrinsic trade-off between spill-over and beam gain cross-over. Fig. 6.1 summarizes the obtained ΔG_{eoc} in an ideal uniform feed scenario versus the sampling condition (or versus the equivalent frequency range in this work). Therefore, in many communications systems, the traditional approach

is to use multiple apertures combined with single-beam-per-feed arrays [147, 148]. In this solution, multiple apertures with frequency and/or polarization discrimination are used in an interleaved configuration to increase the edge of coverage gain. An equivalent solution is to over-dimension a single aperture [149] with a comparable dimension to that of four independent ones. Another, more complex, option is to use beam-forming networks to use multiple-feeds-per-beam [150, 151, 152]. However, losses in these beam-forming networks will be comparable to the losses in spillover. Similarly, the use of aperiodic active lenses has been studied in [153], where power amplifiers compensate spillover and mismatch losses.

In an incoherent imaging scenario, the sampling periodicity should, theoretically, be $d_f = 0.5\lambda F/D$ in order to achieve a diffraction limited angular resolution with a beam separation of $\Delta\theta^{\text{lim}} = \lambda/(2D)$ [111].¹ Therefore, the achieved gain of the quasi-optical system will be extremely low due to the very high spill over loss. Typically, imaging cameras are then designed to have very high sensitivities, compensating the quasi-optical system losses [154], or more commonly, undersampled arrays are combined with scanning mechanisms in order to achieve the desired resolution [31]. Furthermore, the resolution can be compromised via non-diffraction limited cameras [52, 60] where the patterns presented in [142] show a beam roll-off of approximately -7 dB while the beam roll-off of [52] is presented in [83] to be around -3 dB.

In this chapter, the goal is to maximize the directivity of the feeds of tightly sampled FPAs ($d_f \leq 1F_{\#}\lambda$ with $F_{\#} = F/D$) by using an array configuration with overlapping feeds. The array targets imaging applications in the submm-wave regime of the electromagnetic spectrum. In Chapter 3, a case-study was presented of pedestrian detection for the automotive industry. There, it was shown that tightly sampled arrays of $1F_{\#}\lambda$ are desired to achieve sufficient resolution. Here, the design of a 12-pixel THz FPA, containing a connected array of dipoles, supporting a leaky-wave in the presence of a dielectric lens, is presented. The high directivity of the feeds results in an efficiency that is significantly higher w.r.t. the uniform aperture feeds that were used in the analysis in Chapter 3. The increased directivity allows for tightly sampling the array to maximize in resolution while maintaining a high efficiency. Furthermore, the resolution is even more improved, near to the diffraction limit, by efficiently using the array in two polarizations. A micrograph of the fabricated prototype array is shown in Fig. 6.2.

This chapter is structured as follows. In Sec. 6.3, first a generalized geometry of a quasi-optical system consisting of a dielectric lens in combination with a FPA is introduced. From there, the considered figure of merit, ΔG_{eoc} , is introduced and analyzed for a benchmark array consisting of uniform illuminated circular apertures in a hexagonal grid. Then, in Sec. 6.4, the mutual coupling losses in a tightly sampled connected array configuration is studied for different architectures. The preferred architecture, a connected array with tapered dipoles that utilizes two polarizations, is optimized in Sec. 6.5 in combination with a dense dielectric lens, where the $F_{\#}$ determines the physical periodicity as well as the truncation angle of the primary fields. Finally, Sec. 6.6, presents the simulated

¹The diffraction limited resolution of λ/D is achieved with a beam separation of $\Delta\theta^{\text{lim}} = \lambda/(2D)$, according to Nyquist theorem as was discussed in Chapter 2 and shown in Appendix A.

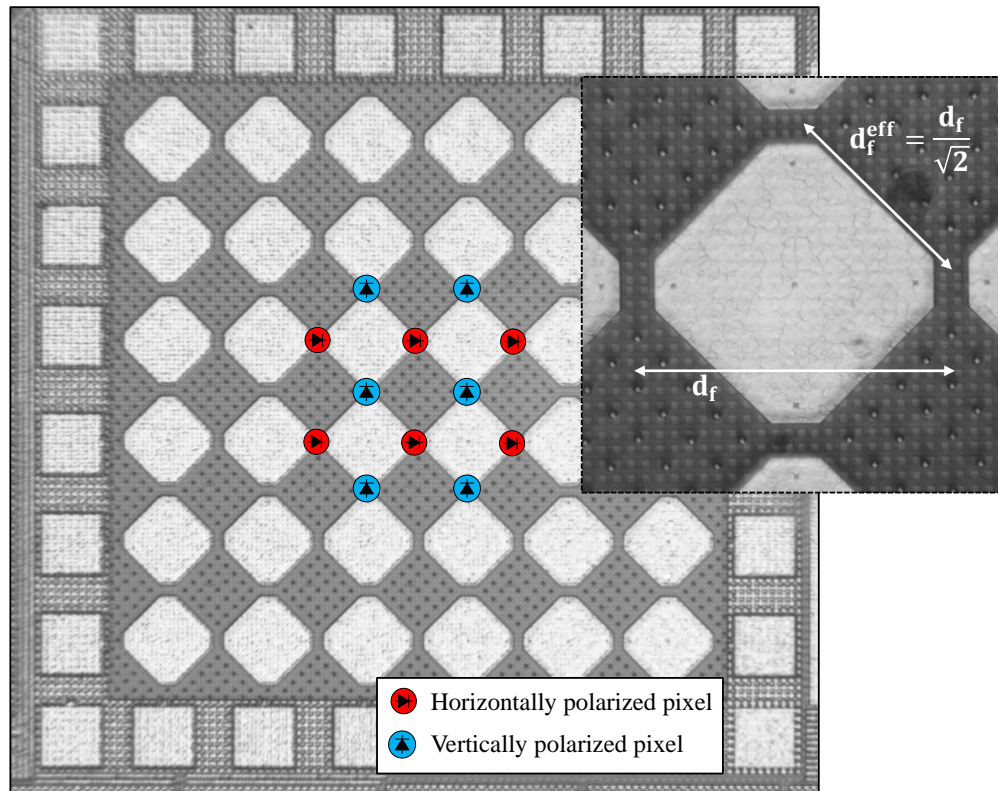


Figure 6.2: A micrograph of the proposed Focal Plane Array, integrated in a CMOS process, is shown. The FPA is based on a connected array of tapered dipoles that supports a 2×3 horizontally polarized array interleaved with a 3×2 vertically polarized array.

performance of the 12-pixel prototype, integrated in a 22-nm FD-SOI CMOS technology, in terms of patterns and edge of coverage gain. Measurements of the prototype, of which a micrograph is shown in Fig. 6.2, will be presented in the paper J1 listed on page 183.

6.2 Leaky-Wave Enhanced Feeds

In this work the goal is to maximize the directivity of the feeds of tightly sampled FPAs ($d_f \leq 1F_{\#}\lambda$ with $F_{\#} = F/D$) by using an array configuration with overlapping feeds. Overlapped feeds are characterized by an effective area that is larger than the physical area associated with the FPA feed, according to the sampling periodicity. This kind of feeds can be achieved by means of leaky-wave type of antennas. This increase in directivity was first identified for an antenna that was placed in close proximity of a partially reflecting screen that allowed for a lateral propagating wave between the antenna plane and reflecting screen [155] which was later characterized as leaky-wave radiation [156]. Using this kind of leaky-wave feeds, as presented in [143,157,158], the gain at the edge of coverage with respect to the diffraction limited directivity can be increased by about 1 dB to 2 dB with respect

to the uniform feeds shown in Fig. 6.1. However, these leaky-wave antenna solutions are based on resonant leaky TE/TM-modes with multiple bounces in a half-wavelength cavity and is therefore an intrinsically narrowband solution, i.e. with fractional bandwidth of 10% or smaller.

Leaky-wave radiation can be generated over an ultra-wide bandwidth in the case of long slots printed in between two infinite media [159]. This radiation can be further enhanced by introducing an electrically small air cavity between the slot and the dense medium [114]. In [65,67], it was shown that this radiation can be combined with a connected array configuration to generate tightly sampled FPAs feeding a dense dielectric lens. This work builds on this concept to design a FPA architecture capable to achieve low ΔG_{eoc} , over a wide bandwidth, by exploiting dual polarized feeds in a connected checkerboard architecture. A micrograph of the fabricated prototype is shown in Fig. 6.2. The tightly sampled connected array is geometrically symmetric in the two orthogonal planes and therefore will support a 2×3 horizontally polarized array interleaved with a 3×2 vertically polarized array. The interleaved rectangular grids effectively reduces the sampling periodicity by a factor of $1/\sqrt{2}$. In Fig. 6.1, the theoretical achievable ΔG_{eoc} over a large relative bandwidth of 3:1 is shown, where the ΔG_{eoc} is indicated in the the main- and diagonal planes of the array. The array features a G_{eoc} that is more than 2.54 dB higher than for ideal feeds when operating with diffraction limited resolution.

6.3 System Parameters and Statement of the Problem

Consider the quasi-optical system as shown in Fig. 6.3, where a FPA is placed in the focal plane of a dielectric lens that is characterized by a focal distance F and effective diameter D . The elements in the focal plane are separated with a sampling periodicity of d_f . The sampling periodicity and focal number determine the angular separation of adjacent beams, $\Delta\theta$. The general relationship between angular resolution and sampling of the antenna feeds, d_f , can be approximated as:

$$d_f = N \cdot 0.5F_{\#}\lambda_d \iff \Delta\theta = N \cdot \Delta\theta^{\text{lim}} \quad (6.1)$$

, where $F_{\#} = F/D$ is the focal number of the optics, $\lambda_d = \lambda_0/\sqrt{\epsilon_r}$ is the wavelength in the dielectric and N is the undersampling factor. For $N = 1$, the array is fully sampled and a diffraction limited resolution, $\Delta\theta^{\text{lim}} = \lambda_0/(2D)$, is achieved in an incoherent imaging scenario. Let us study a focal plane architectures consisting of ideal, electrically large, circular uniform aperture feeds that are placed in a hexagonal grid in the focal plane. The angular resolution (6.1) for the traditional sampling configurations $N = 1, 2, 4$ are summarized in Table 6.1.

Furthermore, Table 6.1 also shows the roll-off at $\theta = \Delta\theta/\sqrt{3}$ (i.e. the least covered point in an hexagonal grid) and approximated aperture efficiencies in terms of spillover and tapering. No (ohmic) dissipation losses are yet included in this approximation. Table

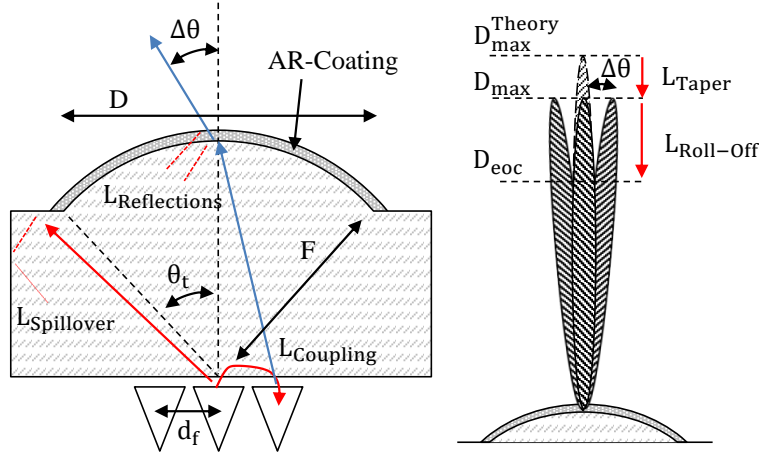


Figure 6.3: Generic quasi-optical system where a FPA, with sampling periodicity d_f , is placed in the focal plane, with focal distance, F , of a dielectric lens with diameter D . The beams of adjacent feeds after the lens are separated by $\Delta\theta$. The difference in gain at the edge of coverage, ΔG_{eoc} (6.2), w.r.t. the maximum gain of the lens with a 100% aperture efficiency, $D_{\text{max}}^{\text{Theory}} = (\pi D/\lambda)^2$, depends on the losses due to mutual coupling, L_{Coupling} , spillover within the lens, $L_{\text{Spillover}}$, reflections at the lens interface, $L_{\text{Reflections}}$, tapering efficiency of the lens surface, L_{Taper} , and roll-off at the cross-over, $L_{\text{Roll-Off}}$.

Table 6.1: Feed Sampling Trade-Off in Efficiency and Resolution for a Uniform Aperture Feed

Feed size	Resolution	Roll-Off	Spillover	Taper
d_f [m]	$\Delta\theta$ [rad]	$L_{\text{Roll-Off}}$ [dB]	$L_{\text{Spillover}}$ [dB]	L_{Taper} [dB]
$0.5F_{\#}\lambda_d$	$\lambda/(2D)$	0.91	8.16	0.00
$1F_{\#}\lambda_d$	λ/D	3.65	3.27	0.04
$2F_{\#}\lambda_d$	$2\lambda/D$	13.18	0.81	0.80

6.1 clearly shows the impact of choosing the sampling periodicity in both resolution and efficiency. A valid figure of merit in the comparison of different focal plane architectures is the summation of these parameters, as it represents the difference in gain in the edge of coverage, ΔG_{eoc} , compared to the maximum directivity that could be achieved theoretically with a 100% aperture efficiency:

$$\Delta G_{\text{eoc}} = -L_{\text{Taper}} - L_{\text{Coupling}} - L_{\text{Roll-Off}} - L_{\text{Spillover}} - L_{\text{Reflections}} \quad (6.2)$$

where the loss contributions are visualized in Fig. 6.3 consisting of the losses due to mutual coupling, L_{Coupling} , spillover within the lens, $L_{\text{Spillover}}$, reflections at the lens interface, $L_{\text{Reflections}}$, tapering efficiency of the lens, L_{Taper} , and roll-off, $L_{\text{Roll-Off}}$. The edge of coverage gain, for the considered hexagonal grid with uniform illuminated apertures and as function of sampling periodicity and frequency, is shown in Fig. 6.1 by the dark gray bar, where the conservative (bottom) side of the gray bar represents the least covered spot in a hexagonal grid ($\theta = \Delta\theta/\sqrt{3}$) while the top side represents the cross-over between two adjacent beams ($\theta = \Delta\theta/2$). Mutual coupling between the electrically large apertures is considered to be

negligible. For realistic feeds, a high overlap of adjacent beams in a multi-beam system, inevitably gives rise to higher mutual coupling between the feeds [160] and will be taken as a loss factor. Note that for larger sampling periodicity, $d_f > 1F_{\#}\lambda_d$, a horn antenna with a tapered field distribution over its feed aperture will result in a slightly higher aperture efficiency.

In this work, we focus on tightly sampled array configurations (i.e. $d_f \leq 1F_{\#}\lambda_d$ at the center frequency) that operate efficiently over a large operational bandwidth from 200 GHz to 600 GHz (relative bandwidth of 3:1). Such array would enable future passive THz imaging applications while simultaneously near-diffraction limited resolutions are achieved as discussed in Chapter 2.

6.4 Mutual Coupling in Tightly Sampled Connected Arrays

Tightly sampled arrays in a single-feed-per-beam scenario are beneficial for realizing closely separated beams. Unfortunately, a high coupling between the adjacent beams inevitably implies a high mutual coupling between the individual feeds [160]. Mutual coupling between individual feeds can not only be considered as a power dissipation loss, but, in the case of non-perfectly matched loads, can also significantly affect radiation patterns due to destructive interference of re-radiated power. Indeed, in [161] it is investigated that, in the case of a densely packed hexagonal array in the presence of a high permittivity superstrate, a -20 dB coupling to the neighboring element is a good trade-off between mutual coupling losses and spill-over. The mutual coupling for a connected array of slots in close presence of a dielectric lens [67] is investigated in [65] for different physical sampling periodicity. In [65], a physical sampling periodicity of $\lambda_0/3$ is chosen at the lowest frequency, which constitutes approximately 0.5 dB of mutual coupling losses thanks to the leaky-wave nature of the array. With this choice of sampling periodicity, however, one is trading off either in angular resolution and beam roll-off, as in [65], or a lens with a larger $F_{\#}$ should be used that will truncate the primary fields and therefore could lead to high spill-over losses. This trade-off, between mutual coupling and spill-over losses, will be presented in Sec. 6.5. Here, the mutual coupling losses will be studied as function of frequency (and thus sampling periodicity in terms of wavelength) from 200 GHz to 600 GHz for a tightly sampled array (i.e. $\lambda_0/5.3$ at 400 GHz).

The different array configurations considered, are shown in Fig. 6.4. In Fig. 6.4(a) the stratification is shown, which is a simplified version of the CMOS stratification in which the prototype presented in Sec. 6.6 is fabricated. The antenna layer, embedded in silicon dioxide (SiO_2) with average relative permittivity $\epsilon_r = 4.2$, is separated with approximately $8 \mu\text{m}$ of SiO_2 from a semi-infinite lossless silicon half-space. Ideally, an airgap between the antenna plane and dense dielectric maximizes the directivity of the feed. In Sec. 4.2, leaky-wave radiation is studied in the presence of an airgap or in the presence of SiO_2 , with and without metal fill to comply to CMOS metal density rules. It is

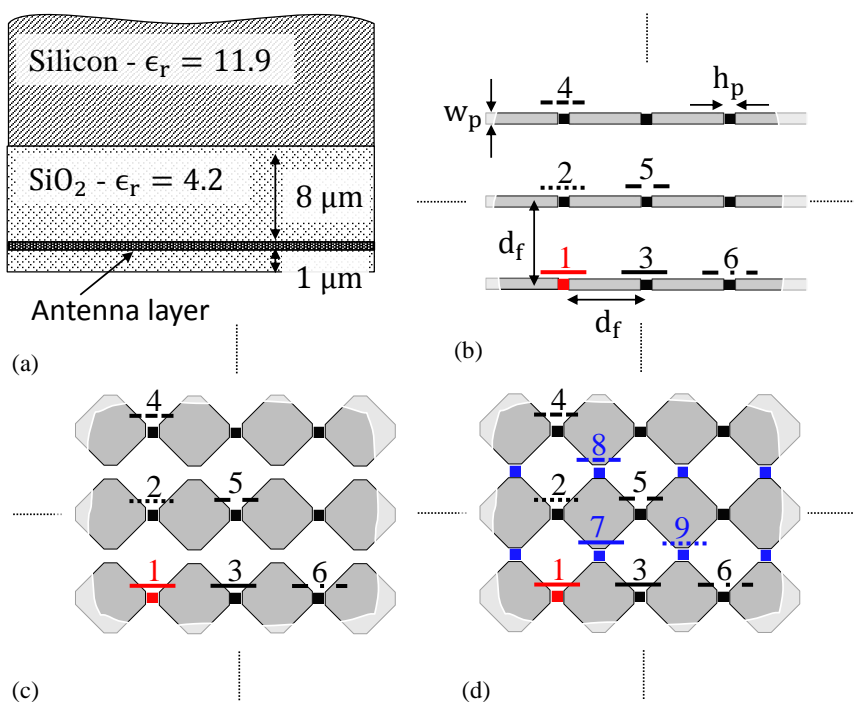


Figure 6.4: Configurations investigated in terms of mutual coupling. The stratification is shown in (a), consisting of a semi-infinite silicon half-space and the antenna layer which is embedded in SiO₂ and separated by 8 μm from the silicon. The considered configurations are (a) untapered dipoles, (b) tapered dipoles w.o. polarization re-usage and (c) with polarization re-usage. The sampling periodicity is $d_f = 141.3 \mu\text{m} \equiv 1F_{\#}\lambda_d$ at 400 GHz with $F_{\#} = 0.65$ and the port dimensions are $w_p = 20 \mu\text{m}$ and $h_p = 15 \mu\text{m}$ for both polarizations.

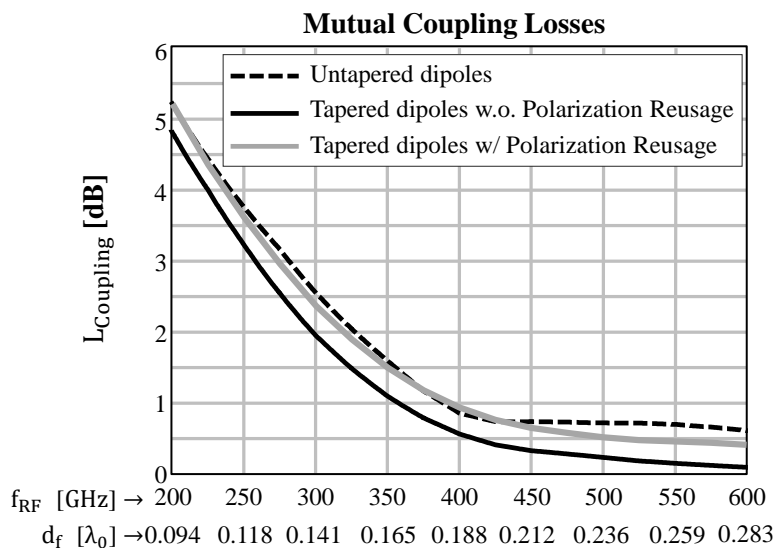


Figure 6.5: Total mutual coupling losses for the array configurations shown in Fig. 6.4.

shown that only a slightly enhanced leaky-wave radiation is achieved. In a tightly sampled connected array configuration, however, an increased feed directivity can also be achieved due to the mutual coupling between the elements [67]. The first array architecture under consideration is an untapered array of dipoles as shown in Fig. 6.4(b). Only a portion of the simulated array is shown, in total $N_{\text{ports}} = 5 \times 5 = 25$ ports are simulated with port #1 (indicated with red) being the centered one. The physical array periodicity is $d_f = 141.3 \mu\text{m}$ which is equivalent to a $d_f = 1F_{\#}\lambda_d$ sampling at 400 GHz with $F_{\#} = 0.65$. Over the full frequency range of 200 GHz to 600 GHz, this periodicity is equivalent to $0.094\lambda_0 \leq d_f \leq 0.283\lambda_0$. The width w_p and height h_p of the Δ -gap ports are $20 \mu\text{m}$ and $15 \mu\text{m}$ respectively. The second architecture, Fig. 6.4(c), has the same periodicity but the dipoles are tapered with an angle of 45° , making the array symmetric in both orthogonal planes. However, only one polarization is utilized. In the third configuration, Fig. 6.4(d), the amount of feeds is doubled by using the orthogonal polarization. Only a portion of the simulated array is shown; port #1 (indicated with red) is the center port of the in total $N_{\text{ports}} = 5 \times 5 + 4 \times 6 = 49$ simulated ports. The arrays, embedded in the stratification as shown by Fig. 6.4(a) are simulated in CST Microwave Studio.

The S-parameters of the untapered dipoles from Fig. 6.4(b) are shown in Fig. 6.6 in the case that port 1 (red) is excited. The S-parameters are normalized to a port impedance of $Z_{\text{port}} = 120 \Omega$. The dominant contribution is $S_{3,1}$, associated with the next port along the dipole. At 400 GHz $S_{3,1} = -11.8 \text{ dB}$. At frequencies $f < 400 \text{ GHz}$, mutual coupling to the second port along the dipole, $S_{6,1}$ is also higher than -20 dB . The total mutual coupling losses are calculated using the S-parameters of all neighboring ports (i.e. $5 \times 5 - 1 = 24$ surrounding ports) as:

$$L_{\text{Coupling}} = 1 - \sum_{i=2}^{N_{\text{ports}}} |S_{i,1}|^2 \quad (6.3)$$

The mutual coupling losses, versus frequency and sampling periodicity in terms of wavelength, are shown in Fig. 6.5 with the dashed black line. It is clear that arrays sampled with $d_f < \lambda_0/5$ yield high mutual coupling losses. These losses, however, are still lower than the spill-over losses for non-overlapping uniform ideal feeds as is evident from Fig. 6.3. Tapering the dipoles is a solution to reduce the mutual coupling losses. The S-parameters for the tapered dipoles in Fig. 6.4(c) are shown in Fig. 6.7. It can be seen that tapering of the dipoles significantly reduces the coupling to the neighboring element $S_{3,1}$ at higher frequencies, but the coupling to the parallel element in the H-plane ($S_{2,1}$) increased. Overall, there is a 0.3 dB to 0.4 dB improvement w.r.t. the untapered dipoles, as shown in Fig. 6.5 by the solid black line. The geometric symmetry of the tapered array allows for doubling the amount of pixels by exploiting the orthogonal polarization as illustrated by Fig. 6.4(d). The S-parameters for this configuration are shown in Fig. 6.8 where the blue curves represent the orthogonal polarized ports. It can be seen that the mutual coupling to the two ports in the main planes ($S_{2,1}$ and $S_{3,1}$) and the orthogonal polarized port in the D-plane $S_{7,1}$ is similar. Mutual coupling to the remaining ports is lower than -22 dB over the full frequency range. The total losses are shown by the gray solid curve in Fig. 6.5.

The losses are equivalent or slightly better than the untapered dipole configuration.

Tapering the dipoles of a tightly sampled connected array configuration and exploiting the orthogonal polarization effectively reduces the sampling periodicity by a factor of $1/\sqrt{2}$ without paying off in additional mutual coupling losses. The considered sampling periodicity in this section is equivalent to a $1F_{\#}\lambda_d$ sampling at 400 GHz for a focal number of $F_{\#} = 0.65$. This focal number turns out to be the optimum for edge of coverage gain when the array is used in combination with a dielectric lens as will be shown in the next section.

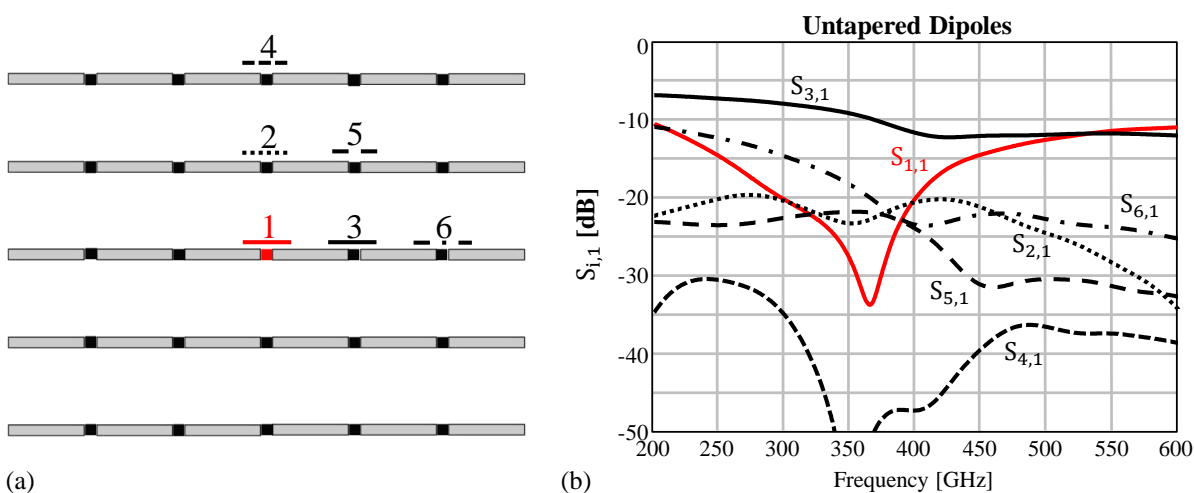


Figure 6.6: S-parameters for the untapered dipoles configuration. The array is sampled with $d_f = 1F_{\#}\lambda_d$ at 400 GHz with $F_{\#} = 0.65$. $Z_{\text{port}} = 120\Omega$. (a) Array architecture, (b) S-parameters.

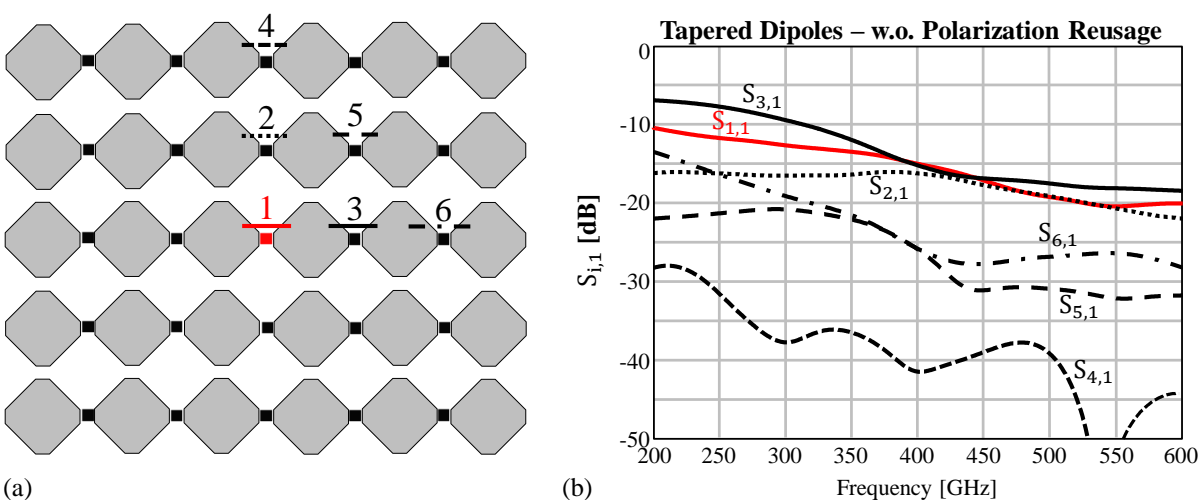


Figure 6.7: S-parameters for the tapered dipoles in single polarization. The array is sampled with $d_f = 1F_{\#}\lambda_d$ at 400 GHz with $F_{\#} = 0.65$. $Z_{\text{port}} = 80\Omega$. (a) Array architecture, (b) S-parameters.

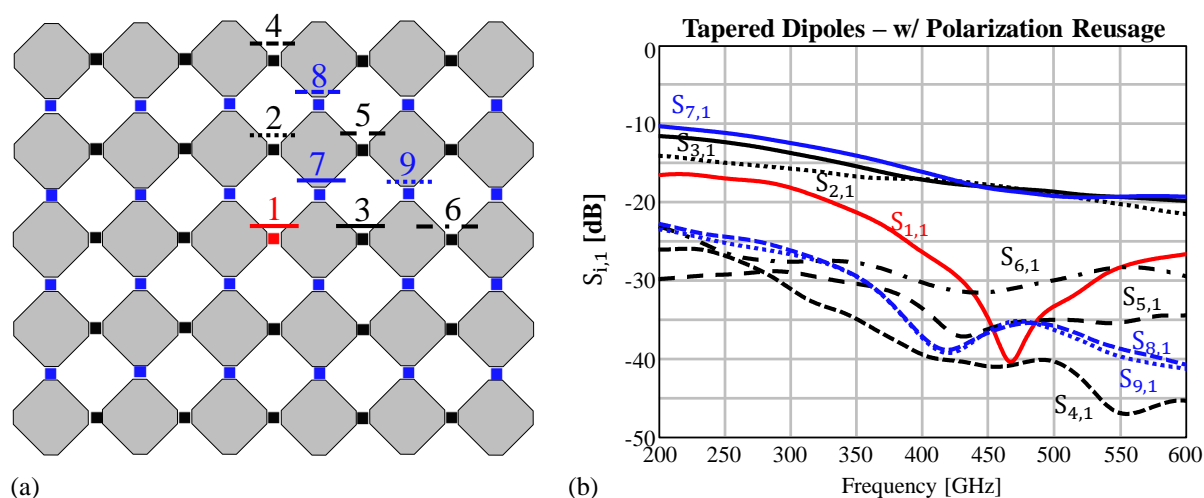


Figure 6.8: S-parameters for the tapered dipoles with dual polarization shown in Fig. 6.4(d). The array is sampled with $d_f = 1F_{\#}\lambda_d$ at 400 GHz with $F_{\#} = 0.65$. $Z_{\text{port}} = 100\Omega$. (a) Array architecture, (b) S-parameters.

6.5 Dual Polarized Array Design

In this section we will investigate the trade-off between mutual coupling losses and spill-over for the dual polarized connected array from Fig. 6.4(d) as function of the focal number of the dielectric lens. The physical sampling periodicity will increase while fulfilling the sampling condition $1F_{\#}\lambda_d$. A larger $F_{\#}$ results in a larger periodicity of the focal plane and therefore lower mutual coupling between the elements. On the other hand, a larger $F_{\#}$ will truncate the primary fields inside the lenses at smaller angles and results in increased spill-over losses. For example, in Fig. 6.9 two different sampling considerations that will

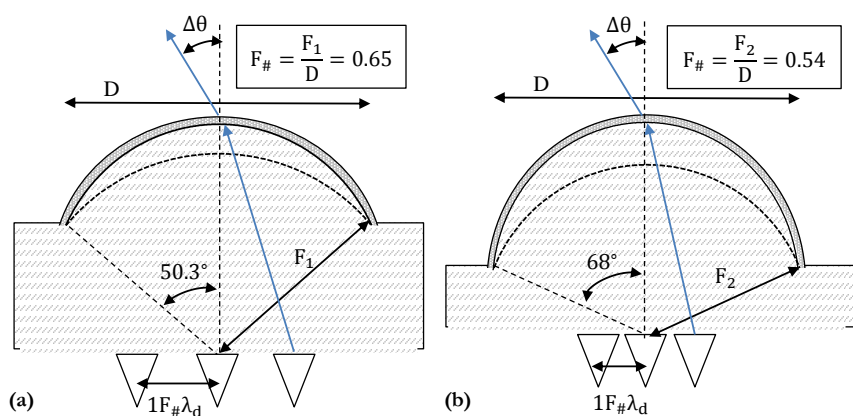


Figure 6.9: Different lens geometries considered in this chapter. The lenses have an (a) $F_{\#} = 0.65$ and (b) $F_{\#} = 0.54$. The sampling periodicity in both configurations is $1F_{\#}\lambda_d$ such that they feature the same angular resolution $\Delta\theta$. The different $F_{\#}$ implies a trade-off between mutual coupling and spill-over efficiency (and in a less degree the tapering efficiency).

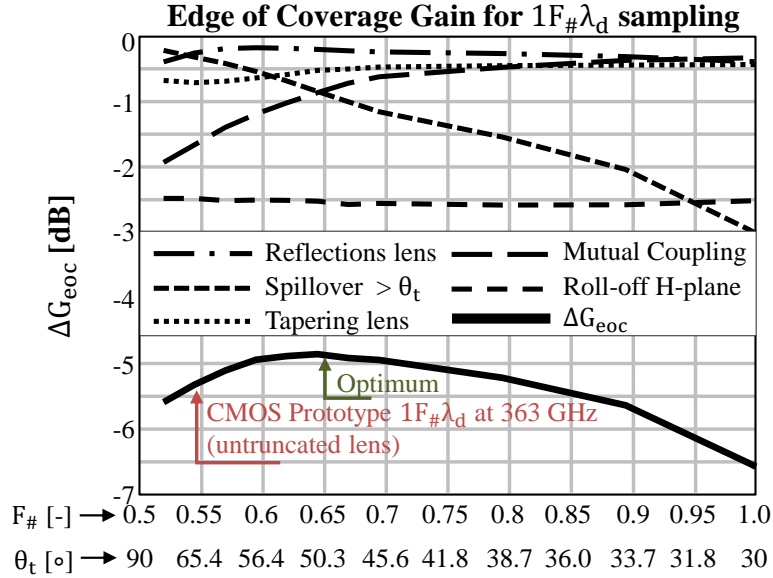


Figure 6.10: Edge of Coverage gain for a $d_f = 1F_{\#}\lambda_d$ sampled array, as function of $F_{\#}$ for the dual polarized leaky-wave connected array as shown in Fig. 6.4(d). The optimal ΔG_{eoc} is obtained for a $F_{\#} = 0.65$. The CMOS prototype, as presented in Sec. 6.6, is fabricated with an untruncated lens ($F_{\#} = 0.54$) and is sampled $d_f = 1F_{\#}\lambda_d$ at 363 GHz.

be considered in this chapter are highlighted. In Fig. 6.9(a), the elliptical lens has an $F_{\#} = 0.65$, resulting in a $\theta_t = 50.3^{\circ}$ truncation of the primary fields. Radiation beyond this angle is considered to be a spill-over loss. The angular resolution is $\Delta\theta = \lambda_0/D$. In Fig. 6.9(b) the $F_{\#} = 0.54$ such that the physical sampling periodicity is reduced. The effective diameter of the lens, D , remains constant such that the angular resolution $\Delta\theta$ does not change. The different lens geometries will have a small effect on the tapering efficiency and reflections at the lens surface, depending on the feed directivity on the truncation angle. In this work, the lenses are provided with an anti-reflection coating to minimize the reflection losses. The edge of coverage gain and its contributions as described by (6.2) are shown in Fig. 6.10 as function of the focal number. The relation between the focal number and truncation angle of the primary fields can be expressed as $\theta_t = \sin^{-1}((1/(2F_{\#})))$. The primary embedded array radiation patterns, inside the semi-infinite silicon half space, are simulated in CST Microwave Studio. Subsequently the performance of the array in combination with the elliptical lens is analyzed using an in-house Physical Optics (PO) tool [130]. As expected, the tapering efficiency is slightly worse for lower focal numbers with higher primary field truncation angles. The roll-off is calculated at $\theta = \Delta\theta/2$ in the H-plane of the considered element and, as expected, remains constant as function of $F_{\#}$ and only changes slightly due to a changing tapering efficiency. It can be seen that the optimum in edge of coverage gain is obtained approximately at the point where the mutual coupling losses and the spillover losses are similar at $F_{\#} = 0.65$, i.e. the lens geometry in Fig. 6.9(a). The remaining part of this section will present the performance of the optimal configuration as indicated in Fig. 6.10.

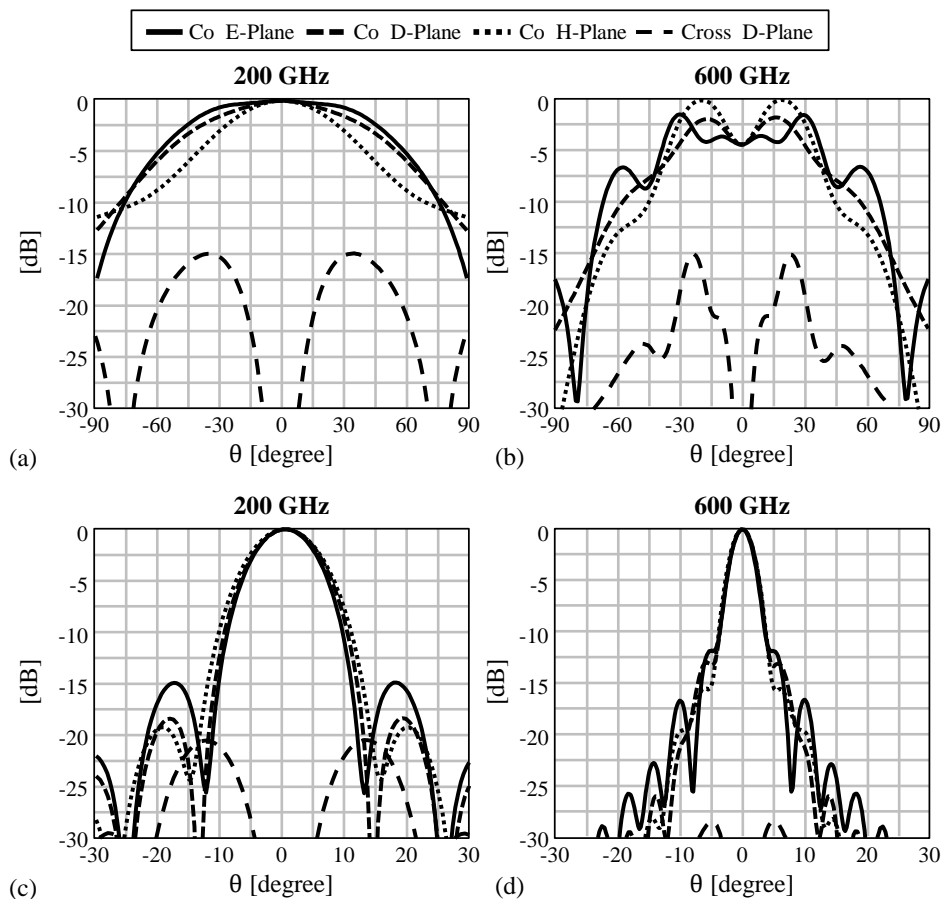


Figure 6.11: The embedded primary fields inside the lens are shown at (a) 200 GHz and (b) 600 GHz for the dual polarized array sampled $d_f = 1F_{\#}\lambda_d$ at 400 GHz with $F_{\#} = 0.65$. The secondary fields, outside the elliptical lens with diameter $D = 7.57$ mm are shown at (c) 200 GHz and (d) 600 GHz.

The primary embedded radiation patterns, inside the dielectric lens, are shown in Fig. 6.11(a) and Fig. 6.11(b) at 200 GHz and 600 GHz, respectively. At lower frequencies the distinct radiation peaks pertaining to leaky-wave radiation completely disappeared while at higher frequencies oscillations in the patterns are observed. This effect is attributed to the mutual coupling between the elements [67, 161] and tapering of the dipoles. The secondary radiation patterns, outside the elliptical lens with diameter $D = 7.57$ mm are shown in Fig. 6.11(c) and Fig. 6.11(d) at 200 GHz and 600 GHz, respectively. A slight asymmetry between the main planes can be observed, which will impact the roll-off in the different planes of the antenna. The aperture efficiency and its different contributions are shown in Fig. 6.12(a) over the full frequency range. Also indicated is the feed sampling, in terms of $F_{\#}\lambda_d$, in the main planes of the array. Note that effectively, with an orthogonally polarized grid, this sampling is actually reduced by a factor $1/\sqrt{2}$. The configuration is the same as evaluated in Sec. 6.4 so that the mutual coupling can be decomposed in the S-parameters as presented in Fig. 6.8. The beam roll-off is shown in Fig. 6.12(b) by the gray

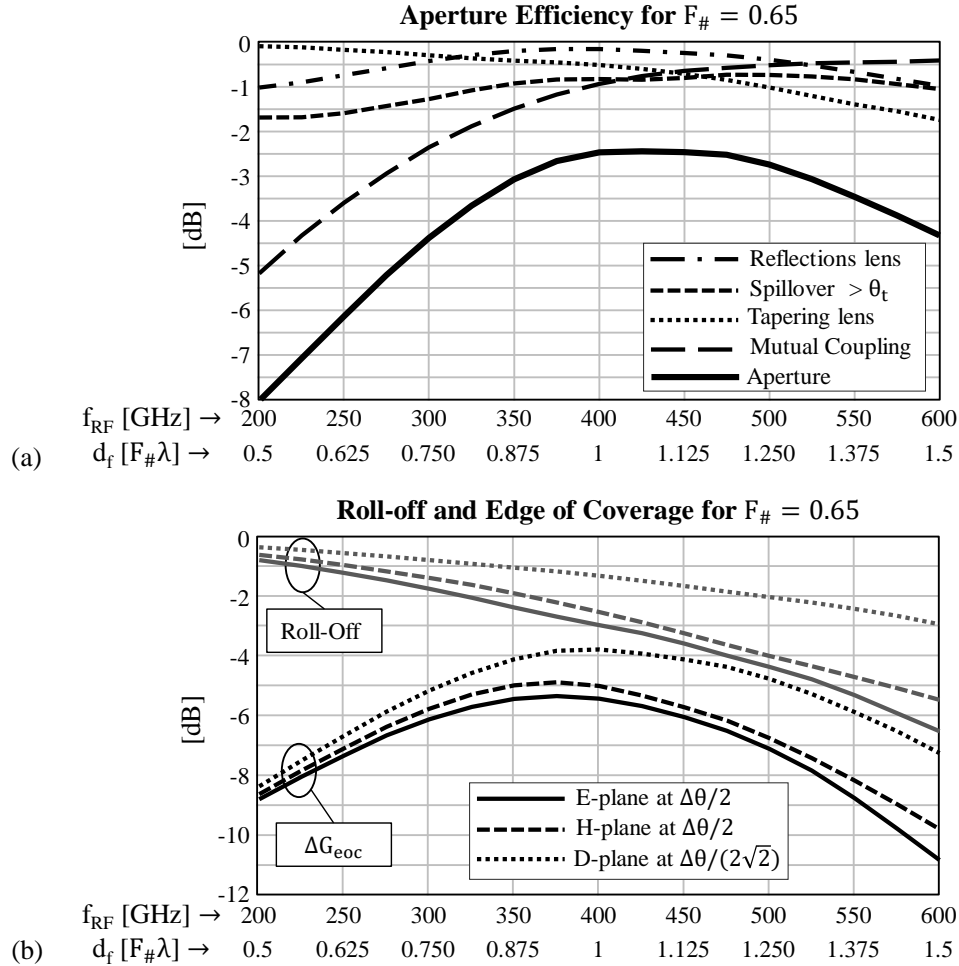


Figure 6.12: Performance of the optimized dual polarized connected array configuration with $F_{\#} = 0.65$. (a) Aperture efficiency and its individual contributions as function of frequency. (b) Roll-off in the main planes of the array (gray curves) that, together with the aperture efficiency, results in the edge of coverage gain as shown by the black lines.

curves for the main planes and diagonal plane. The least covered spots of the interleaved rectangular grid are in the E- and H-planes at $\theta = \Delta\theta/2 = 2.84^\circ$ and slightly different for E- and H-plane. The checkerboard configuration introduces an enormous improvement in roll-off in the diagonal planes and the least covered spot is at $\theta = \Delta\theta/(2\sqrt{2}) = 2.01^\circ$. The edge of coverage gain ΔG_{eoc} (6.2), w.r.t. to the maximum directivity than can be obtained with the same aperture with 100% aperture efficiency, is also shown in Fig. 6.12(b). The ΔG_{eoc} is summarized in Fig. 6.1 and compared with the performance of equivalently sampled uniform feeds in a hexagonal grid. The top boundary of the light gray area represents the ΔG_{eoc} in the D-plane while the bottom side is associated with the E-plane. Note that the sampling periodicity on the x-axis in Fig. 6.1 corresponds to the actual sampling of $d_f/\sqrt{2}$ of the dual polarized grid.

The optimal ΔG_{eoc} that can be achieved with uniform feeds placed in a hexagonal grid

is $\Delta G_{eoc} = -6.9$ dB for a sampling periodicity of $d_f = 0.89F_{\#}\lambda_d$. Instead, for the proposed dual-polarized array, the optimal coverage is $\Delta G_{eoc} = -5.4$ dB. This is an improvement of 1.5 dB while simultaneously a higher angular resolution is achieved. If the same resolution is desired for the hexagonal array of uniform feeds, an improvement of 2.5 dB is achieved by using the dual polarized connected array configuration. Although the array is not optimized for diffraction limited resolution (i.e. when $d_f = 0.5F_{\#}\lambda_d$), and performance might be improved for this scenario, the proposed array configuration already features a 2.5 dB improvement in edge of coverage gain in a diffraction limited scenario.

The lens that is used in the presented analysis is a silicon elliptical lens with a slightly increased $F_{\#}$ w.r.t. a standard untruncated elliptical lens. Nevertheless, the $F_{\#}$ is still relatively low and will therefore limit the scanning performance of the system. In Fig. 6.13, the scanning performance is shown for six adjacent pixels of the considered connected array, evaluated at 400 GHz. The lens that is used for this example has a diameter of $D = 7.57$ mm, i.e. $10\lambda_0$ at 400 GHz, such that the sixth pixel is pointing at a wide-angle of 26° . The secondary patterns, when scanning in the E-plane and the H-plane direction, are shown in Fig. 6.13(a) and (b), where the associated cut in the E-plane or H-plane is shown. At the largest scanning angle of 26° , a scan loss of approximately 4 dB is observed. This scan loss, shown in Fig. 6.13(c) as function of scanning angle for both the E- and H-plane, is in line for what is seen for double-slot feeds [142, 162] and feeds that illuminate wide-angle elliptical lenses [146]. However, the advantage of the proposed leaky connected array configuration with respect to a double-slot [142, 162] is a higher edge-of-coverage and bandwidth. Scan-loss and pattern quality can be further improved by resorting to double-shell dielectric lenses [144, 163].

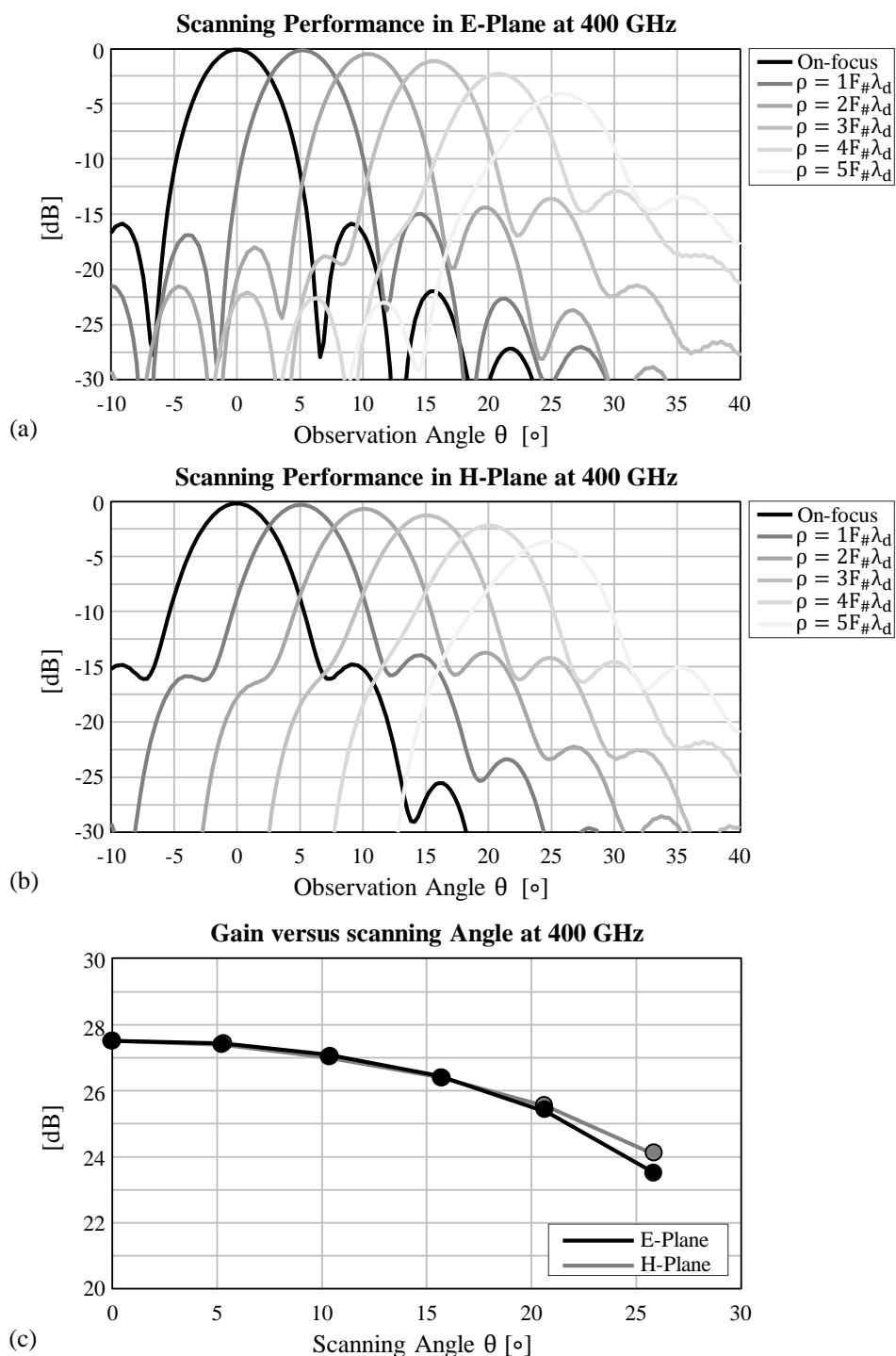


Figure 6.13: Scanning performance for five six adjacent pixels sampled $1F_{\#}\lambda_d$ at 400 GHz with $F_{\#} = 0.65$. This specific example used a lens with diameter $D = 7.57$ mm such that the outer beam is scanning at a wide angle of $\theta = 26^\circ$. (a) Scanning Performance in E-Plane. (b) Scanning Performance in H-Plane. (c) Gain as function of scanning angle in E-plane and H-plane.

6.6 12-Pixel Prototype in 22-nm CMOS

As demonstrator, a 12-pixel prototype is fabricated in a 22-nm CMOS technology, operating in a direct detection scenario from 200 GHz to 600 GHz. The array contains a 2×3 horizontally polarized array interleaved with a 3×2 vertically polarized array as is indicated in the micrograph from Fig. 6.2. A slightly different lens and sampling configuration is used than is discussed in the previous sections. The lens that was available for this prototype is an untruncated elliptical lens as the one that is depicted in Fig. 6.9(b). Indicated in Fig. 6.10, for reference, is the configuration where the CMOS prototype is operating. The prototype is fabricated with an untruncated lens that has a focal number of $F_{\#} = 0.54$ and diameter $D = 7.57$ mm and is provided with a $114 \mu\text{m}$ thick deposition of a Parylene C anti-reflection coating of which the thickness is optimized at a frequency of 400 GHz. A zoom-in of the micrograph from Fig. 6.2 is shown in Fig. 6.14(a), showing the dimensions of the sampling and tapered dipole. The array is sampled $d_f = 1F_{\#}\lambda_d = 130.4 \mu\text{m}$ at 363 GHz in the main planes, which corresponds to an effective sampling in the diagonal plane of $d_f^{\text{eff}} = F_{\#}\lambda_d/\sqrt{2} = 92.2 \mu\text{m}$, when considering the two polarizations. The edges of the dipole are the same as in previous sections $w_p = 20 \mu\text{m}$ and $h_p = 15 \mu\text{m}$. The performance of this lens/array configuration at 363 GHz, in terms of edge of coverage gain, is indicated in Fig. 6.10 for reference. In Fig. 6.14(b) a zoom-in of the dipole edge is shown. In this zoom-in metallic pads that are embedded in the SiO_2 are clearly shown. These metallic pads are present in every metallization layer of the CMOS stratification and are required by the CMOS process. In Sec. 4.2 it was shown that leaky-wave type antennas suffer minimally from additional ohmic dissipation losses (approximately 0.2 dB) due to these minimum metal density rules. The effect of the metallic pads on losses and radiation characteristics is taken into account in the numerical simulations by using

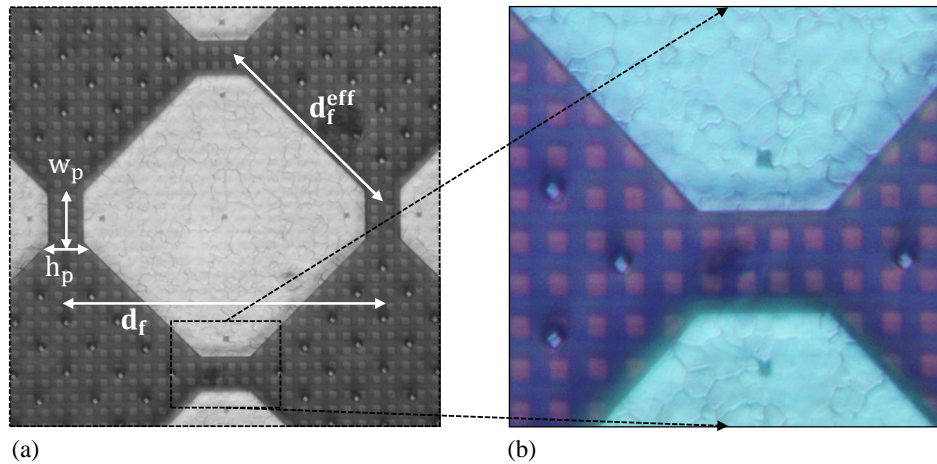


Figure 6.14: CMOS prototype, as is also shown by the micrograph in Fig. 6.2. A zoom-in of the micrograph shows one tapered dipole (a), with the dimensions $d_f = 1F_{\#}\lambda_d = 130.4 \mu\text{m}$, $d_f^{\text{eff}} = F_{\#}\lambda_d/\sqrt{2} = 92.2 \mu\text{m}$, $w_p = 20 \mu\text{m}$ and $h_p = 15 \mu\text{m}$. Indicated is an area that is enlarged in (b), clearly showing metallic pads in the SiO_2 for fulfilling the metal density rules.

equivalent anisotropic media [128] as is more thoroughly explained in Sec. 4.2 .

The array is a THz direct detection FPA and each of the feeds is connected to two Schottky Barrier Diodes (SBDs) in a differential configuration identical to the single pixel presented in Chapter 5 and illustrated in Fig. 5.2. Also the size of the SBD is identical, i.e. the smallest one available in the PDK of $1.6 \mu\text{m} \times 1.6 \mu\text{m}$. The SBDs are biased via the center of the dipoles and connected to a loading resistor that enables a voltage read-out that is proportional to the RF-power that is absorbed by the differential detectors. A reference branch, with identical SBDs that are not connected to an antenna, are integrated to realize a pseudo-differential read-out. The array is still in its assembling and measurement stage. Measurements of the prototype will be presented in the paper J1 listed on page 183. The remaining part of this chapter presents the simulated performance of this array.

The simulated antenna gain is shown in Fig. 6.15(a). Also the theoretical maximum achievable gain for the considered lens is shown, calculated as $D_{\text{max}}^{\text{Theory}} = (\pi D/\lambda_0)^2$. The difference between the antenna gain and maximum achievable directivity are the aperture losses L_{aperture} . The aperture efficiency is shown in Fig. 6.15(b) where it is decomposed in its different contributions. Approximately 1.8 dB of losses are attributed to the ohmic dissipation in the low-resistive silicon of the technology, in the metallic patches that are required to comply to the minimum metal density rules of the considered CMOS process and the dipoles itself. The mutual coupling losses are slightly higher in comparison with the optimal configuration presented in Sec. 6.5 since the physical sampling periodicity is smaller. The simulated beam roll-off and edge of coverage gain are shown in Fig. 6.15(c). The edge of coverage gain is evaluated in the main planes and diagonal plane of the array and does not include the ohmic dissipation losses that are indicated by the red curves in Fig. 6.15(b). The array is sampled $1F_{\#}\lambda_d$ at 363 GHz such that the performance at that (indicated) frequency point can be compared with the same point in the optimization study as presented in Fig. 6.10. Slightly better results would have been achieved using a lens with $F_{\#} = 0.65$. Also, the losses of the CMOS prototype are limited by the ohmic dissipation losses in the low-resistive silicon of the technology. The simulated FoV of all pixels is shown in Fig. 6.16 at 200 GHz (a,c-e) and 600 GHz (b,f-h). The cuts are indicated in the 2D surface plots (a,b) and shown at $\phi = 0^\circ$ (c,f), $\phi = 45^\circ$ (d,g) and $\phi = 90^\circ$ (e,h).

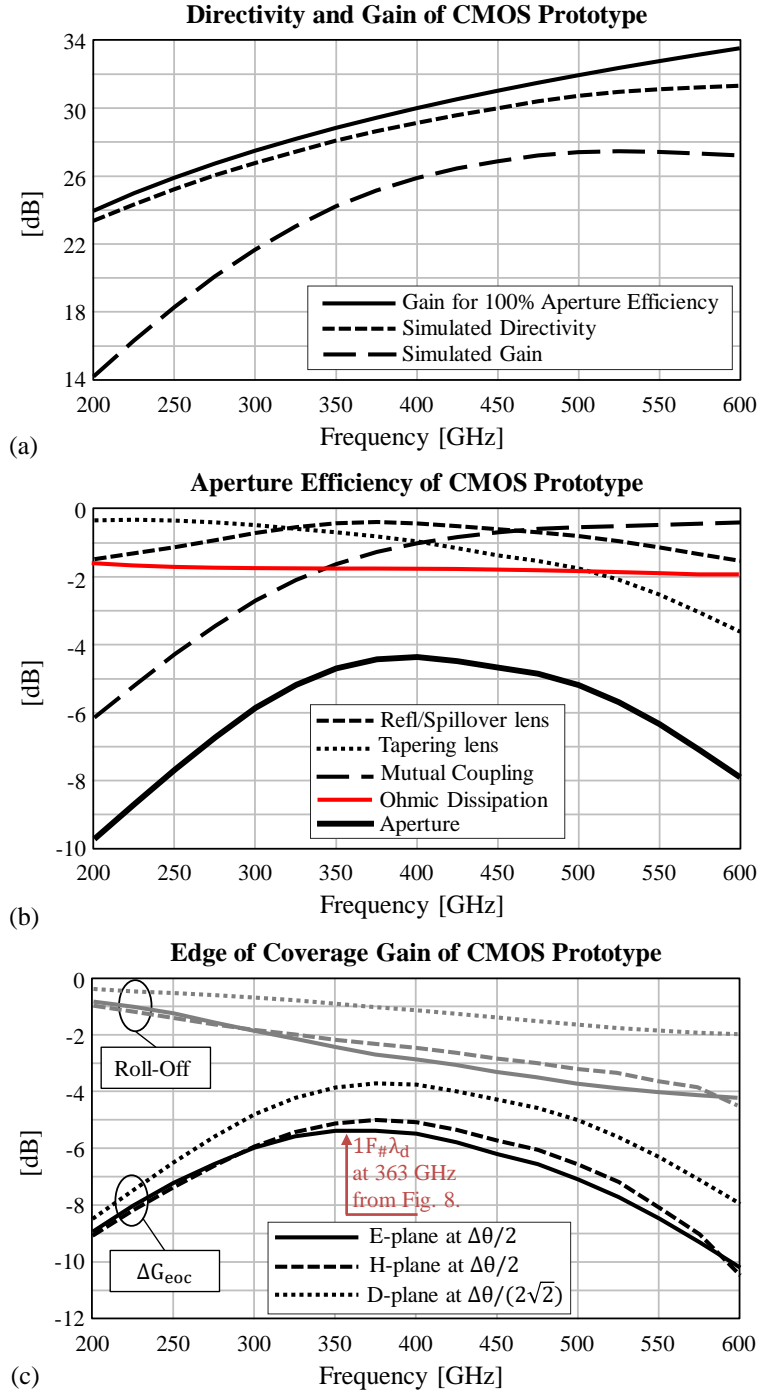


Figure 6.15: Simulated performance of CMOS prototype. (a) Directivity and gain. Also the theoretically maximum achievable gain, with 100% aperture efficiency, is indicated for reference. (b) Aperture efficiency in dB for the CMOS prototype. The red curve represent ohmic dissipation losses in the low-resistive silicon, metal density fill and the dipoles itself and constitutes in total around 1.8 dB of losses. (c) Simulated roll-off and extracted edge of coverage gain ΔG_{eoc} . The edge of coverage gain is calculated without the ohmic dissipation losses. The array is sampled $1F_{\#}\lambda_d$ at 363 GHz such that the performance at that (indicated) frequency point can be compared with the same point in the optimization study as presented in Fig. 6.10.

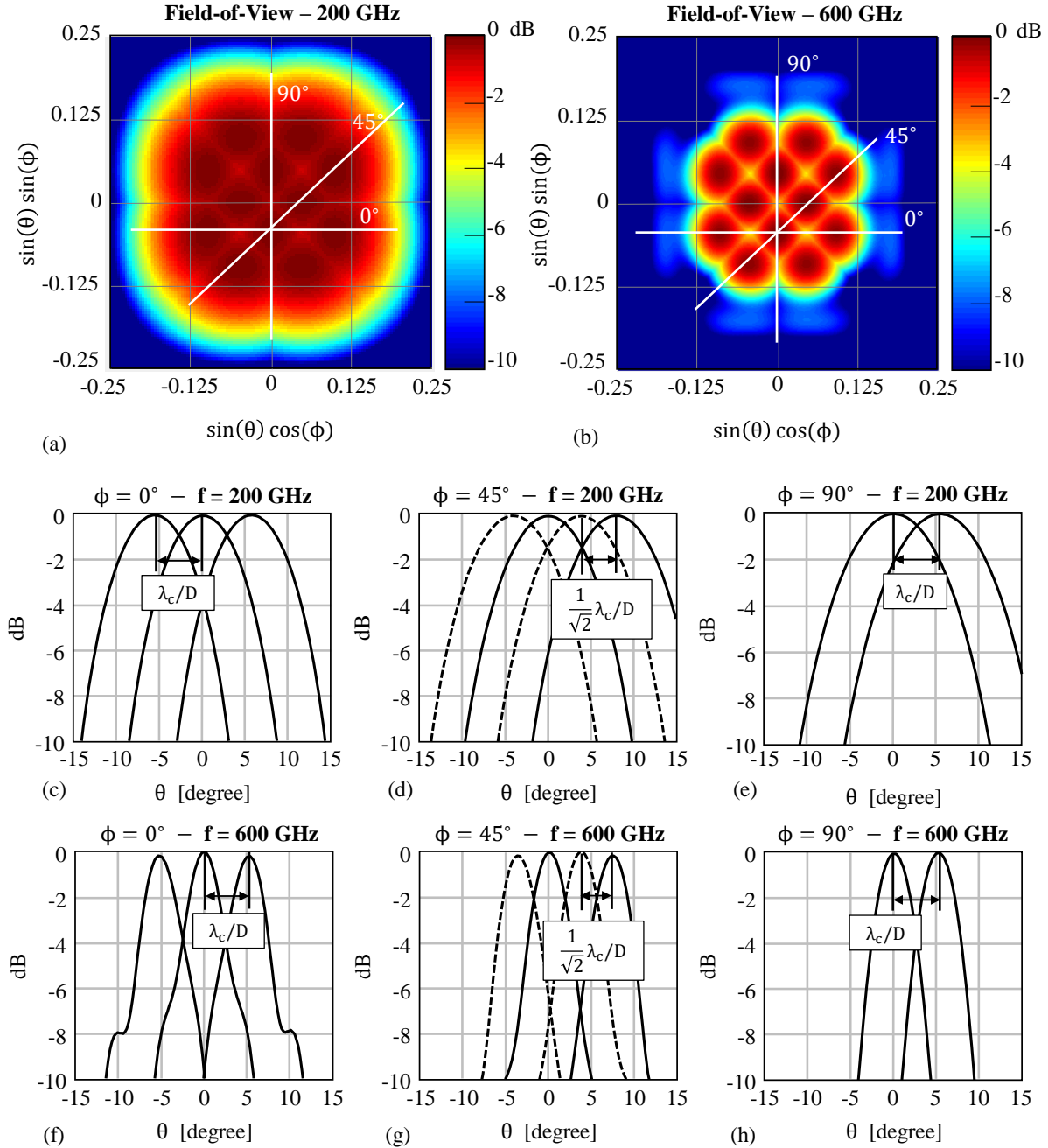


Figure 6.16: The simulated radiation patterns are shown at 200 GHz (a,c,d,e) and 600 GHz (b,f,g,h). The cuts are shown for the main planes at $\phi = 0^\circ$ (c,f), $\phi = 45^\circ$ (d,g) and $\phi = 90^\circ$ (e,h). The angular resolution is indicated, which is $\Delta\theta = \lambda_s/D$ in the main planes and $\Delta\theta = \lambda_s/(\sqrt{2}D)$ in the diagonal plane, where λ_s is the free-space wavelength at the sampling frequency 363 GHz.

6.7 Conclusion

This chapter presented the optimization, design and simulated performance of a tightly sampled connected array of dipoles that offers high edge of coverage gain for high resolution imaging. A checkerboard configuration of the dipoles allows for doubling the resolution by using the orthogonal polarization without paying off in additional mutual coupling losses. A feed sampling optimization study is presented that showed that, for an almost diffraction limited resolution, an improvement of 2.5 dB in edge of coverage gain is achieved with the proposed dual polarized connected array w.r.t. uniform feed apertures. A 12-pixel demonstrator is fabricated in a 22-nm CMOS technology that operates from 200 GHz to 600 GHz to demonstrate the applicability of the concept in imaging applications. Measurements of the prototype will be presented in the paper J1 listed on page 183.

Chapter 7

Conclusions and Future Prospects

This thesis describes the research work carried out over a period of five years (from May 2015 till July 2020) in the Terahertz Sensing Group, in a tight collaboration with the Electronics Research Laboratory, at Delft University of Technology, Delft, the Netherlands. The topic treated in this work is of particular interest in the field of THz technology. THz imaging has been, together with spectroscopy, one of the main applications that are the thriving forces for the development of THz technology and systems. THz imaging is not only extremely interesting for the well-known astronomical applications, but, because of the ability to penetrate through materials such as clothing and plastics, also for terrestrial applications. Up to now, the practicality of THz imaging systems is quite limited since a limited detector sensitivity is either compensated by cooling the system, by operating in combination with an active source or by operating in non-real-time mode. All of these solutions result in system implementations that are non-practical for low-cost and real-time imaging applications such as pedestrian detection for the automotive industry or security screening.

The scope of this thesis was to provide the design guidelines and modeling tools to develop THz Focal Plane Array (FPA) architectures, in a potentially low-cost CMOS technology, that, in combination with a future generation of low-NEP direct detectors, will enable fully passive THz imaging applications. The performance of different FPA architectures in terms of efficiency and resolution was investigated. Depending on the required sensitivity, different design guidelines are provided. It is shown that a higher NEP can be compensated with a large absolute bandwidth of a few hundred of GHz. Subsequently, a single THz direct detector is designed and fabricated in a CMOS technology. This demonstrator showed that leaky-wave type antennas are extremely suitable to operate efficiently over a large frequency bandwidth of 3:1 without suffering significantly of severe metal density rules in CMOS technologies. An accurate system modeling approach, of the antenna together with the direct detection circuit, was proven to be very useful in the prediction of radiometric performance in terms of NEP and temperature sensitivity over an ultra-wide bandwidth. Finally, it was demonstrated that leaky-wave enhanced connected array architectures are an effective solution to maximize imaging speeds while simultaneously achieving a near-diffraction limited imaging resolution.

In this chapter, the conclusions and the most significant results of the research are summarized, and moreover some future prospects of this research will be discussed.

7.1 Analysis of FPA Architectures in Imaging Speed and Resolution

Uncooled sub-millimeter wave direct detectors are characterized by moderate sensitivities due to high electronic noise and thus have not yet been used for real-time fully passive imaging. In Chapter 2, the design guidelines for focal plane architectures based on antenna-coupled direct detectors are proposed with greatly enhanced potential speeds thanks to the efficient use of the available spectral bandwidth at sub-millimeter wavelengths. The analysis starts from the expression of the Signal-to-Noise ratio for direct detectors and Planck's law of blackbody radiation. From there, the temperature sensitivity in radiometric operation is derived. The trade-off between efficiency and resolution is rigorously studied for different focal plane sampling configurations. It is shown that, in a diffraction limited resolution scenario, the imaging speeds is maximized with a slightly undersampled FPA combined with a $\times 4$ mechanical scanning penalty to cover the complete Field-of-View. Ultimately, the imaging speed is maximized when the FPA is undersampled, implying a tradeoff in the size of the optics. The analysis is substantiated by a case study, in simulation, with wideband leaky lens antenna feeds operating from 200 to 600 GHz. With this absolute bandwidth, and by relying on the guidelines and focal plane architectures introduced in Chapter 2, it is shown that real-time imaging with moderate sensitivities might be achieved with detectors that are characterized with a NEP of $1 \text{ pW}/\sqrt{\text{Hz}}$. This value is close to state-of-the-art detectors fabricated in CMOS technologies. This theoretical work was published in an invited contribution in the *IEEE Transactions on THz Science and Technology*.

In Chapter 3, the analysis is applied to a case-study of pedestrian detection for the automotive industry, with a focus on foggy weather conditions. In this analysis, the atmospheric attenuation is taken into account as well as the beam coupling of a pixel to the pedestrian. It is shown that a slightly undersampled array is a good compromise between resolution and sensitivity. Such FPA configuration results in a temperature sensitivity of 2 K to 4 K for the detection of pedestrians up to 10 m with an acceptable resolution. Foggy weather conditions are most likely to appear at lower atmospheric temperatures, implying a high temperature contrast between the atmosphere and the pedestrian that can be 20°C or higher. With such contrast, a pedestrian can be detected with a dynamic range of 5 to 10 times with respect to the noise fluctuations in the image. If the contrast is as low as 3°C , however, the NEP of the detectors should be decreased in order to compensate for the increased sensitivity requirements. An increase of bandwidth is not useful due to the high atmospheric attenuation above 500 GHz. If imaging ranges larger than 10 m are desired, resolution should be improved due to a poor beam coupling efficiency to a pedestrian at larger distances. This can be achieved by using bigger lenses.

7.2 Design of a Wideband THz Direct Detector in a CMOS Technology

Chapter 4 follows up on the conclusion of Chapter 2 and presents the design and performance of two wideband double leaky slot lens antennas. One antenna, center-fed and suitable for direct detection scenarios, efficiently utilizes the submm-wave regime with a large relative bandwidth of 3:1 from 200 GHz to 600 GHz with an average efficiency of 57% over this bandwidth. In Chapter 5, this antenna is used to design a THz direct detector in which the antenna is connected to a differential direct detection circuit based on Schottky barrier diodes that are designed in collaboration with the Electronics Research Laboratory. Key in such design is an accurate wideband modeling of NEP of the antenna-detector combination. A second antenna is CPW-fed and allowed for a spectral evaluation of gain patterns and impedance using landing probes and an ad-hoc quasi-optical measurement setup, in excellent agreement with simulations.

7.2.1 Efficient Wideband Antennas in CMOS

In Chapter 4 it is explained that the challenges in efficient CMOS antenna design lie in complying with the strict minimum metal density rules and avoiding high ohmic dissipation or surface-wave excitation in the low-resistive silicon of CMOS technology. It is shown that leaky-wave type of antennas minimize ohmic dissipation losses that are attributed to the strict metal density rules. The design of two wideband double leaky slot lens antenna, fabricated in a 22-nm FD-SOI CMOS technology, is presented. The first, center-fed, antenna is suitable for direct detection purposes and operates efficiently over a 3:1 relative bandwidth from 200 GHz to 600 GHz with an average efficiency as high as 57%. The double leaky slot antenna radiates through the low-resistive silicon that is glued to a dielectric elliptical lens and which is provided with an anti-reflection coating. A novel approach to truncate the antenna ground-plane improves the pattern quality over the large bandwidth. A second, CPW-fed antenna, is fabricated for verification purposes. A grounded-CPW impedance transformer is part of the antenna and could provide a $35\ \Omega$ impedance matching interface to other on-chip circuitry. The antenna is connected to landing pads suitable for a characterization with landing probes. The antenna is packaged in an ad-hoc quasi-optical focusing system for spectral verification purposes with high dynamic range. The antenna is fully characterized from 225 GHz to 500 GHz in terms of gain patterns and impedance. The CPW-fed antenna has an average efficiency of 47% over the full bandwidth. The proposed antennas are bench marked with CMOS antennas presented in literature and shows state-of-the-art performance as a wideband solution.

7.2.2 Analysis of the Radiometric Performance of THz Direct Detectors

In Chapter 5, the antenna that is designed and evaluated in Chapter 4, is embedded into a THz direct detection system. The double leaky slot antenna efficiently couples radiation from 200 GHz to 600 GHz to a differential detector circuit composed of Schottky Barrier Diodes (SBDs) and a load resistor to enable a voltage read-out. A derivation of the temperature sensitivity, as function of the spectral NEP, is presented, based on the lumped element model of a standalone SBD. Measurements of the THz direct detector in terms of antenna patterns and white-noise show good agreement with simulations. A discrepancy in measured and simulated detector voltage responsivity is attributed to a higher series resistance ($135\ \Omega$ vs $10\ \Omega$) and junction capacitance ($20\ \text{fF}$ vs $8\ \text{fF}$) of the diodes. The reduced voltage responsivity of the detector results in a system NEP of $90\ \text{pW}/\sqrt{\text{Hz}}$. An updated diode model, derived from low-frequency measurements on the diode, show an excellent agreement with the measured responsivity. The low-frequency measurements consists of the IV-characteristic measurement in DC and the input impedance at 10 GHz. This allows for an accurate prediction of NEP up to the submm-wave regime of the EM-spectrum. Overall, Chapter 5 provides an accurate modeling of the radiometric performance in antenna coupled direct detectors based on differential SBDs that operate over a very wide bandwidth. The obtained agreement with the system measurements over such a large frequency band is not common in the existing literature.

7.3 Design of Multi-Beam Wideband THz Direct Detector Arrays

Chapter 6 presents the optimization and design of a tightly sampled connected array of dipoles that offers high edge of coverage gain for high resolution imaging scenarios. The proposed array architecture could also be potentially exploited for future high frequency communications. In deciding the sampling periodicity of a FPA, an intrinsic trade-off between efficiency and angular resolution exists. Together they determine the edge of coverage gain, which in a single-beam-per-feed FPA can be as low as $-7\ \text{dB}$ in the case of uniform feed apertures. In Chapter 6, the trade-off between mutual-coupling and spill-over losses is investigated for a tightly sampled connected array that supports a leaky-wave in the presence of a dielectric lens. Moreover, the dipoles of the array are tapered with an angle of 45° into a checkerboard configuration. The tapering not only reduces mutual coupling but also allows for doubling the resolution by using the orthogonal polarization without paying off in additional mutual coupling losses. The feed sampling optimization study showed that, for an almost diffraction limited resolution, an improvement of $2.5\ \text{dB}$ in edge of coverage gain is achieved with the optimized dual polarized connected array w.r.t. uniform feed apertures. A 12-pixel demonstrator is fabricated in the same 22-nm FD-SOI CMOS technology as the prototype presented in Chapter 4 and Chapter 5 that, again, operates from 200 GHz to 600 GHz to demonstrate the applicability of the concept

in imaging applications. Measurements of the array will be published in paper J1, listed on page 183, that is yet in preparation.

7.4 Future Outlooks

This dissertation provided the design guidelines for wideband direct detection FPAs for passive THz imaging applications. Actual uncooled fully passive THz imaging is not achieved throughout this work and remains yet unprecedented. The long turn-around time in CMOS prototyping did not allow for multiple iterations in detector modeling. However, the set of guidelines provided in this thesis, both in FPA design and in the accurate wideband modeling of radiometric performance for direct detectors, are useful in the design of future passive high-resolution THz imaging cameras. Furthermore, the measurements of the connected array developed in Chapter 6 are not yet part of this dissertation but promise some interesting future prospects. The future prospects opened by this research work are divided in the antenna/quasi-optical part and fully passive real-time imaging and are highlighted below.

7.4.1 Future Prospects for the Wideband Integrated FPA

- The antenna array architecture can be scaled and adapted to be suitable in communication scenarios. The array can be scaled in size to be operating in, e.g., the Ka-band, so that the increased physical sampling periodicity of the FPA allows for the integration of the necessary coherent circuitry to realize transceiving capabilities.
- Scan loss, and thus the scalability to a large number of elements, is not yet thoroughly studied. The proposed array was optimized with a single feed that was placed in the focus of a low $F_{\#}$ elliptical lens. A future prospect is to resort to double-shell lenses that will result in improved scan loss, gain and pattern quality for off-focus pixels.
- A preliminary system study for different applications has been performed which provided sufficient incentive to exploit the proposed antenna array in future research projects. For example, in the scenario of pedestrian detection for the automotive industry, it is possible to realize 3D-imaging capabilities by placing two passive imagers with one meter distance from each-other. Realistic Field-of-Views and range resolutions might be realized.

7.4.2 Future Prospects for Future Passive Imaging Applications

- A tape-out with different types and sized detectors should be fabricated, prior to the fabrication of the full THz direct detector, that allows for constructing a tailored diode model that is valid in the submm-wave regime. Current RF process design kits in CMOS technologies are not focused on submm-wave frequencies and, as such, the provided diode models should be updated accordingly.

- An important topic that is not touched in this dissertation is modulation of the input signal. Modulation is required to avoid high (unpredictable) Flicker-noise contributions. In active imaging scenario's, the active source can easily be modulated, e.g. with IQ-modulators as presented in this work. In a passive imaging scenario this is not possible. Solutions should be investigated.
- It is worthwhile to extend the proposed wideband modeling approaches to different detection architectures. For example, recently, state-of-the-art performance have been achieved with differentially driven nFET transistors. Also, in view of the required modulation frequency for SBDs, it would be worthwhile to optimize pn-junction diodes for THz direct detection as literature showed lower 1/f corner frequencies (kHz rather than MHz). Even if they do not show state-of-the-art performance in NEP, overall they might outperform alternative detectors if the signal cannot be modulated in the white-noise region.
- Different read-out topologies should be studied. In the prototypes presented in this dissertation, the pixels were directly connected to external amplifiers and, subsequently, Analog-Digital Converters (ADC). Instead, for larger arrays, parallel read-out schemes should be implemented. This will be vital to realize real-time imaging scenarios, since a consecutive read-out will have a significant effect on imaging speed.
- The prototypes that are fabricated in this thesis are fabricated in the more low-performance CMOS technologies. Achieving NEPs in the order of $1 \text{ pW/Hz}^{0.5}$ is shown to be a challenging task. Instead, in the more high performance integration technologies, such as GaAs and SiGe, low-NEP detectors are more readily available. Thus it makes sense, as first demonstrators for fully passive THz imaging, to resort to these technologies before realizing such system in a CMOS technology.

7.5 Research Outputs

The work described in this thesis has led to a number of journal and conference publications and the graduation of a M.Sc. student. The list of publications is shown in page 183. In total 4 peer-reviewed journal publications are published or in preparation, related to this work, together with 15 conference publications. The work in Chapter 2 is published as an *Invited Paper*, whereas the work in Chapter 4 and Chapter 5 was nominated, and eventually runner-up, for the *Best Antenna Design and Application Award* in the European Conference on Antennas and Propagation (EuCAP), London, United Kingdom, April 9-13 2018. The initial design considerations of the connected array architecture presented in Chapter 6 were studied in the M.Sc. thesis indicated in page 183 and daily supervision was provided by the author of this dissertation.

Appendix A

Resolution Limits for Isolated and Distributed Sources

In this appendix we will investigate the effect of the sampling periodicity on the angular resolution of the quasi-optical system and show that, with a polynomial interpolation, the diffraction limit is achieved for a sampling periodicity of $d_f = 0.5F_{\#}\lambda$. The study is performed for radiometric scenarios where the sources are incoherent, i.e. blackbody sources of which the spectral radiated power is described by Planck's law and of which the phase is random. Only incoherent detection architectures are considered, that only detect power. In this appendix, resolution limits are investigated for both isolated and distributed sources. Most sources in literature focus on the resolution limit for isolated sources [111, 164]. However, in the case of an automotive or security imaging scenario, sources can often not be considered isolated but rather distributed. The need arises to evaluate the effect of larger, distributed, sources, on imaging resolution.

In this appendix, first the diffraction limit is investigated in Sec. A.1 by separating two isolated or distributed sources in the far-field of the system and analyze the diffracted pattern in the focal plane. Then, in Sec. A.2, different sampling periodicity in the focal plane are investigated and a linear and polynomial interpolation is applied to the sampled field to see when the diffraction limit is achieved.

A.1 Diffraction Limit in the Focal Plane

The resolution of an imaging system can be defined using two-source-experiments as has been similarly conducted in [111, 164]. We differentiate between isolated sources and distributed sources. An isolated source, i.e. a point source, will diffract into an Airy pattern in the focal plane, whereas a distributed source represents a reciprocal problem. We will investigate the ability to differentiate the two sources in the case that the focal plane can be sampled with infinite points.

A.1.1 Isolated Sources

For isolated sources a two-point-source experiment is conducted. Consider two point sources in the far-field, illuminating the passive optics uniformly with a plane-wave. The incident plane-waves of each point source will diffract into an airy disc in the focal plane, also known as the point spread function:

$$\text{Airy disc} = C \frac{J_1(k \frac{\rho}{2F} D)}{k \frac{\rho}{2F} D} \quad (\text{A.1})$$

, where C is a normalization constant, k is the wavenumber, ρ is the focal plane position, F and D are respectively the focal distance and diameter of the optics. The two point-sources, modeled with an angular dimension of $\lambda/(20D)$, are considered to be separated by an angle of $\Delta\theta_s^{\text{real}}$ as is indicated in Fig. A.1(a). In this analysis it is assumed that the angle of separation is small ($\sin(\Delta\theta_s^{\text{real}}/2) \approx \Delta\theta_s^{\text{real}}/2$) and that the system has a large $F\#$ such that the transverse displacement, $\Delta\rho$, of the Airy disc in the focal plane is $\Delta\rho = F\Delta\theta_s^{\text{real}}/2$. The diffracted Airy patterns for a source separation of $\Delta\theta_s^{\text{real}} = 0.5\lambda/D$, $\Delta\theta_s^{\text{real}} = \lambda/D$ and $\Delta\theta_s^{\text{real}} = 1.5\lambda/D$ are shown by the dashed lines in Fig. A.1(b-d) respectively. The total diffracted field, i.e. the summation of the two airy patterns, are shown by the solid curves. It is assumed that no phase information is present as only direct detection scenarios are considered in this work.

By angularly separating the two point sources it is investigated whether or not the two sources can be distinguished in the focal plane image. The displacement of the two peaks in the focal plane image is referred to as the *apparent source separation*, $\Delta\theta_s^{\text{app}}$, whereas the real angular separation $\Delta\theta_s^{\text{real}}$ is referred to as the *real source separation*. It can be seen that, for a source separation of $\Delta\theta_s^{\text{real}} = 0.5\lambda/D$, only one peak can be identified in the superimposed power pattern. The apparent source separation is $\Delta\theta_s^{\text{app}} = 0$. For an increased source separation of $\Delta\theta_s^{\text{real}} = \lambda/D$ two peaks can be identified in the diffracted pattern in the focal plane, as shown in Fig. A.1(c). The angular separation of the peaks, however, is smaller than the actual separation of the individual Airy-discs: $\Delta\theta_s^{\text{app}} < \Delta\theta_s^{\text{real}}$. Also, the *dynamic range*, DR, defined as the normalized interpeak power, is quite low and the two peaks can barely be distinguished. For a source separation of $\Delta\theta_s^{\text{real}} = 1.5\lambda/D$ (Fig. A.1(d)) the apparent source separation is approximately the real source separation and the dynamic range is increased. The resolution limits of this two-source experiment are investigated in Sec. A.1.3.

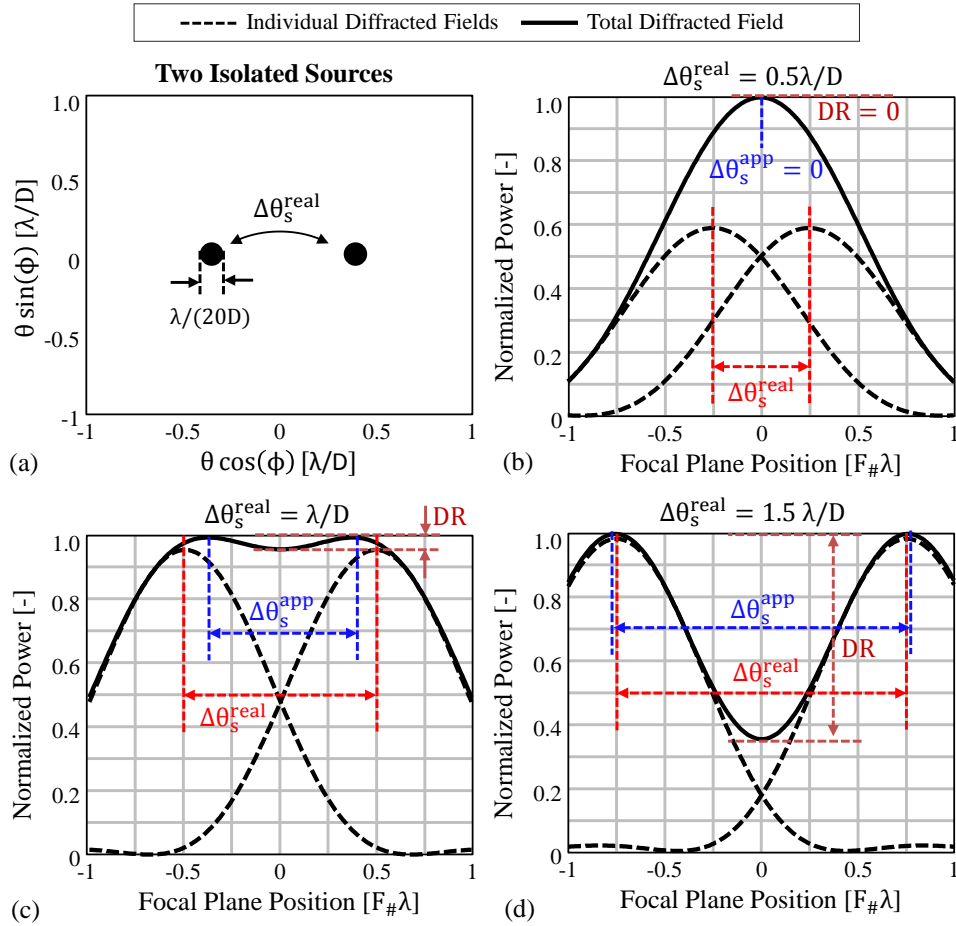


Figure A.1: Two point source experiment. In (a) two isolated sources in the far-field of the optics are defined with an angular dimension of $\lambda/(20D)$ and real source separation of $\Delta\theta_s^{\text{real}}$. The diffracted fields in the focal plane are shown for a source separation of $\Delta\theta_s^{\text{real}} = 0.5\lambda/D$ in (b), $\Delta\theta_s^{\text{real}} = \lambda/D$ in (c) and $\Delta\theta_s^{\text{real}} = 1.5\lambda/D$ in (d). The diffracted fields associated to each point source are shown by the dashed lines, while the summation is shown by the solid line. The definition of real source separation, apparent source separation and dynamic range is indicated.

A.1.2 Distributed Sources

A less commonly used two source experiment is performed with distributed sources. In automotive or security imaging applications, however, sources often can be considered distributed. A source is distributed when the source solid angle is much larger than the antenna solid angle. The two source experiment with distributed sources is explained in Fig. A.2. In Fig. A.2(a), the uv -plane in the far-field of the optical system is shown, containing two distributed source. The sources are considered to be semi-infinite in one dimension, i.e. the u -plane, whereas they are modeled with a $\lambda/(20D)$ thickness in the v -plane. The diffracted patterns in the focal plane, associated to the u -plane ($\phi = 0^\circ$), are shown for a source separation of $\Delta\theta_s^{\text{real}} = 0.5\lambda/D$ in Fig. A.2(b), $\Delta\theta_s^{\text{real}} = 1\lambda/D$ in Fig. A.2(c) and $\Delta\theta_s^{\text{real}} = 1.5\lambda/D$ in Fig. A.2(d). Here, the apparent source separation is

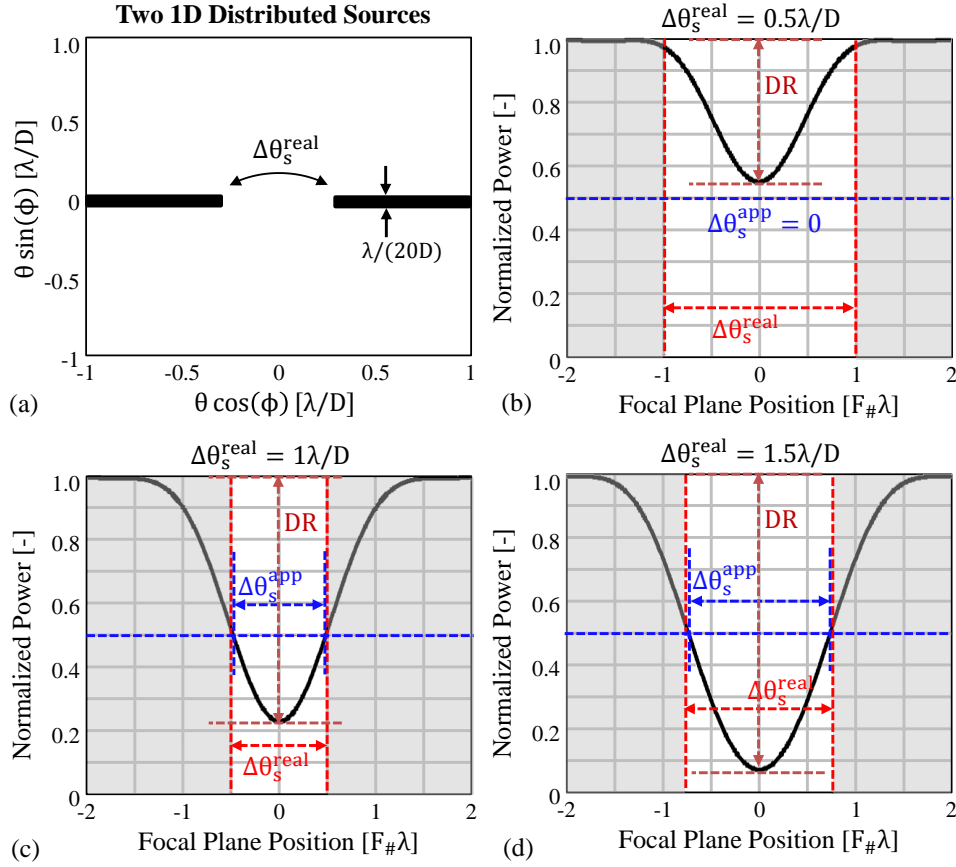


Figure A.2: Two distributed source experiment. In (a) two distributed sources in the far-field of the optics are distributed in the u -plane whereas the sources are defined with an angular dimension of $\lambda/(20D)$ in the v -plane. The sources are angularly separated by $\Delta\theta_s^{\text{real}}$. The diffracted fields in the focal plane are shown for a source separation of $\Delta\theta_s^{\text{real}} = 0.5\lambda/D$ in (b), $\Delta\theta_s^{\text{real}} = \lambda/D$ in (c) and $\Delta\theta_s^{\text{real}} = 1.5\lambda/D$ in (d). The definition of real source separation, apparent source separation and dynamic range is indicated.

defined at the -3 dB decay in the diffracted power pattern. The dynamic range, DR, is defined equivalently as for the two-point-source experiment in the previous subsection.

A.1.3 Rayleigh Limit and Diffraction Limit

The apparent source separation and dynamic range, as function of real source separation, are shown in Fig. A.3(a) and Fig. A.3(b) respectively for both isolated sources (dashed curves) and distributed sources (dotted curves). The desired resolution in Fig. A.3(a) is when $\Delta\theta_s^{\text{app}} = \Delta\theta_s^{\text{real}}$ for any sources separation.

For isolated sources, the point where the two peaks first can be distinguished, i.e. the angle where $\Delta\theta_s^{\text{app}} \neq 0$ for the first time, is referred to as the *Sparrow Limit*, δ_{Sparrow} , and be approximated to be [111, 164]

$$\delta_{\text{Sparrow}} \approx 0.95\lambda/D \quad (\text{A.2})$$

A more commonly used definition of resolution is the angular separation when $\Delta\theta_s^{\text{real}} \approx \Delta\theta_s^{\text{app}}$, which is often referred to as the *diffraction limit* and is in the order of the Rayleigh Limit $\Delta\theta \approx 1.22\lambda/D$ (first null of the Airy function).

$$\delta_{\text{Rayleigh}} \approx 1.22\lambda/D \quad (\text{A.3})$$

In the Rayleigh limit the central maximum of one source falls into the first minimum of the other source. The dynamic range, however, to distinguish the two sources is still very low, as is shown in Fig. A.3(b). At the Rayleigh limit, only a -1.6 dB decay in the diffracted pattern is observed.

Distributed sources can be distinguished sooner than isolated sources. Although the

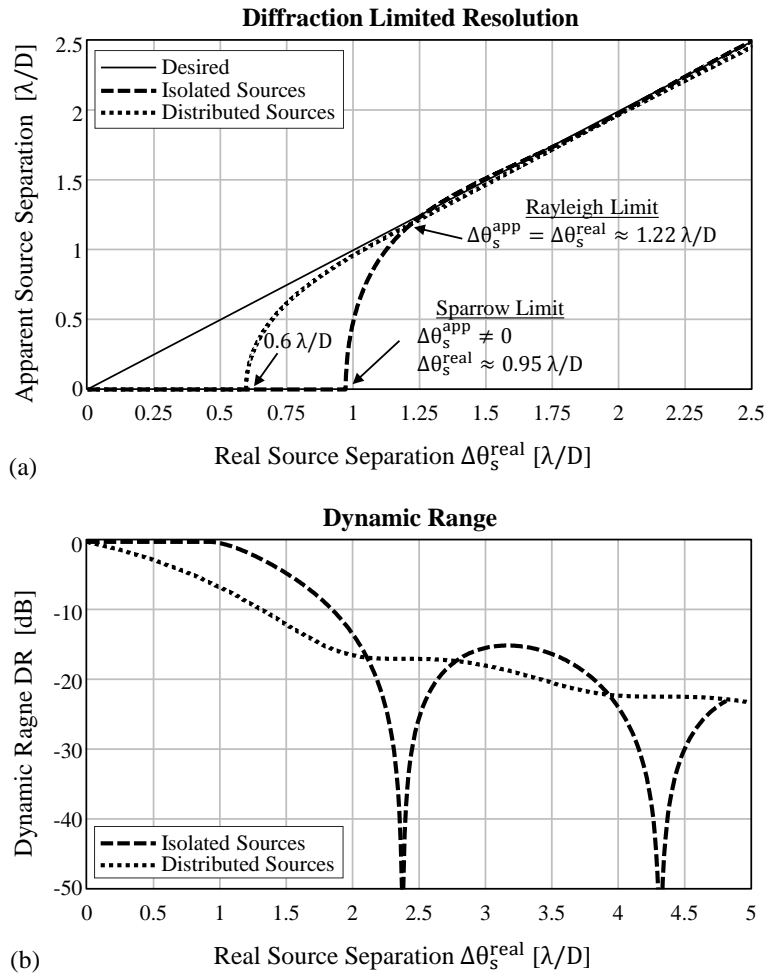


Figure A.3: Resolution and dynamic range of a diffraction limited quasi-optical system of the two point experiment as shown in Fig. A.1 for isolated sources and in Fig. A.2 for distributed sources. In (a) the diffraction limit is shown, defining the first point where two isolated sources can be distinguished as the Sparrow limit, i.e. $\Delta\theta_s^{\text{real}} \approx 0.97\lambda/D$ and the point where the apparent source separation is approximately the real source separation as the Rayleigh limit $\Delta\theta_s^{\text{real}} \approx \Delta\theta_s^{\text{app}} \approx 1.22\lambda/D$. In (b) the dynamic range is shown.

Sparrow limit is not explicitly defined in literature for distributed sources, it can be seen that the smallest angular source separation that two sources can be distinguished with a dynamic range larger than -3 dB is approximately $\Delta\theta_s^{\text{real}} \approx 0.6\lambda/D$. Both the resolution limit as the dynamic range are better for distributed sources w.r.t. isolated sources. Therefore, depending on the type of source, different trade-offs can be made in terms of dynamic range and resolution.

A.2 Sampling and Interpolation

The resolution limits derived in the previous subsection are attributed to the diffraction of the incident fields with the optics. These limits were studied with an infinite number of sampling points in the focal plane. However, in reality the field is sampled with a finite amount of points that is dictated by the sampling periodicity of the array in the focal plane.

Let us consider the two-source-experiment with isolated sources from Sec. A.1.1. The diffracted fields from Fig. A.1 are again summarized in Fig. A.4 for a source separation of $\Delta\theta_s^{\text{real}} = 0.5\lambda/D$ in Fig. A.4(a,b), $\Delta\theta_s^{\text{real}} = 1\lambda/D$ in Fig. A.4(c,d) and $\Delta\theta_s^{\text{real}} = 1.5\lambda/D$ in Fig. A.4(e,f). In the left column, Fig. A.4(a,c,e), the fields are sampled with a sampling periodicity of $d_f = 0.5F_{\#}\lambda$ while in the right column, Fig. A.4(b,d,f), the fields are sampled with a periodicity of $d_f = 1F_{\#}\lambda$. The field in the focal plane is reconstructed using either a linear interpolation method (red lines) or a spline interpolation method (blue lines).

By observing the reconstructed patterns in Fig. A.4, it can be verified that the diffracted field in the focal plane can essentially be fully reconstructed with a sampling periodicity of $0.5F_{\#}\lambda$. A sampling periodicity of $1F_{\#}\lambda$ is not proven to be sufficient to identify the two peaks in Fig. A.4(d), nor to reconstruct adequately the location of peak in Fig. A.4(f).

In Fig. A.5 the apparent source separation, as function of real source separation, is shown for both isolated sources, Fig. A.5(a), and distributed sources, Fig. A.5(b). The three main sampling configurations are considered, i.e. $d_f = 0.5F_{\#}\lambda$, $d_f = 1F_{\#}\lambda$ and $d_f = 2F_{\#}\lambda$ and both the linear interpolation method and spline interpolation method are shown. The Sparrow limit and Rayleigh limit, for both isolated and distributed sources, is achieved for a sampling periodicity of $d_f = 0.5F_{\#}\lambda$ with a spline interpolation.

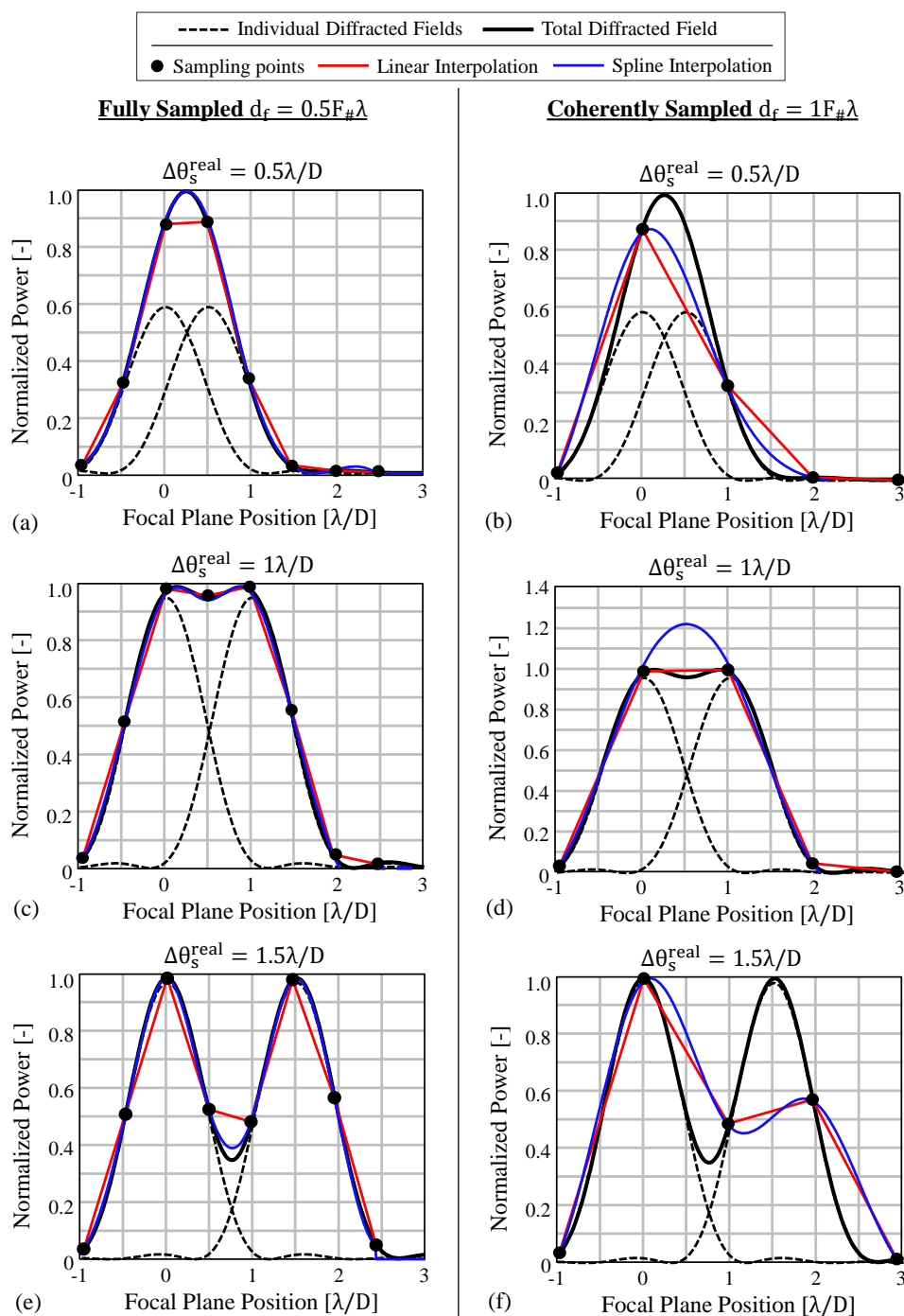


Figure A.4: Sampling and interpolation of the diffracted field in the focal plane coming from two isolated point sources as discussed in Fig. A.1. In the left column (a,c,e) the fields are sampled with a sampling periodicity of $0.5F_{\#}\lambda$ while in the right column (b,d,f) the fields are sampled with $1F_{\#}\lambda$. The field is reconstructed with a linear interpolation (red curves) and spline interpolation (blue curves). A source separation of $\Delta\theta_s^{\text{real}} = 0.5\lambda/D$ (a,b), $\Delta\theta_s^{\text{real}} = 1\lambda/D$ (c,d) and $\Delta\theta_s^{\text{real}} = 1.5\lambda/D$ (e,f) are considered.

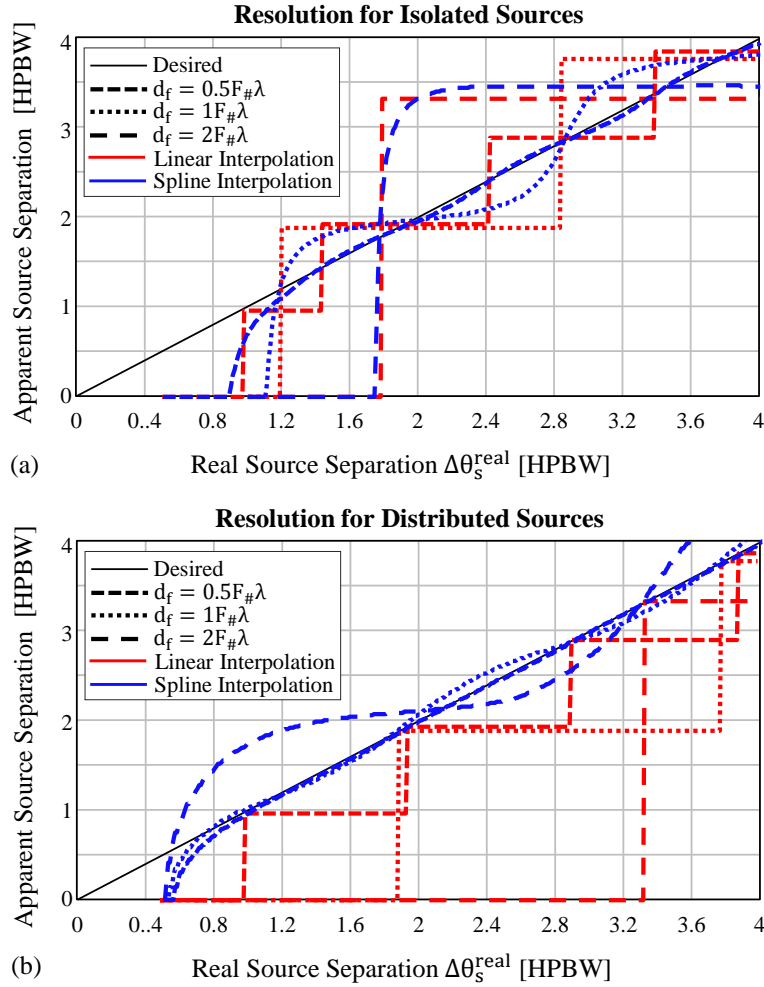


Figure A.5: Two source experiment with a finite amount of sampling points. (a) Isolated sources (b) Distributed sources. The fields are sampled with a sampling periodicity of $d_f = 0.5F_{\#}\lambda$ (densely dashed), $d_f = 1F_{\#}\lambda$ (dotted) and $d_f = 2F_{\#}\lambda$ (sparsely dashed) and interpolated using a linear interpolation method (red curves) and spline interpolation method (blue curves). For both isolated sources and distributed sources, the diffraction limit is achieved with a $0.5F_{\#}\lambda$ sampled focal plane with a spline interpolation method applied.

Appendix B

NEP for Cryogenically Cooled Focal Plane Arrays

The first passive (mm-wave) imaging systems, consisting of diodes operating around 90 GHz [22] and bolometers [54], only had few detectors, resulting in low frame rates and/or a small FoV. Since then, in order to achieve a sufficient SNR for fast frame-rates, or to achieve extreme sensitivities, FPAs have been cryogenically cooled [30, 38, 48] so that the NEP could compensate for the short available integration time. The optimal FPA configurations as discussed in Chapter 2 was based on the assumption that the noise in the system was dominated by the noise introduced by the detectors. Instead, when the FPA is cooled, ultimately the noise can become limited to the noise introduced by the signal fluctuations itself, i.e. *background noise limited*. This appendix studies the effect of cooling the FPA on imaging speed and temperature sensitivity and provides the design guidelines for focal plane sampling in such scenario. In this study it is assumed that the sources are in the Rayleigh-Jeans limit (2.3) w.r.t. the operational frequency band of the radiometer, which is usually the case for commercial applications.

B.1 Temperature Sensitivity, Imaging Speed and Noise Equivalent Power

Let us start by recalling and rewriting the expressions of the temperature sensitivity (2.10) and imaging speed (2.11) as has been derived in Sec. 2.2.1:

$$\text{NETD} \triangleq \Delta T|_{\text{SNR}=1} = \frac{\text{NEP}}{k_B \bar{\eta}_{\text{opt}} \Delta f_{\text{RF}} \sqrt{2\tau_{\text{int}}}} \quad (\text{B.1})$$

$$s = \frac{1}{\tau_i} = \left(\frac{\text{NETD} \cdot k_B \bar{\eta}_{\text{opt}} \Delta f_{\text{RF}}}{\text{NEP}} \right)^2 \frac{2}{N_t} \quad (\text{B.2})$$

In the analysis used throughout the rest of this dissertation, it was assumed that the NEP was dominated by the electronic noise that was introduced by the detector itself.

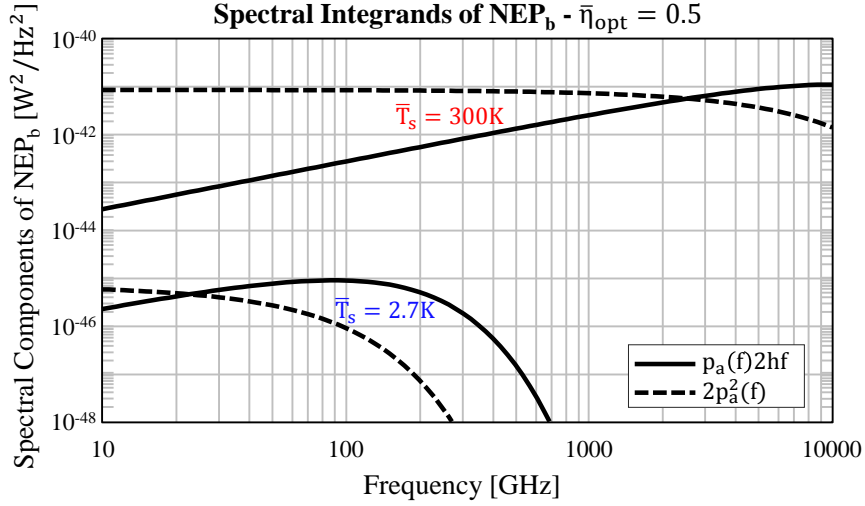


Figure B.1: Spectral integrands of the NEP_b (B.4) for an average source temperature of $\bar{T}_S = 2.7\text{ K}$ and 300 K and average antenna efficiency $\bar{\eta}_{\text{opt}} = 0.5$.

However, usually the NEP can be divided into two contributions:

$$\text{NEP}^2 = \text{NEP}_{\text{det}}^2 + \text{NEP}_b^2 \quad (\text{B.3})$$

In (B.3), NEP_{det} is the detector noise that is considered in this dissertation which was only determined by the detectors and the read-out mechanism, while the background noise, NEP_b , is associated with the thermal fluctuations of the signals arriving at the input of the detector. In the case that $\text{NEP}_b \gg \text{NEP}_{\text{det}}$, the system is referred to as *background-noise limited*. The NEP of a background limited system is estimated in [54, 107, 108] as:

$$\text{NEP}_b = \sqrt{\int_{\Delta f_{\text{RF}}} p_a(f) 2hf df + \int_{\Delta f_{\text{RF}}} 2p_a^2(f) df} \quad (\text{B.4})$$

with $p_a(f)$, the received spectral power, is the integrand in (2.5). The two integrands of the spectral integrations, $p_a(f)2hf$ and $p_a^2(f)$, are shown in Fig. B.1 as function of frequency. An average antenna efficiency of $\bar{\eta}_{\text{opt}} = 0.5$ is assumed and two source temperatures are considered; $\bar{T}_S = 2.7\text{ K}$ for sky observations [100] and $\bar{T}_S = 300\text{ K}$. For cold-sky observations, the $p_a(f)2hf$ -term is of importance. Instead, in the Rayleigh-Jeans limit ($hf \ll k_B T$) of the 300 K source, and for sufficiently high optical efficiency, the first term of (B.4) is much smaller than the second term and can be neglected. When applying the Rayleigh-Jeans approximation and assuming $\bar{\eta}_{\text{opt}}^2 \approx \frac{1}{\Delta f_{\text{RF}}} \int_{\Delta f_{\text{RF}}} (\eta_{\text{opt}}(f))^2 df$, (B.4) simplifies to (B.5) which depends linearly on source temperature, antenna efficiency and with a square-root dependency on operational bandwidth.

$$\text{NEP}_b^{\text{RJ}} = k_B \bar{T}_S \bar{\eta}_{\text{opt}} \sqrt{2\Delta f_{\text{RF}}} \quad (\text{B.5})$$

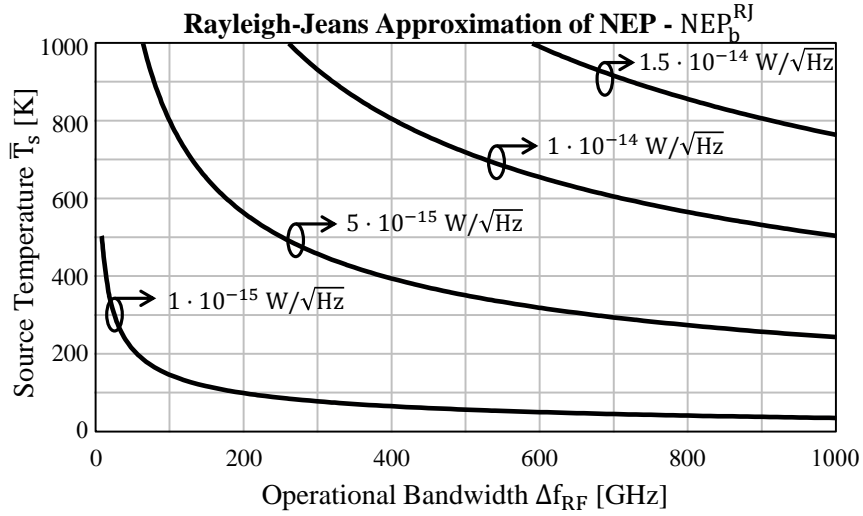


Figure B.2: Background-noise limited NEP_b^{RJ} (B.5) in the Rayleigh-Jeans limit for $\bar{\eta}_{\text{opt}} = 0.5$.

In microwave radiometry, the NEP_b^{RJ} (B.5) is usually the dominant noise contribution. The NEP_b^{RJ} is shown in Fig. B.2 as function of operational bandwidth and black-body temperature ($\bar{\eta}_{\text{opt}} = 0.5$). It can be seen that for a black-body around 300K the NEP_b is in the order of $10^{-15} \text{ W}/\sqrt{\text{Hz}}$.

The NEP_b reported at the antenna terminals can be decomposed in two main contributions; $\text{NEP}_b^2 = \text{NEP}_s^2 + \text{NEP}_{\text{und}}^2$ where NEP_s is associated to thermal fluctuations of the source and NEP_{und} to thermal fluctuations coming from the undesired sources which are either the instrument box or (sky-) background for isolated sources. Therefore, in a background-noise limited system, care has to be taken that the temperature of the instrument box or background is such that NEP_{und} can be neglected as is explained in Appendix C.

The Rayleigh-Jeans limits of the sensitivity (B.1) and imaging speed (B.2) for background-noise limited systems are summarized in Table B.1 together with the detector-noise limited case ($\text{NEP}_b \ll \text{NEP}_{\text{det}}$). The sensitivities in the two cases, have a different dependency on RF bandwidth Δf_{RF} . Only a square-root dependency on bandwidth can be found for

Table B.1: Sensitivity and imaging speed for detector- and background-noise limited systems in the Rayleigh-Jeans Limit

Noise Equivalent Power	Sensitivity	Imaging Speed
$\text{NEP}_{\text{det}} \gg \text{NEP}_b$	$\text{NETD}_{\text{det}} = \frac{\text{NEP}_{\text{det}}}{k_B \bar{\eta}_{\text{opt}} \Delta f_{\text{RF}} \sqrt{\frac{\tau_i}{N_t}}}$	$s_{\text{det}} = \left(\frac{\text{NETD} \cdot k_B \bar{\eta}_{\text{opt}} \Delta f_{\text{RF}}}{\text{NEP}_{\text{det}}} \right)^2 \frac{1}{N_t}$
$\text{NEP}_{\text{det}} \ll \text{NEP}_b$	$\text{NETD}_b = \frac{\bar{T}_S \sqrt{2N_t}}{\sqrt{\Delta f_{\text{RF}} \tau_i}}$	$s_b = \frac{\Delta f_{\text{RF}}}{2N_t} \left(\frac{\text{NETD}}{T_S} \right)^2$

background-noise limited systems while a linear dependence from BW is found for the detector-noise limited case. One should note the apparent cancellation of the optical efficiency in the sensitivity for background limited cases. However, one should also recall that this approximation is only valid for a very high optical efficiency and source temperature.

B.2 FPA Design for Cooled Systems

The previous section showed different expressions for sensitivity and imaging speed in Table B.1, depending on the dominant noise contribution in the system. The FPA architecture needs to be designed accordingly. In this section, we will compare the imaging speed for the different sampling configurations from Fig. 2.4 for the background-noise limited scenario and compare it to the detector-noise limiting scenarios as has been studied in Chapter 2. There, the expression of imaging speed ratio, (2.12), did not depend on NEP since it was assumed that the NEP was only depending on the detector and therefore assumed to be equal for different focal plane architectures. In this study the NEP is different as it depends on both bandwidth and efficiency. The imaging speed ratio (SR) to compare different focal plane architectures is now (B.6):

$$\text{SR} = \frac{s^\alpha}{s^\beta} = \left(\frac{\bar{\eta}_{\text{opt}}^\alpha \Delta f_{\text{RF}}^\alpha \text{NEP}^\beta}{\bar{\eta}_{\text{opt}}^\beta \Delta f_{\text{RF}}^\beta \text{NEP}^\alpha} \right)^2 \frac{N_t^\beta}{N_t^\alpha} \quad (\text{B.6})$$

, where s^α is the imaging speed of configuration α , that is compared to the imaging speed of the reference configuration β , s^β . The imaging speed ratio depends on the average optical efficiency of the quasi-optical system $\bar{\eta}_{\text{opt}}$, absolute frequency bandwidth Δf_{RF} , Noise Equivalent Power NEP and scanning penalty N_t for under sampled array. The different sampling configuration from Fig. 2.4 are compared relatively to each other using the imaging speed ratio defined in (B.6).

B.2.1 FPA Configurations

The different FPAs are assumed to be operating with the same operational bandwidth Δf_{RF} and sampled $d_f = [0.5 \ 1 \ 2] F_{\#} \lambda_c$ at the center frequency f_c . Including only the spill-over efficiency, Fig. 2.2, in the analysis ($\eta_{\text{feed}} = 1$), the average optical efficiency can then be approximated to be the spill-over efficiency at the f_c , i.e. $\bar{\eta}_{\text{opt}} \approx [0.15 \ 0.46 \ 0.84]$ for the sampling configurations $d_f = [0.5 \ 1 \ 2] F_{\#} \lambda_c$ respectively as can be seen in Fig. 2.2. In the comparison of the different sampling configurations, we define the imaging speed ratio $\text{SR} = s^\alpha/s^\beta$ as the speed ratio of the coherent- and maximum gain sampled FPAs, $s^\alpha = s^{[1 \ 2] F_{\#} \lambda_c}$, w.r.t. to the reference case of a fully sampled FPA, $s^\beta = s^{0.5 F_{\#} \lambda_c}$. In Fig. B.3, the imaging speed ratio SR is plotted as function of $\text{NEP}_{\text{det}}/\text{NEP}_{\text{b}}$ where the Rayleigh-Jeans limit $\text{NEP}_{\text{b}}^{\text{RJ}}$ (B.5) is used.

For a detector-noise limited system, i.e. when $\text{NEP}_{\text{det}} \gg \text{NEP}_{\text{b}}$, the imaging speed ratio approaches the limits as are summarized in Table B.2. These are the results as discussed in Sec. 2.3. For a background-noise limited system, i.e. when $\text{NEP}_{\text{det}} \ll \text{NEP}_{\text{b}}$, the imaging

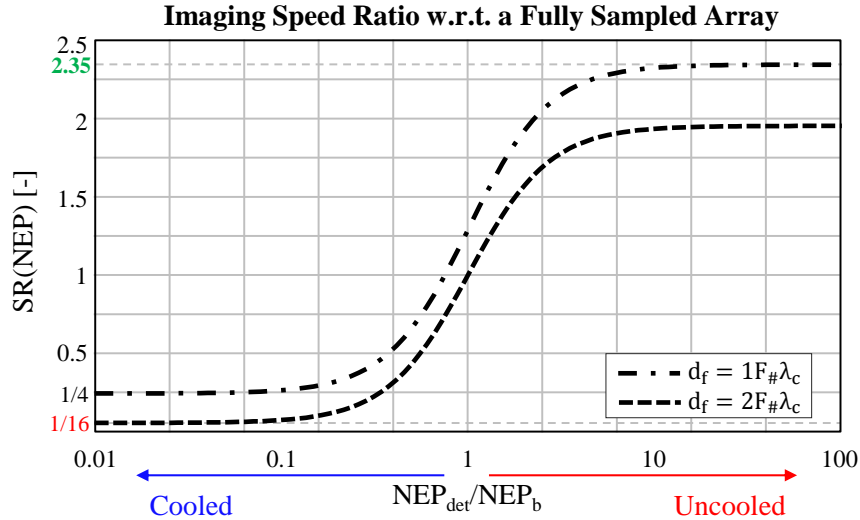


Figure B.3: Imaging Speed Ratio as function of $\text{NEP}_{\text{det}}/\text{NEP}_{\text{b}}$. The imaging speed of the coherent- and maximum gain ($d_f = [1 \ 2]F_{\#}\lambda_c$) FPA configurations is normalized to the speed of the fully sampled $d_f = 0.5F_{\#}\lambda_c$ FPA architecture.

Table B.2: Imaging Speed Ratio w.r.t. a fully sampled array

d_f	$\bar{\eta}_{\text{opt}}$	N_t	SR_{det}	SR_{b}
$0.5F_{\#}\lambda_c$	0.15	1	1	1
$1F_{\#}\lambda_c$	0.46	4	2.35	1/4
$2F_{\#}\lambda_c$	0.84	16	1.96	1/16

speed ratio approaches the limits summarized in the fifth column of Table B.2. As already have been stated, the imaging speed does not depend on optical efficiency (provided that $hf \ll k_B T_S$ and optical efficiency is sufficiently high). In this case, the imaging speed ratio depends purely on the number of detectors in the focal plane; the fully sampled FPA configuration is optimal.

B.2.2 Bandwidth Utilization

Let us investigate the improvement in imaging speed that one can obtain when a relative bandwidth up to 1 : 3 around f_c is used for each of the sampling configurations. This study is equivalent as the study presented in Sec. 2.3.2 for uncooled FPAs and is now extended for background-noise limited FPAs. The imaging speed is defined as function of this relative bandwidth, $\text{SR}(\nu) = s^\alpha(\nu)/s^\beta(\nu = 1.22)$. The reference case $s^\beta(\nu = 1.22)$ is defined with a 20% fractional bandwidth (20% fractional bandwidth is equivalent to a $\nu = f_{\text{max}}/f_{\text{min}} \approx 1.22$ relative bandwidth). This is illustrated in Fig. 2.6(a), where the three sampling configurations $d_f = [0.5 \ 1 \ 2]F_{\#}\lambda_c$ are sampled at f_c and have as reference case a 20% fractional bandwidth (dark gray area below the spill-over efficiency curve).

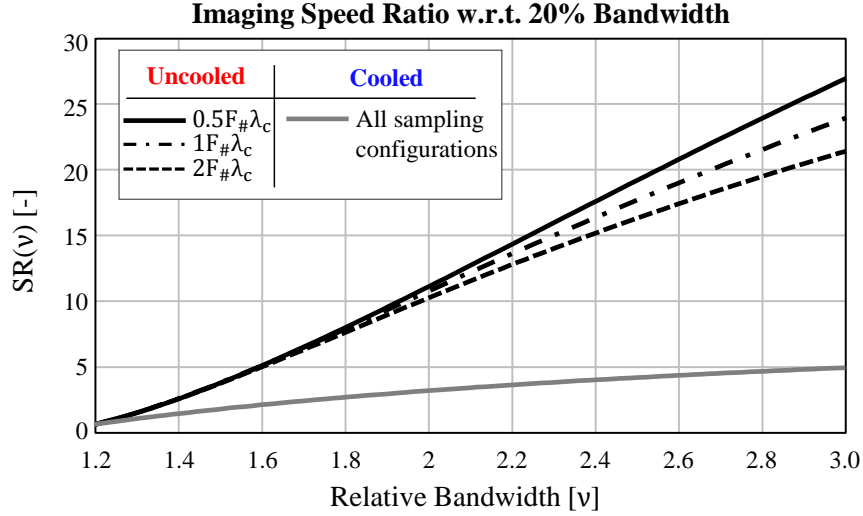


Figure B.4: The imaging Speed Ratio $SR(\nu) = s^\alpha(\nu)/s^\beta(\nu = 1.22)$ as function of relative bandwidth $\nu = f_{max}/f_{min}$. The effect of using a large operational frequency band is studied w.r.t. the reference case of 20% fractional bandwidth as shown in Fig. 2.6(a). The bandwidth around f_c is increased until $\nu = 3$. The results for the detector noise limited FPA systems are discussed in Sec. 2.3.2.

For each configuration the relative bandwidth ν is increased (light gray area below $\eta_{so}^{\Omega_O}$) and is compared in speed to the reference case. This leads to the imaging speed ratios as summarized in Fig. B.4 where the results from Sec. 2.3.2 are summarized by the black curves. The imaging speed ratio for the background-noise limited FPA is indicated by the grey curve.

In a background-noise limited scenario, the imaging speed is linear depending on bandwidth and thus the imaging speed ratio is increasing accordingly for all three sampling configurations. With a relative bandwidth of 1:3 the absolute bandwidth is increased with a factor of 5. Since the imaging speed does not depend on antenna efficiency, at first approximation, the imaging speed ratio for background-noise limited FPAs, does not change for the different FPA configurations.

Appendix C

Greybodies and Sensitivity to Undesired Sources

In this appendix we will introduce the emissivity parameter that describes the radiation of non-perfect blackbody sources. It is shown how, in the Rayleigh Jean limit of Planck's law, a radiometric temperature can be defined for these so-called greybodies. Subsequently, it is investigated how the sensitivity of a radiometer is influenced by undesired incoherent sources and a limit is imposed on the stability of these sources to have a 10% inaccuracy on the NETD. This study is first conducted for detector noise limited FPAs, based on the spill-over in the instrument box or sky-background, and later extended for a background-noise limited scenario. In a background-noise limited scenario not only the stability of the temperature of the instrument box or sky background is important, but also the absolute temperature since the NEP increases with the source temperature. Therefore a limit on the absolute temperature is imposed to have a 10% inaccuracy in the NETD.

C.1 Greybodies and Radiometric Temperature

Planck's law (2.2) describes the radiated power of an ideal radiator, i.e. a *blackbody*. Kirchhoff's law of thermal radiation showed that a perfect radiator should also be a perfect absorber [165]. However, in reality every object/material can also reflect or even transmit incident power and are, instead, referred to as *greybodies*. Of the total incident power flux, S_{inc} , incident on a greybody, ΓS_{inc} is reflected, $T S_{\text{inc}}$ is transmitted and αS_{inc} is absorbed. As is self evident, the summation of the reflectivity, Γ , transmissivity, T , and absorptivity, α , is unity:

$$1 = \Gamma + T + \alpha \tag{C.1}$$

Since Kirchhoff state that the power absorbed by an object in thermal equilibrium must be equal to the power transmitted, an *emissivity*, ϵ , can be defined equivalently to the absorptivity, $\epsilon = \alpha$. For most opaque objects the transmissivity $T = 0$, and

$$\epsilon = 1 - \Gamma \quad (\text{C.2})$$

The spectral radiation of a greybody can be expressed as the emissivity ϵ multiplied by Planck's law of blackbody radiation (2.2):

$$B(f, \Omega) = \epsilon \frac{f^2}{c^2} \frac{2hf}{e^{\frac{hf}{k_B T(\Omega)}} - 1} \quad (\text{C.3})$$

Note that emissivity itself can depend significantly on frequency. In this study the emissivity is assumed to be constant over the frequency range of operation. Also, here it is assumed that the radiometer is operating in the Rayleigh Jeans limit w.r.t. the sources (i.e. $hf \ll k_B T$) such that Planck's law can be approximated to

$$B(f, \Omega)|_{hf \ll k_B T} \approx B^{\text{RJ}}(f, \Omega) = \epsilon \frac{f^2}{c^2} 2k_B T(\Omega) \quad (\text{C.4})$$

In this specific scenario a *radiometric temperature* can be defined as in [166]:

$$T_R(\Omega) = \epsilon T(\Omega) \quad (\text{C.5})$$

In the remaining portion of this appendix, the considered temperatures are therefore radiometric temperatures and can differ from the physical temperature, depending on material and frequency. However, the presented analysis does not include contributions due to reflected power.

Another important note is that, similarly, the radiometric sky temperature can be significantly high at submm-wavelengths [22]. In this study the contribution of atmospheric attenuation and re-radiation can be included in the radiometric temperature of the source or background.

C.2 Received Power by Undesired Sources

In [100] the impact of undesired sources on the SNR is studied in the scenario of astronomical sky observations and is a narrowband approximation. In such scenario both the instrument box and target source (astronomical sky) are in the Wien's limit w.r.t. the frequency band that the radiometer is operating in. Here it is assumed that the radiometer is operating in the Rayleigh Jeans limit w.r.t. the sources (i.e. $hf \ll k_B T$). Consider the radiometric configuration as shown in Fig. C.1. Here, essentially three different incoherent sources that contribute to the total received power will be considered [167]:

1. Radiation from the target source at average radiometric temperature \bar{T}_S resulting in P_S of power absorbed by the detector.
2. Radiation from the background at radiometric temperature T_B resulting in P_B of power absorbed by the detector. This radiation can come from the atmosphere or surrounding objects.

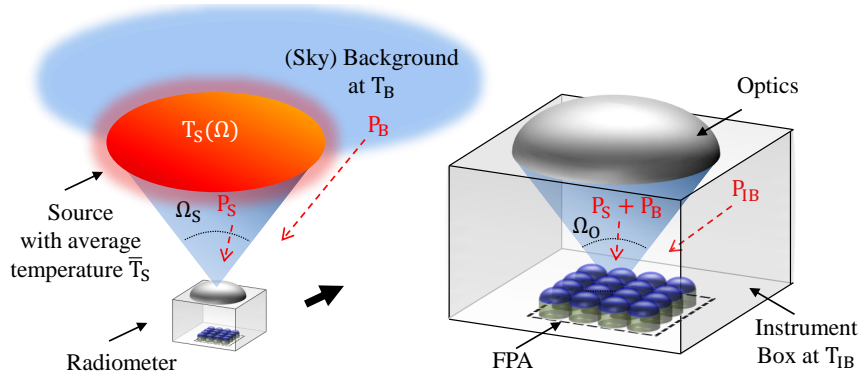


Figure C.1: Investigated quasi-optical system in the presence of an incoherent source with temperature distribution $T_S(\Omega)$ and average temperature \bar{T}_S distributed over a source solid angle Ω_S . The radiometer optics that subtend the FPA with a solid angle of Ω_O . The FPA and optics are placed in an instrument box that is kept at a temperature T_{IB} .

3. Radiation from the optics and instrument box at radiometric temperature T_{IB} resulting in P_{IB} of power absorbed by the detector.

The temperatures of the considered sources are radiometric temperatures and can be used for non-perfect blackbody radiators. The total received power by the central antenna feed (assumed to be representative for the entire array) P_a can be approximated to be the summation of:

$$P_a = P_S + P_{\text{und}} \quad (\text{C.6a})$$

$$P_{\text{und}} = P_B + P_{IB} \quad (\text{C.6b})$$

where P_{und} are the undesired sources. The received power by a single polarized antenna coming from an incoherent source with angular distribution Ω_S can be evaluated by the integration of the spectral brightness from (2.2) over the operational bandwidth $\Delta f_{RF} = f_{\text{max}} - f_{\text{min}}$ and over the solid angle viewed and weighted by the effective area $A_{\text{eff}}(f, \Omega)$:

$$P = \frac{1}{2} \int_{f_{\text{min}}}^{f_{\text{max}}} \int_{\Omega} A_{\text{eff}}(f, \Omega) B(f, \Omega) d\Omega df \quad (\text{C.7})$$

Depending on which incoherent source from Equation C.6 is under investigation, the effective area is associated to either the antenna feed, A_{eff}^f , or the secondary optics, A_{eff}^O :

$$A_{\text{eff}}^f(f, \Omega) = \frac{c^2}{f^2} \frac{1}{4\pi} \eta_{\text{feed}}(f) D^f(f, \Omega) \quad (\text{C.8a})$$

$$A_{\text{eff}}^O(f, \Omega) = \frac{c^2}{f^2} \frac{1}{4\pi} \eta_{\text{opt}}(f) D^O(f, \Omega) \quad (\text{C.8b})$$

where $\eta_{\text{feed}}(f)$ and $\eta_{\text{opt}}(f)$ are the feed's and systems optical efficiency respectively. η_{feed} contains all losses associated to the feed such as matching- and ohmic losses. In (C.8) $D^f(f, \Omega)$ and $D^O(f, \Omega)$ are the directivity associated to the antenna feed or the secondary optics respectively. We apply the Rayleigh-Jeans approximation from (2.3) and assume an average temperature \bar{T} of the incoherent source of interest within the source solid angle. The definition of directivity of antennas implies that $4\pi = \int_{4\pi} D(\Omega)d\Omega$. Therefore, the integration over the solid angle in (C.7) divided by 4π (C.9) defines how much power is coupled to either the secondary optics or source angular dimension. This ratio is defined as the spill-over efficiency with respect to either the optics $\eta_{\text{so}}^{\Omega_O}$ or the source $\eta_{\text{so}}^{\Omega_S}$:

$$\eta_{\text{so}}^{\Omega_O}(f) = \frac{\int^{\Omega_O} D^f(f, \Omega)d\Omega}{4\pi} \quad (\text{C.9a})$$

$$\eta_{\text{so}}^{\Omega_S}(f) = \frac{\int^{\Omega_S} D^O(f, \Omega)d\Omega}{4\pi} \quad (\text{C.9b})$$

The optical efficiency $\eta_{\text{opt}}(f)$ of the quasi-optical system can be expressed as the feed efficiency $\eta_{\text{feed}}(f)$ multiplied with the spill-over efficiency $\eta_{\text{so}}^{\Omega_O}$ w.r.t. the optics $\eta_{\text{opt}}(f) = \eta_{\text{feed}}(f)\eta_{\text{so}}^{\Omega_O}(f)$. Using the Rayleigh-Jeans approximation of the spectral brightness distribution (2.3), the received power (C.7) over the operational bandwidth Δf_{RF} , can now be approximated to be:

$$P \approx k_B \bar{T} \bar{\eta}_{\text{opt}} \Delta f_{RF} \quad (\text{C.10})$$

Where the average efficiency for each of the power contributions from (C.6) can be written as:

$$\bar{\eta}_{\text{opt}}^S = \frac{1}{\Delta f_{RF}} \int_{\Delta f_{RF}} \eta_{\text{feed}}(f) \eta_{\text{so}}^{\Omega_O}(f) \eta_{\text{so}}^{\Omega_S}(f) df \quad (\text{C.11a})$$

$$\bar{\eta}_{\text{opt}}^B = \frac{1}{\Delta f_{RF}} \int_{\Delta f_{RF}} \eta_{\text{feed}}(f) \eta_{\text{so}}^{\Omega_O}(f) (1 - \eta_{\text{so}}^{\Omega_S}(f)) df \quad (\text{C.11b})$$

$$\bar{\eta}_{\text{opt}}^{\text{IB}} = \frac{1}{\Delta f_{RF}} \int_{\Delta f_{RF}} \eta_{\text{feed}}(f) (1 - \eta_{\text{so}}^{\Omega_O}(f)) df \quad (\text{C.11c})$$

Here it is assumed that the optics of the instrument box have a sufficiently high transmissivity (in the case of a lens) or reflectivity (in the case of a reflector), that the thermal radiation of these optics, within solid angle Ω_0 , can be neglected. In the scenario of astronomical sky observations, this effect may not be neglected and can easily be included in the analysis as has been done in [100]. Here the effect of the instrument box and sky-background will be investigated on the sensitivity of the system.

C.3 Sensitivity to Instrument Box and Sky-Background

With direct detection, an important task is to keep the instrument box temperature T_{IB} at a stable temperature in order to be able to calibrate these power contributions out. Assuming we have a distributed source, $P_{\text{B}} = 0$ and the total received power can be expressed as:

$$P_a = P_{\text{S}} + P_{\text{IB}} = k_{\text{B}}(\bar{T}_{\text{S}}\bar{\eta}_{\text{opt}}^{\text{S}} + T_{\text{IB}}\bar{\eta}_{\text{opt}}^{\text{IB}})\Delta f_{\text{RF}} \quad (\text{C.12})$$

When T_{IB} is stable and known it can be calibrated out from the measurement. Suppose now the total received power fluctuates with $\Delta P_a = \Delta P_{\text{S}} + \Delta P_{\text{IB}}$ due to a temperature difference in the source equal to the NETD (2.10) $\Delta T_{\text{S}} = \text{NETD}$ and a small temperature difference in the instrument box with ΔT_{IB} . The power fluctuation can be expressed as:

$$\Delta P_{\text{S}} + \Delta P_{\text{IB}} = k_{\text{B}}(\text{NETD}\bar{\eta}_{\text{opt}}^{\text{S}} + \Delta T_{\text{IB}}\bar{\eta}_{\text{opt}}^{\text{IB}})\Delta f_{\text{RF}} \quad (\text{C.13})$$

In (C.13), ΔP_{S} results in a SNR=1 (2.4). In order to achieve 10% accuracy in the desired sensitivity we must fulfill the requirement:

$$\left. \frac{\Delta P_{\text{IB}}}{\Delta P_{\text{S}}} \right|_{\Delta T_{\text{S}}=\text{NETD}} < 0.1 \quad (\text{C.14})$$

And therefore the instrument box temperature must be kept stable with a maximum temperature fluctuation of:

$$\frac{\Delta T_{\text{IB}}}{\text{NETD}} < 0.1 \frac{\bar{\eta}_{\text{opt}}^{\text{S}}}{\bar{\eta}_{\text{opt}}^{\text{IB}}} \quad (\text{C.15})$$

For distributed sources and a feed efficiency that is sufficiently constant over frequency, we can approximate $\bar{\eta}_{\text{feed}}\bar{\eta}_{\text{so}} \approx \frac{1}{\Delta f_{\text{RF}}} \int_{\Delta f_{\text{RF}}} \eta_{\text{feed}}(f)\eta_{\text{so}}^{\Omega_O}(f)df$ such that

$$\frac{\Delta T_{\text{IB}}}{\text{NETD}} < \frac{0.1\bar{\eta}_{\text{so}}}{1 - \bar{\eta}_{\text{so}}} \quad (\text{C.16})$$

The maximum instrument temperature box fluctuation is shown in Fig. C.2 as function of average spill-over efficiency. As expected, with an increased spill-over within the instrument box, the box must be kept more stable.

Background-Noise limited system

When the system is background-noise limited, the instrument box with non-zero temperature will also contribute to the noise equivalent power; $\text{NEP}_b^2 = \text{NEP}_{\text{S}}^2 + \text{NEP}_{\text{IB}}^2$. Since the NEP directly influences the sensitivity, (2.10), we also must fulfill the requirement $\frac{\text{NEP}_{\text{IB}}}{\text{NEP}_{\text{S}}} < 0.1$ to achieve a 10% accuracy in the desired sensitivity. Using the Rayleigh-Jeans limit of the background NEP (B.5), this will lead to the relationship between the absolute temperature of the instrument box and source:

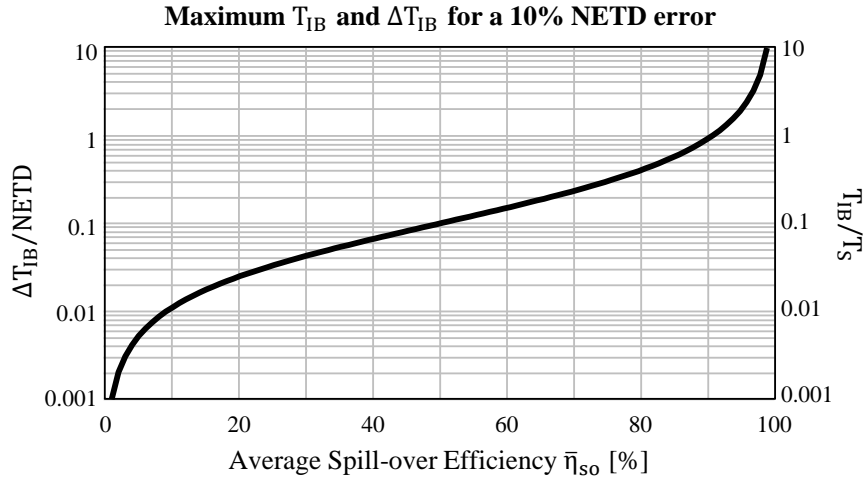


Figure C.2: Instrument box requirements to stay within a 10% error in NETD. When the system is detector-noise limited, the temperature fluctuations ΔT_{IB} is of importance whereas for a background-noise limited system also the absolute temperature T_{IB} must be kept low.

$$\frac{T_{\text{IB}}}{T_{\text{S}}} < \frac{0.1\bar{\eta}_{\text{so}}}{1 - \bar{\eta}_{\text{so}}} \quad (\text{C.17})$$

The relationship is equivalent with (C.16) and is quantified with the right y-axis in Fig. C.2. For example, consider a background-noise limited system with a sensitivity of $\text{NETD} = 100 \text{ mK}$ and sampled such that it has an average reflector spill-over efficiency of $\eta_{\text{so}} = 0.5$. If the system requires to image a $T_{\text{S}} = 300 \text{ K}$ source, the right y-axis in Fig. C.2 tells us that $T_{\text{IB}}^{\text{max}} = 30 \text{ K}$ whereas the left y-axis tells us $\Delta T_{\text{IB}}^{\text{max}} = 10 \text{ mK}$. Therefore, the instrument box needs to be kept at a temperature of $T_{\text{IB}} = 30\text{K} \pm 10 \text{ mK}$. However, please note that the results in Fig. C.2 are for the most pessimistic case since the Rayleigh-Jeans limits used for the derivation, always overestimate the received power for lower temperatures.

Furthermore, Fig. C.2 can also be used to study the effect when the source is not completely distributed. In order to stay within a 10% NETD error margin, the average spill-over efficiency w.r.t the source determines the allowable temperature fluctuations ΔT_{B} and absolute temperature T_{B} for background-noise limited systems. For isolated sources, the system is very sensitive to sky-temperature and its fluctuations which is more difficult to control than the temperature of the instrument box.

Appendix D

Current Responsivity of Schottky Barrier Diodes

In this Appendix the high frequency current responsivity of Schottky Barrier Diodes is derived. The current responsivity is derived from the lumped element model as shown in Fig. D.1, following the steps from [93]. First a low-frequency current responsivity is derived from a fourth order Taylor expansion of the IV-characteristic, after which the junction capacitance is included in the model to calculate the power transfer efficiency to the junction. The high frequency current responsivity can be calculated using the power transfer efficiency and low frequency current responsivity.

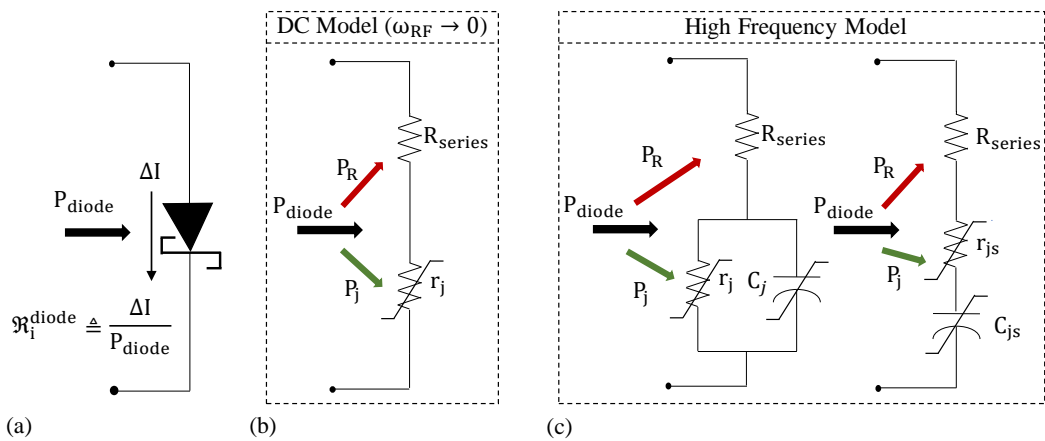


Figure D.1: DC- and High-frequency models of a Schottky Barrier Diode. In (a), the definition of current responsivity, $\mathfrak{R}_i^{\text{diode}}$, is shown. In (b) the DC-model is shown, consisting of the dynamic junction resistance and series resistance of the SBD. In (c) the high-frequency model is shown with on the left-hand side the physical model indicating the junction capacitance and on the right-hand side a series equivalent model.

D.1 Lumped Element Model

A schematic of the SBD is shown in Fig. D.1. In (a), the definition of current responsivity, $\mathfrak{R}_i^{\text{diode}}$, is shown, which is defined as an average incremental change in current, ΔI , flowing through the diode as a result of, P_{diode} , power absorbed in the SBD: $\mathfrak{R}_i^{\text{diode}} = \Delta I / P_{\text{diode}}$. This rectifying behavior is the result of the non-linear voltage-current relationship of the diode. In DC, or near DC, the diode can be approximated with the lumped element model shown in Fig. D.1(b), where R_{series} is the series resistance and r_j is the dynamic junction resistance of the diode. The total diode resistance, R_{diode} , is the summation of the series resistance and dynamic junction resistance and can be evaluated from the first order derivative of the IV-characteristic of the diode.

$$R_{\text{diode}} = R_{\text{series}} + r_j = \left[\frac{dI_D}{dV_D} \right]^{-1} \quad (\text{D.1})$$

with $I_D = f(V_D)$. The simulated IV-curve of the smallest SBD ($1.6 \mu\text{m} \times 1.6 \mu\text{m}$) available

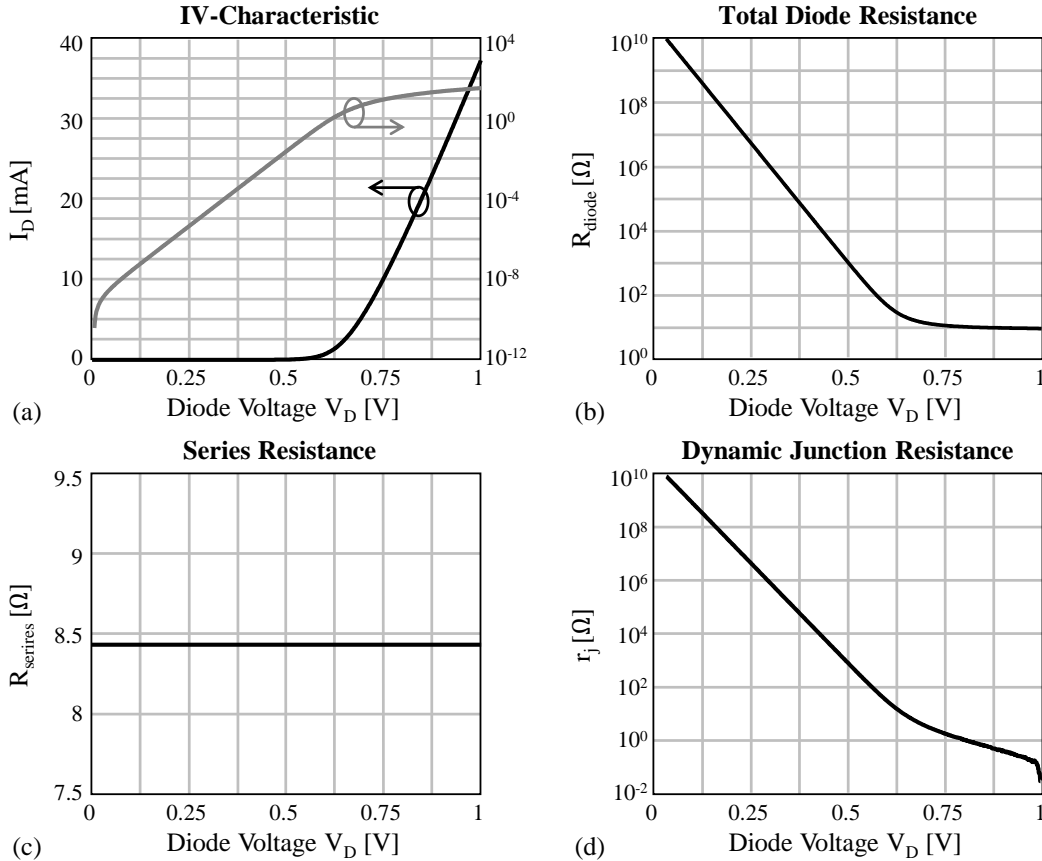


Figure D.2: Simulated DC-characteristics of the smallest SBD available in the PDK. (a) IV-curve in linear and logarithmic scale. (b) Total diode resistance, derived from the IV-curve (D.1). (c) Series resistance R_{series} . (d) Dynamic junction resistance r_j .

in the process design kit of the available technology is shown in Fig. D.2(a). The total diode resistance is shown in Fig. D.2(b). The series resistance accounts for ohmic dissipation losses in the contacts and does not depend on biasing voltage. The dynamic junction resistance describes the non-linear behavior of the junction and decreases with increasing biasing voltage. For $V_D > 1$ V, the junction is almost completely depleted and the total diode resistance can be approximated to be the series resistance $R_{\text{diode}}(V_D > 1 \text{ V}) \approx R_{\text{series}}$. For the considered SBD, the simulated series resistance is shown in Fig. D.2(c). The dynamic junction resistance is shown in Fig. D.2(d).

In addition to the series resistance, another important parasitic effect is the junction capacitance. Together with the series resistance the cut-off frequency, f_T , is determined

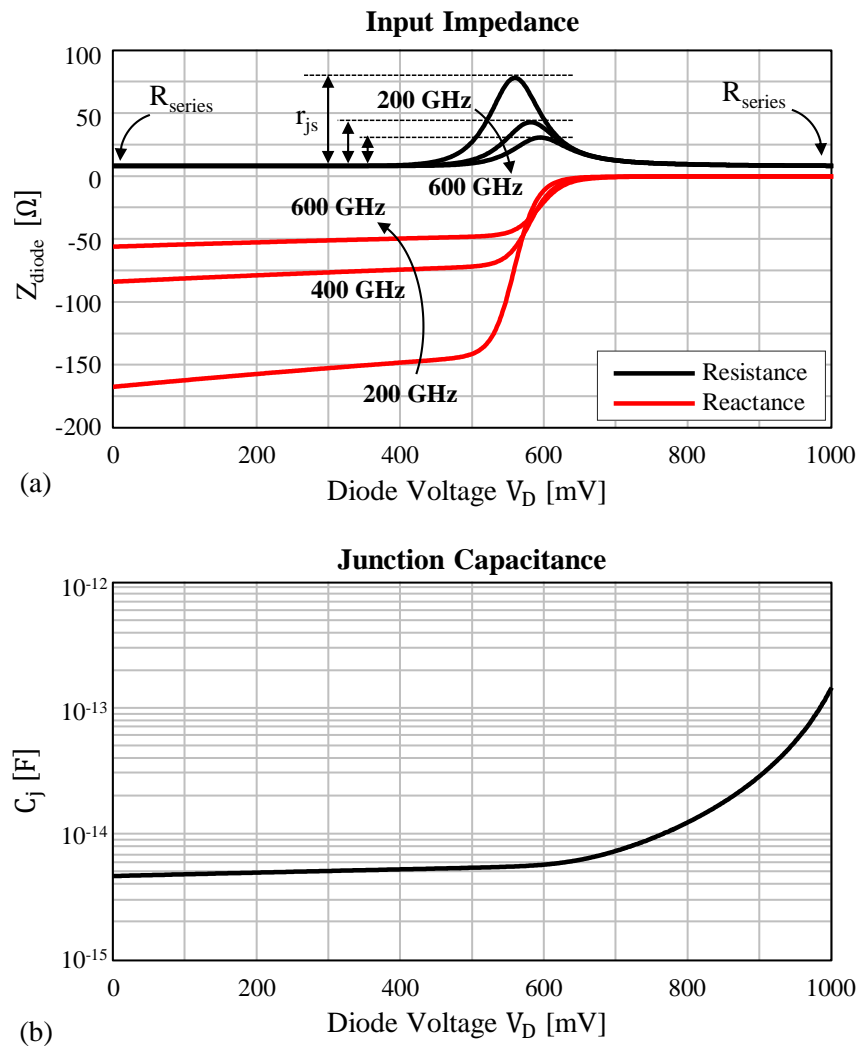


Figure D.3: (a) Input impedance Z_{diode} of SBD at 200 GHz, 400 GHz and 600 GHz. Indicated is the portion that represents the series resistance and the series equivalent dynamic junction resistance. (b) Junction capacitance extracted from input impedance.

as [139]:

$$f_T = \frac{1}{2\pi R_{\text{series}} C_j} \quad (\text{D.2})$$

The high frequency model of the SBD is shown in Fig. D.1(c). The junction capacitance is effectively short-circuiting the junction at higher frequencies. The input impedance at 200 GHz, 400 GHz and 600 GHz is shown in Fig. D.3(a). The real part of the input impedance can be decomposed in the series resistance and series equivalent of the dynamic junction resistance, r_{js} , as defined by the series equivalent circuit shown in the right-hand side of Fig. D.1(c). The contributions are indicated in Fig. D.3(a). At zero biasing condition and at high biasing condition, the real part of the input impedance can be approximated to be the series resistance. The junction capacitance can be extracted from the input impedance and is shown in Fig. D.3(b).

D.2 Current Responsivity

The high-frequency current responsivity of the diode is derived by following the steps from [93]. From the IV-curve the low-frequency current responsivity can be derived. After taking into account the junction capacitance, the power transfer efficiency to the series equivalent of the dynamic junction resistance can be evaluated and the high-frequency current responsivity can be calculated. The current responsivity is defined as:

$$\mathfrak{R}_i^{\text{diode}} = \frac{\Delta I}{P_{\text{diode}}} \quad (\text{D.3})$$

where ΔI is the average mean difference of DC-current flowing through the SBD that is absorbing P_{diode} of power in the complete SBD, i.e. including the series resistance.

D.2.1 Low Frequency Current Responsivity

We will investigate the non-linearity and rectification of an RF-signal by performing a Taylor expansion of the IV-curve. The detector is biased at V_0 . When the SBD is connected to the antenna, the total voltage over the detector, in radiometric operation, is the superposition of the DC biasing voltage, V_0 , and the high frequency signal to be detected, $A \cos(\omega_{RF}t)$:

$$V_D = V_0 + A \cos(\omega_{RF}t) \quad (\text{D.4})$$

Let us consider the IV-curve as shown in Fig. D.2(a). When the IV-curve, $I_D = f_{V_D}$, is expanded in a 4th order Taylor power series, around operating point V_0 , and (D.4) is substituted for V_D , we obtain the following approximation of I_D :

$$\begin{aligned}
I_D &= f(V_D) \approx f(V_0) + \frac{f^{(1)}}{1!}(V_D - V_0) + \frac{f^{(2)}}{2!}(V_D - V_0)^2 + \frac{f^{(3)}}{3!}(V_D - V_0)^3 + \frac{f^{(4)}}{4!}(V_D - V_0)^4 \\
&= f(V_0) + f^{(1)}(A \cos(\omega_{RF}t)) + \frac{f^{(2)}}{2}(A \cos(\omega_{RF}t))^2 + \frac{f^{(3)}}{6}(A \cos(\omega_{RF}t))^3 + \frac{f^{(4)}}{24}(A \cos(\omega_{RF}t))^4
\end{aligned} \tag{D.5}$$

where $f^{(i)}$, is the i -th order derivative of $I_D = f(V_D)$ with respect to V_D , evaluated at V_0 . By using the trigonometric identity $\cos(x)^2 = \frac{1}{2}[1 + \cos(2x)]$ and by only retaining the fundamental and DC-terms, we can simplify to:

$$\begin{aligned}
I_D - I_0 &\approx f^{(1)}A \cos(\omega_{RF}t) + \frac{f^{(2)}}{2}A^2 \cos(\omega_{RF}t)^2 + \frac{f^{(3)}}{6}A^3 \cos(\omega_{RF}t)^3 + \frac{f^{(4)}}{24}A^4 \cos(\omega_{RF}t)^4 \\
&\approx f^{(1)}A \cos(\omega_{RF}t) + \frac{f^{(2)}}{4}A^2 + \frac{f^{(3)}}{6}A^3 \cos(\omega_{RF}t)^3 + \frac{f^{(4)}}{24}A^4 \cos(\omega_{RF}t)^4 \\
&\approx f^{(1)}A \cos(\omega_{RF}t) + \frac{f^{(2)}}{4}A^2 + \frac{f^{(3)}}{12}A^3 \cos(\omega_{RF}t) + \frac{f^{(4)}}{24}A^4 \cos(\omega_{RF}t)^4 \\
&= f^{(1)}A \cos(\omega_{RF}t) + \frac{f^{(2)}}{4}A^2 + \frac{f^{(3)}}{12}A^3 \cos(\omega_{RF}t) + \frac{f^{(4)}}{96}A^4(1 + \cos(2\omega_{RF}t))^2 \\
&\approx f^{(1)}A \cos(\omega_{RF}t) + \frac{f^{(2)}}{4}A^2 + \frac{f^{(3)}}{12}A^3 \cos(\omega_{RF}t) + \frac{f^{(4)}}{96}A^4(1 + \cos(2\omega_{RF}t))^2 \\
&\approx f^{(1)}A \cos(\omega_{RF}t) + \frac{f^{(2)}}{4}A^2 + \frac{f^{(3)}}{12}A^3 \cos(\omega_{RF}t) + \frac{f^{(4)}}{96}A^4 \left(1 + \frac{1}{2}\right) \\
&= f^{(1)}A \cos(\omega_{RF}t) + \frac{f^{(2)}}{4}A^2 + \frac{f^{(3)}}{12}A^3 \cos(\omega_{RF}t) + \frac{f^{(4)}}{64}A^4 \\
&= \left[\frac{A^2}{4}f^{(2)} + \frac{A^4}{64}f^{(4)} \right] + \left[Af^{(1)} + \frac{A^3}{12}f^{(3)} \right] \cos(\omega_{RF}t)
\end{aligned} \tag{D.6}$$

The derivatives are shown in Fig. D.4. The left hand side of (D.6) represents the DC-term and fundamental current terms resulting when the RF-signal $A \cos(\omega_{RF}t)$ is impinging on the diode that is biased at V_0 . The time-average incremental increase in DC-current, ΔI_D , due to the impinging RF-power can be defined as (D.7):

$$\Delta I_D = \left[\frac{A^2}{4}f^{(2)} + \frac{A^4}{64}f^{(4)} \right] \tag{D.7}$$

The fundamental term in the expansion (D.6) can be used to calculate how much RF-power, P_{RF} , is absorbed in the diode. The average RF-power can be calculated by multiplying the input RF-signal, $A \cos(\omega_{RF}t)$, with the total change in current, $I_D - I_0$ (D.6), and integrate it over one period, T , (D.8):

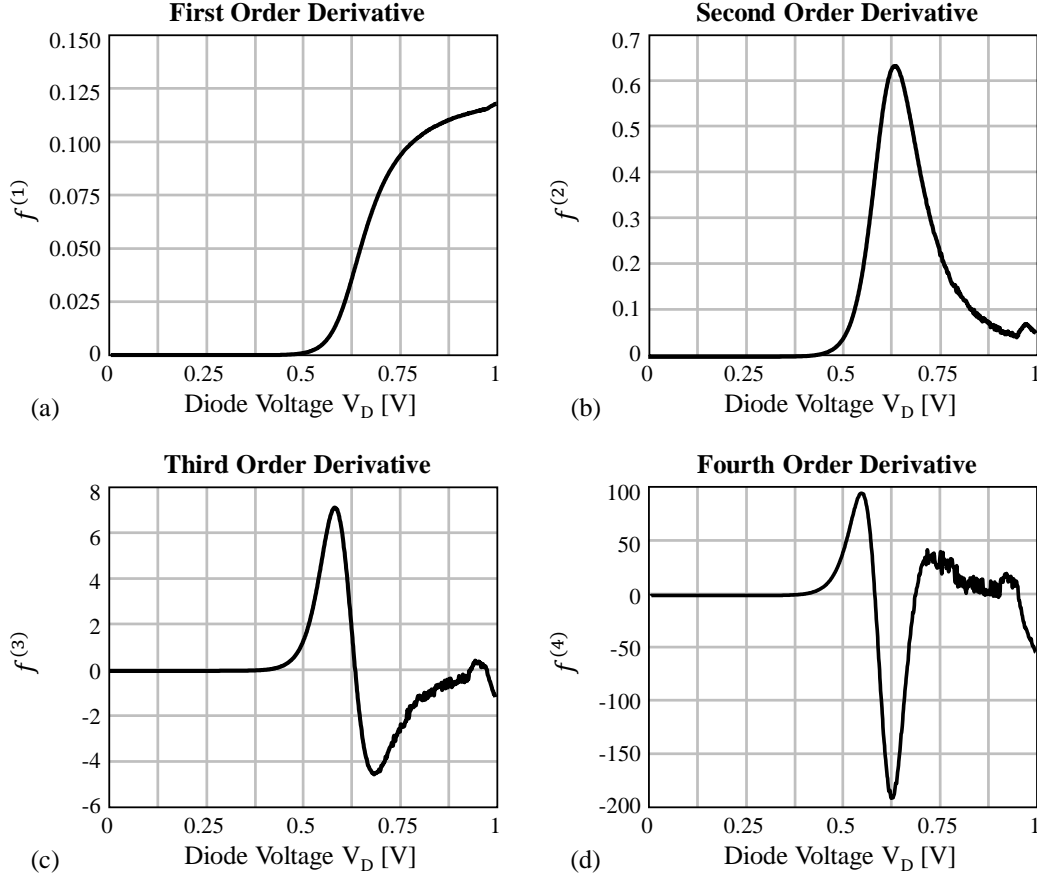


Figure D.4: Derivatives of the IV-curve from Fig. D.2(a). (a) First order derivative $f^{(1)}$, (b) Second order derivative $f^{(2)}$, (c) Third order derivative $f^{(3)}$, (d) Fourth order derivative $f^{(4)}$,

$$\begin{aligned}
P_{RF} &= \frac{1}{T} \int_0^T (I_D(V_D) - I_0) A \cos(\omega_{RF}t) dt \\
&\approx \frac{1}{T} \int_0^T \left(\left[\frac{A^2}{4} f^{(2)} + \frac{A^4}{64} f^{(4)} \right] + \left[A f^{(1)} + \frac{A^3}{12} f^{(3)} \right] \cos(\omega_{RF}t) \right) A \cos(\omega_{RF}t) dt \\
&= \frac{1}{T} \int_0^T \left[A^2 f^{(1)} + \frac{A^4}{12} f^{(3)} \right] \cos^2(\omega_{RF}t) dt \\
&= \frac{1}{T} \int_0^T \left[\frac{A^2}{2} f^{(1)} + \frac{A^4}{24} f^{(3)} \right] [1 + \cos(2\omega_{RF}t)] dt \\
&= \frac{1}{T} \int_0^T \left[\frac{A^2}{2} f^{(1)} + \frac{A^4}{24} f^{(3)} \right] dt \\
&= \frac{A^2}{2} \left[f^{(1)} + \frac{A^2}{12} f^{(3)} \right]
\end{aligned} \tag{D.8}$$

The ratio of the incremental change in time average DC-current, ΔI_D (D.7), to the absorbed

RF-power, P_{RF} , defines the current responsivity (D.9):

$$\mathfrak{R}_i^{\text{diode}}(\omega_{RF} \rightarrow 0) = \frac{\Delta I_D}{P_{RF}} \quad (\text{D.9})$$

Substituting ΔI_D (D.7) and P_{RF} (D.8) into (D.9) results in:

$$\mathfrak{R}_i^{\text{diode}}(\omega_{RF} \rightarrow 0) = \frac{\Delta I_D}{P_{RF}} = \frac{\left[\frac{A^2}{4} f^{(2)} + \frac{A^4}{64} f^{(4)} \right]}{\frac{A^2}{2} \left[f^{(1)} + \frac{A^2}{12} f^{(3)} \right]} = \frac{\left[\frac{1}{2} f^{(2)} + \frac{A^2}{32} f^{(4)} \right]}{\left[f^{(1)} + \frac{A^2}{12} f^{(3)} \right]} = \frac{1}{2} \frac{f^{(2)}}{f^{(1)}} \frac{\left[1 + \frac{A^2}{16} \frac{f^{(4)}}{f^{(2)}} \right]}{\left[1 + \frac{A^2}{12} \frac{f^{(3)}}{f^{(1)}} \right]} \quad (\text{D.10})$$

After defining $\Delta_1 = \frac{A^2}{16} \frac{f^{(4)}}{f^{(2)}}$ and $\Delta_2 = \frac{A^2}{12} \frac{f^{(3)}}{f^{(1)}}$, (D.10) is further approximated to:

$$\mathfrak{R}_i^{\text{diode}}(\omega_{RF} \rightarrow 0) = \mathfrak{R}_{i,0}^{\text{diode}} \frac{[1 + \Delta_1]}{[1 + \Delta_2]} \approx \mathfrak{R}_{i,0}^{\text{diode}} [1 + \Delta_1 - \Delta_2] = \mathfrak{R}_{i,0}^{\text{diode}} [1 + \Delta] \quad (\text{D.11a})$$

with

$$\mathfrak{R}_{i,0}^{\text{diode}} = \frac{1}{2} \frac{f^{(2)}}{f^{(1)}} \quad (\text{D.11b})$$

$$\Delta = \frac{A^2}{16} \frac{f^{(4)}}{f^{(2)}} - \frac{A^2}{12} \frac{f^{(3)}}{f^{(1)}} \quad (\text{D.11c})$$

Here $\mathfrak{R}_{i,0}^{\text{diode}}$ defines the low-frequency, low power level, current responsivity, which is independent from the incident signal. $\mathfrak{R}_{i,0}^{\text{diode}}$ is shown in Fig. D.5(a). A small effect of the

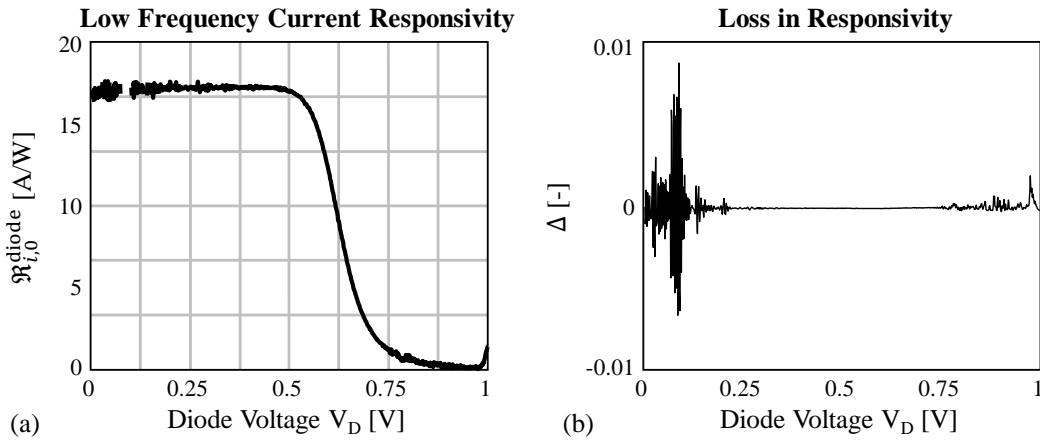


Figure D.5: Low frequency current responsivity $\mathfrak{R}_i^{\text{diode}}(\omega_{RF} \rightarrow 0)$ (D.11). (a) The low-power and low-frequency current responsivity $\mathfrak{R}_{i,0}^{\text{diode}}$ (D.11b). (b) The high incident power loss in responsivity Δ (D.11c) due to the absorbed power of a 1000 K blackbody source captured over 400 GHz of bandwidth. All spikes and oscillations are a numerical error in evaluating the current derivatives.

numerical inaccuracies in the derivative of current at low and high biasing voltage can be seen. For higher biasing voltages the responsivity decreases since the power will be absorbed in the series resistance.

For high power signals, $\Delta < 0$ and the responsivity starts decreasing. In a radiometric configuration, this term can be neglected. Suppose the diode receives power that is radiated from a 1000 K blackbody source. The amount of power that is available to the detector can be approximated using the Rayleigh-Jeans approximation of Planck's law: $P_{RF} \approx k_B T_S \Delta f_{RF} = 5.5 \text{ nW}$ for 400 GHz of operational bandwidth. Suppose that the antenna is conjugate matched to the antenna. The amplitude of the equivalent voltage generator for an antenna in reception, V_g , can then be calculated as:

$$P_{RF} = \frac{1}{2} |V_{oc}|^2 \frac{1}{4R_a} \iff V_{oc} = \sqrt{8R_a P_{RF}} \quad (\text{D.12})$$

Let us take $R_a = 80 \Omega$, i.e. the resistance of the diode at 200 GHz from Fig. D.3(a). The amplitude A of the signal incident over the conjugally matched diode will then be:

$$A = V_{oc}/2 = \sqrt{2R_a P_{RF}} \approx 1 \text{ mV} \quad (\text{D.13})$$

The loss in responsivity, Δ , as defined by (D.11c), for this extreme case is shown in Fig. D.5(b). The spikes and oscillations are attributed to the numerical error in evaluating the current derivatives. It is evident that the low-frequency current responsivity can be evaluated from solely the first and second order derivative of the IV-curve:

$$\mathfrak{R}_i^{\text{diode}}(\omega_{RF} \rightarrow 0) \approx \frac{1}{2} \frac{f^{(2)}}{f^{(1)}} \quad (\text{D.14})$$

Let us now take into account the junction capacitance and evaluate the power transfer efficiency to the junction of the diode.

D.2.2 Power Transfer Efficiency

The current responsivity derived in DC (D.14) assumes that the voltage drop of the RF-signal occurs over the total diode resistance $R_{\text{diode}} = R_{\text{series}} + r_j$. However, as was mentioned in Sec. D.1 and shown in Fig. D.1, a junction capacitance should be taken into account for frequency $\omega_{RF} > 0$. The junction capacitance and series resistance are the main parasitic elements of the SBD that decrease performance. The rectifying characteristic of a diode is the result of the non-linear behavior of the junction current as function of the voltage over the junction. Only RF-power that is actually absorbed in the junction, P_j , contributes to the incremental DC-current ΔI . Therefore, for higher capacitance and series resistance, the current responsivity will decrease. The junction capacitance is effectively short-circuiting the junction at higher frequencies. A series equivalent of the dynamic junction resistance, r_{js} in the right-hand side of (c), can be defined [73, 93] as:

$$r_{js} = \text{Re} \left[\frac{r_j \frac{1}{j\omega_{RF} C_j}}{r_j + \frac{1}{j\omega_{RF} C_j}} \right] = \frac{r_j}{1 + (\omega_{RF} C_j r_j)^2} \quad (\text{D.15})$$

The series equivalent of the dynamic junction resistance is shown in Fig. D.6(a) for the junction resistance and capacitance shown in Fig. D.2(d) and Fig. D.3(b) respectively, for the frequencies 200 GHz, 400 GHz and 600 GHz. The power transfer efficiency, η_{PTE} , of the power absorbed by the complete diode, P_{diode} , to the absorbed power in the junction, P_j , can be written as:

$$\eta_{\text{PTE}}(\omega_{RF}) = \frac{P_j}{P_{\text{diode}}} = \frac{r_{js}}{r_{js} + R_{\text{series}}} \quad (\text{D.16})$$

Since the series equivalent of the dynamic junction resistance decreases with frequency, the power transfer efficiency to the junction also degrades. The power transfer efficiency

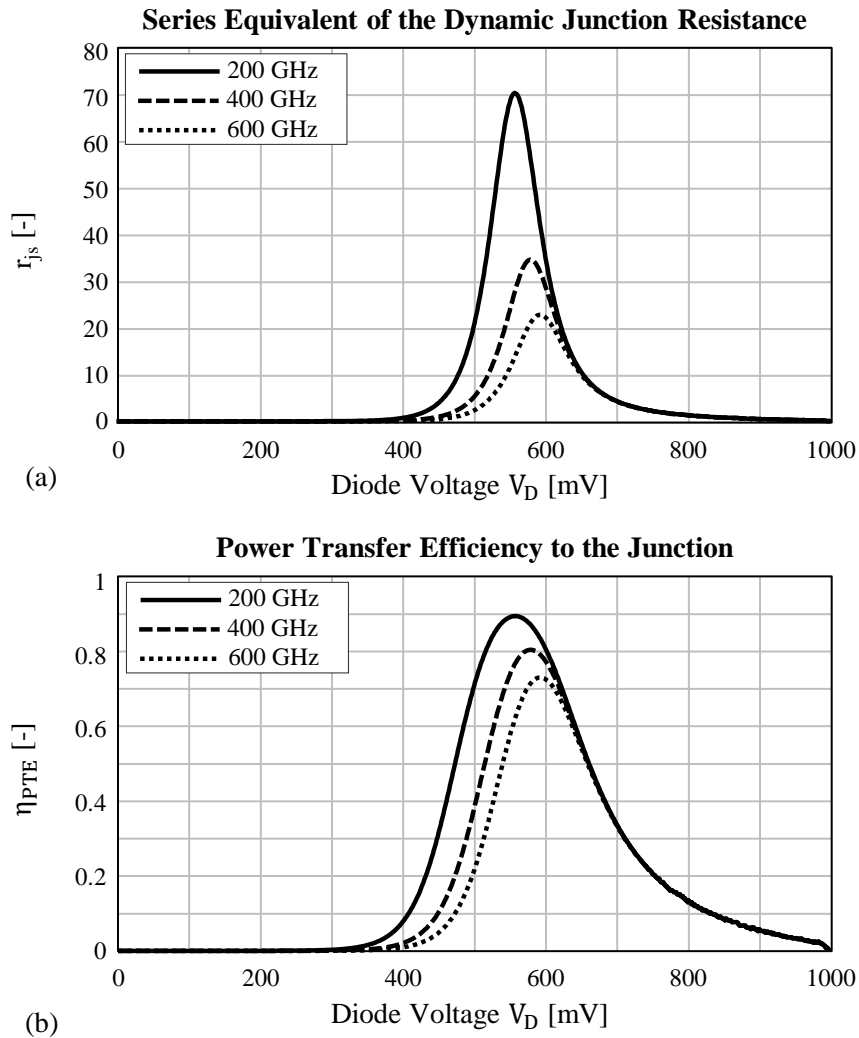


Figure D.6: High frequency effects for the SBD in terms of (a) series equivalent of the dynamic junction resistance, as defined by (D.15) and (b) the power transfer efficiency to the junction, as defined by (D.16), for the frequencies 200 GHz, 400 GHz, 600 GHz.

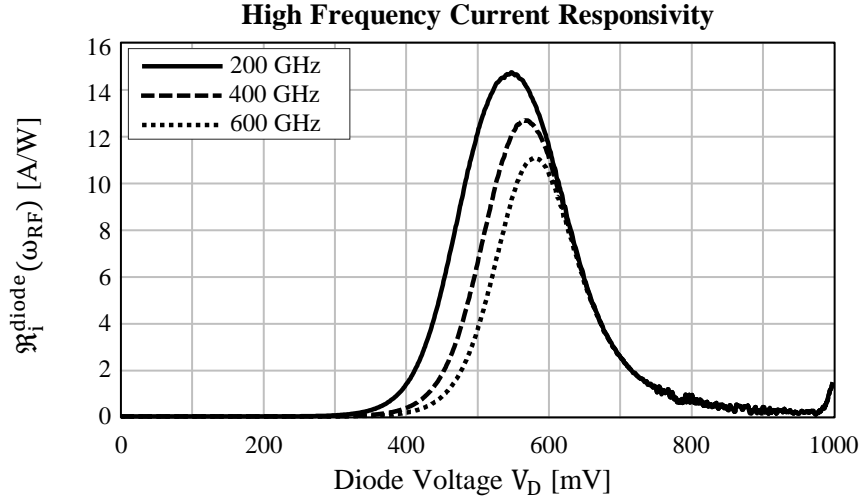


Figure D.7: High frequency current responsivity, as defined by (D.17), for the frequencies 200 GHz, 400 GHz, 600 GHz.

is shown in Fig. D.6(b) for the frequency 200 GHz, 400 GHz and 600 GHz.

D.2.3 High Frequency Current Responsivity

The current responsivity that was derived from the IV-curve (D.14) is for a frequency $\omega_{RF} \rightarrow 0$ with a power transfer efficiency of: $\eta_{\text{PTE}}(\omega_{RF} \rightarrow 0) = r_j / (r_j + R_{\text{series}})$. An expression for the current responsivity, that is also valid at high frequencies, $\mathfrak{R}_i^{\text{diode}}(\omega_{RF})$, can then be derived from the low-frequency current responsivity as follows:

$$\mathfrak{R}_i^{\text{diode}}(\omega_{RF}) = \eta_{\text{PTE}}(\omega_{RF}) \frac{\mathfrak{R}_i^{\text{diode}}(\omega_{RF} \rightarrow 0)}{\eta_{\text{PTE}}(\omega_{RF} \rightarrow 0)} \quad (\text{D.17})$$

The high frequency current responsivity for the frequencies 200 GHz, 400 GHz and 600 GHz is shown in Fig. D.7.

Appendix E

Experimental Extraction of SBD model

The high-frequency current responsivity can be fully predicted when the IV-curve and junction capacitance are known. The extraction of the junction capacitance can be performed at lower frequencies, such that difficult on-chip calibration at submm-wave frequencies is not necessary.

E.1 IV-curve

The IV-curve is measured using the measurement setup that is shown in Fig. E.1(a), which consists of a DC-probing station and a parametric analyzer. The SBD is embedded in a fixture as shown in Fig. E.1(b). A voltage of V_{RAW} is forced on the anode and the ground is forced on the cathode. By using the *Thru* fixture from the on-chip TRL calibration structures, it is measured that the fixture itself, in absence of the SBD, has an ohmic resistance of approximately 11Ω in order to correct the raw measurement. The measured IV-curve, corrected for the Thru resistance, is shown in Fig. E.1(c), together with the simulated IV-curve. The lower *knee* of the measured IV-curve for higher biasing voltages, indicates a higher series resistance than is predicted by the simulation. From the derivative of IV-curve, the total diode resistance in DC, R_{diode} , can be evaluated as shown in Fig. E.1(d) and calculated as:

$$R_{\text{diode}} = R_{\text{series}} + r_j = \left[\frac{dI_{\text{Diode}}}{dV_{\text{Diode}}} \right]^{-1} \quad (\text{E.1})$$

where the two components are highlighted in the figure. It is clear that from $V_{\text{Diode}} > 0.7$, almost no power will be absorbed in the junction and $R_{\text{diode}} \approx R_{\text{series}} \approx 135\Omega$. Note that this series resistance of 135Ω is significantly larger than the simulated series resistance of 10Ω . The simulated IV-curve is obtained after parasitic extraction and is therefore 2Ω higher than the reported 8Ω in Fig. D.2(c). A higher series resistance implies a lower power transfer efficiency to the junction (D.16) and therefore a lower current responsivity.

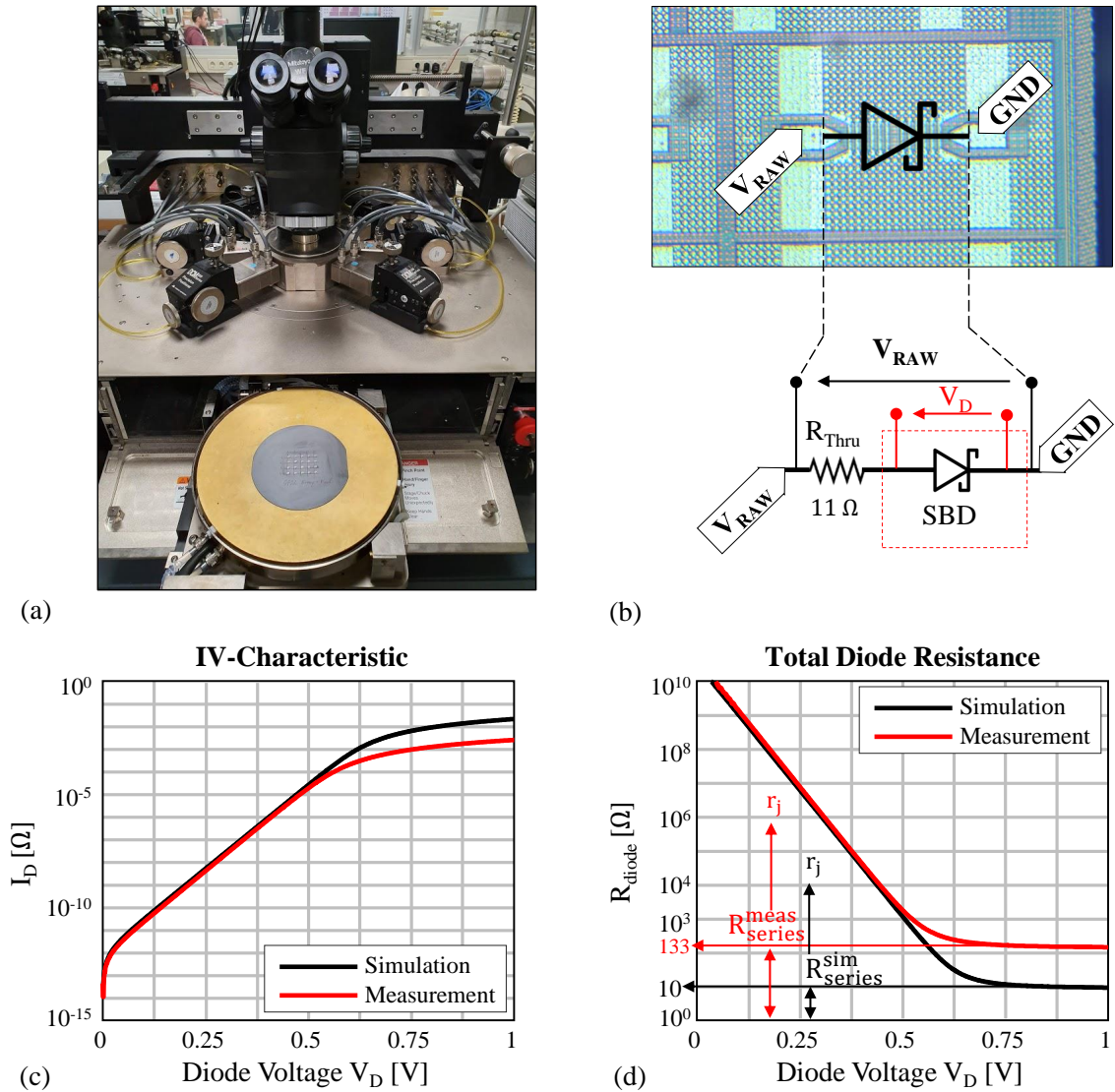


Figure E.1: Measurement of the IV-characteristic. (a) Measurement setup, a DC-probing station attached to a parametric analyzer. (b) On the top a micrograph of a fixture is shown that contains the SBD as indicated. A voltage of V_{RAW} is applied to the anode while the cathode is forced to ground (GND). The resistance of the fixture itself is measured to be 11Ω . (c) The simulated and measured IV-curve. (d) The total diode resistance extracted from the IV-curve. Indicated is the series resistance and dynamic junction resistance.

E.2 Junction Capacitance

The junction capacitance can be extracted from low-frequency measurements. The measurement setup is shown in Fig. E.2. In this setup we use a Microwave Network Analyzer operating from 10 MHz to 26.5 GHz. GSG landing probes with a 100 μm pitch are used to land on the fixtures as shown by the insets. An LRM-calibration is performed (Line (Thru), Reflect, Match) since a TRL calibration at low frequency results in lines that are too long to efficiently print on a CMOS chip. The calibrated input impedance of the SBD at 10 GHz is shown in Fig. E.3(a). Note that this impedance represents the right-hand side of Fig. D.1(c) with the real part a summation of the series resistance R_{series} and series dynamic junction resistance r_{j_s} . The junction capacitance can be calculated using the high-frequency circuits in Fig. D.1(c) as (E.2) and is shown in Fig. E.3(b).

$$C_j = \frac{\text{Im}\left[\frac{1}{Z_{\text{diode}} - R_{\text{series}}}\right]}{\omega_{RF}} \quad (\text{E.2})$$

The measured junction capacitance is compared with simulation. The IV-curve can now be used to calculate the low-frequency current responsivity (D.14) while the extracted C_j can be used to evaluate the power transfer efficiency (D.16) to the junction in high-frequency operation. The higher measured junction capacitance enters quadratically in the denominator of the effective series dynamic junction resistance (D.15). The capacitance is effectively short-circuiting the junction at higher frequencies.

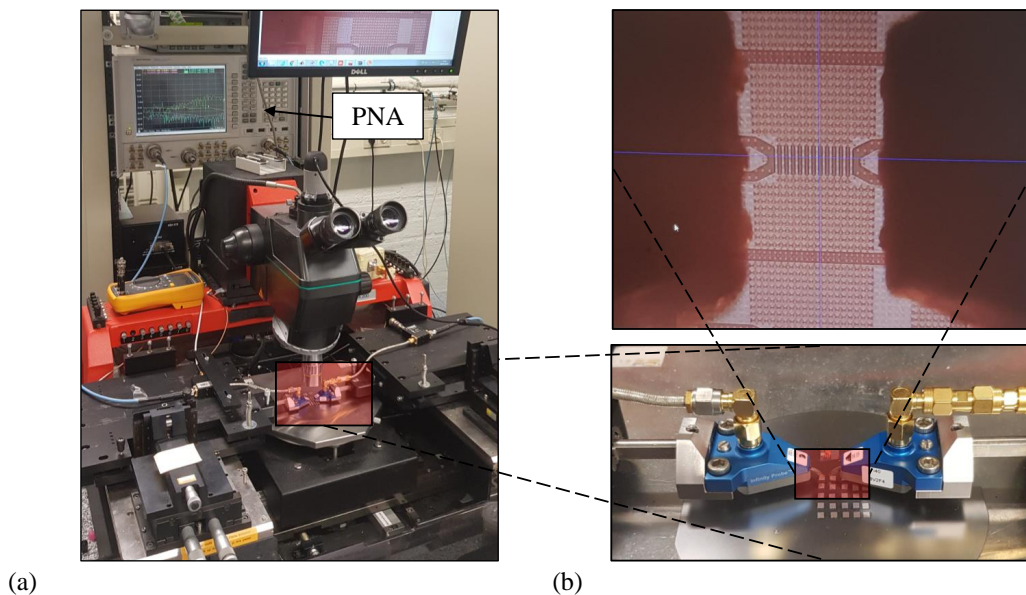


Figure E.2: Measurement setup for the S-parameters of the SBD. (a) The full setup. (b) Zoom-in showing the two Ground-Signal-Ground probes, which are connected on the top to a parametric analyzer for the DC-biasing. Another zoom-in shows the view via the microscope, where the fixture can be seen that contains the SBD.

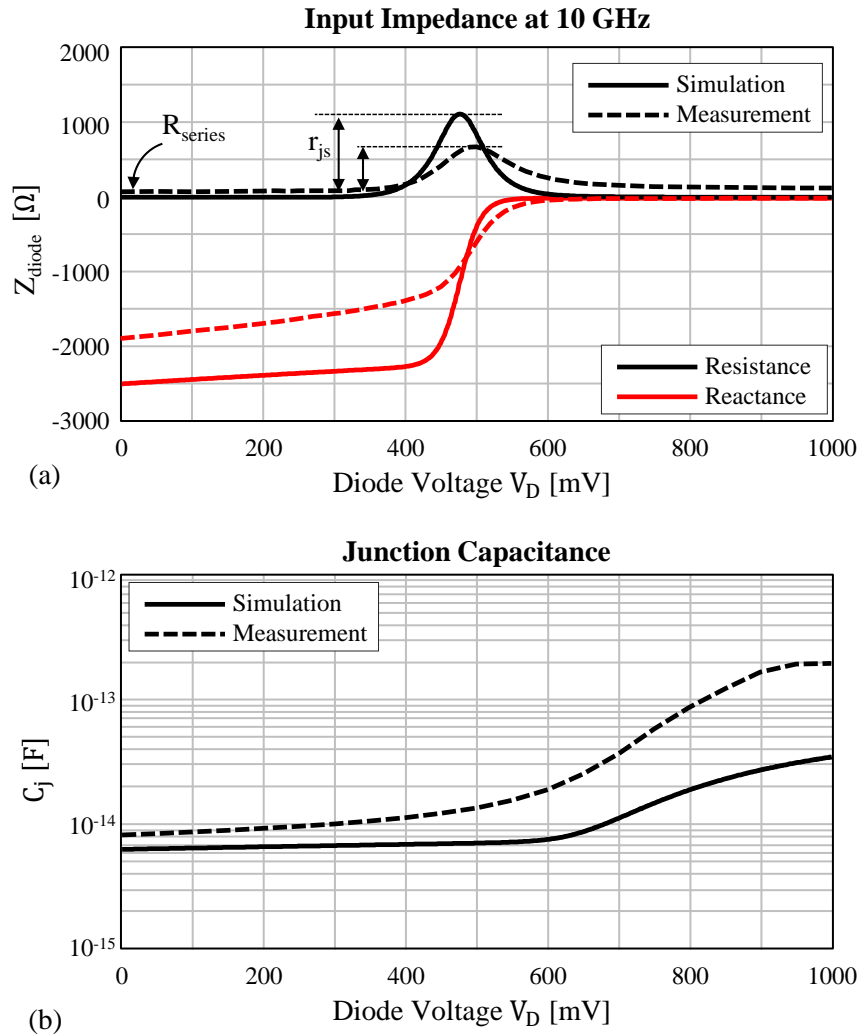


Figure E.3: Measurement results extracted from the two-port S-parameter measurement at 10 GHz. (a) Input impedance extracted from the S-parameters, indicating the series resistance and the series equivalent of the dynamic junction resistance. (b) Junction capacitance extracted from the input impedance.

Bibliography

- [1] W. Herschel, “XIII. Investigation of the powers of the prismatic colours to heat and illuminate objects; with remarks, that prove the different refrangibility of radiant heat. to which is added, an inquiry into the method of viewing the sun advantageously, with telescopes of large apertures and high magnifying powers,” *Philosophical Transactions of the Royal Society of London*, , no. 90, pp. 255–283, 1800.
- [2] L. Nobili, “Description d’un thermo-multiplicateur ou thermoscope électrique,” *Bibliothèque Universelle. Science et Arts*, vol. 30, pp. 225–230, 1830.
- [3] S. P. Langley, “The bolometer and radiant energy,” *Proceedings of the American Academy of Arts and Sciences*, vol. 16, pp. 342–358, 1880.
- [4] L. Bellingham, “Means for detecting the presence at a distance of icebergs, steamships, and other cold or hot objects.,” Nov. 2 1915, US Patent 1,158,967.
- [5] “Illustation of Camera Obscura,” <http://www.beeldbalie.nl/pinhole-fotografie/>, Accessed: 2020-04-07.
- [6] D. Barker, D. Hodges, and T. Hartwick, *Far Infrared Imagery*, vol. 0067 of *19th Annual Technical Symposium*, SPIE, 1975.
- [7] B. B. Hu and M. C. Nuss, “Imaging with terahertz waves,” *Optics Letters*, vol. 20, no. 16, pp. 1716–1718, 1995.
- [8] H. Hertz, “Ueber strahlen electrischer kraft,” *Annalen der Physik*, vol. 272, no. 4, pp. 769–783, 1889.
- [9] J. C. Wiltse, “History of millimeter and submillimeter waves,” *IEEE Transactions on Microwave Theory and Techniques*, vol. 32, no. 9, pp. 1118–1127, 1984.
- [10] TG Phillips and DP Woody, “Millimeter-and submillimeter-wave receivers,” *Annual Review of Astronomy and Astrophysics*, vol. 20, no. 1, pp. 285–321, 1982.
- [11] P. K. Cheo, “Far-infrared laser system for detection of defects in polyethylene-insulated power cables,” *Optics Letters*, vol. 2, no. 2, pp. 42–44, 1978.

- [12] D. T. Hodges, E. E. Reber, F. B. Foote, and R. L. Schellenbaum, "Safeguards applications of far infrared radiometric techniques for the detection of contraband," Report, 1980.
- [13] P. R. Smith, D. H. Auston, and M. C. Nuss, "Subpicosecond photoconducting dipole antennas," *IEEE J. Quantum Electron.*, vol. 24, no. 2, pp. 255–260, 1988.
- [14] Ch. Fattinger and D. Grischkowsky, "Terahertz beams," *Appl. Phys. Lett.*, vol. 54, no. 6, pp. 490–492, 1989.
- [15] D. M. Mittleman, R. H. Jacobsen, and M. C. Nuss, "T-ray imaging," *IEEE J. Sel. Topics Quantum Electron.*, vol. 2, no. 3, pp. 679–692, 1996.
- [16] D. L. Woolard, R. Brown, M. Pepper, and M. Kemp, "Terahertz frequency sensing and imaging: A time of reckoning future applications?," *Proceedings of the IEEE*, vol. 93, no. 10, pp. 1722–1743, 2005.
- [17] W. L. Chan, J. Deibel, and D. M. Mittleman, "Imaging with terahertz radiation," *Reports on Progress in Physics*, vol. 70, no. 8, pp. 1325–1379, 2007.
- [18] K. B. Cooper, R. J. Dengler, N. Llombart, B. Thomas, G. Chattopadhyay, and P. H. Siegel, "THz imaging radar for standoff personnel screening," *IEEE Trans. THz Sci. Technol.*, vol. 1, no. 1, pp. 169–182, 2011.
- [19] C. Kulesa, "Terahertz spectroscopy for astronomy: From comets to cosmology," *IEEE Trans. THz Sci. Technol.*, vol. 1, no. 1, pp. 232–240, 2011.
- [20] L. Öhrström, A. Bitzer, M. Walther, and F. J. Rühli, "Terahertz imaging of ancient mummies and bone," *Am. J. Phys. Anthropol.*, vol. 142, no. 3, pp. 497–500, 2010.
- [21] J. F. Federici, B. Schulkin, F. Huang, D. Gary, R. Barat, F. Oliveira, and D. Zimdars, "THz imaging and sensing for security applications—explosives, weapons and drugs," *Semiconductor Science and Technology*, vol. 20, no. 7, pp. S266–S280, 2005.
- [22] R. Appleby and H. B. Wallace, "Standoff detection of weapons and contraband in the 100 GHz to 1 THz region," *IEEE Trans. Antennas Propag.*, vol. 55, no. 11, pp. 2944–2956, Nov. 2007.
- [23] K. Kawase, Y. Ogawa, Y. Watanabe, and H. Inoue, "Non-destructive terahertz imaging of illicit drugs using spectral fingerprints," *Optics express*, vol. 11, no. 20, pp. 2549–2554, 2003.
- [24] Y. C. Shen, A. T. Lo, P. F. Taday, B. E. Cole, W. R. Tribe, and M. C. Kemp, "Detection and identification of explosives using terahertz pulsed spectroscopic imaging," *Appl. Phys. Lett.*, vol. 86, no. 24, pp. 241116, 2005.

- [25] D. van der Weide, J. Murakowski, and F. Keilmann, *Spectroscopy with electronic terahertz techniques*, vol. 3828 of *Industrial Lasers and Inspection (EUROPTO Series)*, SPIE, 1999.
- [26] R. Crane, “Prediction of attenuation by rain,” *IEEE Trans. Commun.*, vol. 28, no. 9, pp. 1717–1733, 1980.
- [27] H. J. Liebe, “MPM—An atmospheric millimeter-wave propagation model,” *International Journal of Infrared and Millimeter Waves*, vol. 10, no. 6, pp. 631–650, 1989.
- [28] F. Friederich, W. von Spiegel, M. Bauer, F. Meng, M. D. Thomson, S. Boppel, A. Lisauskas, B. Hils, V. Krozer, A. Keil, T. Löffler, R. Henneberger, A. K. Huhn, G. Spickermann, P. H. Bolivar, and H. G. Roskos, “THz active imaging systems with real-time capabilities,” *IEEE Trans. THz Sci. Technol.*, vol. 1, no. 1, pp. 183–200, 2011.
- [29] E. Grossman, C. Dietlein, J. Ala-Laurinaho, M. Leivo, L. Gronberg, M. Gronholm, P. Lappalainen, A. Rautiainen, A. Tamminen, and A. Luukanen, “Passive terahertz camera for standoff security screening,” *Applied Optics*, vol. 49, no. 19, pp. E106–E120, Jul. 2010.
- [30] A. Timofeev, J. Luomahaara, L. Grönberg, A. Mäyrä, H. Sipola, M. Aikio, M. Metso, V. Vesterinen, K. Tappura, J. Ala-Laurinaho, A. Luukanen, and J. Hassel, “Optical and electrical characterization of a large kinetic inductance bolometer focal plane array,” *IEEE THz Sci. Technol.*, vol. 7, no. 2, pp. 218–224, Mar. 2017.
- [31] D. Robertson, D. Macfarlane, R. Hunter, S. Cassidy, N. Llombart, E. Gandini, T. Bryllert, M. Ferndahl, H. Lindström, J. Tenhunen, H. Vasama, J. Huopana, T. Selkälä, and A. Vuotikka, *The CONSORTIS 16-channel 340-GHz security imaging radar*, vol. 10634 of *SPIE Defense + Security*, SPIE, 2018.
- [32] F. García-Rial, D. Montesano, I. Gómez, C. Callejero, F. Bazus, and J. Grajal, “Combining commercially available active and passive sensors into a millimeter-wave imager for concealed weapon detection,” *IEEE Trans. Microw. Theory Techn.*, vol. 67, no. 3, pp. 1167–1183, 2019.
- [33] P. H. Siegel, “Terahertz technology,” *IEEE Trans. Microw. Theory Techn.*, vol. 50, no. 3, pp. 910–928, 2002.
- [34] P. H. Siegel, “Terahertz technology in biology and medicine,” *IEEE Trans. Microw. Theory Techn.*, vol. 52, no. 10, pp. 2438–2447, 2004.
- [35] Z. D. Taylor, R. S. Singh, D. B. Bennett, P. Tewari, C. P. Kealey, N. Bajwa, M. O. Culjat, A. Stojadinovic, H. Lee, and J. Hubschman, “THz medical imaging: in vivo hydration sensing,” *IEEE Trans. THz Sci. Technol.*, vol. 1, no. 1, pp. 201–219, 2011.

- [36] K. Schmalz, N. Rothbart, P. F-X Neumaier, J. Borngräber, H. Hübers, and D. Kissinger, “Gas spectroscopy system for breath analysis at mm-wave/THz using SiGe BiCMOS circuits,” *IEEE Trans. Microw. Theory Techn.*, vol. 65, no. 5, pp. 1807–1818, 2017.
- [37] G. Stacey, S. Parshley, T. Nikola, G. Cortes-Medellin, J. Schoenwald, G. Rajagopalan, M. Niemack, T. Jenness, P. Gallardo, B. Koopman, C. Dowell, P. Day, M. Hollister, A. Kovacs, H. LeDuc, C. McKenney, R. Monroe, H. Yoshida, J. Zmuidzinas, L. Swenson, S. Radford, H. T. Nguyen, A. Mroczkowski, J. Glenn, J. Wheeler, P. Maloney, S. Brugger, J. Adams, F. Bertoldi, R. Schaaf, M. Halpern, D. Scott, G. Marsden, J. Sayers, S. Chapman, and J. Vieira, *SWCam: the short wavelength camera for the CCAT Observatory*, vol. 9153 of *SPIE Astronomical Telescopes + Instrumentation*, SPIE, 2014.
- [38] J. J. A. Baselmans, J. Bueno, S. J. C. Yates, O. Yurduseven, N. Llombart, K. Karatsu, A. M. Baryshev, L. Ferrari, A. Endo, D. J. Thoen, P. J. de Visser, R. M. J. Janssen, V. Murugesan, E. F. C. Driessen, G. Coiffard, J. Martin-Pintado, P. Hargrave, and M. Griffin, “A kilo-pixel imaging system for future space based far-infrared observatories using microwave kinetic inductance detectors,” *A&A*, vol. 601, pp. A89, May. 2017.
- [39] J. Caumes, A. Younus, S. Salort, B. Chassagne, B. Recur, A. Ziéglé, A. Dautant, and E. Abraham, “Terahertz tomographic imaging of XVIIIth dynasty Egyptian sealed pottery,” *Applied optics*, vol. 50, no. 20, pp. 3604–3608, 2011.
- [40] M. Bessou, B. Chassagne, J. Caumes, C. Pradère, P. Maire, M. Tondusson, and E. Abraham, “Three-dimensional terahertz computed tomography of human bones,” *Applied optics*, vol. 51, no. 28, pp. 6738–6744, 2012.
- [41] M. Jewariya, E. Abraham, T. Kitaguchi, Y. Ohgi, M. Minami, T. Araki, and T. Yasui, “Fast three-dimensional terahertz computed tomography using real-time line projection of intense terahertz pulse,” *Optics express*, vol. 21, no. 2, pp. 2423–2433, 2013.
- [42] G. C. Trichopoulos and K. Sertel, “Broadband terahertz computed tomography using a 5k-pixel real-time THz camera,” *J. Infrared Millim. Terahertz Waves*, vol. 36, no. 7, pp. 675–686, 2015.
- [43] P. Hillger, J. Grzyb, R. Jain, and U. R. Pfeiffer, “Terahertz imaging and sensing applications with silicon-based technologies,” *IEEE Trans. THz Sci. Technol.*, vol. 9, no. 1, pp. 1–19, 2019.
- [44] J. Lien, N. Gillian, M. E. Karagozler, P. Amihoud, C. Schwesig, E. Olson, H. Raja, and I. Poupayev, “Soli: ubiquitous gesture sensing with millimeter wave radar,” *ACM Trans. Graph.*, vol. 35, no. 4, pp. Article 142, 2016.

- [45] R. H. Rasshofer and K. Naab, "77 GHz long range radar systems status, ongoing developments and future challenges," in *European Radar Conference, 2005. EURAD 2005.*, 2005, pp. 161–164.
- [46] J. Hasch, E. Topak, R. Schnabel, T. Zwick, R. Weigel, and C. Waldschmidt, "Millimeter-wave technology for automotive radar sensors in the 77 GHz frequency band," *IEEE Trans. Microw. Theory Techn.*, vol. 60, no. 3, pp. 845–860, 2012.
- [47] M. Köhler, J. Hasch, H. L. Blöcher, and L. Schmidt, "Feasibility of automotive radar at frequencies beyond 100 GHz," *Int. J. Microw. Wirel. T.*, vol. 5, no. 1, pp. 49–54, 2013.
- [48] T. May, G. Zieger, S. Anders, V. Zakosarenko, H. G. Meyer, M. Schubert, M. Starkloff, M. Rössler, G. Thorwirth, and U. Krause, "Safe VISITOR: visible, infrared, and terahertz object recognition for security screening application," in *SPIE Defense, Security, and Sensing*. May. 2009, pp. 73090E–73090E–8, International Society for Optics and Photonics.
- [49] R. A. Lewis, "A review of terahertz detectors," *Journal of Physics D: Applied Physics*, vol. 52, no. 43, pp. 433001, 2019.
- [50] P. H. Siegel and R. J. Dengler, "Terahertz heterodyne imaging part II: Instruments," *International Journal of Infrared and Millimeter Waves*, vol. 27, no. 5, pp. 631–655, 2006.
- [51] E. Seok, D. Shim, C. Mao, R. Han, S. Sankaran, C. Cao, W. Knap, and O. K. K, "Progress and challenges towards terahertz CMOS integrated circuits," *IEEE J. Solid-State Circuits*, vol. 45, no. 8, pp. 1554–1564, 2010.
- [52] R. A. Hadi, H. Sherry, J. Grzyb, Y. Zhao, W. Forster, H. M. Keller, A. Cathelin, A. Kaiser, and U. R. Pfeiffer, "A 1 k-pixel video camera for 0.7-1.1 terahertz imaging applications in 65-nm CMOS," *IEEE J. Solid-State Circuits*, vol. 47, no. 12, pp. 2999–3012, Dec. 2012.
- [53] S. Rowe, E. Pascale, S. Doyle, C. Dunscombe, P. Hargrave, A. Papageorgio, K. Wood, P. A. R. Ade, P. Barry, A. Bidaud, T. Brien, C. Dodd, W. Grainger, J. House, P. Mauskopf, P. Moseley, L. Spencer, R. Sudiwala, C. Tucker, and I. Walker, "A passive terahertz video camera based on lumped element kinetic inductance detectors," *Review of Scientific Instruments*, vol. 87, no. 3, pp. 033105, Mar. 2016.
- [54] P. L. Richards, "Bolometers for infrared and millimeter waves," *J. Appl. Phys.*, vol. 76, no. 1, pp. 1–24, Jul. 1994.
- [55] C. Dietlein, A. Luukanen, F. Meyer, Z. Popovic, and E. N. Grossman, "Phenomenology of passive broadband terahertz images," in *4th ESA Workshop on Millimetre-wave Technology and Applications*, Feb. 2006, pp. 405–410.

- [56] S. Malz, R. Jain, and U. R. Pfeiffer, "Towards passive imaging with CMOS THz cameras," in *41st International Conference on Infrared, Millimeter, and Terahertz waves*, 2016, pp. 1–2.
- [57] J. Oden, J. Meilhan, J. Lalanne-Dera, J. Roux, F. Garet, J. Coutaz, and F. Simoens, "Imaging of broadband terahertz beams using an array of antenna-coupled microbolometers operating at room temperature," *Optics Express*, vol. 21, no. 4, pp. 4817–4825, Feb. 2013.
- [58] N. Oda, S. Kurashina, M. Miyoshi, K. Doi, T. Ishi, T. Sudou, T. Morimoto, H. Goto, and T. Sasaki, "Microbolometer terahertz focal plane array and camera with improved sensitivity in the sub-terahertz region," *J. Infrared Millim. Terahertz Waves*, vol. 36, no. 10, pp. 947–960, Oct. 2015.
- [59] D. Dufour, L. Marchese, M. Terroux, H. Oulachgar, F. Généreux, M. Doucet, L. Mercier, B. Tremblay, C. Alain, P. Beaupré, N. Blanchard, M. Bolduc, C. Chevalier, D. D'Amato, Y. Desroches, F. Duchesne, L. Gagnon, S. Ilias, H. Jerominek, F. Lagacé, J. Lambert, F. Lamontagne, L. Le Noc, A. Martel, O. Pancrati, J. Paultre, T. Pope, F. Provençal, P. Topart, C. Vachon, S. Verreault, and A. Bergeron, "Review of terahertz technology development at INO," *J. Infrared Millim. Terahertz Waves*, vol. 36, no. 10, pp. 922–946, Oct. 2015.
- [60] G. C. Trichopoulos, H. L. Mosbacker, D. Burdette, and K. Sertel, "A broadband focal plane array camera for real-time THz imaging applications," *IEEE Trans. Antennas Propag.*, vol. 61, no. 4, pp. 1733–1740, Apr. 2013.
- [61] A. Boukhayma, A. Dupret, J. Rostaing, and C. Enz, "A low-noise CMOS THz imager based on source modulation and an in-pixel high-Q passive switched-capacitor N-path filter," *Sensors*, vol. 16, no. 3, pp. 325, 2016.
- [62] J. Zmuidzinas and H. G. LeDuc, "Quasi-optical slot antenna SIS mixers," *IEEE Trans. Microw. Theory Techn.*, vol. 40, no. 9, pp. 1797–1804, 1992.
- [63] D. F. Filipovic, S. S. Gearhart, and G. M. Rebeiz, "Double-slot antennas on extended hemispherical and elliptical silicon dielectric lenses," *IEEE Trans. Microw. Theory Techn.*, vol. 41, no. 10, pp. 1738–1749, Oct. 1993.
- [64] A. J. Alazemi, H. H. Yang, and G. M. Rebeiz, "Double bow-tie slot antennas for wideband millimeter-wave and terahertz applications," *IEEE THz Sci. Technol.*, vol. 6, no. 5, pp. 682–689, Aug. 2016.
- [65] O. Yurduseven, D. Cavallo, A. Neto, G. Carluccio, and M. Albani, "Parametric analysis of extended hemispherical dielectric lenses fed by a broadband connected array of leaky-wave slots," *IET Microw. Antennas Propag.*, vol. 9, no. 7, pp. 611–617, May. 2015.

- [66] O. Yurduseven, N. Llombart, and A. Neto, "A dual-polarized leaky lens antenna for wideband focal plane arrays," *IEEE Trans. Antennas Propag.*, vol. 64, no. 8, pp. 3330–3337, Aug. 2016.
- [67] D. Cavallo and A. Neto, "A connected array of slots supporting broadband leaky waves," *IEEE Trans. Antennas Propag.*, vol. 61, no. 4, pp. 1986–1994, 2013.
- [68] L. Liu, J. L. Hesler, H. Xu, A. W. Lichtenberger, and R. M. Weikle, "A broadband quasi-optical terahertz detector utilizing a zero bias Schottky diode," *IEEE Microw. and Wirel. Compon. Lett.*, vol. 20, no. 9, pp. 504–506, 2010.
- [69] J. Grzyb, M. Andree, R. Jain, B. Heinemann, and U. Pfeiffer, "A lens-coupled on-chip antenna for dual-polarization SiGe HBT THz direct detector," *IEEE Antennas Wireless Propag. Lett.*, pp. 1–1, 2019.
- [70] K. Sengupta, D. Seo, L. Yang, and A. Hajimiri, "Silicon integrated 280 GHz imaging chipset with 4×4 SiGe receiver array and CMOS source," *IEEE Trans. THz Sci. Technol.*, vol. 5, no. 3, pp. 427–437, 2015.
- [71] S. Hsu, K. Wei, C. Hsu, and H. Ru-Chuang, "A 60-GHz millimeter-wave CPW-fed Yagi antenna fabricated by using 0.18- μ m CMOS technology," *IEEE Electron Device Lett.*, vol. 29, no. 6, pp. 625–627, 2008.
- [72] S. Pan and F. Capolino, "Design of a CMOS on-chip slot antenna with extremely flat cavity at 140 GHz," *IEEE Antennas Wireless Propag. Lett.*, vol. 10, pp. 827–830, 2011.
- [73] R. Han, Y. Zhang, D. Coquillat, H. Videlier, W. Knap, E. Brown, and K. Kenneth, "A 280-GHz Schottky diode detector in 130-nm digital CMOS," *IEEE J. Solid-State Circuits*, vol. 46, no. 11, pp. 2602–2612, Nov. 2011.
- [74] R. Han, Y. Zhang, Y. Kim, D. Y. Kim, H. Shichijo, E. Afshari, and O. K. K., "Active terahertz imaging using Schottky diodes in CMOS: Array and 860-GHz pixel," *IEEE J. Solid-State Circuits*, vol. 48, no. 10, pp. 2296–2308, Oct. 2013.
- [75] M. Uzunkol, O. D. Gurbuz, F. Golcuk, and G. M. Rebeiz, "A 0.32 THz SiGe 4x4 imaging array using high-efficiency on-chip antennas," *IEEE J. Solid-State Circuits*, vol. 48, no. 9, pp. 2056–2066, 2013.
- [76] N. Chahat, A. Tang, C. Lee, R. Sauleau, and G. Chattopadhyay, "Efficient CMOS systems with beam-lead interconnects for space instruments," *IEEE Trans. THz Sci. Technol.*, vol. 5, no. 4, pp. 637–644, 2015.
- [77] R. Jain, R. Zatta, J. Grzyb, D. Harame, and U. R. Pfeiffer, "A terahertz direct detector in 22nm FD-SOI CMOS," in *2018 13th European Microwave Integrated Circuits Conference (EuMIC)*, 2018, pp. 25–28.

- [78] D. B. Rutledge, D. P. Neikirk, and D. P. Kasilingam, "Integrated circuit antennas," *Infrared and millimeter waves*, vol. 10, no. part 2, pp. 1–90, 1983.
- [79] H. M. Cheema and A. Shamim, "The last barrier: on-chip antennas," *IEEE Microw. Mag.*, vol. 14, no. 1, pp. 79–91, 2013.
- [80] A. Babakhani, X. Guan, A. Komijani, A. Natarajan, and A. Hajimiri, "A 77-GHz phased-array transceiver with on-chip antennas in silicon: Receiver and antennas," *IEEE J. Solid-State Circuits*, vol. 41, no. 12, pp. 2795–2806, 2006.
- [81] E. Ojefors, U. R. Pfeiffer, A. Lisauskas, and H. G. Roskos, "A 0.65 THz focal-plane array in a quarter-micron CMOS process technology," *IEEE J. Solid-State Circuits*, vol. 44, no. 7, pp. 1968–1976, 2009.
- [82] W. H. Syed, G. Fiorentino, D. Cavallo, M. Spirito, P. M. Sarro, and A. Neto, "Design, fabrication, and measurements of a 0.3 THz on-chip double slot antenna enhanced by artificial dielectrics," *IEEE Transactions on Terahertz Science and Technology*, vol. 5, no. 2, pp. 288–298, 2015.
- [83] J. Grzyb, H. Sherry, Y. Zhao, R. Al Hadi, A. Cathelin, A. Kaiser, and U. Pfeiffer, "Real-time video rate imaging with a 1k-pixel THz CMOS focal plane array," in *2012 SPIE Defense, Security, and Sensing, 2012, Baltimore, Maryland, United States*, 2012, vol. 8362, pp. 83620C–83620C–12.
- [84] R. Carter, J. Mazurier, L. Pirro, J. Sachse, P. Baars, J. Faul, C. Grass, G. Grasshoff, P. Javorka, T. Kammler, A. Preusse, S. Nielsen, T. Heller, J. Schmidt, H. Niebojewski, P. Chou, E. Smith, E. Erben, C. Metzke, C. Bao, Y. Andee, I. Aydin, S. Morvan, J. Bernard, E. Bourjot, T. Feudel, D. Harame, R. Nelluri, H. Thees, L. M. Meskamp, J. Kluth, R. Mulfinger, M. Rashed, R. Taylor, C. Weintraub, J. Hoentschel, M. Vinet, J. Schaeffer, and B. Rice, "22nm FDSOI technology for emerging mobile, Internet-of-Things, and RF applications," in *2016 IEEE International Electron Devices Meeting (IEDM)*, 2016, pp. 2.2.1–2.2.4.
- [85] L. Liu, S. M. Rahman, Z. Jiang, W. Li, and P. Fay, "Advanced terahertz sensing and imaging systems based on integrated III-V interband tunneling devices," *Proceedings of the IEEE*, vol. 105, no. 6, pp. 1020–1034, 2017.
- [86] Z. Ahmad and O. K. K., "THz detection using pn-well diodes fabricated in 45-nm CMOS," *IEEE Electron Device Lett.*, vol. 37, no. 7, pp. 823–826, 2016.
- [87] U. R. Pfeiffer and E. Ojefors, "A 600-GHz CMOS focal-plane array for terahertz imaging applications," in *ESSCIRC 2008 - 34th European Solid-State Circuits Conference*, 2008, pp. 110–113.

- [88] A. Lisauskas, U. Pfeiffer, E. Öjefors, P. H. Bolívar, D. Glaab, and H. G. Roskos, “Rational design of high-responsivity detectors of terahertz radiation based on distributed self-mixing in silicon field-effect transistors,” *J. Appl. Phys.*, vol. 105, no. 11, pp. 114511, 2009.
- [89] M. Dyakonov and M. Shur, “Detection, mixing, and frequency multiplication of terahertz radiation by two-dimensional electronic fluid,” *IEEE Trans. Electron Dev.*, vol. 43, no. 3, pp. 380–387, 1996.
- [90] S. Boppel, A. Lisauskas, M. Mundt, D. Seliuta, L. Minkevicius, I. Kasalynas, G. Valusis, M. Mittendorff, S. Winnerl, V. Krozer, and H. G. Roskos, “CMOS integrated antenna-coupled field-effect transistors for the detection of radiation from 0.2 to 4.3 THz,” *IEEE Trans. Microw. Theory Techn.*, vol. 60, no. 12, pp. 3834–3843, 2012.
- [91] S. Sankaran and O. K. K, “Schottky barrier diodes for millimeter wave detection in a foundry CMOS process,” *IEEE Electron Device Lett.*, vol. 26, no. 7, pp. 492–494, 2005.
- [92] I. Mehdi, J. V. Siles, C. Lee, and E. Schlecht, “THz diode technology: Status, prospects, and applications,” *Proceedings of the IEEE*, vol. 105, no. 6, pp. 990–1007, 2017.
- [93] A. M. Cowley and H. O. Sorensen, “Quantitative comparison of solid-state microwave detectors,” *IEEE Trans. Microw. Theory Techn.*, vol. 14, no. 12, pp. 588–602, 1966.
- [94] D. Y. Kim, S. Park, R. Han, and O. K. K, “Design and demonstration of 820-GHz array using diode-connected NMOS transistors in 130-nm CMOS for active imaging,” *IEEE THz Sci. Technol.*, vol. 6, no. 2, pp. 306–317, Mar. 2016.
- [95] U. R. Pfeiffer, J. Grzyb, H. Sherry, A. Cathelin, and A. Kaiser, “Toward low-NEP room-temperature THz MOSFET direct detectors in CMOS technology,” in *2013 38th International Conference on Infrared, Millimeter, and Terahertz Waves (IRMMW-THz)*, 2013, pp. 1–2.
- [96] M. A. Andersson and J. Stake, “An accurate empirical model based on Volterra series for FET power detectors,” *IEEE Trans. on Microw. Theory and Techn.*, vol. 64, no. 5, pp. 1431–1441, 2016.
- [97] M. I. W. Khan, S. Kim, D. Park, H. Kim, S. Han, and S. Lee, “Nonlinear analysis of nonresonant THz response of MOSFET and implementation of a high-responsivity cross-coupled THz detector,” *IEEE Transactions on Terahertz Science and Technology*, vol. 8, no. 1, pp. 108–120, 2018.
- [98] A. A. Generalov, M. A. Andersson, X. Yang, A. Vorobiev, and J. Stake, “A 400-GHz graphene FET detector,” *IEEE Trans. on Microw. Theory and Techn.*, vol. 7, no. 5, pp. 614–616, 2017.

- [99] N. Weimann, M. Hossain, V. Krozer, W. Heinrich, M. Lisker, A. Mai, and B. Tillack, “Tight focus toward the future: Tight material combination for millimeter-wave RF power applications: InP HBT SiGe BiCMOS heterogeneous wafer-level integration,” *IEEE Microw. Mag.*, vol. 18, no. 2, pp. 74–82, 2017.
- [100] M. J. Griffin, J. J. Bock, and W. K. Gear, “Relative performance of filled and feedhorn-coupled focal-plane architectures,” *Applied Optics*, vol. 41, no. 31, pp. 6543–6554, Nov. 2002.
- [101] E. R. Brown and D. Segovia-Vargas, *Principles of THz Direct Detection*, pp. 212–253, in *Semiconductor Terahertz Technology: Devices and Systems at Room Temperature Operation* (eds G. Carpintero, L. E. García Muñoz, H. L. Hartnagel, S. Preu and A. V. Räsänen), John Wiley & Sons, Ltd, Chichester, UK, Jul. 2015.
- [102] G. Rieke, *Detection of light: from the ultraviolet to the submillimeter*, Cambridge University Press, 2003.
- [103] William J Riley, “Handbook of frequency stability analysis,” 2008.
- [104] Virginia Diodes, Inc, “Accessed on: 18 July 2017,” .
- [105] M. Planck, “The theory of heat radiation,” *molecules*, vol. 6, pp. 1023, 1914.
- [106] A. Luukanen, R. Appleby, M. Kemp, and N. Salmon, *Millimeter-wave and terahertz imaging in security applications*, pp. 491–520, in *Terahertz Spectroscopy and Imaging* (eds KE. Peiponen, A. Zeitler and M. Kuwata-Gonokami), Optical Sciences, vol 171. Springer, 2012.
- [107] R. W. Boyd, “Photon bunching and the photon-noise-limited performance of infrared detectors,” *Infrared Physics*, vol. 22, no. 3, pp. 157–162, May. 1982.
- [108] D. Flanigan, H. McCarrick, G. Jones, B. R. Johnson, M. H. Abitbol, P. Ade, D. Araujo, K. Bradford, R. Cantor, G. Che, P. Day, S. Doyle, C. B. Kjellstrand, H. Leduc, M. Limon, V. Luu, P. Mauskopf, A. Miller, T. Mroczkowski, C. Tucker, and J. Zmuidzinas, “Photon noise from chaotic and coherent millimeter-wave sources measured with horn-coupled, aluminum lumped-element kinetic inductance detectors,” *Appl. Phys. Lett.*, vol. 108, no. 8, pp. 083504, Feb. 2016.
- [109] M. Tiuri, “Radio astronomy receivers,” *IEEE Trans. Antennas Propag.*, vol. 12, no. 7, pp. 930–938, Dec. 1964.
- [110] J. W. May, *SiGe integrated circuits for millimeter-wave imaging and phased arrays*, Ph.d. dissertation, 2009.
- [111] J. F. Johansson, “Millimeter-wave imaging theory and experiments,” *Onsala Space Observatory Research Report*, , no. 151, 1986.

- [112] E. Gandini, J. Svedin, T. Bryllert, and N. Llombart, "Optomechanical system design for dual-mode stand-off submillimeter wavelength imagers," *IEEE THz Sci. Technol.*, vol. 7, no. 4, pp. 393–403, Jul. 2017.
- [113] L. Ferrari, O. Yurduseven, N. Llombart, S. J. C. Yates, J. Bueno, V. Murugesan, D. J. Thoen, A. Endo, A. M. Baryshev, and J. J. A. Baselmans, "Antenna coupled MKID performance verification at 850 GHz for large format astrophysics arrays," *IEEE Trans. THz Sci. Technol.*, vol. 8, no. 1, pp. 127–139, 2018.
- [114] A. Neto, S. Monni, and F. Nennie, "UWB, non dispersive radiation from the planarly fed leaky lens antenna - Part II: Demonstrators and measurements," *IEEE Trans. Antennas Propag.*, vol. 58, no. 7, pp. 2248–2258, Jul. 2010.
- [115] A. Neto, N. Llombart, J. J. A. Baselmans, A. Baryshev, and S. J. C. Yates, "Demonstration of the leaky lens antenna at submillimeter wavelengths," *IEEE THz Sci. Technol.*, vol. 4, no. 1, pp. 26–32, Jan. 2014.
- [116] J. Bueno, O. Yurduseven, S. J. C. Yates, N. Llombart, V. Murugesan, D. J. Thoen, A. M. Baryshev, A. Neto, and J. J. A. Baselmans, "Full characterisation of a background limited antenna coupled KID over an octave of bandwidth for THz radiation," *Appl. Phys. Lett.*, vol. 110, no. 23, pp. 233503, Jun. 2017.
- [117] Computer Simulation Technology AG, "CST Microwave Studio," version 2014.00, 2014.
- [118] TICRA, "GRASP," version 10.5.0, 2015.
- [119] J. W. Kooi, G. Chattopadhyay, S. Withington, F. Rice, J. Zmuidzinas, C. Walker, and G. Yassin, "A full-height waveguide to thin-film microstrip transition with exceptional RF bandwidth and coupling efficiency," *International Journal of Infrared and Millimeter Waves*, vol. 24, no. 3, pp. 261–284, Sep. 2003.
- [120] J. Bueno, O. Yurduseven, N. Llombart, S. Yates, A. Neto, and J. Baselmans, "Experimental validation of an MKID coupled dual polarized leaky lens antenna," in *42th International Conference on Infrared, Millimeter and Terahertz Waves*, 2017.
- [121] ITU Radiocommunication Sector, "Recommendation ITU-R P. 676–10, attenuation by atmospheric gases," *International Telecommunications Union*, 2013.
- [122] ITU Radiocommunication Sector, "Recommendation ITU-R P. 840–6 attenuation due to clouds and fog," *International Telecommunications Union*, 2013.
- [123] Kenneth K.O, Wooyeol Choi, Qian Zhong, Navneet Sharma, Yaming Zhang, Ruonan Han, Z. Ahmad, Dae-Yeon Kim, Sandeep Kshattray, Ivan R. Medvedev, David J. Lary, Hyun-Joo Nam, Philip Raskin, and Insoo Kim, "Opening Terahertz for everyday applications," *IEEE Communications Magazine*, vol. 57, no. 8, pp. 70–76, 2019.

- [124] J. M. Edwards and G. M. Rebeiz, "High-efficiency elliptical slot antennas with quartz superstrates for silicon RFICs," *IEEE Trans. Antennas Propag.*, vol. 60, no. 11, pp. 5010–5020, 2012.
- [125] S. Maci and A. Neto, "Green's function of an infinite slot printed between two homogeneous dielectrics-part ii: uniform asymptotic solution," *IEEE Trans. Antennas Propag.*, vol. 52, no. 3, pp. 666–676, 2004.
- [126] D. P. Kasilingam and D. B. Rutledge, "Surface-wave losses of coplanar transmission lines," in *1983 IEEE MTT-S International Microwave Symposium Digest*, May 1983, pp. 113–116.
- [127] Computer Simulation Technology AG, "CST Microwave Studio," version 2017.00, 2017.
- [128] D. Cohen and R. Shavit, "Bi-anisotropic metamaterials effective constitutive parameters extraction using oblique incidence S-parameters method," *IEEE Trans. Antennas Propag.*, vol. 63, no. 5, pp. 2071–2078, 2015.
- [129] "Analytical tool for artificial dielectric layers (ADL GUI)," <http://terahertz.tudelft.nl/Research/project.php?id=114&pid=81>, Accessed: 2020-01-07.
- [130] G. Carluccio and M. Albani, "Efficient adaptive numerical integration algorithms for the evaluation of surface radiation integrals in the high-frequency regime," *Radio Science*, vol. 46, no. 5, 2011.
- [131] M Spirito, G Gentile, and A Akhnoukh, "Multimode analysis of transmission lines and substrates for (sub) mm-wave calibration," in *82nd ARFTG Microwave Measurement Conference*. 2013, pp. 1–6, IEEE.
- [132] E. Gandini, A. Tamminen, A. Luukanen, and N. Llombart, "Wide field of view inversely magnified dual-lens for near-field submillimeter wavelength imagers," *IEEE Trans. Antennas Propag.*, vol. 66, no. 2, pp. 541–549, 2018.
- [133] C. De Martino, Z. Hu, L. Galatro, G. Sarris, and M. Spirito, "Power level control of mm-wave test benches for accurate small and large-signal DUT measurements," in *2016 88th ARFTG Microwave Measurement Conference (ARFTG)*. 2016, pp. 1–4, IEEE.
- [134] R. Hansen, "Focal region characteristics of focused array antennas," *IEEE Trans. Antennas Propag.*, vol. 33, no. 12, pp. 1328–1337, 1985.
- [135] R. Han, Y. Zhang, Y. Kim, D. Y. Kim, H. Shichijo, E. Afshari, and O. Kenneth, "280GHz and 860GHz image sensors using Schottky-barrier diodes in 0.13um digital CMOS," in *2012 IEEE International Solid-State Circuits Conference*, 2012, pp. 254–256.

- [136] R. Al Hadi, J. Grzyb, B. Heinemann, and U. R. Pfeiffer, "A terahertz detector array in a SiGe HBT technology," *IEEE J. Solid-State Circuits*, vol. 48, no. 9, pp. 2002–2010, 2013.
- [137] S. J. Orfanidis, "Electromagnetic waves and antennas," *Rutgers University New Brunswick, NJ*, 2002.
- [138] L. Galatro, A. Pawlak, M. Schroter, and M. Spirito, "Capacitively loaded inverted CPWs for distributed TRL-based de-embedding at (sub) mm-waves," *IEEE Trans. Microw. Theory Techn.*, vol. 65, no. 12, pp. 4914–4924, 2017.
- [139] K. S. Champlin and G. Eisenstein, "Cutoff frequency of submillimeter Schottky-barrier diodes," *IEEE Trans. Microw. Theory Techn.*, vol. 26, no. 1, pp. 31–34, 1978.
- [140] B. Schoenlinner, Wu Xidong, J. P. Ebling, G. V. Eleftheriades, and G. M. Rebeiz, "Wide-scan spherical-lens antennas for automotive radars," *IEEE Trans. Microw. Theory Techn.*, vol. 50, no. 9, pp. 2166–2175, 2002.
- [141] M. K. Saleem, H. Vettikaladi, M. A. S. Alkanhal, and M. Himdi, "Lens antenna for wide angle beam scanning at 79 GHz for automotive short range radar applications," *IEEE Trans. Antennas Propag.*, vol. 65, no. 4, pp. 2041–2046, 2017.
- [142] G. C. Trichopoulos, G. Mumcu, K. Sertel, H. L. Mosbacker, and P. Smith, "A novel approach for improving off-axis pixel performance of terahertz focal plane arrays," *IEEE Trans. Microw. Theory Techn.*, vol. 58, no. 7, pp. 2014–2021, 2010.
- [143] N. Llombart, A. Neto, G. Gerini, M. Bonnedal, and P. de Maagt, "Leaky wave enhanced feed arrays for the improvement of the edge of coverage gain in multibeam reflector antennas," *IEEE Trans. Antennas Propag.*, vol. 56, no. 5, pp. 1280–1291, 2008.
- [144] C. C. Cruz, J. R. Costa, C. A. Fernandes, and S. A. Matos, "Focal-plane multibeam dual-band dielectric lens for Ka-band," *IEEE Antennas Wireless Propag. Lett.*, vol. 16, pp. 432–436, 2017.
- [145] W. Hong, Z. H. Jiang, C. Yu, J. Zhou, P. Chen, Z. Yu, H. Zhang, B. Yang, X. Pang, M. Jiang, Y. Cheng, M. K. T. Al-Nuaimi, Y. Zhang, J. Chen, and S. He, "Multi-beam antenna technologies for 5G wireless communications," *IEEE Trans. Antennas Propag.*, vol. 65, no. 12, pp. 6231–6249, 2017.
- [146] M. Arias Campo, D. Blanco, S. Bruni, A. Neto, and N. Llombart, "On the use of fly's eye lenses with leaky-wave feeds for wideband communications," *IEEE Trans. Antennas Propag.*, vol. 68, no. 4, pp. 2480–2493, 2020.
- [147] S. K. Rao, "Design and analysis of multiple-beam reflector antennas," *IEEE Antennas and Propag. Mag.*, vol. 41, no. 4, pp. 53–59, 1999.

- [148] N. Llombart, D. Emer, M. Arias, and E. McCune, “Fly’s eye spherical antenna system for future Tbps wireless communications,” in *2017 11th European Conference on Antennas and Propagation (EuCAP)*, 2017.
- [149] P. Balling, C. Mangenot, and A. G. Roederer, “Shaped single-feed-per-beam multi-beam reflector antenna,” in *2006 First European Conference on Antennas and Propagation*, 2006, pp. 1–6.
- [150] K. S. Rao, M. Cuchanski, and M. Q. Tang, “Multiple beam antenna concepts for satellite communications,” in *Symposium on Antenna Technology and Applied Electromagnetics [ANTEM 1994]*. 1994, pp. 289–292, IEEE.
- [151] M. Ettorre, R. Sauleau, and L. Le Coq, “Multi-beam multi-layer leaky-wave SIW pillbox antenna for millimeter-wave applications,” *IEEE Trans. Antennas Propag.*, vol. 59, no. 4, pp. 1093–1100, 2011.
- [152] O. A. Iupikov, M. V. Ivashina, N. Skou, C. Cappellin, K. Pontoppidan, and C. G. M. van ’t Klooster, “Multibeam focal plane arrays with digital beamforming for high precision space-borne ocean remote sensing,” *IEEE Trans. Antennas Propag.*, vol. 66, no. 2, pp. 737–748, 2018.
- [153] G. Ruggerini, G. Toso, and P. Angeletti, “An aperiodic active lens for multibeam satellite applications: From the design to the breadboard manufacturing and testing,” in *Proceedings of the 5th European Conference on Antennas and Propagation (EuCAP)*, 2011, pp. 3697–3701.
- [154] J. Hassel, S. O. Dabironezare, E. Gandini, L. Grönberg, H. Sipola, A. Rautiainen, A. Tamminen, M. Leivo, H. Lindström, H. Vasama, A. Luukanen, and N. Llombart, *Dual-band submillimeter-wave kinetic inductance bolometers and an imaging system for contraband object detection*, vol. 10634 of *SPIE Defense + Security*, SPIE, 2018.
- [155] G. V. Trentini, “Partially reflecting sheet arrays,” *IRE Transactions on Antennas and Propagation*, vol. 4, no. 4, pp. 666–671, 1956.
- [156] D. R. Jackson, A. A. Oliner, and A. Ip, “Leaky-wave propagation and radiation for a narrow-beam multiple-layer dielectric structure,” *IEEE Trans. Antennas Propag.*, vol. 41, no. 3, pp. 344–348, 1993.
- [157] H. Chreim, R. Chantalat, M. Thèvenot, U. Naeem, S. Bila, T. Monédière, B. Palacin, Y. Cailloce, G. Caille, and P. De Maagt, “An enhanced Ka -band reflector focal-plane array using a multifeed EBG structure,” *IEEE Antennas Wireless Propag. Lett.*, vol. 9, pp. 1152–1156, 2010.
- [158] A. Neto, M. Ettorre, G. Gerini, and P. De Maagt, “Leaky wave enhanced feeds for multibeam reflectors to be used for telecom satellite based links,” *IEEE Trans. Antennas Propag.*, vol. 60, no. 1, pp. 110–120, 2012.

-
- [159] A. Neto and S. Maci, “Green’s function for an infinite slot printed between two homogeneous dielectrics. i. magnetic currents,” *IEEE Trans. Antennas Propag.*, vol. 51, no. 7, pp. 1572–1581, 2003.
- [160] S. Stein, “On cross coupling in multiple-beam antennas,” *IRE Transactions on Antennas and Propagation*, vol. 10, no. 5, pp. 548–557, 1962.
- [161] N. Llombart, A. Neto, G. Gerini, M. Bonnedal, and P. De Maagt, “Impact of mutual coupling in leaky wave enhanced imaging arrays,” *IEEE Trans. Antennas Propag.*, vol. 56, no. 4, pp. 1201–1206, 2008.
- [162] D. F. Filipovic, G. P. Gauthier, S. Raman, and G. M. Rebeiz, “Off-axis properties of silicon and quartz dielectric lens antennas,” *IEEE Trans. Antennas Propag.*, vol. 45, no. 5, pp. 760–766, 1997.
- [163] J. R. Costa, M. G. Silveirinha, and C. A. Fernandes, “Evaluation of a double-shell integrated scanning lens antenna,” *IEEE Antennas Wireless Propag. Lett.*, vol. 7, pp. 781–784, 2008.
- [164] D. E. Stoltzman, “The perfect point spread function,” *Applied Optics and Optical Engineering*, vol. 9, pp. 113, 1983.
- [165] G. Kirchhoff, “Ueber das verhältniss zwischen dem emissionsvermögen und dem absorptionsvermögen der körper für wärme und licht,” *Annalen der Physik*, vol. 185, no. 2, pp. 275–301, 1860.
- [166] J. A. Nanzer, *Microwave and millimeter-wave remote sensing for security applications*, Artech House, 2012.
- [167] T. G. Blaney, “Radiation detection at submillimetre wavelengths,” *Journal of Physics E: Scientific Instruments*, vol. 11, no. 9, pp. 856, Sep. 1978.

Summary

On the Development of Wideband Direct Detection Focal Plane Arrays for THz Passive Imaging Applications

In the design of millimeter and sub-millimeter wave radiometric imaging systems a persistent goal is the increase in the speed of acquisition of the image while maintaining a high sensitivity. Typically, the highest sensitivity is achieved by cryogenically cooling the detectors, specifically in astronomical applications. However, for the purpose of low-cost imaging applications it is desirable to operate at room temperature. Without cryogenically cooling, the electronic noise introduced by the detectors becomes dominant, making the detectors less sensitive. Resorting to detection architectures containing amplification circuitry might be impractical for implementation in large focal plane arrays (FPAs) fabricated in integrated technologies. This work derives the focal plane architecture that maximizes the imaging speed of radiometers operating at room temperature without using any amplification circuitry. It is shown that in such scenario a practical image acquisition speed can still be achieved when a very broad portion of the THz-band is exploited. Ultimately the imaging speed is maximized when the FPA is undersampled, implying a trade-off in the size of the optics. The analysis is substantiated by a case study using wideband leaky lens antenna feeds operating over a 3:1 relative frequency band.

A wideband leaky slot antenna, integrated in a CMOS technology and suitable for incoherent detection architectures, is demonstrated to efficiently operate from 200 GHz to 600 GHz. Up-to-date, on-chip antennas fabricated in CMOS processes are typically narrowband and are often characterized by low radiation efficiencies. Challenges in efficient CMOS antenna design lie in complying with the strict metal density rules and/or avoiding high ohmic dissipation / surface-wave excitation in the low-resistive bulk silicon. Here, it is shown that antennas that are of leaky-wave nature are in fact extremely suitable for CMOS integration as the effect of the metal density rules is minimized while simultaneously a dielectric lens can be efficiently illuminated over a large portion of the spectrum. The wideband antenna features an average efficiency of 57% over the full bandwidth from 200 GHz to 600 GHz and, with that, it enables ultra wideband applications in CMOS technologies. A second designed double leaky-slot lens antenna is CPW-fed and allowed for a spectral evaluation of gain patterns and impedance using landing probes and an ad-hoc quasi-optical measurement setup, in excellent agreement with simulations.

In order to achieve the required performance for passive imaging, a wideband antenna should efficiently couple incident THz radiation to detectors that are characterized with a

Noise Equivalent Power (NEP) in the order of a $\text{pW}/\text{Hz}^{0.5}$. An accurate modeling of the antenna-detector combination and read-out circuit over a large frequency band is crucial in order to predict radiometric performance in terms of NEP and temperature sensitivity. Here, the lumped element model of a Schottky Barrier Diode (SBD) is extended to predict the circuit performance of a differential diode direct detection circuit that is directly connected to the designed wideband double leaky slot antenna. The differential detection circuit is connected to a load resistor to enable a voltage read-out. A wideband equivalent circuit is constructed that accurately predicts the final performance of the fabricated prototype, verified by high frequency measurements. The measured prototype is characterized with a minimum NEP of $20 \text{ pW}/\text{Hz}^{0.5}$ and an average NEP of $90 \text{ pW}/\text{Hz}^{0.5}$ from 200 GHz to 600 GHz. The deviation from the initially simulated average NEP of $2.7 \text{ pW}/\text{Hz}^{0.5}$ is caused by a discrepancy in the SBDs series resistance and junction capacitance, which compromises the diode responsivity. By using the proposed modeling approaches, the reduction in diode efficiency and system performance is accurately predicted.

Lastly, the preferred antenna architecture is investigated for multi-pixel FPAs that offers high imaging resolutions while maintaining a high efficiency. In multi-beam systems, the performance of a single-beam-per-feed configuration is limited in edge of coverage gain due to either a low roll-off at the cross-over with adjacent beams or a low aperture efficiency of the lens/reflector. A tight sampling of the feeds in the focal plane, required for a high angular resolution and a low roll-off, is directly imposing a limit on the feed directivity and thus the overall gain of the quasi-optical system. In this work, an enhanced feed directivity is realized by resorting to a connected array configuration, supporting a leaky-wave in the presence of a dielectric lens. The dipoles of the array are tapered with a 45° angle such that the amount of pixels is doubled by using the orthogonal polarization. In this manner, a minimum loss in edge of coverage gain of only -5.4 dB is realized w.r.t. the maximum directivity when the considered aperture would have a 100% aperture efficiency. This is an increase of 2.5 dB w.r.t. an equivalently sampled FPA of uniformly illuminated circular apertures. Moreover, the large 3:1 relative bandwidth from 200 GHz to 600 GHz, makes the array very suitable for future passive THz imaging applications. As demonstrator, twelve pixels of the array are connected to Schottky Barrier Diodes to realize a direct detection scenario. Measurements of this demonstrator will be published in paper J1, listed on page 183, that is yet in preparation.

Samenvatting

Over de Ontwikkeling van Breedbandige Incoherente Antenne Clusters voor Passieve THz Cameras

Een bekend probleem bij het ontwerpen van passieve Terahertz (THz) camera's is het verhogen van de verversnelheid van het beeld terwijl de camera gevoelig genoeg blijft om objecten te detecteren. Met name voor astronomische en beveiligings toepassingen worden de camera's daarom vaak cryogeen gekoeld om de extreme gevoeligheid, die voor deze applicaties nodig is, te bereiken. Een groot nadeel van het koelen is dat de camera groot en duur wordt. Daarom is het wenselijk om, ongekoeld, op kamertemperatuur te werken. Helaas wordt zonder cryogene koeling de elektronische ruis, die door de detectoren wordt geïntroduceerd, dominant, waardoor de detectoren minder gevoelig zijn. Wanneer er gebruik wordt gemaakt van detectiearchitecturen die versterkers bevatten, om de camera gevoeliger te maken, kunnen de pixels niet dicht op elkaar zitten waardoor de beeldresolutie wordt verslechterd. Deze dissertatie onderzoekt hoe de pixels naast elkaar moeten worden gezet, i.e. het antenne-cluster, om de verversnelheid van het beeld te maximaliseren terwijl de camera niet gekoeld wordt en wanneer er geen gebruik wordt gemaakt van versterkers. Dit werk laat zien dat, in een dergelijk scenario, een praktische beeldverversingssnelheid nog steeds kan worden behaald wanneer een zeer groot deel van het THz gedeelte van het elektromagnetische spectrum wordt benut. Uiteindelijk wordt de beeldsnelheid gemaximaliseerd wanneer er een afweging wordt gemaakt in de resolutie, hetgeen dat gecompenseerd kan worden door de quasi-optische componenten groter te maken. De analyse wordt onderbouwd met een case study met breedbandige lekkende-golf antennes die een relatieve frequentie bandbreedte hebben van 3:1.

In deze dissertatie is het vervolgens aangetoond dat zulke breedbandige antennes eenvoudig geïntegreerd kunnen worden in CMOS technologieën en daarin met een hoge efficiëntie kunnen opereren van 200 GHz tot 600 GHz. Top op heden zijn on-chip antennes, gefabriceerd in CMOS processen, meestal niet breedbandig en worden vaak gekenmerkt door lage efficiënties. De reden hiervoor is dat het uitdagend is om te voldoen aan de strikte metaaldichtheidsregels die hoge Ohmse verliezen met zich mee kunnen brengen, alsmede kan het exciteren van oppervlaktegolven in het silicium van deze technologie problematisch zijn. In deze dissertatie wordt er gedemonstreerd dat antennes die gebaseerd zijn op het exciteren van lekkende golven uitermate geschikt zijn voor CMOS integratie omdat het effect van de metaaldichtheidsregels wordt geminimaliseerd en tegelijkertijd kan er een diëlektrische lens efficiënt worden gebruikt om de oppervlaktegolven te vermijden. De

breedbandige antenne die hier voorgesteld wordt, biedt een gemiddelde efficiëntie van 57% over de volledige bandbreedte van 200 GHz tot 600 GHz en maakt daarmee ultrabreedbandige toepassingen in CMOS technologieën mogelijk. De metingen van een gefabriceerd prototype lieten een uitstekende overeenkomst zien met de simulaties in zowel de radiatiepatronen, efficiëntie als ingangsimpedantie.

Om de vereiste prestaties voor passieve beeldvorming te kunnen bereiken, moet een breedbandige antenne op een efficiënte wijze de ontvangen THz straling koppelen aan detectoren die gekenmerkt worden met een equivalente ruisvermogen (aangeduid met NEP) die in de orde grootte is van $1 \text{ pW/Hz}^{0.5}$. Een nauwkeurige modellering van de antenne-detectorcombinatie en het detectiecircuit over een grote frequentieband is cruciaal om de radiometrische prestaties te kunnen voorspellen in termen van NEP en de temperatuur gevoeligheid van de camera. In deze dissertatie wordt het equivalente circuit-model van een Schottky Barrier Diode (SBD) uitgebreid om de prestaties van de complete detectiearchitectuur te kunnen voorspellen. De detectiearchitectuur bestaat uit twee SBDs, geplaatst in een differentiële configuratie, verbonden aan de antenne. Een weerstand, geplaatst tussen de twee SBDs, zorgt ervoor dat een verschil in DC-spanning uitgelezen kan worden die proportioneel is aan de ontvangen THz straling. Het breedbandige equivalente circuit van het complete camera systeem is geverifieerd door middel van hoogfrequente metingen die gedaan zijn op een prototype. Het gemeten prototype had een minimale NEP van $20 \text{ pW/Hz}^{0.5}$ en een gemiddelde NEP van $90 \text{ pW/Hz}^{0.5}$ van 200 GHz tot 600 GHz. De gemeten NEP wijkt af van de aanvankelijk gesimuleerde NEP van $2.7 \text{ pW/Hz}^{0.5}$. Het verschil in NEP is verklaard door een afwijking in de weerstand van de SBDs en een hogere junctiecapaciteit, waardoor de responsiviteit van de diode lager was dan aanvankelijk was verwacht. Dankzij de voorgestelde modellerings technieken kon het model eenvoudig worden geüpdatet door middel van laag-frequente metingen. Hierdoor kon de vermindering in efficiëntie van de diode en de uiteindelijke hoog-frequente systeemprestaties nauwkeurig worden voorspeld.

Ten slotte wordt de optimale antenna architectuur onderzocht voor antenne-clusters die een hoge resolutie moeten hebben en tevens een hoge efficiëntie moeten behouden. De prestaties van een configuratie waarin elke pixel van de camera uit maar één antenne bestaat, zijn beperkt. Dit soort configuraties hebben dan een slechte beelddekking tussen aangrenzende pixels in, of ze hebben een lage efficiëntie. Een goede resolutie vereist dat de pixels dicht op elkaar zitten, hetgeen dat dan direct een beperking legt op hoe efficiënt een lens gebruikt kan worden. In deze dissertatie wordt er een betere lensbelichting gerealiseerd door gebruik te maken van antennes die aan elkaar verbonden zijn en tegelijkertijd een lekkende golf kunnen exciteren in de aanwezigheid van een diëlektrische lens. De verbonden antennes zijn dipolen die taps toe lopen met een 45° hoek, zodat het aantal pixels wordt verdubbeld met behulp van de orthogonale polarisatie. Op deze manier wordt een minimaal verlies van dekking, tussen twee pixels in, van slechts -5.4 dB gerealiseerd, in vergelijking tot de maximale dekking die theoretisch mogelijk is wanneer de lens met een 100% efficiëntie belicht zou worden. Dit is een toename van 2.5 dB in vergelijking met een antenne-cluster, met eenzelfde resolutie, maar die bestaat uit ideale antennes die niet overlappen. Bovendien maakt de grote 3:1 relatieve bandbreedte van 200 GHz tot

600 GHz het voorgestelde antenne-cluster zeer geschikt voor toekomstige passieve THz-beeldvormingsapplicaties. Als prototype zijn er twaalf pixels van de array verbonden met SBDs. Metingen van deze demonstrator worden gepubliceerd in paper J1, vermeld op page 183, welke nog in voorbereiding is.

List of Publications

Journal Papers

- J1.** S.L. van Berkel, D. Cavallo, E.S. Malotiaux, M. Spirito, A. Neto and N. Llombart, "Leaky-Wave Enhanced Connected Array with Polarization Re-Usage for Tightly Sampled Multi-Beam Applications," *IEEE Transaction on Antennas and Propagation*, in preparation.
- J2.** S.L. van Berkel, E.S. Malotiaux, C. De Martino, M. Spirito, D. Cavallo, A. Neto and N. Llombart, "Wideband Modeling of Radiometric Performance for a Differential THz Direct Detector in CMOS," *IEEE Transaction on Terahertz Science and Technology*, in preparation.
- J3.** S.L. van Berkel, E.S. Malotiaux, C. De Martino, M. Spirito, D. Cavallo, A. Neto and N. Llombart, "Wideband Double Leaky Slot Lens Antennas in CMOS Technology at Sub-millimeter Wavelengths," *IEEE Transaction on Terahertz Science and Technology*, available for early access.
- J4.** S. Hahnle, O. Yurduseven, S.L. van Berkel, N. Llombart, J. Bueno, S. Yates, V. Murugesan, D. Thoen, A. Neto, J. Baselmans, "An Ultra-Wideband Leaky Lens Antenna for Broadband Spectroscopic Imaging Applications," *IEEE Transactions on Antennas and Propagation*, vol. 68, no. 7, pp. 5675-5679, 2020.
- J5.** S.L. van Berkel, O. Yurduseven, A. Freni, A. Neto, N. Llombart, "THz Imaging Using Uncooled Wideband Direct Detection Focal Plane Arrays," *IEEE Transactions on Antennas and Propagation*, vol. 7, no. 5, pp. 481-492, 2017.
- J6.** S.L. van Berkel, A. Garufo, N. Llombart, A. Neto, "A Quasi-Analytical Tool for the Characterization of Transmission Lines at High Frequencies," *IEEE Antennas and Propagation Magazine*, vol. 58, no. 3, pp. 82-90, 2016.

Conference Papers

- C1.** S.L. van Berkel, E.S. Malotiaux, C. de Martino, M. Spirito, D. Cavallo, A. Neto and N. Llombart, "System NEP Verification of a Wideband THz Direct Detector

- in CMOS," *In Proc. of 45th International Conference on Infrared, Millimeter, and Terahertz Waves (IRMMW-THz 2020)*, Buffalo, New York, USA, Nov. 8-13 2020.
- C2.** S.L. van Berkel, E.S. Malotiaux, C. de Martino, M. Spirito, D. Cavallo, A. Neto and N. Llombart, "Experimental Modeling and High-Frequency Characterization of NEP for a CMOS THz Imager," *In Proc. of IEEE Antennas and Propagation Society International Symposium (APS 2020)*, Montreal, Canada, July. 5-10 2020.
- C3.** S.L. van Berkel, E.S. Malotiaux, C. de Martino, M. Spirito, D. Cavallo, A. Neto and N. Llombart, "Experimental Validation of System NEP of a Single-Pixel THz Imaging Camera in CMOS," *In Proc. of 13th European Conference on Antennas and Propagation (EuCAP 2020)*, Copenhagen, Denmark, March. 16-20 2020.
- C4.** S.L. van Berkel, E.S. Malotiaux, B. van den Bogert, M. Spirito, D. Cavallo, A. Neto and N. Llombart, "High resolution passive THz imaging array with polarization reusage in 22nm CMOS," *In Proc. of 44th International Conference on Infrared, Millimeter, and Terahertz Waves (IRMMW-THz 2019)*, Paris, France, Sep. 1-6 2019.
- C5.** S.L. van Berkel, E.S. Malotiaux, B. van den Bogert, M. Spirito, D. Cavallo, A. Neto and N. Llombart, "Dual Polarized THz Imaging FPA in 22nm CMOS," *In Proc. of IEEE Antennas and Propagation Society International Symposium (APS 2019)*, Atlanta, Georgia, USA, Jul. 7-12 2019.
- C6.** S.L. van Berkel, E.S. Malotiaux, M. Spirito, D. Cavallo, A. Neto and N. Llombart, "Wideband single-pixel THz imager in 28nm CMOS," *In Proc. of IEEE Antennas and Propagation Society International Symposium (APS 2019)*, Atlanta, Georgia, USA, Jul. 7-12 2019.
- C7.** S.L. van Berkel, E.S. Malotiaux, D. Cavallo, M. Spirito, A. Neto and N. Llombart, "CMOS connected array with polarization reusage for passive THz imaging applications," *In Proc. of 13th European Conference on Antennas and Propagation (EuCAP 2019)*, Krakow, Poland, Mar. 31 - Apr. 5 2019.
- C8.** S.L. van Berkel, E.S. Malotiaux, D. Cavallo, M. Spirito, A. Neto and N. Llombart, "Optical performance of a wideband 28nm CMOS double bow-tie slot antenna for imaging applications," *In Proc. of 43rd International Conference on Infrared, Millimeter and Terahertz Waves (IRMMW-THz 2018)*, Nagoya, Japan, Sep. 9-14 2018.
- C9.** S.L. van Berkel, E.S. Malotiaux, D. Cavallo, M. Spirito, A. Neto and N. Llombart, "Wideband single pixel radiometer in 28 nm CMOS technology for low-cost imaging applications," *In Proc. of 12th European Conference on Antennas and Propagation (EuCAP 2018)*, London, U.K., Apr. 9-13 2018. Nominated, and runner-up, for the Best Antenna Design and Application Award

- C10.** S.L. van Berkel, E.S. Malotaux, D. Cavallo, M. Spirito, A. Neto and N. Llombart, "Wideband single pixel radiometer in CMOS," *In Proc. of 42nd International Conference on Infrared, Millimeter and Terahertz Waves (IRMMW-THz 2018)*, Cancun, Mexico, Aug. 27 - Sep. 1 2017.
- C11.** S.L. van Berkel, O. Yurduseven, A. Freni, A. Neto and N. Llombart, "On the Imaging Speed of Wideband Direct Detection FPAs," *In Proc. of IEEE Antennas and Propagation Society International Symposium (APS 2017)*, San Diego, CA, USA, July 2017.
- C12.** S.L. van Berkel, O. Yurduseven, A. Freni, A. Neto and N. Llombart, "On the Design of Uncooled Wideband Direct Detection Focal Plane Arrays," *In Proc. of 11th European Conference on Antennas and Propagation (EuCAP 2017)*, Paris, France, March 2017.
- C13.** S.L. van Berkel, N. Llombart and A. Neto, "Complex Characteristic Impedance of Transmission Lines At High Frequencies," *In Proc. of 10th European Conference on Antennas and Propagation (EuCAP 2016)*, Davos, Switzerland, 10-15 April 2016.
- C14.** S.L. van Berkel, D. Cavallo, N. Llombart and A. Neto, "THz silicon-integrated CAMERA for low-cost imaging applications (TiCAM)," *In Joint Symposium URSI-Benelux, NARF, and IEEE AP-S Meeting on Smart Antennas and Propagation*, Enschede, The Netherlands, December 2015.
- C15.** S.L. van Berkel, A. Garufo, A. Endo, N. Llombart and A. Neto, "Characterization of Printed Transmission Lines at High Frequencies," *In Proc. of 9th European conference on Antennas and Propagation (EuCAP 2015)*, Lisbon, Portugal, April 2015.

Thesis Co-Supervised

- T1.** B. van den Bogert, "28 nm CMOS Array of Strips for Pedestrian Detection," M.Sc. thesis, Delft University of Technology, Delft, The Netherlands, July. 2017.

Propositions Accompanying the Doctoral Thesis

1. Wideband antennas have not yet been truly exploited for THz imaging applications. (this thesis)
2. The key contribution of this work is to provide the understanding that a rigorous wideband modelling of the system and, together with a careful detector characterization, will be sufficient to connect all the dots in the near future for enabling fully passive THz imaging. (this thesis)
3. Leaky-wave connected array configurations are the only likely candidate to realize a diffraction limited resolution in lens-coupled THz imaging arrays while maintaining a high efficiency over a broad frequency bandwidth. (this thesis)
4. Measuring device properties at 500 GHz can be extremely challenging. Fortunately, sometimes all you need to know is the behaviour at 10 GHz and the proper tools to extrapolate this to the submm-wave band. (this thesis)
5. When one is prototyping in CMOS technologies and at THz frequencies, the turnaround time from a design to an actual measurement is of such long duration that it does not allow for learning by trial and error and succeeding by chance.
6. Collaborating with people from different technical disciplines on a system development requires patience and forces you to learn the jargon of other communities. It is however most useful and rewarding as it expands your knowledge in areas where you have less experience.
7. A failed prototype might be the best thing that can happen in a Ph.D., how ironic it may sound.
8. The path towards the Ph.D. degree is certainly not all fun and can be extremely frustrating. But once the end is in sight, you see that these are not the disadvantages, but merely the reasons that doing a Ph.D. is a valuable experience.
9. For a technical dissertation such as this one, it is virtually impossible that the translated version of the Summary to the Dutch language is clearer to the Dutch readers than the English version.

10. *“It is through science that we prove, but through intuition that we discover.”* – Henri Poincaré. Intuition can only be obtained with experience in the study of proven science.
11. As long as you have a safety net that is your family, friends and loved ones, never decorate the walls of your comfort zone with your favorite excuses. Tear these walls down and allow yourself to fail and grow.

These propositions are considered opposable and defensible, and as such have been approved by the promoters prof. dr. ir. A. Neto and prof. dr. N. Llombart Juan

About the Author



Sven van Berkel was born on May 1st, 1991 in Leiden, the Netherlands. Sven received the B.Sc. and M.Sc. (cum laude) degrees in Electrical Engineering from Delft University of Technology (TUDelft), Delft, the Netherlands, in 2012 and 2015 respectively. During his master he specialized in telecommunications engineering with a focus on radar systems, antennas and electromagnetic wave theory. He performed an internship and his M.Sc. thesis project at the THz-Sensing group at TU Delft. During his M.Sc. thesis, he developed a quasi-analytical software-tool that can characterize printed transmission lines in terms of radiation losses, ohmic losses and characteristic impedance.

From May 2015 till July 2020, he pursued the Ph.D. degree at the THz-Sensing Group. During this period, his research interests included passive imaging systems, ultra-wideband antennas for millimeter and sub-millimeter wave applications, quasi-optical systems and analytical/numerical techniques in electromagnetics, antenna design and transmission line characterization. This research has been carried out under the supervision of Prof. Andrea Neto and Prof. Nuria Llombart as promoters, and Dr. Daniele Cavallo as co-promoter. The work resulted in 6 journal publications (1 Invited Paper) and 15 conference papers (1 nominated and runner up for the *Best Antenna Design and Application Award* in the European Conference on Antennas and Propagation (EuCAP), London, United Kingdom, April 9-13 2018). During his Ph.D., he has co-supervised one M.Sc. student in the THz-Sensing group.

Acknowledgments

It is a strange and special feeling, arriving at the writing of the *Acknowledgments* of my own doctoral dissertation. I have read many of those in the past years, of friends and colleagues, but mine always seemed to be still far away. And suddenly I realize that I am there, the end of an era arrived (i.e. nearly 11 years at TU Delft of which 7 years at the THz-Sensing group). And indeed, although my name is written on the front cover, I arrive at this writing knowing that this work could not have been realized without the support from and collaboration with countless of people. I feel very grateful that I had the opportunity to arrive here and I have many people to thank for it.

Foremost, I would like to thank Prof. Andrea Neto and Prof. Nuria Llombart. I think it is impossible to get any luckier than with having you two both as my promoters. Not only your boundless knowledge, dedication and work ethics brings you to the top of our research field. But also the time, energy and trust that you put in your students never seem to deplete. This combination defines a personality that makes you both true role models to look up to, and I really think that the high quality of leadership and supervision that you communicate, is quite rare. Andrea, I am very thankful you convinced me to do an internship at the THz-sensing group, that you saw potential in me which I still needed to unlock myself. The time you personally spent on me during those first years made me confident and really prepared me to do a PhD, it would have been impossible without. Nuria, that you are helping me on a major revision of my paper for hours on your free Saturday (sorry Juan) says it all. I feel blessed to have learned a lot of my academic skills from you personally. I hope to be able to work with you both for many years to come; it for sure has been a pleasure to work with you in the past 7 years.

I would like to thank Dr. Daniele Cavallo for being my co-promoter and supervisor. Your door was always open to ask technical questions and to discuss any antenna design problems I encountered. You always took the patience and time and you have taught me several essential analytical skills in antenna design.

The TiCAM project was certainly tough to manage thanks to its multi-disciplinary nature and the ambitious goals that were set. Thank you, Dr. Marco Spirito for guiding and shaping this project with your continued enthusiasm. I hope that the project can have a continuation in some form, as we are close to some major breakthroughs!

Important driving forces of the TiCAM project came from the much valued user committee meetings with Maarten Vertregt and Prof. Kostas Doris, both from NXP Semi-

conductors. Your time and input throughout the past years shaped the project on many technical and system levels. I would like to give a special thanks to Kostas for his time to thoroughly read this thesis and his willingness to be part of the defense committee.

And of course, this dissertation would end after Chapter 3, if it were not for Satoshi and Carmine. I learned an incredible amount from you both and the major part of this thesis is thanks to your inputs of many many hours. Satoshi, you showed me a world of tape-outs, the “all-nighters” on the university to reach those deadlines and the immense difficulties in designing in CMOS technology. Your knowledge about electronics goes way beyond my horizon and I am glad you could show me some of it. Carmine, you managed to do a PhD in the most tough field of electrical engineering I have ever encountered in my life: calibration and characterization at submm-wavelengths is truly wizardry. Getting acquainted to that, by annoyingly standing by your side while you were landing the probes with an incredible precision, was most valuable to me. It was very nice to have had the opportunity to work with and learn from you both. Going beyond the boundary of merely designing an antenna, to touch the worlds of electronics, detector design and measurements is one my most treasured outcomes of my PhD.

Besides the people that first-hand contributed to this dissertation, it is a work environment that defined how happy you are in going to work. And I must say that a lot of people contributed to that.

As an intern, I started in the office with Dr. Daniele Cavallo, Dr. Erio Gandini and Dr. Maria Alonso. Wow, quite overwhelming to work in an office with so many doctors while I was an undergraduate. Erio, you taught me some words of Italian, but more importantly, you made my first conference to Lisbon a very fun experience. Maria, thank you very much for helping me to realize the most incredible next career step I could ever imagine. I look forward working together with you!

In my time as an undergraduate I became familiar with how its like to do a PhD, thanks to the first generation of Spartans: Waqas, Beatriz, Ozan and Alessandro. When we moved from the 14th floor to the lower building I finally started my own PhD and I was in luck to share the office with Waqas, Ozan and Alessandro. I really enjoyed that time and I have seen you all defend your thesis one by one. Waqas, your motivation was one of the reasons to do a PhD myself. Alessandro, we not only shared the office and many conferences, but also the smallest bed that was available in whole of Florence.

I was not alone during this 7-year course. No, there was always Shahab and Harshitha to count on. The brothers in arms. You were both there from the very beginning and we all made it to the end. It was so nice to do this journey with you both. Shahab, we look like an old couple traveling all over the world together and do hours of sightseeing. Croatia, England, Switzerland, Mexico, Poland, Japan and France. We visited Maya ruins, the Nachi falls and the weirdest shops in Japan. It is good we didn't share the office, because I would not be finished by now. Instead, I shared the office with three amazing women, i.e. Harshitha, Marta and Cristina. I really looked forward every day to go to the office thanks to you guys! Although we were never roommates and we didn't start at the same time, Alejandro and Ralph, the gang wouldn't be complete without you two guys. I loved

working with you, as well as the great times at conferences.

But of course, this amazing work environment is thanks to a lot of other people I have worked with in the past years: Sebastian, Sjoerd, Arturo, Huasheng, Riccardo, David, Everdine, Paolo, Akira, prof. Jochem Baselmans, Kenichi, Juan, Bruno, Sander, Kevin, Pieter, Giorgio, Darwin and the many bright bachelor- and master students that are working or already graduated in this group. A special thanks to Bart, I got the pleasure to supervise you during your master thesis from which I also learned very much.

Combining work with a good personal life is vital. I would like to thank the co-founders of *Haus Wunderlich*, Sven and Ruben, for the crazy times we had and still have in Rotterdam. Your rooms in the house were later filled by Michel and Koos, and we are, according to tradition, still using the *Escalation Furniture* on almost a weekly basis, that helped me through the writing of this thesis during Corona times. This 11-year story of TU Delft could never have been completed without my dear friends of *JC Kabel*. I am looking forward to our next *lustrumreis* somewhere in this world! I also would like to thank my dear friends from my hometown Lisse. Guido, it has been too long ago that we went for mountaineering in the Alpes, or that we brewed some *Code Rood* with you, Thijs.

My beautiful love and better half, Elske, wow ... I still cannot believe this is happening. I only believe how lucky and happy I feel since I met you. It should not have been easy, to start a relationship knowing that I had an opportunity to work in a time-zone 9-hours away. But for us, it turned out... it was easy: Here we are, a ring on our fingers after our *Zoom* wedding during Corona times, and hopefully soon an appointment ready to get our visa to emigrate to California for a couple of years. Thank you for taking this leap with me, I love you.

To my lovely family, bedankt pap en mam. Het is heel fijn om te weten dat ik altijd zo'n liefhebbende en zorgzame familie achter me heb staan. Jullie hebben mij altijd gesteund in wat ik doe en het is natuurlijk niet makkelijk dat ik en je lieve schoondochter voor een aantal jaar naar de andere kant van de wereld gaan. De familie is zeker niet compleet zonder mijn lieve tweelingzus Amber, mijn broer en schoonzus Niels & Kirsten, op wie ik altijd kan bouwen. Ik hou van jullie allemaal.